

# **Targeted therapeutics against cancer and infections**

Identification and characterization of  
human ecto-nucleotidase (CD39) and  
coronaviral protease (M<sup>pro</sup>) inhibitors

Dissertation

zur

Erlangung des Doktorgrades (Dr. rer. nat.)

der

Mathematisch-Naturwissenschaftlichen Fakultät

der

Rheinischen Friedrich-Wilhelms-Universität Bonn

vorgelegt von

**Laura Freya Andrea Schäkel**

aus

Düren

Bonn 2022



Angefertigt mit Genehmigung der Mathematisch-Naturwissenschaftlichen Fakultät  
der Rheinischen Friedrich-Wilhelms-Universität Bonn

Gutachterin: Prof. Dr. Christa E. Müller

Gutachter: Prof. Dr. Gerd Bendas

Tag der Promotion: 21.09.2022

Erscheinungsjahr: 2022

Die vorliegende Arbeit wurde in der Zeit von August 2018 bis Juni 2022 am Pharmazeutischen Institut der Rheinischen Friedrich-Wilhelms-Universität Bonn unter Leitung von Prof. Christa E. Müller durchgeführt.

## Content

1	Abstract .....	3
2	Introduction.....	5
2.1	Enzymes .....	5
2.1.1	General function and relevance .....	5
2.1.2	Classification .....	5
2.1.3	Enzymes as drug targets.....	6
2.1.4	Characterization of enzymatic activity .....	8
2.2	Ecto-nucleotidases .....	18
2.2.1	Purinergic signaling.....	18
2.2.2	Nucleotide metabolism .....	22
2.2.3	Ecto-nucleoside triphosphate diphosphohydrolases (E-NTPDases).....	24
2.2.4	Ecto-5'-nucleotidase (eN, CD73) .....	53
2.2.5	CD39-CD73 Axis.....	56
2.3	SARS-CoV-2 Main protease .....	57
2.3.1	Viral replication and function of proteases.....	57
2.3.2	Structure of M <sup>pro</sup> .....	58
2.3.3	Relevance of M <sup>pro</sup> as a drug target .....	59
2.3.4	Assays for determination of M <sup>pro</sup> activity .....	60
2.3.5	Inhibitors of M <sup>pro</sup> .....	66
3	Publications on NTPDases.....	78
3.1	Anthraquinone derivatives .....	78
3.2	ARL67156.....	81
3.3	2-Substituted Thienotetrahydropyridines .....	85
3.4	Ceritinib.....	88
4	SARS-CoV-2 Main protease experiments.....	91
4.1	Development of an activity assay for SARS-CoV-2 M <sup>pro</sup> .....	91
4.1.1	Assay establishment and validation.....	92
4.1.2	Comparison of substrates .....	95
4.2	Characterization of first inhibitors of M <sup>pro</sup> .....	98
4.2.1	Reference inhibitors disulfiram and ebselen .....	98
4.2.2	Chloroacetamide derivatives .....	99
4.2.3	Pathogen Box .....	101
4.2.4	SARS-CoV-1 M <sup>pro</sup> inhibiting pyridyl esters .....	102
4.3	High-throughput screening campaign for M <sup>pro</sup> inhibitors .....	107
4.4	Characterization of hit compounds .....	109
4.4.1	Tocris library.....	109
4.4.2	Xanthine derivatives .....	111
4.4.3	Apicidine derivatives .....	113

---

4.4.4	Characterization of guanidine derivatives .....	115
4.5	M <sup>pro</sup> inhibition by pyridyl esters and related compounds .....	120
4.5.1	Structure-activity relationship studies of pyridyl esters .....	120
4.5.2	Stability of pyridyl esters towards glutathione .....	142
4.5.3	Stability of enzymatic activity and enzyme-pyridyl thioester bond.....	148
4.6	Experimental .....	151
4.6.1	SARS-CoV-2 M <sup>pro</sup> activity assay.....	151
5	Publications on M <sup>pro</sup> .....	154
5.1	Electrophilic Arylketones .....	154
6	Summary .....	157
6.1	Ecto-Nucleoside triphosphate diphosphohydrolases (NTPDases) .....	157
6.2	SARS-CoV-2 main protease .....	160
7	Abbreviations .....	164
8	References .....	167
9	Acknowledgements.....	188
10	Appendices .....	I
10.1	Featured publications .....	I

## 1 Abstract

The main objectives of this thesis were the development, characterization and optimization of enzyme inhibitors (i) for the human ecto-nucleotidase CD39, and (ii) for the main protease of the human-pathogenic coronavirus SARS-CoV-2, to provide novel treatment options for tumors and infections. Inhibitors of these enzymes have the potential to abrogate the damaging proliferation of cancer cells, or viruses, respectively, with only limited or negligible harming of the human organism. The search for small molecule inhibitors was conducted by analyzing the compounds' effects on enzyme kinetics using optical plate reader- and capillary electrophoresis-based assays. By critical evaluation of the generated data, we were able to identify and subsequently optimize potent, selective, and metabolically stable inhibitors for both target enzymes.

Ecto-nucleoside triphosphate diphosphohydrolase 1 (NTPDase1/CD39) is the most prominent enzyme hydrolyzing extracellular nucleotides, e.g. ATP and ADP, yielding AMP. Its inhibitors have the potential to increase the concentrations of extracellular adenosine triphosphate (ATP), which stimulates the cellular immune system by activation of purinergic P2X and P2Y receptors. At the beginning of the work for this thesis no potent small molecule CD39 inhibitor with suitable pharmacokinetic properties was available. Therefore, we set out to improve known inhibitors, and to identify new lead structures. For this purpose, structure-activity-relationships of anthraquinone derivatives, nucleotide derivatives and analogs, and various heterocyclic compounds were analyzed. The analog ARL67156 of the CD39 substrate ATP, and its two most potent derivatives were found to be moderately potent, competitive inhibitors of NTPDases, also inhibiting the AMP-hydrolyzing enzyme ecto-5'-nucleotidase (CD73). We discovered that these nucleotide derivatives possess only poor metabolic stability, which limits their utilization in *in vivo* studies. We confirmed that the unmetabolized anti-thrombotic prodrug ticlopidine acts as a non-competitive inhibitor of CD39. Furthermore, we demonstrated that closely related, but metabolically stable 2-substituted thienotetrahydropyridine derivatives have equal potencies in inhibiting CD39, but improved target selectivity. A screening approach focused on a self-assembled approved protein kinase inhibitor library was successful leading to the identification of the CD39-inhibitory activity of ceritinib. This anti-cancer drug has an excellent metabolic stability. It inhibits CD39 non-

competitively with a potency in the low micromolar range, which might contribute to its potent anti-cancer activity.

A project on the development of antiviral drugs against COVID-19 was initiated at the start of the pandemic in 2020. We selected the coronavirus main protease (SARS-CoV-2 M<sup>pro</sup>) as a suitable target, since it is essential for the viral replication cycle. By collaborating within an interdisciplinary team, we quickly established an enzyme activity assay utilizing a novel fluorogenic substrate. This enabled us to screen and evaluate various inhibitor classes. The focus of this part of the thesis was on the characterization of pyridyl esters, which are covalently binding inhibitors with nanomolar potencies. Along with their time-dependent effect on protease activity, their stabilities were assessed, in order to select the most promising lead structures for future drug development.



## 2 Introduction

### 2.1 Enzymes

#### 2.1.1 General function and relevance

Biological life is defined by growth, metabolism and reproduction. This necessitates biochemical reactions, which transform and combine molecules in a timely manner. The cleavage and formation of chemical bonds is accelerated by enzymes up to a trillion ( $10^{12}$ )-fold,<sup>1</sup> which are therefore designated as the body's catalysts. Enzymes contain a so-called active site, which accommodates the chemically active groups of the reactants and decreases the activation energy by stabilizing the transition state of the chemical reaction.<sup>2</sup> Thereby, the equilibrium concentration of educt and product are achieved faster,<sup>3</sup> which allows the biological organism to adapt to its environment. The velocity of the reactant substrate conversion to its respective product is influenced by concentrations of substrate and enzyme, pH, temperature and in some cases the presence of cofactors.<sup>1</sup> Furthermore, essentially all enzymes are regulated by substances that modulate their catalytic activity or expression levels and thereby manage physiological processes and signaling. For example, some biochemical pathways are subjected to a feedback control, where the product of the enzymatic reaction inhibits further enzymatic conversion of the substrate.<sup>3</sup>

Next to their importance for physiological processes, enzymes are utilized in biotechnological products and manufacturing. Technical companies add enzymes to consumer products, like lipases in washing powder, to increase their effectiveness. Food production relies on enzymes for the transformation of ingredients, e.g. rennet contains a mix of protease, pepsin and lipase enzymes, which curdle milk in cheese production. In medicine, enzymes are used as therapeutics in replacement therapy,<sup>4</sup> as well as in diagnostics and as target structure for drugs which treat diseases by modulation of the enzyme's activity.

#### 2.1.2 Classification

The International Union for Biochemistry and Molecular Biology (IUBMB) categorizes enzymes by type of catalyzed reaction into seven major classes (see **Table 1**).<sup>1</sup> The enzyme commission number (EC number) entails a code consisting of four numbers,

which define the catalyzed reaction with increasing precision. In 2018 a 7<sup>th</sup> category was amended, comprising the translocases, which move molecules through membranes *versus* a concentration gradient by consumption of the energy-carrier and co-factor adenosine triphosphate (ATP).

**Table 1.** Enzyme commission (EC) classification system and examples of drugs targeting an enzyme of this class.<sup>3</sup> Examples and EC codes were obtained from the comprehensive enzyme information system BRENDA.

<b>EC number</b>	<b>Enzyme class</b>	<b>Type of reaction</b>	<b>Example</b>	<b>Drug targeting example</b>
<b>1</b>	Oxidoreductases	Oxidation and reductions	Cyclooxygenase (COX) <b>EC 1.14.99.1</b>	Acetylsalicylic acid
<b>2</b>	Transferases	Group transfer reactions	Anaplastic lymphoma kinase (ALK) <b>EC 2.7.10.1</b>	Ceritinib
<b>3</b>	Hydrolases	Hydrolysis reactions	Phosphodiesterase enzyme (PDE5) <b>EC 3.1.4.17</b>	Sildenafil
<b>4</b>	Lyases	Non-hydrolytic substitution, elimination or oxidation	Aromatic-L-amino-acid decarboxylase (DDC) <b>EC 4.1.1.28</b>	Carbidopa
<b>5</b>	Isomerases	Isomerization and intramolecular group transfers	Steroid DELTA-isomerase <b>EC 5.3.3.1</b>	Trilostane
<b>6</b>	Ligases	Joining two substrates at the expense of ATP hydrolysis	Acetyl-CoA carboxylase <b>EC 6.4.1.2</b>	Firsocostat (GS-0976) (investigational, not approved)
<b>7</b>	Translocases	Transport of ions or molecules across membranes	Gastric H <sup>+</sup> /K <sup>+</sup> ATPase <b>EC 7.2.2.19</b>	Omeprazol (prodrug)

### 2.1.3 Enzymes as drug targets

Therapeutic drugs aim to modulate physiological functions of human organisms. This is mostly achieved by ligands binding to target proteins, such as transporters, receptors and

enzymes.<sup>3,5</sup> As enzymes are involved in many pathophysiological and physiological conditions, it is no surprise that the largest group of human drug targets, with approximately 41.6 %, are enzymes.<sup>6</sup> Most druggable proteins are embedded within cell membranes (32.9%), while extracellular targets comprise 10.5% and intracellular targets, which are located in the cytoplasm (23.8%), organelles (18.9%) or the nucleus (8.4%) constitute a lower amount as they are more difficult to attack.<sup>7</sup>

Furthermore, bacterial and viral infections can be combated by preventing essential pathogen enzyme-catalyzed reactions, resulting in death or decrease of reproductive rates. Advantageously, pathogen enzymes are distinct from their human analogs or, more ideally, human analogs are nonexistent, which allows for a targeted, effective inhibition with few side effects.<sup>3</sup> Examples are antibiotics like penicillins and cephalosporins abrogating the construction of the bacterial cell wall by inhibition of transpeptidases, named penicillin binding proteins, which catalyze the peptidoglycan synthesis.<sup>3</sup> The antiviral prodrug aciclovir is converted by the viral thymidine kinases to the monophosphate and subsequently by cellular kinases to its active triphosphate, which inhibits the viral DNA polymerase. This mechanism results in accumulation of the active drug solely in infected cells, effectively decreasing viral replication.<sup>8</sup>

Most of the small molecules inhibiting enzymes competitively bind to the orthosteric, substrate binding site. Reversible inhibitors associate and dissociate to and from the enzyme in an equilibrium depending on their binding affinity to each other.<sup>1</sup> Rational design based on the substrate angiotensin I enabled the development of angiotensin converting enzyme (ACE) inhibitors captopril and enalapril. These false substrates are binding to, and reversibly block the catalytic site of the enzyme, thereby preventing the conversion of the natural substrate to the product angiotensin II.<sup>8</sup> Inhibitors designed to mimic the transition state between substrate and product show increased potency, compared to substrate analogs. For example, the renin inhibitor aliskiren resembles the tetrahedral structure of the intermediate, but is stable to hydrolysis.<sup>3</sup> Alternatively, competitive inhibitors can attach to the co-factor binding site. The mechanism of action of competitive protein kinase inhibitors, like ceritinib, comprises the occupation of the co-factor ATP binding region, which impedes the transfer of phosphate groups.<sup>9</sup>

Irreversible inhibitors covalently bind to key residues of the active site of the enzyme rendering it inactive for the remainder of its lifespan.<sup>3</sup> Two well-known examples of

irreversible enzyme inhibitors are acetylsalicylic acid, a cyclooxygenase (COX) inhibitor and selegiline an inhibitor of monoaminooxidase B (MAO-B).<sup>8</sup> Pseudo-irreversible inhibitors bind so tightly to the enzyme, that they basically have the same effect as an irreversible inhibitor. The acetylcholinesterase (AChE) inhibitor rivastigmine is a representative of this inhibitor class.<sup>8</sup> So-called suicide substrates are transformed to reactive irreversible inhibitors by their respective target enzyme. For example, clavulanic acid mimics the substrate of  $\beta$ -lactamase, penicillin. The  $\beta$ -lactam ring structure is attacked by  $\beta$ -lactamase, which leads to a ring-opening and irreversible, covalent bond formation of clavulanic acid to the active site residues serine and histidine. This mechanism of action prevents the hydrolysis of penicillin, overcoming penicillin resistance of bacteria.<sup>3</sup>

Other classes of inhibitors do not target the catalytic site, but attach to an allosteric binding site. These compounds can be subdivided into non-competitive and un-competitive inhibitors. Non-competitive inhibitors bind to the free enzyme without affecting its substrate binding affinity. One well-known example of a non-competitive inhibitor is efavirenz, a human immunodeficiency virus (HIV) reverse transcriptase inhibitor.<sup>3</sup> Un-competitive inhibitors only adhere to their respective allosteric pocket of an enzyme-substrate (ES) complex. In contrast to competitive inhibitors, an increased substrate concentration cannot neutralize an un-competitive inhibitor, but will increase its potency due to the high availability of the ES-complex.<sup>3</sup> This inhibition type is uncommon and few drugs with this mechanism are approved, as these modulators can derail physiological processes and lead to cell death.<sup>10</sup> Lithium ions were shown to increasingly inhibit inositol monophosphatase at higher substrate concentrations.<sup>5</sup>

#### 2.1.4 Characterization of enzymatic activity

##### **Basal enzymatic activity**

The course of an enzymatic conversion of a single substrate can be represented as depicted in **Figure 1**.



**Figure 1.** Reaction of a single substrate enzyme. The enzyme (E) binds to the free substrate (S) to form a transitional ES-complex, which dissociates back to enzyme and substrate, characterized by the dissociation constant  $K_s$ , or converts the substrate to product (P) at the catalytic rate  $k_{cat}$ . At low substrate concentrations the velocity will depend mainly on the formation of the ES-complex and thereby on the dissociation constant  $K_s$ .<sup>1</sup>

The analysis of enzyme-catalyzed reactions in a laboratory setting relies on standardized protocols and the establishment of steady-state conditions, which enable the determination of parameters, like catalytic efficiency and substrate affinity that describe the enzyme's kinetics.<sup>1</sup> In the time course of the substrate's conversion to product, the initial reaction rate during the catalysis of the first 10% of substrate can be described by a linear function.<sup>11</sup> The velocity of this steady-state reaction can be determined with Henri-Michaelis-Menten equation:

$$v = \frac{V_{max}[S]}{K_m + [S]} = \frac{V_{max}}{1 + \frac{K_m}{[S]}}$$

**Equation 1.** Henri-Michaelis-Menten equation

The Michaelis constant  $K_m$  is defined as the substrate concentration for half maximal velocity ( $V_{max}$ ) of an enzyme's catalytic capability, which is achieved at infinite substrate concentrations.<sup>1</sup> The  $K_m$  values are dependent on temperature, pH, substrate and type of enzyme preparation. The turnover number  $k_{cat}$  can be defined as the number of substrate molecules that are converted in a given time [ $s^{-1}$  or  $min^{-1}$ ] by a fixed amount of enzyme and infinite substrate availability.<sup>1</sup> The  $k_{cat}$  can be mathematically calculated by dividing the maximal velocity ( $v_{max}$ ) by the molar concentration of the enzyme [E]. The single-first order constant  $k_{cat}$  thereby incorporates the rate of all combined chemical steps needed for substrate transformation.<sup>1</sup> As a result  $k_{cat}$  is a measurement for the catalytic efficiency of the enzyme at substrate saturation and provides an instrument for comparing different isoforms of an enzyme (e.g. brought about by mutagenesis), test conditions (temperature, pH) or dissimilar enzymes without the influence of substrate affinity.

Under physiological conditions, enzymes are usually not saturated with substrate. Therefore, the velocity depends on the binding affinity and, more importantly, on the turnover number. In the presence of low substrate concentrations, the encounter of

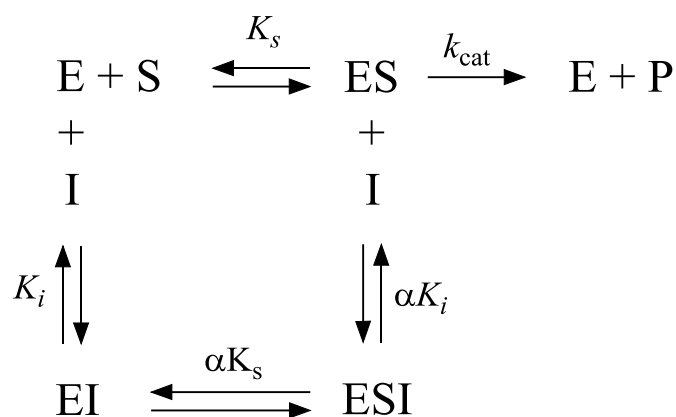
substrate and enzyme by means of diffusion is unlikely and the affinity of the substrate is less relevant than the speed of the turnover reaction. It is therefore practical to utilize the ratio of these kinetic constants,  $k_{cat}/K_m$ .<sup>1</sup> This constant enables the comparison of substrate efficiency or the comparison of substrate conversion by various enzymes.

### **Modulation of enzyme activity by inhibitors**

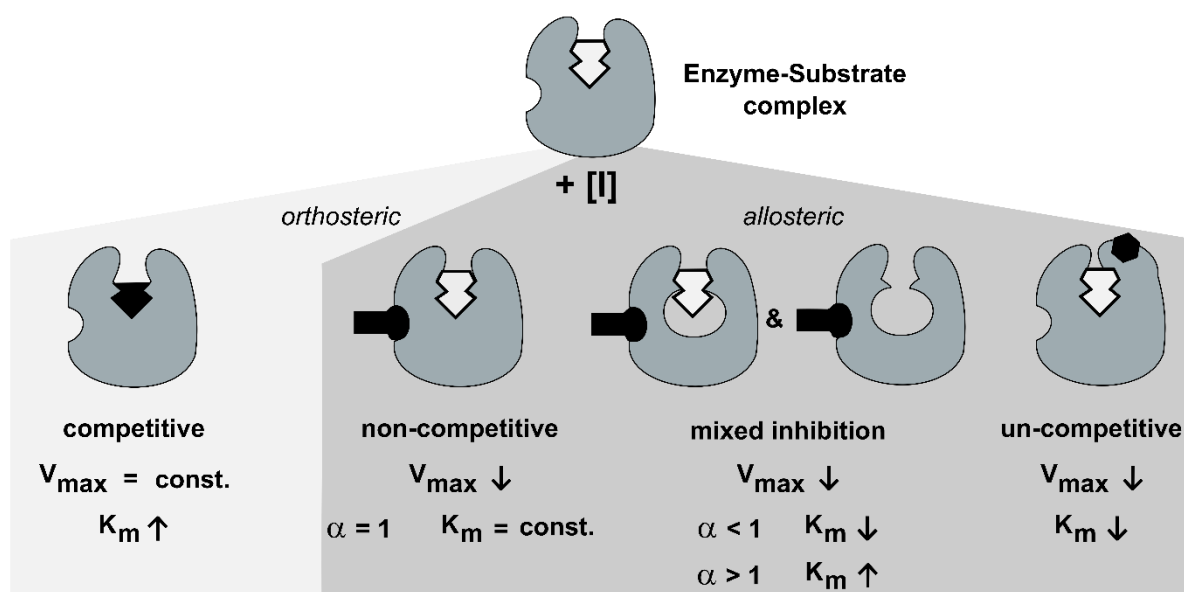
In the research for enzyme inhibiting drugs it is vital to compare the relative binding affinities of the respective lead compounds to their target in order to define structure-activity relationships (SARs) and to infer the physiological effect.<sup>1</sup> The development and optimization of lead compounds is conducted with the help of *in vitro* assay systems. These should imitate physiological conditions in order to allow the translation of potency data to *in vivo* applications.<sup>10</sup> The mechanism of action becomes important in the quantitative comparison of distinct inhibitor classes on a common target enzyme, as it allows the determination of the enzyme-inhibitor dissociation constant  $K_i$ , which is the best potency indicator for a specific experimental setup. The  $K_i$  value for an inhibitor is influenced by the enzyme-substrate combination, pH and buffer-composition of the assay system.<sup>10</sup>

### **Reversible enzyme inhibitors**

Modulators that decrease the catalytic ability of the enzyme by non-covalent interactions are defined as reversible inhibitors. The substrate conversion is impeded by inhibitors binding to the free enzyme at the substrate binding pocket (competitive inhibition) or an allosteric binding site (non-competitive inhibition). While compounds binding to both free enzyme and ES complex are referred to as mixed type inhibitors (see Figure 2 and Figure 3,  $\alpha \neq 1$ ).<sup>1</sup> Alternatively, inhibitors binding exclusively to an allosteric site of the ES complex, thereby increasing its stability, are defined as un-competitive (see **Figure 2** and **Figure 3**).<sup>10</sup>



**Figure 2.** Equilibrium scheme for enzymatic turnover of a single substrate in the presence and absence of reversible inhibitors.<sup>1</sup>  $K_i$  represents the equilibrium dissociation constant for the EI complex and  $\alpha K_i$  represents the equilibrium dissociation constant for the ESI complex.<sup>10</sup> The value of  $\alpha$  depends on alterations in substrate affinity due to the formation of the EI-complex. Increased affinity of the enzyme for the substrate results in  $\alpha < 1$ , while diminished affinity is indicated by  $\alpha > 1$ .<sup>10</sup>



**Figure 3.** Overview of reversible inhibition mechanisms and the respective impact of competitive, non-competitive, mixed and un-competitive inhibitors on apparent enzyme activity constants of maximum velocity ( $V_{\text{max}}$ ) and substrate affinity ( $K_m$ ). Inhibitor shown in black, substrate in white.

The potencies of inhibitors can be determined by preparing concentration inhibition plots and subsequent determination of  $IC_{50}$  and  $K_i$  values.<sup>11</sup> The  $IC_{50}$  value is the inhibitor concentration at 50 % of residual enzyme activity compared to the positive control without inhibitor. This value is strongly dependent on the experimental setup including the substrate concentration in relation to its  $K_m$  value and the inhibition mechanism.<sup>10</sup>

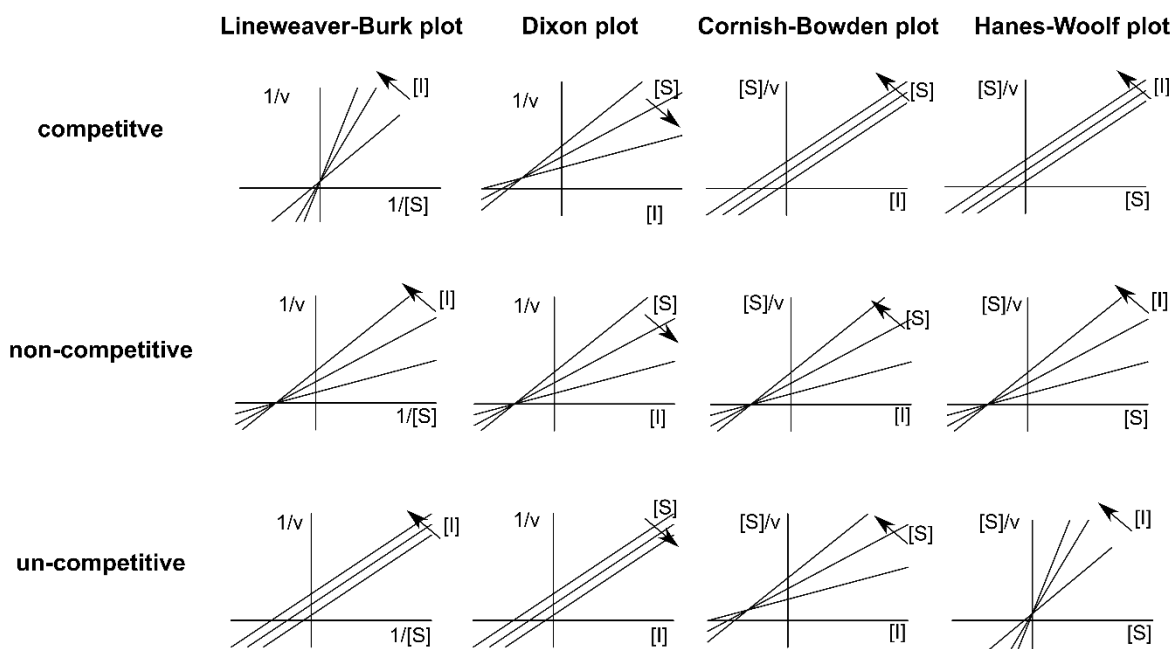
Thus, the inhibitory constant  $K_i$  is a better parameter for describing an inhibitor's potency than the  $IC_{50}$  value, as this constant is not dependent on the substrate concentration.<sup>1</sup> In case of competitive inhibitors, the  $IC_{50}$  value increases in proportion to the substrate concentration, which enables the calculation of  $K_i$  values with the Cheng-Prusoff equation.<sup>1</sup>

$$K_i = \frac{IC_{50}}{1 + \frac{[S]}{K_m}}$$

### Equation 2. Cheng-Prusoff equation

The inhibition mechanism of an enzyme inhibitor pairing is determined from kinetic parameters of the enzymatic reaction at multiple substrate and inhibitor concentrations. Similar to Henri-Michaelis-Menten kinetics, the velocity is fitted *versus* the substrate concentration in a non-linear regression, and increasing inhibitor concentrations are compared. The double reciprocal representation of this data, called Lineweaver-Burk-plot, allows for the simple evaluation in form of a linear regression ( $1/v$  vs.  $1/[S]$ ). However, this plot has shown to possess high statistical errors, as small values are weighted more strongly. To overcome this problem, the data may be analyzed directly by non-linear regression, or compared in additional linearized representations like Hanes-Woolf, Dixon or Cornish-Bowden plots. These plots are all based on a single reciprocal representation, which leads to a reduction of statistical errors as compared to the Lineweaver-Burk-plot (e.g., Hanes-Woolf plot ( $[S]/v$  vs.  $[S]$ ), the Dixon plot ( $1/v$  vs.  $[I]$ ) and the Cornish-Bowden plot ( $[S]/v$  vs.  $[I]$ ). In the Hanes-Woolf and the Cornish-Bowden plots the  $1/v$  is multiplied with another variable  $[S]$ , which leads to further reduction of the statistic errors by compensating the variances of two variables. Therefore, the Hanes-Woolf and the Cornish-Bowden plots are the most suited linear representation plots.<sup>1</sup> The inhibition type can be derived from the graphical evaluation of the plots (see **Figure 4**). The lines for different substrate or inhibitor concentrations either run parallel or intersect at specific coordinates, which enables the direct determination of inhibition constants. For competitive inhibitors, all lines of the Dixon plot meet at the point  $-K_i$  on the x- and  $1/V_{max}$  on the y-axis, while for un-competitive inhibitors the lines nest at the point  $(-K_i, K_m/V_{max})$  in the Cornish-Bowden plot.<sup>1</sup>





**Figure 4.** Patterns of lines in the reciprocal plots of inhibition type determination experiments of competitive, non-competitive and un-competitive enzyme inhibitors. [S] and [I] refer to the substrate and inhibitor concentrations, while  $v$  is the enzymatic velocity of substrate turnover in the experiment.

### Drug-target residence time

In pharmaceutical drug development, the potency of compounds is most frequently evaluated by their respective binding affinities to the target structure. Structure-activity relationships, which are based on the thermodynamic dissociation constant  $K_i$  as primary measure of comparison, will not necessarily optimize the drugs for their *in vivo* effectiveness.<sup>10,12</sup> In open biological settings, the temporal frame of drug target interactions is relevant for the intended as well as the off-target effects.<sup>10</sup> The stability of the binary enzyme-inhibitor complex is defined by the association rate constant or on-rate ( $k_{on}$ ) and by the dissociation rate constant or off-rate ( $k_{off}$ ). The duration of occupation, or residence time ( $\tau$ ), of the inhibitor to its target enzyme is essentially regulated by the dissociation rate ( $k_{off}$ ). Hence, the residence time is the reciprocal value of the dissociation rate constant ( $\tau = 1/k_{off}$ ).<sup>10</sup> Furthermore, drug-target occupancy may be expressed as the half-life of the enzyme-inhibitor complex, which is in direct proportion to the residence time ( $t_{1/2} = -\ln(0.5)/k_{off}$ ).<sup>10,12</sup>

Slow dissociation rates lead to a prolonged interaction and more durable pharmacological effects. This uncouples the relation of systemic pharmacokinetics and pharmacodynamics, meaning that the concentration of the drug in cells and tissues is no longer an indicator of its effectiveness.<sup>2</sup> Substances, which are bound to a protein, are unavailable to elimination and metabolism resulting in the clearance of unbound drug. If the residence time is longer than the pharmacokinetic half-life, the bound drug maintains its pharmacologic effect. Under this circumstance, the dosing scheme can be adapted to ensure high therapeutic activity, limiting off-target toxicities due to prolonged high concentrations of the drug.<sup>2,10</sup>

The temporal stability and reversibility of an enzyme-inhibitor complex can be assessed *in vitro* by experimental methods. In jump-dilution protocols, the enzyme and inhibitor are preincubated until a state of equilibrium is generated, then the mixture is diluted to an inhibitor concentration below 10% of the  $IC_{50}$  value, and the progression curves upon substrate addition are observed (see **Figure 6**). The rate at which the enzyme recovers its catalytic activity is an indicator for inhibitor dissociation. The progression curves of product formation in a continuous assay readout will be curvilinear (see **Figure 6**).<sup>10</sup> Alternatively, the inhibitor is directly detected by a spectroscopic signal or radioisotope label. The unbound ligand is separated from the equilibrated protein-ligand complex, e.g. by filtration or chromatography, and subsequently quantified.<sup>12</sup> Other ligands enable their direct quantification without prior separation, as they display a detectable change in physiochemical properties upon binding to a protein structure. An example are fluorescent small molecules, which scatter plane-polarized light. This so-called fluorescence polarization (FP) decreases upon binding to a larger structure as the rotation of the small molecule is restricted.<sup>12</sup>

### **Irreversible enzyme inhibitors**

Inhibitors that permanently prevent the catalytic turnover of substrate are referred to as irreversible enzyme inhibitors or inactivators.<sup>10</sup> The inactivation is typically achieved by covalent modification of key residues in the binding pocket. Therefore, inactivators must possess a level of chemical reactivity that enables specific reactions with the target, but prevents promiscuous reactions with other proteins, which would lead to off-target effects and toxicity.<sup>10</sup> Enzyme inactivators that are potential drugs, often contain weakly electrophilic functional groups, so-called warheads, that attack a nucleophile within the

enzyme's active site subsequent to non-covalent binding (see Figure 5). For effective inhibition, the nucleophilic group, e.g. the thiol group of cysteine, should be essential in the catalytic turn-over of the substrate.<sup>10</sup>

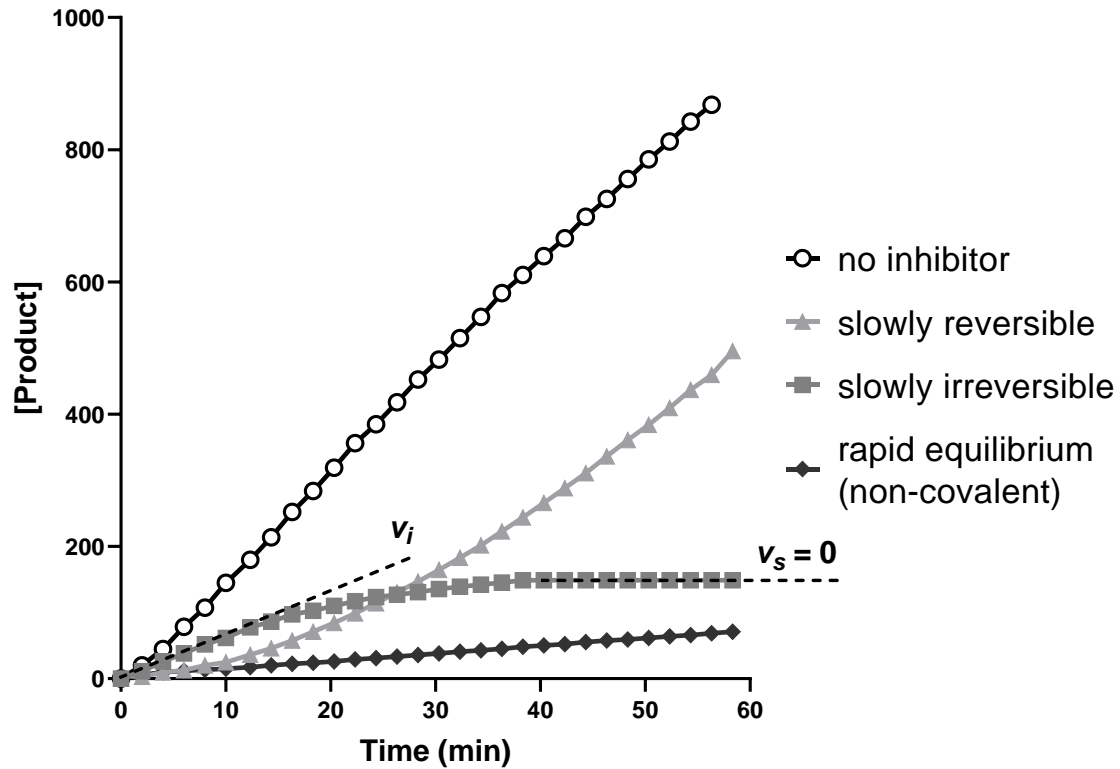


**Figure 5.** Mechanism of enzyme inactivation by initial non-covalent association of the enzyme-inhibitor complex EI and subsequent covalent modification of catalytic residues, leading to the inactivated enzyme E-I. The first step is defined by the dissociation constant  $K_i$ , and the first-order rate constant of inhibition  $k_{\text{inac}}$  describes the velocity of the irreversible inhibition.<sup>1,10,13</sup>

It is vital to consider the time course of enzyme inactivators. Due to the covalent bond formation, the onset of inhibition is delayed and defined by slow binding kinetics.<sup>10</sup> The generation of concentration-inhibition curves and  $IC_{50}$  values will strongly depend on the incubation time of the enzyme and inhibitor before substrate addition. Longer incubation times will cause lower  $IC_{50}$  values as the initial velocity ( $v_i$ ) of the enzyme catalysis will decrease over time and approach zero in the steady-state velocity ( $v_s$ ), once all of the enzyme is occupied by inhibitor (see **Figure 6**).<sup>13</sup> Therefore, solely  $IC_{50}$  values obtained from the slopes corresponding to the initial reaction velocity can be used to compare batches of substances with common warheads to distinguish their non-covalent binding affinities. The subsequent phase of the two-step inhibition mechanism is defined by the first-order rate constant of inhibition  $k_{\text{inac}}$ , as well as the second-order rate constant of inhibition  $k_{2nd} = k_{\text{inac}}/K_i$ , which are determined by evaluation of the time-dependent formation of product.<sup>13</sup>

For the investigation of these types of inhibitors a continuous assay readout is of advantage, as the shape of the progress curves, depicting the product increase over time, will be an indicator of the inhibition modality (see **Figure 6**). Non-covalent, reversible inhibitors form a rapid equilibrium and decrease the substrate turnover, which leads to a linear progress curve with decreased slope of product formation compared to the enzyme without inhibitor. Irreversible inhibitors follow an exponential equation, where the velocity decreases as successively less enzyme is available. Inhibitors with a reversible

time-dependent inhibition will detach from the protein, leading to a resumption of activity and a non-linear increase in velocity.<sup>10</sup>



**Figure 6.** Progress curves of enzymatic product generation for different inhibition modalities. The initial velocity ( $v_i$ ) of product formation decreases over time for covalent (slowly irreversible) inhibitors and approaches zero in the steady-state velocity ( $v_s$ ).

The rate of covalent bond formation and synonymous inactivation is described by the pseudo-first-order rate constant  $k_{obs}$ , which is dependent on the inhibitor concentration and can be determined by fitting the progress curve to the equation:

$$[P] = \frac{v_i}{k_{obs}} [1 - \exp(-k_{obs} t)]$$

**Equation 3.**  $k_{obs}$  determination for slowly-irreversible enzyme inactivators<sup>10</sup>

The obtained  $k_{obs}$  values are plotted in a secondary plot *versus* the respective inhibitor concentrations. The data can be fitted by nonlinear and linear regression, depending of the saturation of inhibitor, which leads to a plateau in  $k_{obs}$  values. With the use of the nonlinear equation, the first- and second-order rate constants can be resolved, while the linear equation solely provides the second order rate constant  $k_{inac}/K_i$ .

$$k_{obs} = \frac{k_{inac} * [I]}{[I] + K_i^{app}} = \frac{k_{inac} * [I]}{[I] + K_i * (1 + \frac{[S]}{K_m})}$$

**Equation 4.** Nonlinear equation for secondary plot of  $k_{obs}$  in the determination of  $k_{inac}$  and  $K_i$  for slowly irreversible enzyme inactivators.<sup>10</sup> Correction of the apparent  $K_i^{app}$  to zero substrate concentration yields the  $K_i$  value.<sup>13</sup>

$$k_{2nd} = \frac{k_{inac}}{K_i} = \left(1 + \frac{[S]}{K_m}\right) * \left(\frac{k_{obs}}{[I]}\right)$$

**Equation 5.** Linear equation for secondary plot of  $k_{obs}$  in the determination of  $k_{inac}/K_i$  for slowly irreversible enzyme inactivators.<sup>10</sup>

For definitive proof of an irreversible inhibition mechanism, additional experiments including dialysis or jump dilution, which separate or dilute free inhibitor from the enzyme-inhibitor complex, should be performed. Further information on the targeted residues can be derived from mass spectrometry after tryptic digest, or from X-ray crystallography experiments.<sup>13</sup>

## 2.2 Ecto-nucleotidases

### 2.2.1 Purinergic signaling

#### Extracellular ATP

Adenosine 5'-triphosphate (ATP) is an ubiquitous molecule in biological systems, which is involved in a wide range of physiological processes. Among other functions, it acts as a signaling molecule, a building block for RNA, a co-substrate for enzymatic reactions, provides energy in the respiratory chain and enables active transport against concentration gradients.<sup>14,15</sup> Intracellular ATP concentrations are in the high micromolar to low millimolar range; in contrast, the basal extracellular concentrations are only around 2-5 nM.<sup>16-18</sup> This ATP gradient enabled a basic evolutionary form of chemical cell-to-cell communication.<sup>19</sup> The sensitivity of cells towards ATP is utilized as a danger signal indicating damaged cells in close proximity, which release high concentrations of their cytosolic ATP upon disintegration.<sup>19</sup> This basic principle of chemical transmission further evolved into a complex purinergic signaling network, which regulates a broad selection of biological activities by means of extracellular ATP and other nucleotides.<sup>20</sup> For example, the damage-associated release of ATP initiates repair and defense mechanisms towards potential pathogens.<sup>19</sup> Next to the lytic discharge, cytosolic ATP and other nucleotides can be released from intracellular storage pools by exocytosis of granules and vesicles, pannexin and connexin hemichannels (see **Figure 7**).<sup>21-23</sup>

#### Purinergic receptors

The cells involved in purinergic signaling cascades express purinergic receptors, which are subdivided into three groups in relation to their main ligands: the endogenous agonist of P0 receptors is adenine, that of P1 receptors is adenosine, whereas P2 receptors are activated by nucleotides like ADP, ATP, UDP and UTP.<sup>20,24</sup> Both P0 and P1 receptors are G protein-coupled receptors. Adenine receptors (AdeR) were initially identified in rodents, and pharmacological results suggest the existence of a human ortholog.<sup>25,26</sup> There are four subtypes of P1 receptors, namely adenosine A<sub>1</sub>, A<sub>2A</sub>, A<sub>2B</sub> and A<sub>3</sub> receptors.<sup>27</sup> P2 receptors are sub-classified into two distinct classes with different structures, the ATP-gated ion channels P2X and G protein-coupled receptors P2Y. Seven P2X receptor subunits (P2X<sub>1-7</sub>) and eight P2Y receptors (P2Y<sub>1</sub>, P2Y<sub>2</sub>, P2Y<sub>4</sub>, P2Y<sub>6</sub>, P2Y<sub>11-14</sub>) have been identified

in humans.<sup>20</sup> An overview of purinergic receptor subtypes with their respective endogenous agonists is shown in **Table 2**.

**Table 2.** Purinergic receptors and their endogenous agonists. Adapted from Lazarowski et al. with addition of adenine.<sup>21</sup>

Endogeneous agonist	Purinergic receptors
ATP	P2X1-7, P2Y <sub>2</sub> , P2Y <sub>11</sub>
ADP	P2Y <sub>1</sub> , P2Y <sub>12</sub> , P2Y <sub>13</sub>
UTP	P2Y <sub>2</sub> , P2Y <sub>4</sub>
UDP	P2Y <sub>6</sub> , P2Y <sub>14</sub>
UDP-glucose	P2Y <sub>14</sub>
Adenosine	A <sub>1</sub> , A <sub>2A</sub> , A <sub>2B</sub> , A <sub>3</sub>
Adenine	AdeR

### Physiologic and pathophysiologic purinergic signaling

The effects of extracellular nucleotides depend on the type of transmembrane purinergic receptors (P2, P1 and P0).<sup>20,28</sup> The binding of an agonist elicits an activation which relays the signal into the cytosol inducing the activation or inhibition of enzymes like phospholipase C, adenylate cyclase or mitogen-activated protein kinase (MAPK) resulting in a change in the concentration of second messengers, e.g. calcium ions (Ca<sup>2+</sup>), reactive oxygen species or cyclic adenosine monophosphate (cAMP).<sup>15</sup> ATP is a co-transmitter in the peripheral and central nervous system.<sup>14,18</sup> The modulation of non-neuronal cell activity via purinergic signaling is prevalent in fast biologic processes like exocrine and endocrine secretion, platelet aggregation, vasodilatation, and nociceptive mechanosensory transduction.<sup>29</sup> Moreover, slower trophic processes are induced and regulated by purinergic signaling including wound healing, cell differentiation, proliferation and apoptosis in embryonic development.<sup>15</sup>

The following paragraphs provide examples of selected physiologic and pathophysiologic processes, which are relevant regarding our studies.

#### *Vascular fluidity*

The vascular tone of blood vessels is in part regulated by purines. P2X receptors on smooth muscle cells are activated by ATP released from perivascular sympathetic neurons, leading to a vasoconstriction. In contrast, tissue hypoxia or shear stress trigger

ATP liberation from endothelial cells. Intravascular ATP induces the production of nitric oxide (NO) by binding to endothelial P2Y and P2X receptors, which causes vasodilatation. The dephosphorylation product of ATP, adenosine, perpetuates the vasodilatation by activation of P1 receptors located on vascular smooth muscle cells.<sup>15</sup>

#### *Exo- and endocrine secretion*

The secretion of hormones is regulated by purinoceptors expressed on endocrine glands. For example, ATP and UTP decrease the secretion of estradiol and progesterone from the ovary, and P2Y receptors expressed on  $\beta$ -cells in the pancreas are controlling insulin release (see physiological function of NTPDase3 section **2.2.3**).<sup>15</sup>

#### *Inflammatory processes*

Various immune cells express P1 and P2 receptors, depending on cell type and differentiation state.<sup>28</sup> In general, ATP stimulates the immune response, whereas adenosine has the opposite effect.<sup>30</sup> ATP elicits the inflammation process by binding to P2X and P2Y receptors, thereby increasing the release of mediators like histamine from mast cells, prostaglandins and cytokines, e.g. Interleukin-6 (IL-6),<sup>28</sup> from immune cells.<sup>29</sup> These molecules activate fibroblasts or resident inflammatory cells, which in turn mobilize the cellular immune response.<sup>28</sup> Additional immune cells like dendritic cells and macrophages are guided to sites of inflammation by purinergic chemotaxis, in which immune cells move along a gradient towards increasing ATP concentrations.<sup>23</sup> The concentration of extracellular ATP peaks at the center of the inflammation site up to high micromolar levels. Once the immune cells reach this location the elevated ATP level is proposed to stop any further movement and facilitates cell differentiation and production of mediators, which reinforce inflammation.<sup>28</sup>

The inflammation-promoting signaling of ATP is terminated by hydrolysis of the nucleotide by ecto-nucleotidases. The degradation product adenosine binds to P1 receptors, which typically have the opposite effect of P2 receptors.<sup>23</sup> Adenosine exerts anti-inflammatory effects and acts as an immune-regulatory feedback modulator, thereby reducing the risk of pathological inflammation and promoting wound healing.<sup>15,23,28</sup> Furthermore, adenosine has cardioprotective, anti-nociceptive, neuroprotective and pro-angiogenic effects.



*Pathologic purinergic signaling*

Several diseases have been associated with purinergic signaling, e.g. atherosclerosis, ischemia-reperfusion injury, autoimmune reactions, and cancer.<sup>15</sup> Tumor cells contain mutations and alterations in gene expression, which, for example, increase their proliferation rates or increase their resistance to apoptosis. As a result, solid cancerous tissues are characterized by tissue hypoxia and the release the hypoxia-inducible factor 1 $\alpha$  (HIF-1 $\alpha$ ).<sup>31</sup> Inter alia, this factor increases the production of extracellular adenosine from ATP by upregulation of nucleotide-degrading enzymes in both resident, as well as recruited inflammatory cells.<sup>31</sup> This endogenous feedback loop aims to dampen exuberant inflammatory and autoimmune reactions and promotes healing via adenosine receptors in normal tissues.<sup>31,32</sup> However, cancer cells and some pathogens like bacteria take advantage of this anti-inflammatory pathway by releasing increased concentrations of ATP in concert with high expression of nucleotide-degrading enzymes in order to facilitate immune escape.

Novel pharmaceutical approaches in cancer treatment include the abrogation of immunoevasive mechanisms mediated by HIF-1 $\alpha$  and other hypoxia-response elements.<sup>33</sup> Next to a reduction of adenosine signaling, increased concentrations of ATP were demonstrated to contribute to the treatment of cancers by inhibiting tumor growth, protecting healthy tissue from chemo- and radiation therapy, and reduction of cachexia including decreased weight loss, anorexia and hormonal imbalances.<sup>15</sup> Potential modes of action include selective modulation of P1 and P2 receptors, inhibition of extracellular ATP degradation and enhancement of ATP release from intracellular compartments.<sup>32,34</sup>

For example, the adenosine A<sub>2A</sub>R antagonist, ciferadenant was shown to be an effective therapeutic in cancer treatment as inhibitor of the hypoxia-A<sub>2</sub>-adenosinergic pathway.<sup>33,35,36</sup> The compound is able to reactivate tumor-reactive T and natural killer cells and thereby reverses the immunosuppression in cancerous tissues.<sup>36</sup> The compound is a potential drug for monotherapy or in combination, e.g. with PD-1 blockade, for the therapy of selected cancers.<sup>36</sup> In the future, multi-targeted combinations of immune therapies for cancer can potentially overcome the blockade of immunosuppressive regulators and thereby decrease the dose of and resistance to individual blocking antibodies and therapeutics.<sup>33,35,36</sup>

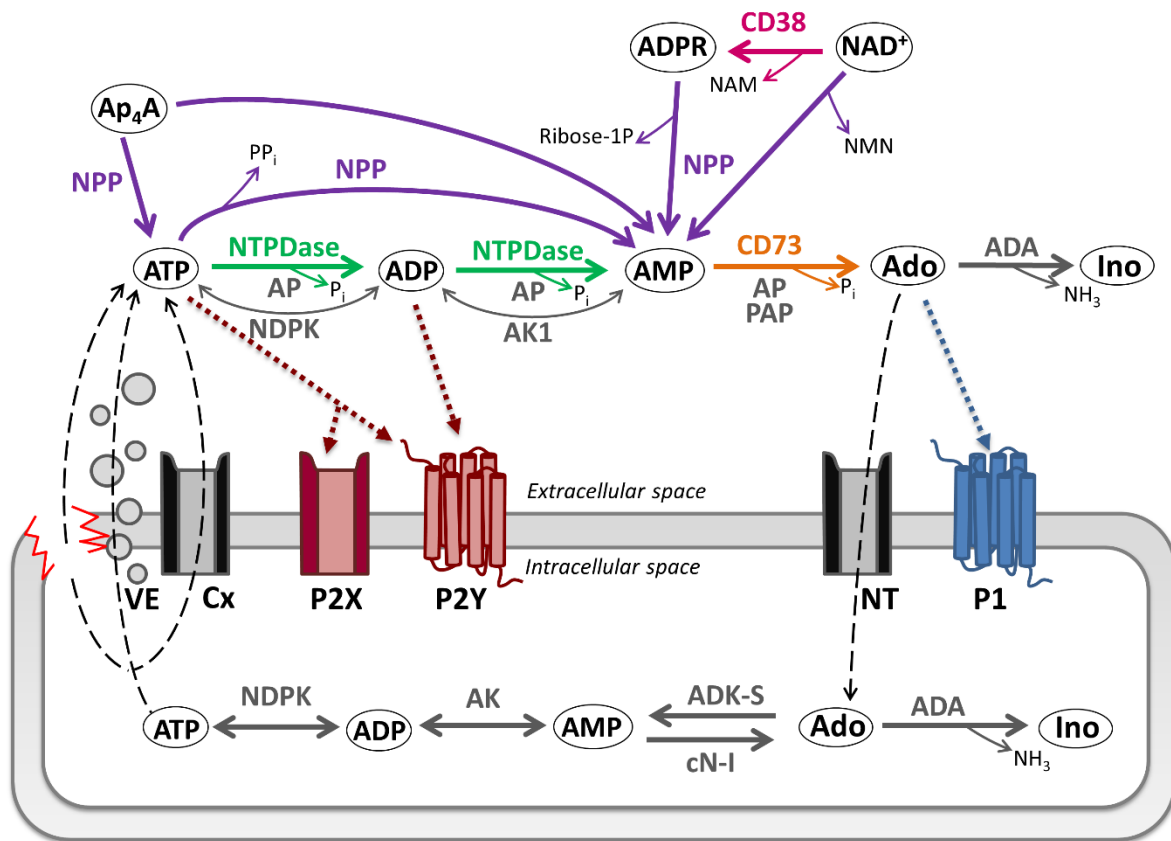
## 2.2.2 Nucleotide metabolism

The aforementioned purinergic signaling activities of nucleotides via P2 receptors, and of nucleosides via P1 receptors, are controlled by receptor desensitization or downregulation, and most importantly through removal of agonists by ecto-nucleotidases.<sup>37</sup> The concerted actions of the ecto-nucleotidase network transforms an ATP-induced inflammatory environment into an immunosuppressive, anti-inflammatory environment through the generation of adenosine.<sup>32</sup> In brief, extracellular ATP and other nucleotides are cleaved into phosphates and nucleosides, which are able to re-enter the cells via nucleoside transporters and are recycled by nucleotide resynthesis.<sup>38</sup> There are four main groups of ecto-nucleotidases including ecto-nucleoside triphosphate diphosphohydrolases (E-NTPDases), ecto-5'-nucleotidase (eN, CD73), ecto-nucleotide pyrophosphatases/ phosphodiesterases (E-NPPs) and alkaline phosphatases (APs) (see **Figure 7**).<sup>37</sup> These enzymes are mostly associated to cell membranes but some can be shedded in extracellular vesicles or excreted in their soluble form.<sup>39</sup>

The most prominent group of enzymes contributing to the degradation of extracellular nucleoside triphosphates (NTPs) and nucleoside diphosphates (NDPs) are the E-NTPDases, which will be discussed in detail in section **2.2.3**.<sup>37</sup>

Alternatively, AMP may be generated by NPP1-NPP3 from a variety of substrates, including NTPs, NDPs, nicotinamide dinucleotide (NAD<sup>+</sup>), flavin adenine dinucleotide (FAD), UDP sugars and dinucleoside polyphosphates, by hydrolysis of pyrophosphate and phosphodiester bonds.<sup>37</sup> ATP is directly hydrolyzed by NPPs to AMP by cleaving off diphosphate (pyrophosphate/PP<sub>i</sub>). The enzymes NPP1-3 have a wide tissue distribution and are often localized on epithelial surfaces, e.g. in lung, liver, kidney and intestine.<sup>37</sup> NPP1 (also named CD203a) has a high expression in bone and cartilage. Here, its function is essential for the control of calcification homeostasis by generation of PP<sub>i</sub>, which is an important inhibitor of bone mineralization and vascular smooth muscle calcification.<sup>22</sup> An additional pathway for adenosine production is the concerted action of CD38 and NPP1. NAD<sup>+</sup> is converted to nicotinamide and ADP-ribose (ADPR), which is subsequently metabolized to AMP by NPPs.<sup>40</sup> CD38 is a cell-surface marker with receptor and enzymatic functionalities. It contributes to the ecto-nucleotidase network by NAD<sup>+</sup> glycohydrolase, ADP-ribosyl cyclase and cyclic ADP-ribose hydrolase activities.<sup>40</sup> CD38 was identified as an immune checkpoint, which is upregulated in hematological cancers and correlated

with the resistance towards PD-1 inhibitors.<sup>36</sup> Hence, the monoclonal antibody daratumumab, which binds to and inactivates CD38, was developed by Janssen Biotech and is clinically used for the immunological treatment of cancers.<sup>32</sup>



**Figure 7.** Principal pathways of nucleotide metabolism: Endogenous ATP is released upon cell damage or via non-lytic mechanisms of vesicular exocytosis (VE), connexin hemichannels (Cx), and other ion channels and transporters; Purinergic signaling via nucleotide (P2X and P2Y) and adenosine (P1) selective receptors; Extracellular nucleotide metabolizing enzymes include nucleoside triphosphate diphosphohydrolase (NTPDase), nucleoside pyrophosphatase /phosphodiesterase (NPP), NADase (CD38), alkaline phosphatase (AP), prostatic acid phosphatase (PAP), ecto-5'-nucleotidase (CD73) and adenosine deaminase (ADA); Counteracting adenylate kinase-1 (AK1) and nucleotide diphosphokinase (NDPK) contribute to the regeneration of extracellular ATP via reversible phosphotransfer reactions; Additional substrates for nucleotide metabolism include diadenosine tetraphosphate ( $Ap_4A$ ), adenosine diphosphate ribose (ADPR), and nicotinamide adenine dinucleotide ( $NAD^+$ ), releasing nicotinamide (NAM) and nicotinamide mononucleotide (NMN) upon hydrolysis; Adenosine uptake by nucleoside transporters (NT); Intracellular adenosine metabolism depends on the cytoplasmatic form of adenylate kinase (ADK-S), and the enzymes NDPK, AK, ADA and cytosolic nucleotidase (cN-I); Figure adapted from Boison and Yegutkin 2019 and Zimmermann et al. 2012.<sup>32,37</sup>

All aforementioned enzymes generate nucleoside monophosphates, which are predominantly hydrolyzed to nucleosides by CD73. In particular, CD73 transforms AMP to adenosine. The structure and function of CD73 is further detailed in section 2.2.4.

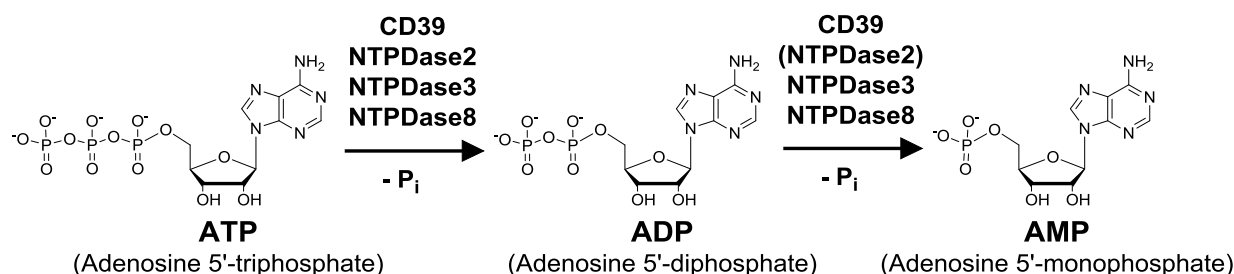
Aside from CD73, adenosine can be produced by alkaline phosphatases (AP).<sup>30</sup> This family of enzymes is expressed in essentially all mammalian tissues, and is able to sequentially dephosphorylate nucleoside triphosphates to the respective nucleoside.<sup>37</sup> Their pH optimum is in the high alkaline range (>9), and each catalytic site contains three metal ions, two Zn<sup>2+</sup> ions, and one Mg<sup>2+</sup> ion that are essential for catalytic activity.<sup>37</sup> The tissue non-specific AP interferes with NPP1 activity in bone tissue by hydrolyzing PP<sub>i</sub>, thereby preventing the accumulation of the mineralization inhibitor PP<sub>i</sub>, one of the products of NPP1.<sup>22</sup>

Extracellular adenosine can be further transformed to inosine by adenosine deaminase or it can be salvaged by cellular reuptake. ATP is recycled by extracellular and intracellular pathways: A minor portion of extracellular ATP is regenerated by the activity of adenylate kinase-1 (AK1) and nucleotide diphosphokinase (NDPK), performing reversible phosphotransfer reactions.<sup>32</sup> The majority of ATP is produced by cellular reuptake of adenosine and its rephosphorylation by cytoplasmic adenosine kinase (ADK-S) to AMP. Two more phosphates are added by cellular AK and NDPK reconstructing intracellular ATP (see **Figure 7**).<sup>30,32</sup>

### 2.2.3 Ecto-nucleoside triphosphate diphosphohydrolases (E-NTPDases)

E-NTPDases are the most prominent enzyme family contributing to the degradation of extracellular NTPs and NDPs to NMPs (see **Figure 8**). Therefore, they are a major factor in the control of purinergic signaling via nucleotide (P2) and indirectly via adenosine (P1) receptors.<sup>37</sup> The hydrolysis of extracellular nucleotides prevents the activation and desensitization of P2 receptors and affects the activation of P2Y<sub>1</sub>, P2Y<sub>6</sub>, P2Y<sub>12</sub> and P2Y<sub>13</sub> receptor subtypes by generation of NDPs.<sup>41</sup> Consequently, the activity of an ATP-activated receptor can be downregulated in favor of an ADP-specific receptor by the actions of E-NTPDases 2, -3 and 8. NTPDase 1 (CD39) in turn prevents signaling at ADP-specific receptors, as the enzyme directly catalyzes the hydrolysis to AMP, without intermediate ADP release. In addition, NTPDases were proposed to interact with intracellular proteins,

like Ran-binding protein microtubule-organizing center (RanBPM), and to modulate extracellular-signal-regulated kinase (ERK)/Ras signaling pathways.<sup>22</sup>



**Figure 8.** Ecto-NTPDase-catalyzed hydrolysis of adenosine nucleotides. The ATP:ADP hydrolysis ratios of CD39 and NTPDases-2, -3 and -8 are 1–1.5:1, 10–40:1, 3–4:1 and 2:1, respectively. Thus, the hydrolysis of ADP by NTPDase2 is not relevant in practice.<sup>41–43</sup>

In humans the NTPDase family comprises eight isoforms. Among these, four subtypes are located in the cell membrane, namely NTPDase1 (CD39), -2, -3 and -8. NTPDase4 and -7 are exclusively found in membranes of intracellular organelles, while NTPDase5 and -6 can be expressed on the cell surface or be secreted as soluble exoenzymes.<sup>41</sup>

### Structure of ecto-nucleoside triphosphate diphosphohydrolases (E-NTPDases)

In general, the ecto-NTPDases consist of two transmembrane domains and a large extracellular loop which contains the catalytic domain. Their molecular weight is approximately 70 to 80 kDa.<sup>37</sup> The N- and C-termini are located intracellularly, and the N-termini are glycosylated.<sup>37</sup> Although the enzymes originate from the same family, their amino acid identity is not very similar (see **Table 3** for sequence alignment of human NTPDases). Five highly conserved sequence motifs, the so-called apyrase-conserved regions (ACRs), were identified and found to be essential for catalytic activity and substrate specificity.<sup>37,44</sup> For example, exchanging one amino acid in ACR1 was proven to restrict the catalytic competence of CD39 from being able to hydrolyze both, NTPs and NDPs, to a pure ADPase.<sup>45,46</sup>

**Table 3.** Sequence alignment of human NTPDase isoforms created with EMBOSS needle

	NTPDase isoform	Identity %							
		1	2	3	4	5	6	7	8
Similarity %	1		38.9	35.3	23.0	23.9	21.1	23.6	43.0
	2	56.0		38.1	24.7	22.4	20.8	25.4	42.6
	3	53.8	55.6		22.8	22.1	19.4	22.7	37.5
	4	39.8	36.5	36.4		19.3	21.5	61.3	22.2
	5	37.6	34.2	34.8	32.1		41.7	20.1	23.7
	6	34.5	31.1	32.3	31.3	54.1		20.4	20.1
	7	38.2	35.9	35.9	74.8	33.5	31.5		21.8
	8	60.1	58.7	53.2	36.1	36.4	35.1	38.2	

Ecto-NTPDases have been shown to form di- or oligomers on cell-surfaces.<sup>47,48</sup> NTPDase1-3 were found to predominantly exist as dimers and tetramers. The state of oligomerization is correlated with increased catalytic activities compared to monomers. The enzymatic activity of ecto-NTPDases is influenced by interactions of the transmembrane domains, since mutants deficient of one or both of these domains tend to oligomerize less and show decreased enzymatic activity.<sup>37,48</sup> For example, soluble CD39, which lacks both transmembrane domains, has a decreased catalytic activity and an altered substrate specificity: while the membrane-bound form almost immediately hydrolyzes ATP to AMP, the soluble isoform releases the intermediate ADP.<sup>48</sup>

The optimal catalytic conditions of CD39 and NTPDases2, -3 and -8 are found at physiological extracellular pH (pH = 7–8) and in the presence of millimolar concentrations of divalent cations like Ca<sup>2+</sup> or Mg<sup>2+</sup> ions as cofactors.<sup>38</sup> The enzymes sequentially hydrolyze the terminal phosphates of NTPs and NDPs, to NMPs at the same active site.<sup>37,49</sup> This entails that the nucleoside binding site is highly flexible and can adopt both relaxed and stretched conformations to accommodate NTPs and NDPs. However, this flexibility results in a loss of substrate specificity. At the start of the catalytic process the enzyme's catalytic center forms a complex with a divalent cation. Then the nucleotide binds to the active site in its open conformation and thereby induces a domain closure motion, which encloses the metal-nucleotide complex. The hydrolysis is facilitated by a nucleophilic attack of a base-activated water molecule on the terminal phosphate group. The

negatively charged transition state is stabilized by proton-donating phosphate binding loops and the divalent metal ion cofactor.<sup>49</sup>

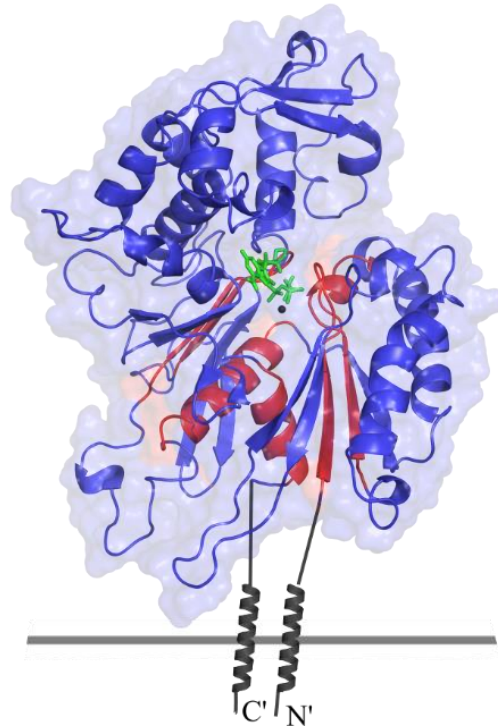
Despite the closely related catalytic centers, the subtypes differ in their substrate preferences, illustrated by varying  $K_m$  values for the respective nucleotides (see **Table 4**).<sup>37,38,42</sup> CD39 has an almost equal affinity for ATP and ADP, whereas NTPDase2 mainly recognizes NTPs as substrates.<sup>37,42</sup> NTPDase3 and NTPDase8 are functional intermediates between CD39 and NTPDase2 with respect to their substrate affinities. The substrate preferences are collected in **Table 4**. High binding affinities are indicated by low  $K_m$  values.

**Table 4.** Substrate preferences of human ecto-NTPDases (modified from Zimmermann *et al.* 2012,<sup>37</sup> Kukulski *et al.* 2005 and,<sup>42</sup> NTPDase8 from Fausther *et al.* 2006)<sup>50</sup>

Protein name	Main substrates	Substrate affinity ( $K_m$ ), $\mu\text{M}$
NTPDase1 (CD39)	NTP, NDP	ATP (17) ~ ADP (22) > UTP (47) > UDP (135)
NTPDase2	NTP	ATP (70) > UTP (393)
NTPDase3	NTP, NDP	ADP (31) > UTP (58) > UDP (65) > ATP (75)
NTPDase8	NTP, NDP	ATP (81) > ADP (137) > UDP (241) > UTP (480)

To date, no crystal structure of the human CD39 is available. Homology models of the extracellular domain were built based on X-ray structures of rat CD39 (PDB: 3ZX3)<sup>51</sup> and rat NTPDase2 (PDB:4BR5) as templates (see **Figure 9**).<sup>52</sup>

The generation of crystal structures was successful for the extracellular domain of rat NTPDase2 (PDB-ID: 3CJA, 3CJ1, 3CJ9, 3CJ7).<sup>53</sup> This enabled the generation of co-crystals with substrate analogs (e.g. Adenylyl imidodiphosphate (AMPPNP), PDB-ID: 4BR5)<sup>49</sup> and inhibitors (e.g. PSB-071, PDB-ID: 4CD1, 4CD3),<sup>54</sup> which gave critical insights into the residues involved in the catalytic mechanism and substrate specificity. No crystal structures of NTPDase3 and NTPDase8 are available so far.



**Figure 9.** Homology model of human CD39 with docked ATP as substrate (in green) and a Ca<sup>2+</sup> ion as a cofactor (in black).<sup>52</sup> The five apyrase-conserved regions (ACR) are marked in red. The transmembrane domains are not part of the homology model and were added manually to the representation. The overall sequence identities of human CD39 with rat CD39 and rat NTPDase2 are 74.2%, and 45.3%, respectively.

### Expression, physiological function and related diseases

Ecto-NTPDases are ubiquitously expressed in humans and have a broad tissue distribution.<sup>41,55</sup> The following paragraphs aim to provide an overview of the distinct expression patterns, related physiologic functions and diseases that may be treated by targeting the respective cell-surface NTPDases.

#### *NTPDase1 (CD39)*

NTPDase1 was initially identified as a cluster of differentiation (CD39) and lymphocyte activation marker. Through its expression on monocytes, natural killer, dendritic, and subsets of activated T cells it plays an important role in purinergic signaling and controls the cellular immune response by hydrolyzing inflammatory ATP.<sup>17,56–58</sup> Regulatory T cells can be differentiated from resting or activated T cells by evidence of CD39 on the cell surface. Furthermore, CD39 is the most prominent ecto-nucleotidase in various tissues including the vascular endothelium and thrombocytes, where it modulates vascular



inflammation and thrombosis. An increased enzyme activity contributes to cerebro- and cardioprotection, by hydrolysis of the prothrombotic ADP.<sup>59</sup> CD39 on the surface of vascular smooth muscle cells regulates the nucleotide-dependent vasodilation facilitated by P2Y receptors.<sup>60</sup>

Next to the cell-surface, CD39 was identified on microparticles hinting at a role in the exchange of signals between leucocytes and vascular cells.<sup>37,61</sup> Active forms of soluble CD39 are scarcely found under physiological conditions.<sup>37</sup> Artificial constructs of soluble NTPDases were investigated as antithrombotic drugs (e.g. chimeric CD39-CD73-ectodomain proteins or CD39-human serum albumin fusion proteins).<sup>22,32,62,63</sup> CD39 was found in both membranes and in exosomes of diverse cancer cell types, where it suppresses the immune response by generation of adenosine.<sup>37,64</sup> Therefore, activators of CD39 would have immunosuppressive effects, whereas inhibitors would promote the immune function.

CD39 expression is elevated in patients with chronic obstructive pulmonary disease (COPD), especially during acute exacerbations.<sup>65,66</sup> Chronic pulmonary and systemic inflammations are often induced and worsened by bacterial or viral infections. Microorganisms are reported to express ecto-nucleotidases on their cell surface in order to escape immune reactions of the host.<sup>67</sup> Blocking CD39 on T cells is investigated as novel treatment approach to activate the autoimmune response and to reduce the use of antibiotics.<sup>65</sup>

Another field of application for CD39 inhibitors is regenerative medicine. Hematopoietic transplants are performed with stem cell-enriched peripheral blood.<sup>68</sup> Elevated ATP levels stimulate the chemotaxis and release of hematopoietic stem progenitor cells.<sup>67</sup> A therapy, which intentionally increases ATP concentrations by inhibition of CD39 is proposed to boost stem cell mobilization from the bone marrow. In an *in vivo* study, mice preconditioned with CD39 and CD73 inhibitors, ARL67156 and  $\alpha,\beta$ -methylene adenosine 5'-diphosphate (AMPCP), exhibited increased mobilization of bone marrow-residing stem cells into the peripheral blood.<sup>69</sup> Hence, CD39 inhibitors may be added to the treatment regime of stem cell transplants in order to achieve sufficient quantities of stem cells for lifelong hematopoiesis in patients.<sup>68,69</sup>

The link between CD39 and cancer is broadly investigated in current research papers.<sup>70-72</sup> The enzyme was shown to stimulate tumor growth and increase metastasis.<sup>73-78</sup> Moreover, the expression of CD39 was found to be a predictor of disease progression (e.g. in gastric cancer).<sup>79,80</sup> CD39 is often the rate-limiting ATPase in the tumor microenvironment and facilitates a mechanism of immune-escape by the generation of immuno-suppressive adenosine.<sup>77</sup> The development of CD39-inhibiting small molecules and antibodies is a promising strategy to restore the antitumor immune response and adjuvant antitumor therapy.<sup>74,75,78</sup>

In conclusion, CD39 is a promising target for the modulation of several pathological conditions. Activators of the enzymes could be applied in the treatment of autoimmune diseases, atherosclerosis, ischemia-reperfusion injury; whereas inhibitors would be useful in the therapy of acquired immune deficiency syndrome (AIDS), infections, and cancers.<sup>57,78,81-84</sup>

### *NTPDase2*

The NTPDase2 enzyme hydrolyzes ATP and UTP, but shows a significantly decreased dephosphorylation of dinucleotides, leading to accumulation of ADP and UDP. Thereby, the enzyme modulates the activation of ADP and UDP receptors, namely P2Y<sub>1</sub>, P2Y<sub>11</sub>, P2Y<sub>12</sub>, and P2Y<sub>13</sub> by generation of ADP, and P2Y<sub>6</sub>, and P2Y<sub>14</sub> by the generation of UDP. NTPDase2 is expressed in a broad variety of tissues, including brain, muscle and testis.<sup>85</sup> The enzyme controls purinergic signaling in embryonic development of the nervous system and in the initiation of eye formation.<sup>22,85,86</sup> Furthermore, NTPDase2 was found on astrocytes and glial cells in the central and peripheral nervous system and is present in gastrointestinal epithelia, such as salivary cells and type 1 cells of taste buds, where it contributes to taste transduction.<sup>37</sup> NTPDase2 is named CD39-like enzyme 1 (CD39L1) in immunological contexts, and was identified in a variety of tumor cells.<sup>37</sup>

Finally, NTPDase2 contributes to vascular integrity and homeostasis. Upon injuries large amounts of ATP are released on the surface of vascular adventitial cells and are locally converted by the membrane-bound NTPDase2 to ADP. The nucleotide differentially activates P2Y<sub>1</sub> and P2Y<sub>12</sub> receptors on platelets leading to thrombosis and sealing of the wound. In addition, high concentrations of ADP inhibit CD73, preventing the formation of adenosine, which has opposing, namely antithrombotic and vasodilator effects. Therefore,

selective inhibitors of NTPDase2 could be beneficial in antithrombotic and cardioprotective treatments.

### *NTPDase3*

An alternative, but rarely used name for NTPDase3 is CD39-like enzyme 3. NTPDase3 is found in the brain, where it is hypothesized to regulate pre-synaptic concentrations of extracellular ATP and to influence feeding, sleep-wake and other behaviors in concert with P2X receptors.<sup>22,85</sup> On account of its expression pattern and involvement in the control of nociceptive nucleotide transmission, NTPDase3 represents a potential target for research on neuroinflammatory and neurodegenerative diseases.<sup>37</sup>

NTPDase3 is co-expressed with other ecto-nucleotidases on epithelial surfaces including airways, kidneys, reproductive and digestive systems.<sup>37</sup> The enzyme is concentrated in Langerhans islet cells of the pancreas, where it modulates the activation of P2 receptors.<sup>87</sup> The insulin release from a rat  $\beta$ -cell line (INS-1 (832/13)) was increased by inhibition of NTPDase3.<sup>85,87</sup> Consequently, potent inhibitors of NTPDase3 are promising drugs, that could be utilized to stimulate glucose-induced insulin secretion.

### *NTPDase8*

NTPDase8 is expressed at high concentrations in inner organs including kidney and intestine.<sup>37,41</sup> The enzyme is the main ecto-nucleotidase in the liver,<sup>50</sup> where it is abundant in bile canaliculi and blood vessels and is therefore proposed to regulate bile secretion and reabsorption of nucleosides.<sup>22,85</sup>

## **Small molecule modulators**

As detailed in the previous paragraphs, NTPDases influence several physiological and pathological conditions. Their enzymatic activity can potentially be increased or inhibited by small molecules or antibodies. So far, no positive allosteric modulators of CD39 and other ecto-NTPDases are known. In comparison to purinergic receptors, an advantage of targeting NTPDases is that these enzymes potentially require lower doses for the same pharmacological effect as, e.g. adenosine receptor antagonists. NTPDase inhibitors are expected to have a broad therapeutic range.

An ideal inhibitor should be selective and not affect the activation of nucleotide receptors or other ecto-nucleotidases. The selectivity is more important for pharmacological tool compounds than for drugs. Pharmacological tool compounds are selective inhibitors and utilized to study a target's effect on physiological and pathological processes in *in vitro* and *in vivo* studies. The modulator should be stable in the context of its application, e.g. show chemical stability in the assay system, and metabolic stability for use *in vivo*. This entails the resistance to degradation by the target enzyme and a reasonable elimination half-life in human and model organisms.<sup>88</sup>

However, the development of potent and specific small molecular inhibitors of NTPDases has so far been met with limited success. In general, NTPDase inhibitors are classified into nucleotide analogs, which mimic the substrates or products of NTPDases, and non-nucleotides. The latter group includes polyoxometalates, anthraquinone derivatives and heterocyclic compounds.<sup>88</sup> The following sections aim to give an overview of the current ecto-NTPDase inhibitor classes, recommendations for their application and an assessment of their potential for drug development. **Table 5** to **Table 8** summarize the most potent inhibitors for the respective isoenzymes from each publication along with their potencies.

**Classic inhibitors** of ecto-NTPDases include suramin (and its derivative NF279), sulfonate dyes like reactive blue 2 (**E-31**), PPADS (pyridoxal phosphate-6-azophenyl-2',4'-disulfonic acid), and BG0136 (1-naphthol-3, 6-disulfonic acid).<sup>89,90</sup> These compounds are only moderately potent and non-selective with regard to P2 receptors, which antagonizes the intended effect and therefore limits their usefulness in complex *in vitro* and *in vivo* experiments.<sup>87,90</sup>

**Nucleotide analogs** have been studied intensely as CD39 and NTPDase inhibitors. The resistance of substrate analogs towards hydrolysis by the enzymes is crucial for their effectiveness. Adenine derivatives with electron-donating groups at C8 were shown to be more resistant to hydrolysis than 8-unsubstituted nucleotides.<sup>91,92</sup> 8-BuS-ATP (**E-3**), 8-BuS-ADP and 8-BuS-AMP(**E-4**) were shown to be competitive inhibitors of CD39 with low micromolar potencies ( $K_i = 0.8 \mu\text{M}$  see **Table 5**). They do not modulate P2 receptors, but their high polarity is a challenge for drug development.<sup>91,92</sup> From this series, 8-BuS-AMP (**E-4**) is a promising lead structure for derivatization and drug development. ARL67156 (**E-1**) and its derivatives (e.g. the 8-BuS-analog (**E-2**)) are multi-NTPDase

inhibitors and were proposed to be stable towards hydrolysis by NTPDases, because the cleavage site is blocked by a  $\beta,\gamma$ -dibromomethylene moiety.<sup>93</sup> Yet their metabolic stability towards liver microsomes proved to be poor.<sup>94</sup> Currently, ARL67156 (**E-1**) is the only commercially available small molecule NTPDase/CD39 inhibitor and therefore frequently used in both *in vitro* and *in vivo* studies.<sup>95-97</sup> In light of its recently discovered poor metabolic stability, the inhibitor should only be used in *in vitro* assay systems.<sup>94</sup>

The related structure 2-hexylthio- $\beta,\gamma$ -methylene-ATP (**E-19**) is a mixed-type, predominantly competitive, selective inhibitor of NTPDase2 (see **Table 6**).<sup>98</sup> The substitution at the C2-position is proposed to be important for its inhibitory potency and selectivity ( $K_i = 21 \mu\text{M}$ ).<sup>98</sup> The uncharged nucleotide analog PSB-6426 (**E-20**), an uridine-5'-carboxylic acid derivative, is a selective inhibitor of NTPDase2 (NTPDase2:  $K_i = 8.2 \mu\text{M}$ , CD39:  $\text{IC}_{50} \approx 1000 \mu\text{M}$ ).<sup>99</sup> It is metabolically stable and does not interact with P2Y<sub>2</sub>-, P2Y<sub>4</sub>- and P2Y<sub>6</sub> receptors.<sup>99</sup> Due to its uncharged state at a physiological pH value of 7.4, and due to its chemical as well as metabolic stability, this compound has the potential for per oral bioavailability.<sup>99</sup> So far, it has not been further studied in cell-based or *in vivo* experiments.

**Polyoxometalates (POMs)** are covalently bridged cluster compounds, which were reported to exert pharmacological effects by modulation of extracellular targets. POMs are generally stable, but their high molecular mass and multiple negative charges restrict their oral bioavailability, as they are not able to pass through epithelial cells.<sup>100</sup> PSB-POM1 (**E-5**) and PSB-POM142 (**E-6**) are potent inhibitors of CD39 and NTPDase3 (see **Table 5** and **Table 7**), but also block the activity of several other ecto-nucleotidases, in particular NPP1.<sup>100,101</sup> PSB-POM142 (**E-6**) is among the most potent CD39 inhibitors described so far ( $K_i = 3.88 \text{ nM}$ ).<sup>100</sup> PSB-POM1 (**E-5**) is commercially available and was successfully applied in *in vivo* experiments, where it increased the activity of natural killer cells in mice, leading to less metastases in various tumor models.<sup>102</sup> However, its multi-targeted inhibition of various ecto-nucleotidases including NPP1 and AP,<sup>100</sup> but also off-target effects on synaptic transmission are challenges for the interpretation of more complex animal models.<sup>32,103</sup>

**Anthraquinones** were developed from the classic NTPDase inhibitor reactive blue 2 (**E-31**). The study of structure-activity-relationships and the synthesis of derivatives generated potent and selective inhibitors of NTPDase2 and NTPDase3 (**E-21 - E-23** and

**E-32**, **E-33**, see **Table 6** and **Table 7**).<sup>104</sup> A crystal structure of rat NTPDase2 with PSB-071 (**E-23**) was published, which illuminated the binding mode of this compound (PDB-ID: 4CD1, 4CD3).<sup>54</sup> In the crystal structure of rat NTPDase2 two molecules of PSB-071 (**E-23**) were bound sandwiched near the active site. Interestingly, this anthraquinone (**E-23**) was no particularly potent inhibitor of human NTPDase2 (rat NTPDase2: IC<sub>50</sub> = 12.8 μM; human NTPDase2: IC<sub>50</sub> > 2 μM (22 % inhibition)).<sup>105</sup> Comparison of selective NTPDase2 and -3 anthraquinones, reveals that NTPDase2 inhibitors have more lipophilic residues, such as polynuclear-aromatic rings, while NTPDase3 inhibitors bear smaller polar substituents.<sup>105</sup> The most potent NTPDase2 inhibitor, compound **E-21** (PSB-16131) was characterized as a non-competitive inhibitor, and NTPDase3 was inhibited with a mixed-type inhibition by compound **E-33** (PSB-1011). The anthraquinone scaffold bears the disadvantage of a polar sulfonate function, which decreases its membrane permeability. Furthermore, the blue to green color of the compounds potentially interfere with *in vitro* assay readouts. In consequence, anthraquinone derivatives cannot be applied universally, but are useful tool compounds for the study of NTPDase2 and NTPDase3.

**Clopidogrel (E-8)** and **ticlopidine (E-9)** are prodrugs used in anti-thrombotic prophylaxis of stroke and heart infarction.<sup>106,107</sup> Oxidative metabolism of both drugs generates cysteine-reactive derivatives, which block the pro-thrombotic activity of P2Y<sub>12</sub> receptors. Compounds **E-8** and **E-9** were shown to directly inhibit CD39 activities.<sup>108</sup> This inhibition was confirmed in subsequent studies, although the compounds were found to be less potent than previously reported (see **Table 5**).<sup>108-110</sup> A ticlopidine-related 2-substituted thienotetrahydropyridine (**E-10**) was demonstrated to be an equally potent inhibitor of CD39 as ticlopidine (**E-9**) and it additionally decreased the activity of CD73.<sup>110</sup> The substitution at the 2-position prevents oxidative metabolism to reactive thiols. Ticlopidine (**E-8**) and its 2-substituted derivative (**E-10**) have a limited water solubility at pH 7.4 and are not sufficiently potent to be recommended as tool compounds, but the scaffold is promising for the development of drug-like inhibitors of CD39.

In recent years, a series of papers on ecto-NTPDase inhibitors were published by Prof. Iqbal's group, which focus on the synthesis and characterization of **heterocyclic scaffolds**. These include Schiff bases of tryptamine, oxindolines, quinolines, and thiadiazolopyrimidones.<sup>111-117</sup> The compounds were studied for their *in vitro* inhibitory potency on all ecto-NTPDases. The most potent derivatives for each isoenzyme are

collected in **Table 5** to **Table 8**. The compounds inhibited all ecto-NTPDases in the micromolar to nanomolar range, each series containing NTPDase subtype-selective compounds as well, e.g. **E-25** (NTPDase2:  $IC_{50} = 0.16 \mu M$ ).<sup>114</sup>

The most potent CD39-inhibiting Schiff bases of tryptamine, **E-11** proved to be less potent in our hands (future publication, data not shown). In addition, Schiff base **E-11** was found to be hydrolytically unstable and is therefore not a suitable pharmacological tool compound.

The oxoindolines **E-35** and **E-36** were potent inhibitors of NTPDase3 (**E-35**:  $IC_{50} = 0.30 \mu M$ ; **E-36**:  $IC_{50} = 0.30 \mu M$ ).<sup>113,114</sup> The carbothioamide **E-35** exhibited some selectivity and did not affect NTPDase2 and -8, but carboxamide **E-36** inhibited the other ecto-NTPDases with equal potency (see Table 7). Interestingly, different types of inhibition were determined (**E-35** non-competitive, **E-36** competitive) although the structures are closely related. As NTPDase3 is connected to the control of insulin release, the effects of both compounds, **E-35** and **E-36**, were tested in mice Langerhans islets. The compounds successfully decreased the ecto-nucleotidase activity and increased insulin secretion.<sup>113,114</sup> The authors of the study claim that the conducted experiments qualify compound **E-36** to be a valuable pharmacological tool compound,<sup>113</sup> but since this inhibitor cannot discriminate the functions of ecto-NTPDase isoenzymes, it cannot be recommended for this purpose by the author of this thesis.

Quinoline derivatives have high inhibition efficiencies as multi-NTPDase inhibitors. The most potent inhibitor of CD39 had a non-competitive inhibition type, while NTPDases2, -3 and -8 were competitively inhibited by the respective derivatives.<sup>116,117</sup> Compound **E-44** exhibited a competitive inhibition of NTPDase8 with more than 100-fold selectivity towards the other tested ecto-NTPDases (**E-44**:  $IC_{50} = 0.65 \mu M$ , see Table 8).<sup>117</sup> Since there are so far no suitable inhibitors of NTPDase8, this compound should be further studied for its potential as a pharmacological tool compound. Due to their similar structures to purines, tryptamine and quinoline derivatives might penetrate cells and induce unintended off-target effects.<sup>103</sup>

Thiadiazolopyrimidones were characterized as unselective inhibitors of all ecto-NTPDases with an emphasis on NTPDase8 (see compound **E-45** in **Table 8**).<sup>115</sup> The synthesis of these compounds was previously published along with their characterization

as non-specific inhibitors of human alkaline phosphatases (h-TNAP and h-IAP) with potencies in the low micromolar range;<sup>118</sup> which is lower than the reported inhibition constants for ecto-NTPDases.<sup>115</sup>

In summary, the heterocyclic compounds from Prof. Iqbal's group were mostly unselective ecto-NTPDase inhibitors, some of which have relatively high reported *in vitro* potencies. The effects on other targets involved in nucleotide metabolism were not studied or not referenced.<sup>115,118</sup> Therefore, further studies confirming the potencies in orthogonal assay systems, selectivity and chemical as well as metabolic stability need to be conducted by independent laboratories.

In a virtual screening effort based on a homology model of CD39 a triazinoindole derivative (SMI211, **E-18**) was identified and characterized as a CD39 inhibitor ( $IC_{50} = 27.42 \mu\text{M}$ ).<sup>119</sup> Compound **E-18** was reported to inhibit AMP generation and proliferation of colorectal cancer cell lines (HT29 and MC38). As the  $K_m$  value of CD39 was increased in the presence of 100  $\mu\text{M}$  inhibitor, a competitive inhibition type was proposed.<sup>119</sup> These findings warrant further studies and identify SMI211 (**E-18**) as an interesting starting point for the design of derivatives with improved potencies.



**Table 5.** Representative small molecule inhibitors of human NTPDase1 (CD39)

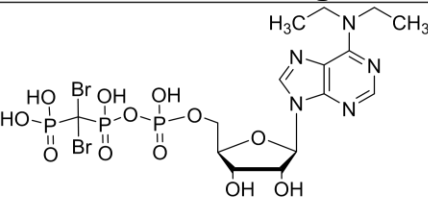
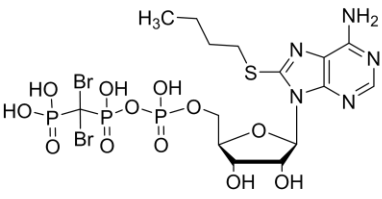
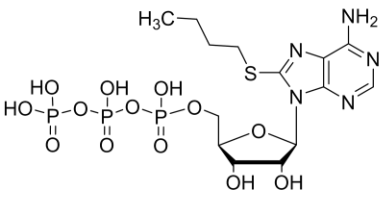
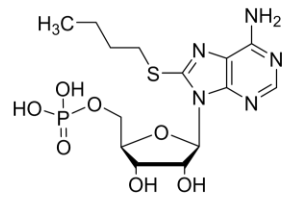
#	Name E- (No. in original publication)	Structure	Potency at human CD39	Potencies at relevant human ecto- nucleotidases
<b>Nucleotide-analogs</b>				
1	ARL67156		$K_i = 11 \mu\text{M}^{93}$ $K_i = 0.973 \mu\text{M}^{94}$	NTPDase3: $K_i = 7.94 \mu\text{M}$ CD73: $K_i = 0.451 \mu\text{M}$ NPP1: $K_i = 4.41 \mu\text{M}^{94}$
2	PSB-172102 (31)		$K_i = 1.13 \mu\text{M}^{94}$	NTPDase2: $K_i = 22.2 \mu\text{M}$ NTPDase3: $K_i = 1.54 \mu\text{M}$ CD73: $K_i = 0.831 \mu\text{M}$ NPP1: $K_i = 5.17 \mu\text{M}^{94}$
3	8-BuS-ATP (1)		$K_i = 0.8 \mu\text{M}^{91}$	Selective vs. other ecto- NTPDases ( $\text{IC}_{50} > 100 \mu\text{M}$ ) <sup>91</sup>
4	8-BuS-AMP (10)		$K_i = 0.8 \mu\text{M}^{91}$	Selective vs. other ecto- NTPDases ( $\text{IC}_{50} > 100 \mu\text{M}$ ) <sup>91</sup>

Table 5. continued


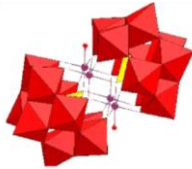
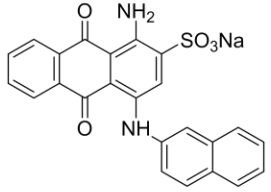
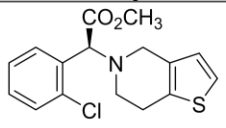
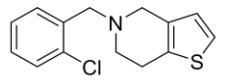
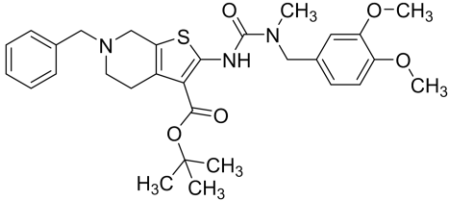
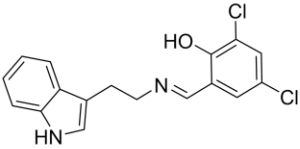
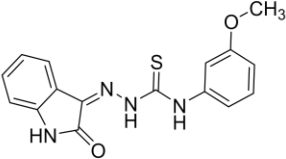
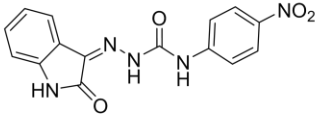
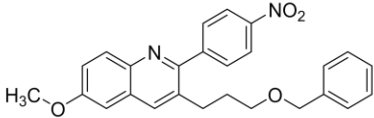
#	Name E- (No. in original publication)	Structure	Potency at human CD39	Potencies at relevant human ecto-nucleotidases
<b>Polyoxometalates</b>				
5	PSB-POM1	 $\text{Na}_{10}[\text{H}_2\text{W}_{12}\text{O}_{40}] \cdot 21 \text{H}_2\text{O}$	$K_i = 0.800 \mu\text{M}^{100,101}$	NTPDase3: $K_i = 0.663 \mu\text{M}$ NPP1: $K_i = 0.0118 \mu\text{M}^{100,101}$
6	PSB-POM142 (5)	 $\text{K}_{10}[\text{Co}_4(\text{H}_2\text{O})_2(\text{PW}_9\text{O}_{34})_2] \cdot 22 \text{H}_2\text{O}$	$K_i = 0.00388 \mu\text{M}^{100}$	NTPDase2: $K_i = 0.0882 \mu\text{M}$ NTPDase3: $K_i = 0.0596 \mu\text{M}$ NPP1: $K_i = 0.069 \mu\text{M}^{100}$
<b>Anthraquinones</b>				
7	1-Amino-2-sulfo-4-(2-naphthylamino) anthraquinone (18)		ratCD39: $\text{IC}_{50} = 0.328 \mu\text{M}^{104}$ humanCD39: $\text{IC}_{50} > 2 \mu\text{M}^{105}$	Rat NTPDase2: $\text{IC}_{50} = 19.1 \mu\text{M}$ Rat NTPDase3: $\text{IC}_{50} = 2.22 \mu\text{M}^{104}$ Human ecto-NTPDases $\text{IC}_{50} > 2 \mu\text{M}^{105}$
<b>Heterocycles</b>				
8	Clopidogrel		$K_i = 10 \mu\text{M}^{108}$ $\text{IC}_{50} = 113 \mu\text{M}^{110}$	Selective vs. other ecto-NTPDases ( $\text{IC}_{50} > 100 \mu\text{M}$ ) <sup>109</sup>
9	Ticlopidine		$K_i = 14 \mu\text{M}^{108}$ $\text{IC}_{50} = 81.7 \mu\text{M}$ (non-competitive) <sup>110</sup>	Selective vs. other ecto-NTPDases $\text{IC}_{50} > 100 \mu\text{M}^{109,110}$

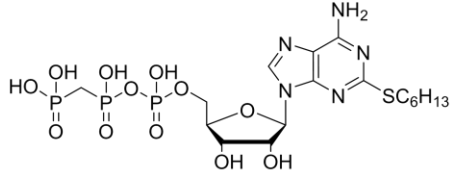
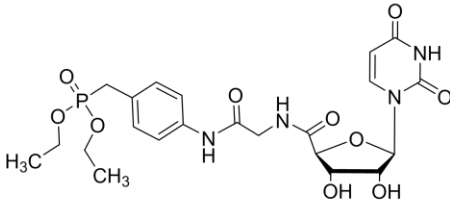
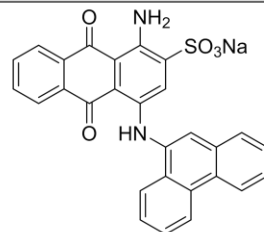
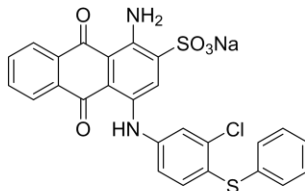
Table 5. continued

#	Name (No. in original publication)	Structure	Potency at human CD39	Potencies at relevant human ecto-nucleotidases
10	2-substituted thienotetrahydropyridine (32)		IC <sub>50</sub> = 84.8 μM (non-competitive) <sup>110</sup>	soluble CD39: IC <sub>50</sub> = 45.2 μM CD73: IC <sub>50</sub> = 45.8 μM <sup>110</sup>
11	Schiff base of tryptamine derivative (6)		K <sub>i</sub> = 0.021 μM (competitive) <sup>111</sup>	NTPDase3: K <sub>i</sub> = 0.112 μM NTPDase8: K <sub>i</sub> = 0.220 μM <sup>111</sup>
12	Oxoindolin phenyl hydrazine carbothioamide derivative (8e)		IC <sub>50</sub> = 0.15 μM (non-competitive) <sup>114</sup>	ecto-NTPDases IC <sub>50</sub> > 100 μM <sup>114</sup>
13	Oxoindolin phenyl hydrazine carboxamide derivative (2h)		IC <sub>50</sub> = 0.12 μM (un-competitive) <sup>113</sup>	ecto-NTPDases IC <sub>50</sub> > 25 μM <sup>113</sup>
14	Quinoline derivative (3p)		IC <sub>50</sub> = 0.23 μM (un-competitive) <sup>116</sup>	NTPDase2: IC <sub>50</sub> = 34.1 μM NTPDase3: IC <sub>50</sub> = 37.0 μM NTPDase8: IC <sub>50</sub> = 8.44 μM <sup>116</sup>

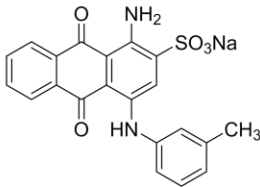
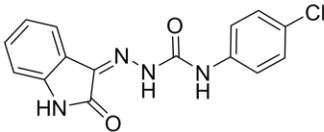
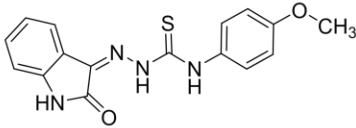
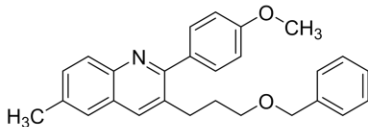
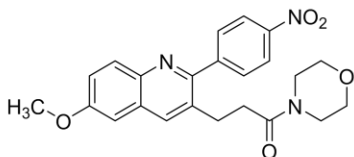
**Table 5.** continued

#	Name E- (No. in original publication)	Structure	Potency at human CD39	Potencies at relevant human ecto-nucleotidases
15	Quinoline derivative (3f)		IC <sub>50</sub> = 0.20 μM (mixed-type inhibition) <sup>117</sup>	NTPDase3: IC <sub>50</sub> = 5.50 μM NTPDase2,-8 IC <sub>50</sub> > 100 μM <sup>117</sup>
16	2-substituted-7-trifluoro- methyl- thiadiazolopyrimidone derivative (4m)		IC <sub>50</sub> = 1.13 μM <sup>115</sup>	NTPDase2: IC <sub>50</sub> = 11.42 μM NTPDase3: IC <sub>50</sub> = 10.44 μM NTPDase8: IC <sub>50</sub> = 0.47 μM <sup>115</sup> TNAP: IC <sub>50</sub> = 1.53 μM <sup>118</sup>
17	Thiadiazole amide derivative (5a)		IC <sub>50</sub> = 0.05 μM (non-competitive) <sup>112</sup>	NTPDase2: IC <sub>50</sub> = 0.23 μM NTPDase8: IC <sub>50</sub> = 0.54 μM <sup>112</sup>
18	SMI211		IC <sub>50</sub> = 27.42 μM <sup>119</sup>	not determined

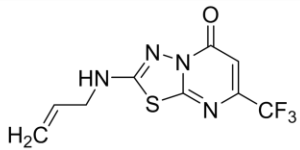
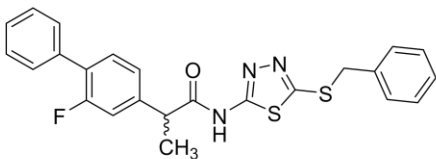
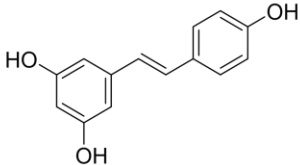
**Table 6.** Representative small molecule inhibitors of human NTPDase2

#	Name (No. in original publication)	Structure	Potency at human NTPDase2	Potencies at relevant human ecto-nucleotidases
<b>Nucleotide-analogs</b>				
19	2-Hexylthio- $\beta,\gamma$ -methylene-ATP (2)		$K_i = 21 \mu\text{M}^{98}$	Selective vs. other ecto-NTPDases, CD73, NPP3 ( $\text{IC}_{50} > 100 \mu\text{M}$ ), NPP1 $\text{IC}_{50} \approx 100 \mu\text{M}^{98}$
20	PSB-6426 (19a)		$K_i = 8.2 \mu\text{M}$ (competitive) <sup>99</sup>	CD39 $\text{IC}_{50} \approx 1000 \mu\text{M}$ , no inhibition of NTPDases3 and -8 at $1000 \mu\text{M}^{99}$
<b>Anthraquinones</b>				
21	PSB-16131 (20)		$\text{IC}_{50} = 0.539 \mu\text{M}$ (non-competitive) <sup>105</sup>	Selective vs other ecto-NTPDases ( $\text{IC}_{50} > 2 \mu\text{M}$ ) <sup>105</sup>
22	PSB-2020 (48)		$\text{IC}_{50} = 0.551 \mu\text{M}^{105}$	Selective vs other ecto-NTPDases ( $\text{IC}_{50} > 2 \mu\text{M}$ ) <sup>105</sup>

**Table 6.** continued

#	Name (No. in original E-publication)	Structure	Potency at human NTPDase2	Potencies at relevant human ecto-nucleotidases
23	PSB-071		rat NTPDase2: IC <sub>50</sub> = 12.8 μM human NTPDase2: IC <sub>50</sub> > 2 μM (22 % inhibition) Crystal structure PDB-ID: 4CD1, 4CD3 <sup>54,104</sup>	Rat CD39: IC <sub>50</sub> = 51.5 μM Rat NTPDase3: IC <sub>50</sub> = 19.1 μM No significant inhibition of human ecto-NTPDases at 2 μM <sup>104,105</sup>
<b>Heterocycles</b>				
24	Oxindolin phenylhydrazine carboxamide derivative (2d)		IC <sub>50</sub> = 0.15 μM (competitive) <sup>113</sup>	CD39: IC <sub>50</sub> = 0.16 μM NTPDase3 and -8: IC <sub>50</sub> ≈ 40 μM <sup>113</sup>
25	Oxindolin phenylhydrazine carbothioamide derivative (8k)		IC <sub>50</sub> = 0.16 μM <sup>114</sup>	Selective vs other ecto-NTPDases (IC <sub>50</sub> > 100 μM) <sup>114</sup>
26	Quinoline derivative (3j)		IC <sub>50</sub> = 21.0 μM <sup>116</sup>	CD39: IC <sub>50</sub> = 1.04 μM NTPDase3: IC <sub>50</sub> = 8.19 μM NTPDase8: IC <sub>50</sub> = 18.3 μM <sup>116</sup>
27	Quinoline derivative (3b)		IC <sub>50</sub> = 0.77 μM (competitive) <sup>117</sup>	CD39: IC <sub>50</sub> = 0.50 μM NTPDase3 and -8: IC <sub>50</sub> ≈ 100 μM <sup>117</sup>

**Table 6.** continued

#	Name (No. in original E-publication)	Structure	Potency at human NTPDase2	Potencies at relevant human ecto-nucleotidases
28	2-substituted-7-trifluoromethyl-thiadiazolopyrimidone derivative (4g)		IC <sub>50</sub> = 1.72 μM <sup>115</sup>	CD39: IC <sub>50</sub> = 15.67 μM NTPDase3: IC <sub>50</sub> = 14.82 μM NTPDase8: IC <sub>50</sub> = 0.21 μM <sup>115</sup> TNAP: IC <sub>50</sub> = 0.29 μM <sup>118</sup>
29	Thiadiazole amide derivative (5g)		IC <sub>50</sub> = 0.04 μM (non-competitive) <sup>112</sup>	NTPDase8: IC <sub>50</sub> = 2.27 μM, selective vs CD39 and NTPDase3 (IC <sub>50</sub> > 100 μM) <sup>112</sup>
<b>Miscellaneous</b>				
30	Resveratrol		IC <sub>50</sub> = 2.71 μM <sup>120</sup>	Selective vs other ecto-NTPDases (IC <sub>50</sub> >> 20 μM) <sup>120</sup>

**Table 7.** Representative small molecule inhibitors of human NTPDase3

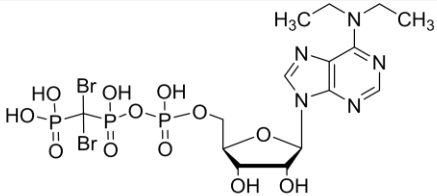
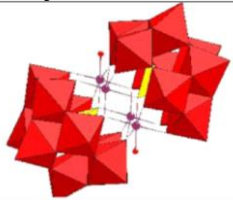
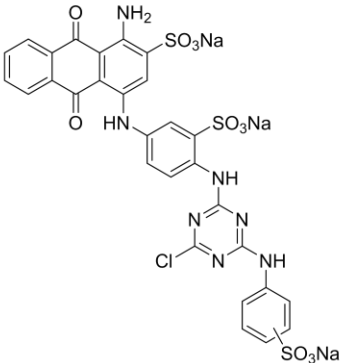
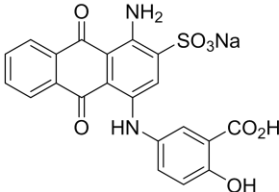
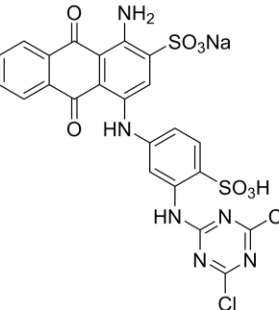
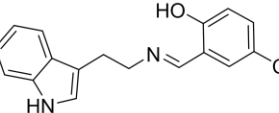
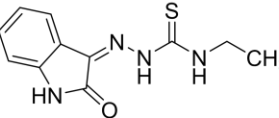
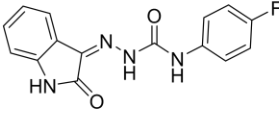
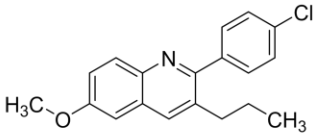
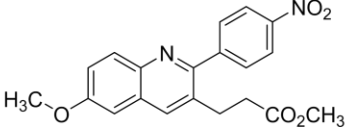
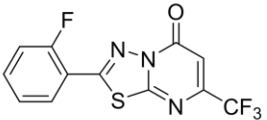
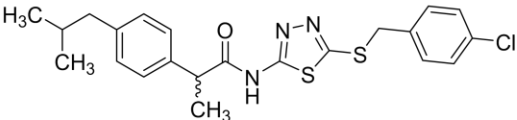
#	Name (No. in original E-publication)	Structure	Potency at human NTPDase3	Potencies at relevant human ecto-nucleotidases
<b>Nucleotide-analogs</b>				
1	ARL67156		$K_i = 18 \mu\text{M}$ (competitive) <sup>93</sup> $K_i = 7.94 \mu\text{M}$ <sup>94</sup>	CD39: $K_i = 0.973 \mu\text{M}$ <sup>94</sup> CD73: $K_i = 0.451 \mu\text{M}$ NPP1: $K_i = 4.41 \mu\text{M}$ <sup>94</sup>
<b>Polyoxometalates</b>				
6	PSB-POM142 (5)	 <p style="text-align: center;"><math>\text{K}_{10}[\text{Co}_4(\text{H}_2\text{O})_2(\text{PW}_9\text{O}_{34})_2] \cdot 22 \text{H}_2\text{O}</math></p>	$K_i = 0.0596 \mu\text{M}$ <sup>100</sup>	CD39: $K_i = 0.00388 \mu\text{M}$ NTPDase2: $K_i = 0.0882 \mu\text{M}$ NPP1: $K_i = 0.069 \mu\text{M}$ <sup>100</sup>
<b>Anthraquinones</b>				
31	Reactive Blue 2 (RB-2)		$\text{IC}_{50} = 0.942 \mu\text{M}$ <sup>105</sup>	Selective vs other ecto-NTPDases ( $\text{IC}_{50} > 2 \mu\text{M}$ ) <sup>105</sup>



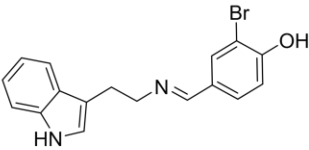
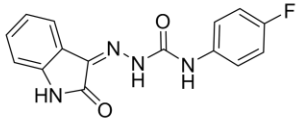
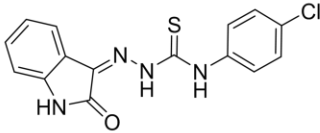
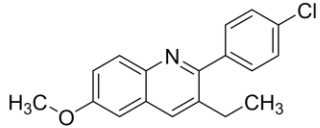
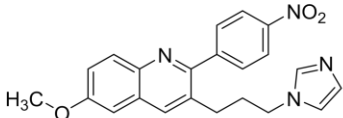
Table 7. continued

#	Name (No. in original publication)	Structure	Potency at human NTPDase3	Potencies at relevant human ecto-nucleotidases
32	PSB-2046 (33)		IC <sub>50</sub> = 0.723 μM <sup>105</sup>	Selective vs other ecto-NTPDases (IC <sub>50</sub> > 2 μM) <sup>105</sup>
33	PSB-1011 (42)		IC <sub>50</sub> = 0.390 μM <sup>105</sup>	Selective vs other ecto-NTPDases (IC <sub>50</sub> > 2 μM) <sup>105</sup>
<b>Heterocycles</b>				
34	Schiff base of tryptamine derivative (5)		K <sub>i</sub> = 0.071 μM (competitive) <sup>111</sup>	CD39: K <sub>i</sub> = 0.13 μM NTPDase8: K <sub>i</sub> = 0.12 μM <sup>111</sup>
35	Oxoindolin hydrazine carbothioamide derivatives (8m)		IC <sub>50</sub> = 0.30 μM (non-competitive) <sup>114</sup>	CD39: IC <sub>50</sub> = 2.60 μM, selective vs. NTPDase2 and -8 (IC <sub>50</sub> > 100 μM) <sup>114</sup>
36	Oxoindolin phenylhydrazine carboxamide derivative (2a)		IC <sub>50</sub> = 0.30 μM (competitive) <sup>113</sup>	CD39: IC <sub>50</sub> = 0.37 μM NTPDase2: IC <sub>50</sub> = 0.27 μM NTPDase8: IC <sub>50</sub> = 0.16 μM <sup>113</sup>

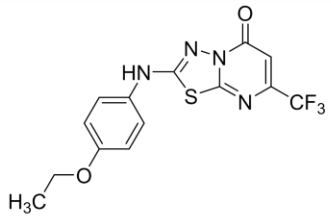
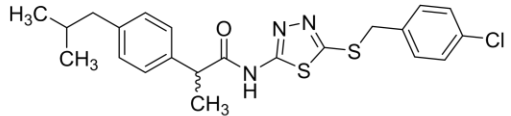
**Table 7.** continued

# E-	Name (No. in original publication)	Structure	Potency at human NTPDase3	Potencies at relevant human ecto- nucleotidases
37	Quinoline derivative (3d)		IC <sub>50</sub> = 5.38 μM (competitive) <sup>116</sup>	CD39: IC <sub>50</sub> = 3.15 μM NTPDase2: IC <sub>50</sub> = 20.0 μM NTPDase8: IC <sub>50</sub> = 65.6 μM <sup>116</sup>
38	Quinoline derivative (2h)		IC <sub>50</sub> = 0.36 μM (competitive) <sup>117</sup>	CD39: IC <sub>50</sub> = 1.34 μM NTPDase2: IC <sub>50</sub> = 1.70 μM NTPDase8: IC <sub>50</sub> = 1.82 μM <sup>117</sup>
39	2-substituted-7-trifluoro- methyl- thiadiazolopyrimidone derivative (5n)		IC <sub>50</sub> = 1.22 μM <sup>115</sup>	CD39: IC <sub>50</sub> = 10.88 μM NTPDase2: IC <sub>50</sub> = 18.37 μM NTPDase8: IC <sub>50</sub> = 4.31 μM <sup>115</sup>
40	Thiadiazole amide derivative (5e)		IC <sub>50</sub> = 0.38 μM (uncompetitive) <sup>112</sup>	CD39: IC <sub>50</sub> = 0.21 μM NTPDase2: IC <sub>50</sub> = 1.07 μM NTPDase8: IC <sub>50</sub> = 0.05 μM <sup>112</sup>

**Table 8.** Representative small molecule inhibitors of human NTPDase8

# E-	Name (No. in original publication)	Structure	Potency at human NTPDase8	Potencies at relevant human ecto-nucleotidases
<b>Heterocycles</b>				
41	Schiff base of tryptamine derivative (8)		$K_i = 0.520 \mu\text{M}$ (competitive) <sup>111</sup>	CD39: $K_i = 0.050 \mu\text{M}$ NTPDase3: no inhibition <sup>111</sup>
36	Oxindolin phenylhydrazine carboxamide derivative (2a)		$\text{IC}_{50} = 0.16 \mu\text{M}$ (competitive) <sup>113</sup>	CD39: $\text{IC}_{50} = 0.37 \mu\text{M}$ NTPDase3: $\text{IC}_{50} = 0.30 \mu\text{M}$ NTPDase2: $\text{IC}_{50} = 0.27 \mu\text{M}$ <sup>113</sup>
42	Oxindolin hydrazine carbothioamide derivatives (8c)		$\text{IC}_{50} = 0.24 \mu\text{M}$ $K_i = 0.11 \mu\text{M}$ (competitive) <sup>114</sup>	CD39: $\text{IC}_{50} = 0.23 \mu\text{M}$ NTPDase2: $\text{IC}_{50} \approx 100 \mu\text{M}$ NTPDase3: $\text{IC}_{50} = 0.19 \mu\text{M}$ <sup>114</sup>
43	Quinoline derivative (3c)		$\text{IC}_{50} = 1.13 \mu\text{M}$ (competitive) <sup>116</sup>	CD39: $\text{IC}_{50} = 2.77 \mu\text{M}$ NTPDase2: $\text{IC}_{50} = 22.8 \mu\text{M}$ NTPDase3: $\text{IC}_{50} = 12.5 \mu\text{M}$ <sup>116</sup>
44	Quinoline derivative (5c)		$\text{IC}_{50} = 0.65 \mu\text{M}$ (competitive) <sup>117</sup>	Selective vs. other ecto-NTPDases ( $\text{IC}_{50} > 100 \mu\text{M}$ ) <sup>117</sup>

**Table 8.** continued

# E-	Name (No. in original publication)	Structure	Potency at human NTPDase8	Potencies at relevant human ecto-nucleotidases
45	2-substituted-7-trifluoromethyl-thiadiazolopyrimidone derivative (4d)		IC <sub>50</sub> = 0.21 μM <sup>115</sup>	CD39: IC <sub>50</sub> = 17.08 μM NTPDase2: IC <sub>50</sub> = 7.77 μM NTPDase3: IC <sub>50</sub> = 1.25 μM <sup>115</sup> TNAP: IC <sub>50</sub> = 0.29 μM <sup>118</sup>
40	Thiadiazole amide derivative (5e)		IC <sub>50</sub> = 0.05 μM (uncompetitive) <sup>112</sup>	CD39 IC <sub>50</sub> = 0.21 μM NTPDase2: IC <sub>50</sub> = 1.07 μM NTPDase3: IC <sub>50</sub> = 0.38 μM <sup>112</sup>

## Biologicals

**Sulfated polysaccharides** from macroalgae were found to be dual inhibitors of NPP1 and CD39.<sup>121</sup> The brown algae-derived fucoidan extract from *Saccharina latissimi* (compound no. 6 in publication by Lopez et al.)<sup>121</sup> inhibited CD39 with a  $K_i$  value of 408 pM and NPP1 with a  $K_i$  value of 136 pM.<sup>121</sup> The inhibition of the two main ATP-metabolizing enzymes decreased adenosine generation by a human glioblastoma cell line (U87) in a concentration-dependent manner. The experiments offer a rationale for the previously noted anticancer properties of these natural products.

Several NTPDase-blocking **monoclonal antibodies** (mAbs) were developed. While only few mAbs have been generated for NTPDases 2, -3 and -8,<sup>122-124</sup> an increasing number of CD39 blocking antibodies have been published and are currently in clinical trials. Examples of humanized or fully human anti-CD39 antibodies targeting the ATP-adenosine immune-checkpoint pathway for cancer immunotherapy include TTX-030 (Tizona Therapeutics, NCT03884556), SRF617 (Surface Oncology, NCT04336098, NCT05177770), PUR001 (Purinomia Biotech, NCT05234853), OREG-103/BY40 (Orega Biontech), and Innate Pharma (IPH52).<sup>32,75,125-127</sup> The antibodies are evaluated in clinical trials as monotherapy and in combination with chemotherapeutics, in order to study potential synergistic effects, in the decrease of tumor proliferation.<sup>72,103</sup>

An alternative route of therapy are **miRNAs**, which regulate the post-transcriptional gene expression by attaching to the sequences of mRNAs, leading to a selective downregulation of expression.<sup>128,129</sup> This therapeutic strategy could be used in the treatment of cancers to normalize dysregulated purinergic signaling. Proof-of-concept studies are in process. miRNAs have to be delivered into the cells; possible routes of cell delivery are erythrocyte ghosts, cationic lipoplexes, neutral lipid emulsions (NLEs), nanoparticles, and cell-penetrating peptides.<sup>129</sup> Along with siRNAs and antibody-drug conjugates, the developed biological treatments may represent novel therapeutic checkpoint inhibitors.<sup>103</sup>

## Experimental characterization of NTPDase activities

The characterization of substrate and inhibitor affinities for the various NTPDase isoenzymes, is performed by assessing the hydrolysis of the substrate in the presence or absence of potential modulators in various assays. Experiments either determine the decreasing concentration of the substrate, increasing concentrations of the

dephosphorylated product, or phosphate release. In the course of the experimental work for this thesis, the malachite green assay, capillary electrophoresis-coupled assays with natural or fluorescence-labeled substrates, and a fluorescence polarization immunoassay were applied to characterize the inhibition constants of various compound classes.<sup>94,105,110,121</sup> It is important to consider that the tested substances may interfere with the assay system. Therefore, it is good scientific practice to determine the effect of a new inhibitor in at least two orthogonal assays, and to always use appropriate control samples. The following paragraphs explain the basic principles for the determination of NTPDase activity.

#### *Malachite green assay*

The enzymatic degradation of ATP to AMP by ecto-NTPDases releases two phosphate molecules (see **Figure 8**). These can be made visible by adding detection reagents, leading to the formation of a malachite green-phosphomolybdate complex, which results in a color change from the yellow malachite green to the green phosphate complex at pH < 2.<sup>130</sup> The absorptions of samples are detected colorimetrically at 600 nm by a spectrophotometer. The assay allows a fast, inexpensive and user-friendly operation. However, the results can be distorted by phosphate contamination, resulting in a high background signal and low sensitivity.<sup>43</sup> For the investigation of complex samples or living cells with this assay, the activities of alternative phosphate generating enzymes has to be blocked by specific inhibitors.

#### *Capillary electrophoresis*

The enzyme and substrates are incubated for a set time, at which the enzymatic activity is stopped (e.g. by heating) and the sample composition is analyzed by means of capillary electrophoresis (CE). Alternatively, the reaction of enzyme, substrate and co-factors can be performed inside the capillary and stopped by the separation process.<sup>131</sup> Various natural substrates like ATP and ADP, but also fluorescence-labeled substrates (e.g. *N*<sup>6</sup>-[6-fluoresceinyl-5'-carboxamidoethyl]-ATP (PSB-170621A))<sup>52</sup> may be distinguished from their corresponding monophosphates based on negative charge and size. The application of fluorescent substrates allows for lower substrate concentrations as the detection method is more sensitive.<sup>52</sup> Moreover, many compounds potentially absorb UV-light at the absorption wavelength of nucleotides (260 nm), especially if they are structurally

similar (e.g. nucleotide analogs), and thereby potentially interfere with the results. Advantages of CE-coupled assays include simple sample preparation, use of water-based solvents, and automatization. But depending on the detection method, high substrate concentrations are necessary, and the measurement of samples is time-consuming, which deems this methods unsuitable for high-throughput screening.<sup>43</sup>

#### *Fluorescence polarization-based immunoassay (FPIA)*

The FPIA enables the direct quantification of the product of NTPDases, AMP, yielded from the substrate ADP. The assay is based on investigating the fluorescence polarization of an Alexa633-AMP tracer, by displacement from its binding site at an AMP-selective antibody.<sup>132-134</sup> If a fluorophore is excited by plane-polarized light, it emits polarized light of a different wavelength. The intensity of polarization is dependent on the size of the molecule. Larger molecules have less rotation energy, which affects the direction of the emitted photons. High polarization values are detected if the tracer is bound to the antibody, while lower values are measured if the tracer is unbound. As stated above, the large molecule complex of tracer and antibody has a lower rotation rate and predominantly emits light on the vertical axis. Small molecules, like the unbound tracer, have a higher rotation rate and scatter the plane-polarized light during the excited state,<sup>132</sup> therefore the emitted light is less polarized, and smaller polarization values are detected.

Advantages of this assay are its plate-based format, high robustness, flexibility, precision and reproducibility.<sup>132</sup> Therefore it can be used for high-throughput screening with substrate concentrations below the  $K_m$  value.<sup>132</sup> This facilitates the identification of competitive inhibitors, as their identification is usually more difficult at high substrate concentrations.<sup>132</sup> However, the high complexity, pipetting of small volumes, and expensive materials required for the assay are disadvantages for routine laboratory practice. Furthermore, FPIA is not well applicable for certain investigations like the determination of the inhibition type, because the antibody concentration has to be adjusted to each substrate concentration.

#### *High performance liquid chromatography (HPLC)*

In analogy to CE-coupled enzyme assays, nucleotides and nucleosides can be separated by liquid chromatography. HPLC is able to resolve mixtures of closely related chemicals with high resolution and sensitive quantification.<sup>135</sup> The method is extremely versatile

and is therefore among the standard analytical methods in research and industry. The sensitivity is strongly dependent on the detection method. Nucleotides are routinely detected by absorption of ultraviolet (UV) light at 254 nm. *N*<sup>6</sup>-etheno derivatives of nucleotides can be detected with fluorescent detectors, which enables lower concentrations of the artificial substrate and observation of nucleotide metabolism in cell-based experiments. Mass spectrometry-coupled HPLC additionally enables the identification of analytes. Internal standards are required for the quantification of the sample composition ensuing NTPDase incubation. Disadvantages of HPLC-coupled enzyme assays are time-consuming instrument and sample preparations. Analytes need to be extracted from complex matrices, in order to prevent occlusion of columns.<sup>136</sup>

#### *Luciferase assay*

The concentration of ATP can be quantified by utilization of a second enzymatic reaction, namely luciferase. Following the partial hydrolysis by NTPDases, the remaining ATP is a co-factor in the oxidation of luciferin, generating a detectable bioluminescence.<sup>137</sup> The assay preparation is easy, fast and scalable to a high-throughput format.<sup>137</sup> However, it is more sensible to quantify the formation of products, instead of leftover substrate, since the characterization of enzyme activities is ideally performed at 5-15% conversion rates. The accuracy of the determination of small changes of ATP concentration is low and the additional enzymatic reaction can result in high statistical errors.<sup>43</sup>

#### *Isothermal titration calorimetry (ITC)*

ITC detects the energy that is released by the dephosphorylation reaction in the form of heat.<sup>51</sup> This assay principle is suitable for the determination of NTPDase activities but restricted by its low sensitivity and limited specificity due to the indirect measurement of the chemical reaction. Possible interferences are buffer composition and pH, as well as alternative chemical reactions elicited by test compounds.<sup>43</sup>

#### *Radioactively labeled substrates*

Similar to the malachite green assay, the phosphate liberation by NTPDases can be quantified using radioactively labeled substrates, e.g. [ $\gamma$ -<sup>32</sup>P]ATP. The radioactivity in the supernatant subsequent to separation of the non-metabolized <sup>32</sup>P-nucleotide by precipitation or filtration correlates with the catalytic activity. This method is versatile,



sensitive and highly specific, and can be applied for the characterization of enzyme kinetics in complex samples.<sup>138</sup> However, the substrates are expensive and have a short half-life depending on the <sup>32</sup>P isotope (~14 days). As phosphate is potentially produced by other purinergic enzymes, specific tool compounds, blocking alternative phosphate-generating pathways or purified enzymes have to be used.<sup>43</sup> Furthermore, the regulations for working with radioactivity require special laboratories, equipment and qualified personnel. In summary, this particular method is no longer used for the characterization of NTPDases, as methods using fluorescence-labeled ligands are sufficiently sensitive and more environmentally friendly.

#### *Thin layer chromatography (TLC)*

Finally, nucleotides and nucleosides may be separated by TLC. Purine substrates containing the radioactive isotopes <sup>3</sup>H or <sup>14</sup>C are incubated with the enzyme sample or cells. The reaction is stopped by separation of the components on TLC plates. Identification of the nucleotides is achieved by co-migration of un-labeled standards, which are visible under UV-light. In the next step, the radioactivity is quantified by scratching off the silica gel at the position of the standards, subsequent extraction and scintillation counting. The selectivity and sensitivity of radio-assays are very high but, as previously mentioned, the complex regulations, combined with high costs, limit the broad application of radioisotope-based techniques.<sup>43</sup>

#### 2.2.4 Ecto-5'-nucleotidase (eN, CD73)

Although the family of 5'-nucleotidases consists of seven subtypes, only one, namely CD73, is an ectoenzyme.<sup>41</sup> The human homodimeric protein is fixed in the plasma membrane via a glycosylphosphatidylinositol (GPI) anchor at the C-terminus, which can be cleaved by phospholipases.<sup>88</sup> CD73-containing vesicles and soluble forms of the enzyme released into the extracellular environment were found to modulate purinergic signaling at sites of inflammation.<sup>39</sup>

CD73 is able to hydrolyze several ribo- and desoxyribonucleoside-5'-monophosphates. Most importantly, it effectively transforms AMP to adenosine ( $K_m = 1\text{--}50 \mu\text{M}$ ).<sup>37</sup> The catalytic domain of the enzyme faces the extracellular medium, and two divalent cations,

namely  $\text{Zn}^{2+}$  ions, are required for its activity.<sup>37,41</sup> The enzyme is expressed in various tissues including the endothelial cells of blood vessels, subpopulations of human T- and B-lymphocytes, and tumor cells.<sup>37</sup>

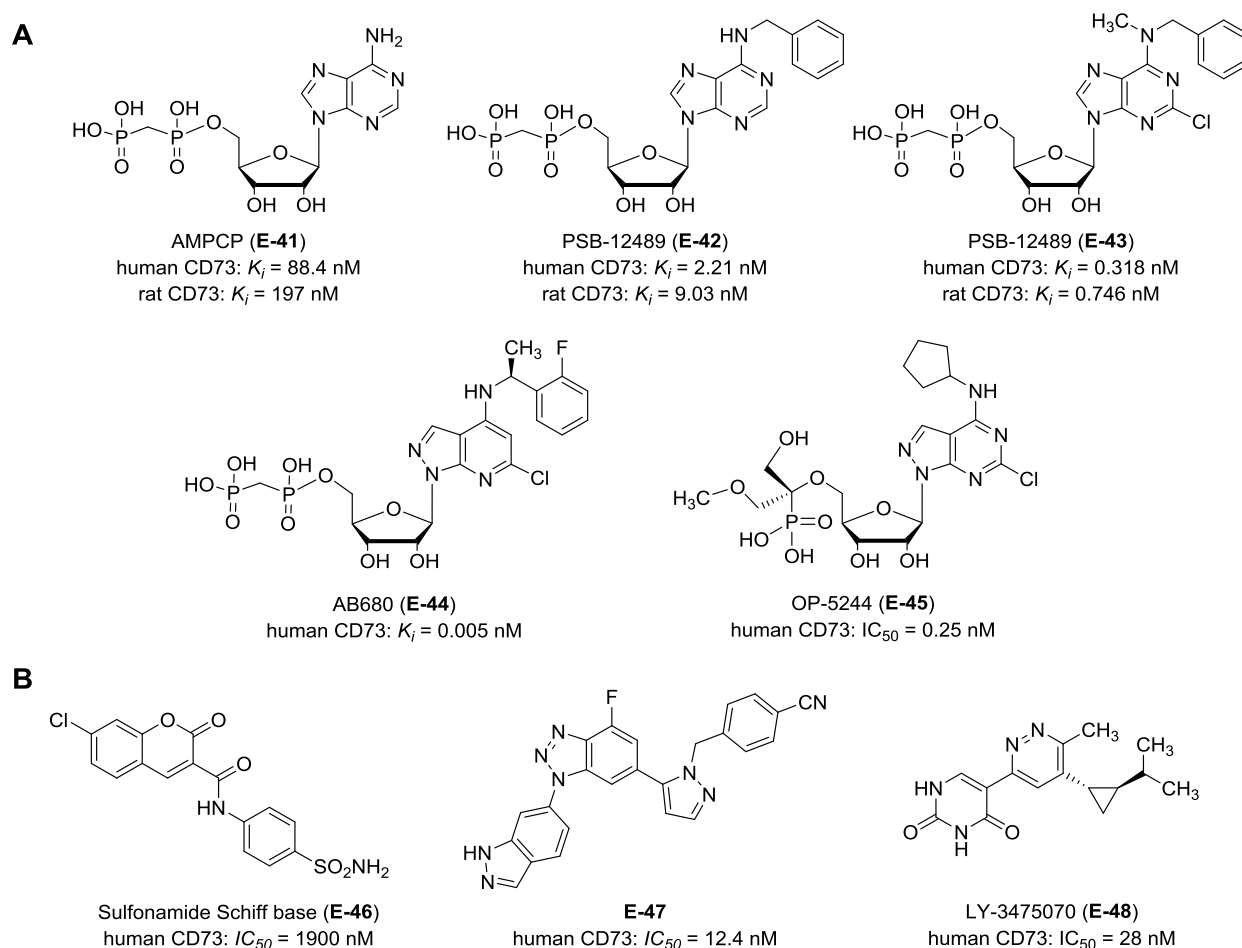
The main purpose of CD73 is the production of extracellular adenosine, which modulates biological processes via activation of P1 receptors. This leads to a downregulation of the immune system, which is important for maintaining tissue integrity and recovery from chronic and acute injuries. However, this signaling pathway can be hijacked by pathogens and tumors, leading to their immune escape and pathogenic proliferation.<sup>37,88</sup> Furthermore, CD73 contributes to vascular fluidity by production of adenosine, which leads to vasodilation via the adenosine  $A_{2A}$  receptor.<sup>139</sup>

ATP and ADP are endogenous CD73 inhibitors blocking its catalytic site with low micromolar potencies.<sup>37</sup> This feed-forward inhibition prohibits a simultaneous activation of P2 and P1 receptors, since the concentration of P2 receptor agonists, ATP and ADP, have to be decreased, to enable the effective generation of adenosine and subsequent P1 receptor activation.<sup>37,41</sup>

CD73 has become a promising target for the immunotherapeutic treatment of cancers via inhibition of the hypoxia-adenosine signaling pathway.<sup>41</sup> Monoclonal antibodies against CD73 were successfully developed and are in clinical trials for cancers (e.g. Oleclumab (MEDI9447), Mupadolimab (CPI-006/CPX-006), Dalutrafusp alfa (AGEN-1423/GS-1423), BMS986179, SRF373/NZV930, IPH5301, TJ004309).<sup>140,141</sup> These antibodies could provide specific and potent inhibition of CD73 but potentially face problems in penetrating solid tumors. Small molecule inhibitors of CD73 could have more favorable pharmacokinetics and were recently reviewed.<sup>142</sup> The first X-ray crystal structure of human CD73 with AMPCP (PDB 4H2I)<sup>143</sup> led to a breakthrough in the development of nucleotide-based CD73 inhibitors. Substitution of AMPCP (compound **41** in **Figure 10**) at  $N^6$ - and C2-positions of the adenine ring lead to effective CD73 inhibitors with sub-nanomolar potencies in PSB-12379 (**E-42**) and PSB-12489 (**E-43**).<sup>144</sup> A closely related compound, AB680 (**E-44**) was characterized as a slow onset competitive inhibitor with a  $K_i$  value of 5 pM.<sup>145,146</sup> The compound has been clinically investigated, but to date no results are published (NCT03677973, NCT04575311). A clinical trial investigating AB680 (**E-44**) in combination with cytostatic drugs for the treatment of gastric cancer is ongoing (NCT04104672). In addition, the orally available AMPCP analog OP-5244 (**E-45**) was

shown to inhibit adenosine production in human cancer cells and was able to reverse the immunosuppression in mouse models.<sup>147</sup>

The identification of non-nucleotide inhibitors of CD73 was similarly accelerated by structure elucidation and virtual screening efforts (see compound **E-46** in **Figure 10B**).<sup>148</sup> The highly potent, competitive, non-nucleotide inhibitor **E-47** was able to inhibit CD73 activity with an  $IC_{50}$  of 12.4 nM.<sup>149</sup> The company Eli Lilly patented the un-competitive CD73 inhibitor LY3475070 (**E-48**), which is orally available and currently studied in clinical trials (NCT04148937).<sup>150</sup> The compound binds to the enzyme-phosphate complex, but not the free enzyme, leading to its inactivation and internalization.<sup>150</sup>



**Figure 10.** Selection of small molecule CD73 inhibitors with their respective potencies; **A.** Nucleotide based inhibitors, namely AMPCP (**E-41**),<sup>151</sup> and its analogs PSB-12379 (**E-42**),<sup>151</sup> PSB-12489 (**E-43**),<sup>144</sup> AB680 (**E-44**),<sup>145,146</sup> and OP-5244 (**E-45**).<sup>147</sup> **B.** Non-nucleotide inhibitors **E-46**,<sup>148</sup> **E-47**,<sup>149</sup> and LY-3475070 (**E-48**).<sup>150</sup>

In conclusion, the search and optimization of CD73 inhibitors was rewarded with several inhibitors showing sub nanomolar potencies. Several antibodies and small-molecule inhibitors are in clinical trials and may be applied for the immunotherapy of cancers in the near future.<sup>103</sup>

### 2.2.5 CD39-CD73 Axis

As previously elaborated, the concerted actions of CD39 and CD73 transform an ATP-mediated inflammatory state into an immunosuppressive tumor microenvironment through the generation of adenosine.<sup>32</sup> The enzymes are often co-expressed in tumor endothelia and most immune cells infiltrating the cancerous tissue.<sup>152</sup> In addition, the enzymes are present in extracellular vesicles that may infiltrate tumor tissues.<sup>32</sup> Furthermore, the expression of both enzymes is increased in response to tissue hypoxia, inflammation, and oxidative stress.<sup>31,35</sup> Therefore, the detection of the clusters of differentiation (CD)39 and -73 is correlated with negative outcomes in variety of tumor types.<sup>74</sup>

So far, the interventions targeting adenosine-regulating pathways appear to possess a wide therapeutic range and good safety profiles. This is likely due to alternative nucleotide metabolism pathways preventing excessive accumulation of extracellular nucleotides and thereby decreasing unwanted off-target effects. Targeted therapy of the rate-limiting, deregulated and overexpressed ecto-nucleotidases, or of adenosine  $A_{2A}$  and  $A_{2B}$  receptors, is a promising strategy.<sup>35</sup> Most importantly, the combination of therapies, e.g. anti-CD73 antibodies and  $A_{2A}$ R blockers, may have synergistic effects.<sup>30,103</sup> Likewise, the combination of CD39 and CD73 inhibitors is advantageous, as lower doses are probably required for an equivalent effect, due to the dual inhibition of the ATP-hydrolysis cascade. This synergy concept was already validated in an *in vitro* T cell suppression assay. The combination of CD39 and CD73 antibodies (IPH52 and IPH53 developed by Innate Pharma) at sub-optimal doses was able reverse the immune cell inhibition in the presence of ATP.<sup>125,153</sup>

On account of these synergistic effects, research on small molecule inhibitors of extracellular nucleotide metabolism also focuses on the development of dual CD39 and CD73 inhibitors.

## 2.3 SARS-CoV-2 Main protease

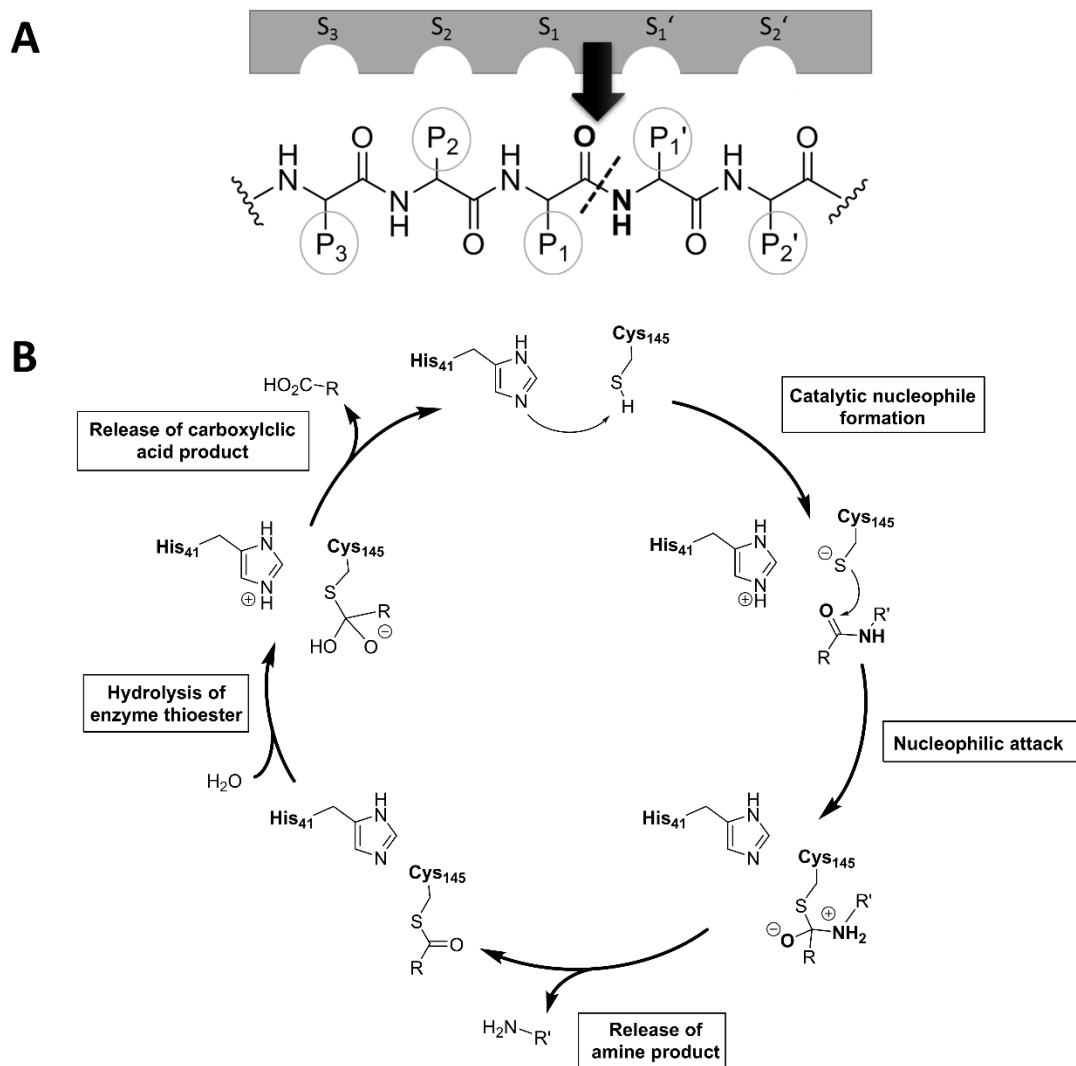
### 2.3.1 Viral replication and function of proteases

In 2019, a global pandemic named COVID-19 (coronavirus disease 2019) emerged. The disease causes symptoms ranging from a mild cough and headaches to pneumonia and inflammation leading to multi-organ failure. The culprit of these infections is severe acute respiratory syndrome coronavirus 2 (SARS-CoV-2). This new virus belongs to the family of coronaviridae, single stranded, positive-sense RNA viruses with characteristic spike proteins on their envelope, that appear as a crown under the electron microscope and thereby inspired the family name.

Previously, the most concerning coronaviruses, causing fatal respiratory disease in humans, were SARS-CoV-1 with a contained outbreak in China during 2002/2003 and MERS (Middle East respiratory syndrome, ongoing outbreak since 2012, endemic, camels as potential source). Other coronaviruses known to infect humans (HCoV-229E, HCoV-HKU1, HCoV-NL63 and HCoV-OC43) are less severe, only causing common cold symptoms. This virus family is also common in zoonotic reservoirs, like bats and palm civets. Animal hosts that have varying susceptibility for the various coronaviruses and co-infection with multiple strains can cause viral recombination and the emergence of new virus variants. These viruses in turn have the potential to spillover and become pathogenic to the human population.<sup>154</sup>

SARS-CoV-2 is generally transmitted via aerosols contaminated with viral particles. Once the virus enters the human body, it attaches to cell surfaces expressing the angiotensin-converting enzyme 2 (ACE 2) with a spike glycoprotein on the viral capsule, inducing cell entry and the start of the viral replication.<sup>155</sup> The genomic RNA is translated into two polyproteins, pp1a and pp1ab, encoding 16 nonstructural proteins (nsp), which form the viral replicase–transcriptase complex, subsequent to proteolysis by two proteases.<sup>156</sup> The papain-like protease (PL<sup>pro</sup>) and the 3chymotrypsin-like protease (3CL<sup>pro</sup>) are part of the polyproteins (nsp3 and nsp5, respectively) and become active after autoproteolytic cleavage. As 3CL<sup>pro</sup> is responsible for the majority of 11 out of 14 cleavage sites, it is assigned as the main protease (M<sup>pro</sup>) of the coronavirus. Replication and translation of viral RNA and structural proteins like envelope and spike are followed by the assembly of viral particles in vesicles. Finally, these vesicles release the virus from the cell by fusing

with the plasma membrane.<sup>156</sup> Uninhibited, the virus is able to spread exponentially in human hosts, as well as in the population.



**Figure 11. A.** Peptide substrate recognition sequence with nomenclature for proteolytic enzymes. In  $M^{\text{pro}}$  the amino acid residues prior to the cleavage site are leucine at the  $P_2$  and glutamine at the  $P_1$  position. After the scissile amide bond at  $P_1'$  position serine, alanine or glycine are most common. The sub-pockets of the protease are designated with the corresponding  $S$  labels; **B.** Proteolysis reaction mechanism; both parts of the figure were adapted from Gao et al.<sup>157</sup>

### 2.3.2 Structure of $M^{\text{pro}}$

$M^{\text{pro}}$  can be characterized as a cysteine protease, with a size of 33.8 kDa, exhibiting enzymatic activity in its homodimeric form. The target peptide substrate enters the active center of the  $M^{\text{pro}}$  protein, and is cut upon recognition of the amino acid sequence motive

Leu-Gln↓(Ser/Ala/Gly) (↓marks the cleavage site, see **Figure 11A**).<sup>158</sup> In detail, the proteolysis is catalyzed by a catalytic dyad consisting of cysteine 145 (Cys<sub>145</sub>) and histidine 41 (His<sub>41</sub>). The thiol group of the cysteine side chain is deprotonated by the imidazole. Subsequently, the nucleophilic thiolate attacks the peptide amide bond. Finally, the primary amine is released and the catalytic dyad is restored by hydrolysis of the intermediate thioester (**Figure 11B**).<sup>155,159</sup>

As the function of M<sup>pro</sup> is essential to the viral replication cycle, its structure is highly conserved between different coronaviridae strains.<sup>155</sup> The amino acid sequence identity of SARS-CoV-2 M<sup>pro</sup> is ~96% compared to SARS-CoV-1 M<sup>pro</sup>, and MERS-CoV M<sup>pro</sup> shares a sequence identity of ~50%. The conservation is even higher in the substrate-recognition pocket. Crystal structures of M<sup>pro</sup> in complex with its inhibitors are used in rational drug design.<sup>158,160,161</sup>

### 2.3.3 Relevance of M<sup>pro</sup> as a drug target

In the course of the COVID-19 pandemic it became evident, that multiple tools are required for managing this global pandemic. Spreading infections may be limited by social distancing, masks, improved hygiene and, very importantly, by vaccination, which also successfully decreases morbidity and mortality in patients with COVID-19. Post-infection patients can be treated with antivirals (e.g. remdesivir, nirmatrelvir, molnupiravir), monoclonal antibodies directed at the spike protein (sotrovimab) and anti-inflammatory drugs, which aim to reduce an exacerbation of lung and other tissue damage (e.g. the corticosteroid dexamethasone).

All approved vaccines focus on the spike protein, which is the antigen on the viral envelope initiating cell entry and viral replication. However, mutations in new variants are common, and in consequence vaccines have to be adjusted. Furthermore, vaccines cannot help in the treatment of already infected, unvaccinated patients and are less effective in the immune-suppressed ones. Unfortunately, global distribution of vaccines is lacking, in part due to complicated logistics and temperature instabilities. In the omicron variant of SARS-CoV-2 increased mutations on the spike protein lead to an attenuated protection by the approved vaccines. Other drug targets of the virus, like the RNA-polymerase, NTPase/helicase and proteases are less affected, as mutations on these enzymes can lead to a loss of fitness.<sup>155</sup> For example, there are few mutations of M<sup>pro</sup> in

the omicron variant, and the protease is highly conserved in other CoVs.<sup>155,162</sup> Therefore, M<sup>pro</sup> inhibitors have the potential to be pan-coronaviral drugs,<sup>163</sup> and can overcome the challenge of viral resistance due to changes in the spike protein.

M<sup>pro</sup> has a pivotal role in the viral replication cycle, as it enables essential enzymes and proteins to fold into their functional shape by proteolytic cleavage.<sup>155</sup> No human protease possesses a homologous protein recognition sequence with glutamine at the P<sub>1</sub> position. This permits the design of specific peptidomimetic inhibitors and limits potential side effects. A further advantage of M<sup>pro</sup> targeted antivirals, is that they can be made orally available and used in both hospital and out-patient settings. In conclusion, M<sup>pro</sup> is an eligible drug target for specific antivirals.<sup>155,164</sup>

As of June 2022, one drug targeting M<sup>pro</sup> is approved for treatment of COVID-19. PF-07321332 also called nirmatrelvir (Paxlovid®) was developed by Pfizer and is a peptidomimetic non-covalent inhibitor of M<sup>pro</sup>. It is approved by the FDA and EMA for the use in adults with positive results of direct SARS-CoV-2 viral testing, who are at risk for a severe course of the disease. The per oral drug was shown to reduce the risk of hospitalization or death by 89% and is administered in combination with ritonavir, which boosts the metabolic availability. A second compound by the Pfizer company, PF-07304814 is currently in phase 3 clinical trials (NCT04501978). Further information is compiled in the section on M<sup>pro</sup> inhibitors.

#### 2.3.4 Assays for determination of M<sup>pro</sup> activity

In order to effectively study the specific activity of a target enzyme, *in vitro* assay systems are employed. Most laboratories utilize artificial substrates to monitor the activity of M<sup>pro</sup> either by HPLC analysis or more commonly, by detection of a change in fluorescence upon cleavage of the peptide substrate.

##### **Fluorogenic substrate-based assays**

Most frequently, the activity of recombinant SARS-CoV-1 or -2 M<sup>pro</sup> (e.g. expressed in BL21 *E. coli*)<sup>160,165</sup> is tracked using fluorogenic or fluorescence resonance energy transfer (FRET) substrates. The relative increase in fluorescence is in linear proportion to the product concentration. This enables the continuous determination of the activity rate by fitting the linear portion of the progression curves,<sup>160</sup> or detection of the fluorescence



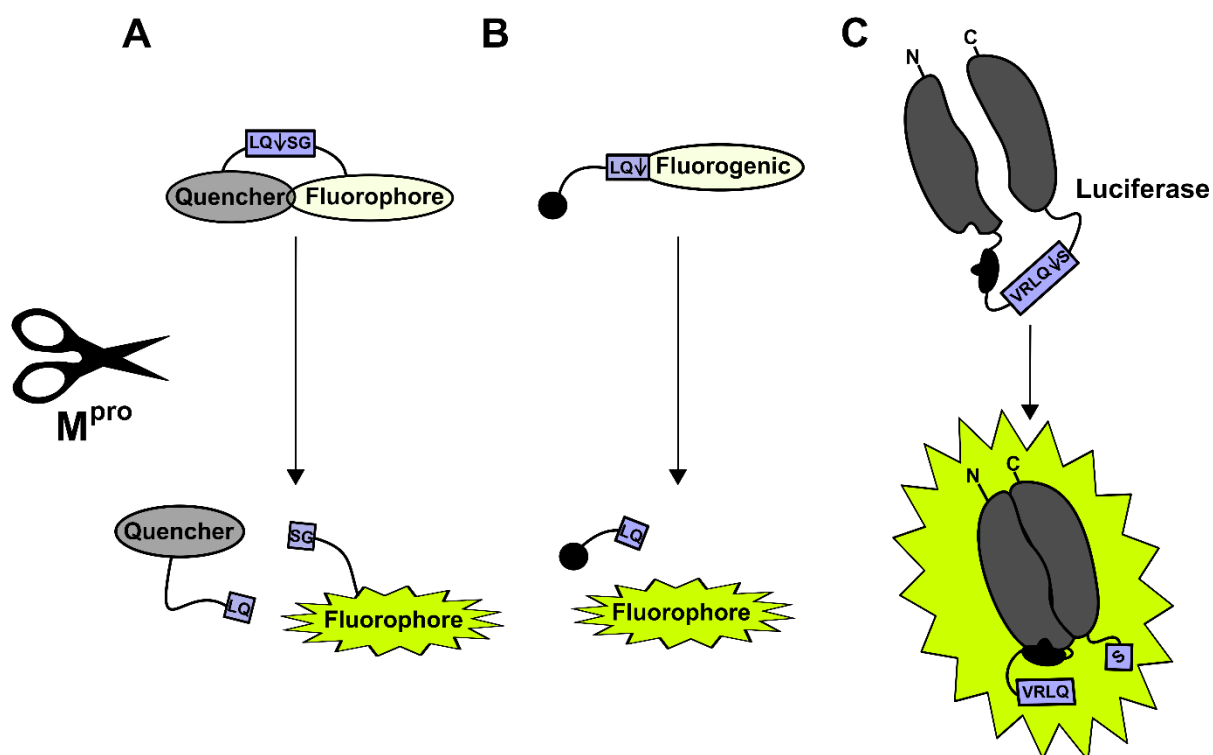
increase after a defined incubation time (endpoint detection). Inhibitors can be characterized according to their concentration- and/or time-dependent decrease in enzymatic activity.

FRET substrates consist of a fluorophore and a quencher, which are connected by a peptide containing the recognition sequence of the studied protease (see **Figure 12A**). Before enzyme addition, the fluorescent fluorophore is undetectable due to the close proximity to the quencher. Upon separation of the peptide linker the fluorophore is released, leading to an increase in the detected fluorescence. This method enables the continuous observation of enzyme kinetics and is more sensitive than HPLC.<sup>160</sup> For SARS-CoV-2 M<sup>pro</sup> various FRET-substrates harboring a selective cleavage site (recognition sequence in bold, cleavage site indicated by an arrow) were published.<sup>166,167</sup> For example Dabcyl-KTSAVL**Q↓SG**FRKME(Edans)-NH<sub>2</sub>, (FRET pair: EDANS (5-[(2-aminoethyl)amino]naphthalene-1-sulfonic acid) fluorophore and DABCYL (4-[(4'-dimethylamino)phenyl]azo)benzoyl) quencher),<sup>158,168-170</sup> MCA-AVL**Q↓SG**FR-Lys(Dnp)-Lys-NH<sub>2</sub> (FRET pair: MCA (7-methoxycoumarin) fluorophore and Dnp (4-dinitrophenyl) quencher)<sup>160</sup> and CFP-TSAVL**Q↓SG**FRKM-YFP) (FRET pair: CFP (cyan fluorescent protein) fluorophore and YFP (yellow fluorescent protein) quencher).<sup>171</sup>

Alternatively, fluorogenic substrates gain their fluorescence by cleavage from the peptide (**Figure 12B**). An example is an aminomethylcoumarin-based substrate consisting of non-proteinogenic amino acids and the proteinogenic recognition sequence, Boc-Abu-Tle-**LQ**-AMC (Boc (t-butyloxycarbonyl); Abu (2-aminobutyric acid); Tle (*tert*-leucine), AMC (7-amino-4-methylcoumarin)).<sup>165</sup> At the start of the reaction the AMC-moiety, located at the C-terminus of the peptide, is non-fluorescent as it is conjugated to the rest of the peptide. Then, upon liberation by M<sup>pro</sup>, AMC gains an electron pair, which shifts its fluorescence into the UV-region ( $\lambda_{\text{ex}}=360$  nm,  $\lambda_{\text{em}}=450$  nm).

The assay buffer usually consists of a buffering agent at physiological pH, e.g. Tris-HCl (2-amino-2-(hydroxymethyl)propane-1,3-diol hydrochloride) or MOPS (3-(N-morpholino)propanesulfonic acid).<sup>165,172,173</sup> Additives are employed to ensure an optimal enzymatic activity or avoid measurement errors. Ethylenediaminetetraacetic acid (EDTA) prevents denaturation of the enzyme by divalent cations, while DTT (1,4-dithiothreitol) reduces the active cysteine in the substrate binding site, but can also influence measurement results with thiol-reactive covalent inhibitors.<sup>174,175</sup> Triton X-100 is a detergent that

should be added at low concentrations (0.001 – 0.01%) in order to prevent non-specific binding of compounds that would lead to protein aggregation, thereby acting as false-positive inhibitors.<sup>160</sup> An alternative additive to prevent aggregation is bovine serum albumin (BSA). Furthermore, compounds may quench the emitted fluorescence of the product leading to an apparent inhibition of substrate conversion. This so-called inner filter effect may be noticed by a shift of the progression curve compared to the control on the y-axis.<sup>174,176</sup> The choice of assay buffer may influence the binding of a drug to its target. For example, electrostatic interactions are sensitive to the ionic strength and pH of the buffer. Therefore, the buffer should be optimized with regard to physiological conditions, and allowing the identification of potential lead structures.<sup>177</sup>



**Figure 12.** Assay principles of **A.** FRET, **B.** fluorogenic and **C.** luciferase-based artificial substrates containing a recognition sequence for the M<sup>pro</sup> enzyme (violet). Upon cleavage of the oligopeptide fluorescence or luminescence can be measured (green). The depiction of the luciferase-based substrate was adapted from O'Brien et al.<sup>178</sup>

### Luciferase-based biosensors

Luciferases are enzymes that are able to generate chemo luminescence. This enables their utilization as reporters for the activity of other enzymes. Specific substrates were

designed in order to measure the activity of M<sup>pro</sup>, consisting of multiple units that are held in an inactive conformation by a peptide linker containing the M<sup>pro</sup> recognition sequence. For example, HEK293T cells were transfected with the biosensor, SARS-CoV-2 M<sup>pro</sup> expression plasmid and renilla luciferase in order to control for transfection efficiency and toxicity.<sup>178</sup> The cells were not reported to be harmed by the expression of M<sup>pro</sup> or the biosensor. Upon peptide cleavage the conformation shifts and the luciferase assembles itself leading to an increase of luminescence (**Figure 12C**). These biosensors allow for endpoint detection of isolated enzyme activity as well as live cell imaging.<sup>179</sup> By testing of the inhibitors in cell culture, the antiviral efficacy of drug candidates can be estimated without use of the active virus, positioning the experiment at biosafety level 2.<sup>178</sup>

### Fluorescent reporter assay

As an alternative, a 'flipGFP CoV reporter' was developed by Froggat et al. in order to study M<sup>pro</sup> activity in a cell environment without viral infection. The reporter consists of two green fluorescent protein (GFP) beta-strands and a linker accommodating an M<sup>pro</sup>-specific cleavage site.<sup>180</sup> Both reporter and SARS-CoV-2 M<sup>pro</sup> were coexpressed in human HEK293T cells (human embryonic kidney 293T). The proteolysis of the linker enables the assembly of the complete GFP resulting in a detectable fluorescence at 24 h post-transfection, which concentration-dependently decreased upon addition of a SARS-CoV M<sup>pro</sup> inhibitor.<sup>180</sup>

### Thermal shift assay

This method determines the thermal stability of a protein upon addition of a ligand. The interactions of a protein with a small molecule can strengthen or weaken its structural integrity and thereby influence its thermostability, causing increased or decreased melting points.<sup>171</sup> A direct correlation between the inhibitory potency and the binding affinity for the M<sup>pro</sup> enzyme was shown by Ma et al.<sup>169</sup> Covalent inhibitors lead to an apparent destabilization of the protein.<sup>181</sup> The melting point is usually determined by means of a fluorogenic ligand, SYPRO Orange, which is a merocyanine dye that selectively binds to the hydrophobic domains of proteins, which are exposed as it is unfolding at rising temperatures. Upon binding to the protein, the dye is shielded from the excited state-quenching effect of water resulting in an increase of the fluorescence intensity ( $\lambda_{\text{ex}} = 470$  nm,  $\lambda_{\text{em}} = 569$  nm).<sup>182,183</sup>

### **Isothermal titration calorimetry (ITC)**

In relation to the thermal shift assay, the energy that gets released when a ligand binds to a protein can also be evaluated by ITC. The experimental setup consists of two adiabatic cells that are kept at the same temperature. The energy for retaining this isothermal state is quantified. By this means, the thermodynamic parameters of M<sup>pro</sup> with its inhibitors in solution, namely changes in enthalpy ( $\Delta H$ ), entropy ( $\Delta S$ ), and dissociation constants ( $K_D$ ) can be directly determined.<sup>171</sup>

### **Microscale thermophoresis (MST)**

In a temperature gradient, molecules move towards or away from the heat source. This directed movement is termed thermophoresis.<sup>184</sup> The extent and speed of the migration is influenced by the hydration shell of a substance or aggregate, which is in turn determined by the charge, size, conformation and composition of the putative complex.<sup>184</sup> In the experiment the sample, contained within a glass capillary, is locally heated by 2-6°C using an infrared (IR) laser. The relative concentration of the target molecule at the position of the temperature gradient is quantified by changes of the emitted fluorescence before and during the laser operation. Macromolecules are either covalently tagged with fluorescent labels or inherently fluorescent.<sup>184</sup> Proteins which contain the fluorescent amino acid tryptophan, can be used without prior labeling.<sup>184</sup> On this basis, the MST technique is able to analyze a broad variety of biomolecular interactions including protein unfolding, thermodynamics, enzyme kinetics, binding stoichiometry and modes and most importantly the binding of small molecules to macromolecules and determination of their dissociation constants ( $K_D$ ).<sup>184</sup>

MST was applied in binding affinity experiments using label-free SARS-CoV-2 M<sup>pro</sup>.<sup>185</sup> The thermophoresis of the enzyme in relation to the EI-complex is determined by increasing compound concentrations for the calculation of equilibrium binding constants.<sup>184</sup> Advantages of MST are its high sensitivity and precision, the broad application range, and especially its low sample consumption, as only micromolar protein concentrations and volumes in the microliter range are required.<sup>184,185</sup> The application of this method is limited by the ligand's solubility and fluorescence, that may interfere with the measurement of the proteins intrinsic fluorescence.<sup>185</sup>

### **HPLC and mass spectrometry (MS)**

The proteolytic activity of M<sup>pro</sup> can furthermore be assessed via the cleavage of a non-labeled artificial oligopeptide substrate containing a specific cleavage site for M<sup>pro</sup>. After a set incubation period, the cleavage products or residual substrate are quantified by HPLC coupled to MS.<sup>186,187</sup> These assays enable the investigation of compounds with an inner filter effect, if the detection does not rely on UV-absorption. Apart from that, fluorescence-based substrates offer higher sensitivities and faster data accumulation as they may be performed in a plate-based design, while samples have to be processed sequentially with chromatographic based methods.

### **Antiviral activity assays**

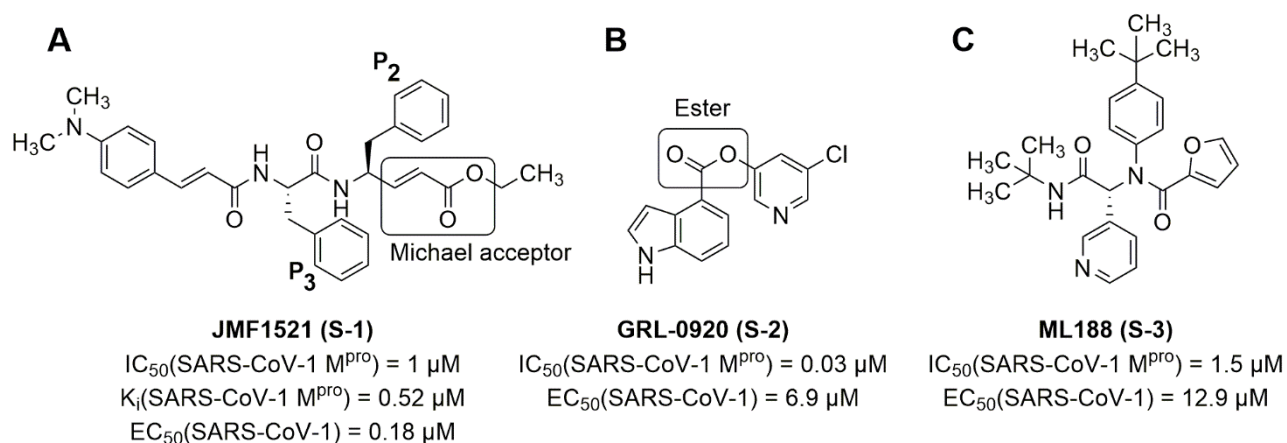
Before application of a drug candidate in animal models of viral disease, its effect is tested in cell culture experiments. Specific cell lines are infected with SARS-CoV-2, and the viral replication with and without inhibitor is quantified by quantitative real-time polymerase chain reaction (qRT-PCR).<sup>160</sup> Due to the use of active virus, these experiments must be conducted under biosafety level 3 (BSL-3). Drugs are frequently evaluated by infecting VeroE6 cells (Vero (African green monkey kidney)). Alternatively, Vero-based cells overexpressing TMPRSS2 (transmembrane protease serine subtype 2), Caco2 cells, Huh-7 cells, and the human lung epithelial cell line Calu-3 are commonly used for these experiments.<sup>178,181</sup> The cells have to express both ACE-2 and TMPRSS2 for effective cell entry. The ACE-2 acts as an entry receptor, while the cellular serine protease TMPRSS2 is responsible for spike protein priming.<sup>188</sup> In addition to a reduction of the viral load, treatment with M<sup>pro</sup> inhibitors may prevent cytopathic effects (e.g. cell lysis caused by virus infection).<sup>160</sup> Apart from that, the cellular toxicity of test compounds needs to be considered in additional experiments, as the qRT-PCR cannot ascertain, if the amount of virus is reduced due to an antiviral effect or by reduced cell proliferation.<sup>181</sup>

## 2.3.5 Inhibitors of M<sup>pro</sup>

### SARS-CoV-1 M<sup>pro</sup> inhibitors

Ensuing the SARS-CoV-1 pandemic of 2003, scientists designed potential drugs to treat the disease by targeting the viral M<sup>pro</sup>.<sup>159</sup> The subsequently emerged SARS-CoV-2 is closely related to SARS-CoV-1. Both possess an M<sup>pro</sup> enzyme, sharing a sequence identity of 96.1 % and an identical binding site sequence.<sup>189</sup> Therefore, it is logical to consider SARS-CoV-1 M<sup>pro</sup> inhibitors, as they are likely to be equally potent at SARS-CoV-2 M<sup>pro</sup>.

Three examples of SARS-CoV-1 inhibitors are shown in **Figure 13**. The compound JMF1521 (**S-1**) mimics the physiological recognition sequence, and its phenyl groups are able to occupy the S<sub>2</sub> and S<sub>3</sub> pockets of the protease substrate binding site. The enzyme is blocked by covalent reaction of the Michael acceptor ( $\alpha,\beta$ -unsaturated ester) with the active cysteine. This leads to a permanent loss of function and decreases viral production, which was demonstrated in Vero E6 cells with an EC<sub>50</sub> of 0.18  $\mu$ M.<sup>170</sup> Furthermore, small orthosteric inhibitors were identified with GRL-0920 (**S-2**) and ML188 (**S-3**), which form covalent and non-covalent bonds to the enzyme active site, respectively. Inhibitor classes will be described in more detail in the next section.



**Figure 13.** Representative SARS-CoV-1 M<sup>pro</sup> inhibitors and their respective potencies **A.** peptidomimetic inhibitor JMF1521 (**S-1**) with Michael acceptor warhead;<sup>170</sup> **B.** small molecule GRL-0920 (**S-2**) with pyridyl ester warhead;<sup>190,191</sup> **C.** non-covalent competitive inhibitor ML188 (**S-3**).<sup>192</sup>

### SARS-CoV-2 M<sup>pro</sup> inhibitors

Following the outbreak of SARS-CoV-2 at the end of 2019, the interest in M<sup>pro</sup> inhibitors reawakened. Universities and companies alike initiated the further development of SARS-CoV-1 inhibitors and searched for novel inhibitors with high throughput screening (HTS) campaigns, computer-aided and rational drug design. Therefore, a great and daily expanding variety of inhibitors exists, that has extensively been summarized in recent review articles.<sup>155,157,193–195</sup> Inhibitors of M<sup>pro</sup> are classified as covalent or non-covalent, depending on their ability to react with the catalytic Cys<sub>145</sub>. Furthermore, peptidomimetics, which simulate the peptide recognition sequence, and small molecules have to be distinguished. This introduction will highlight the most important inhibitor classes and compounds with potential for further development as antiviral drugs.

#### *Covalent peptide analogs*

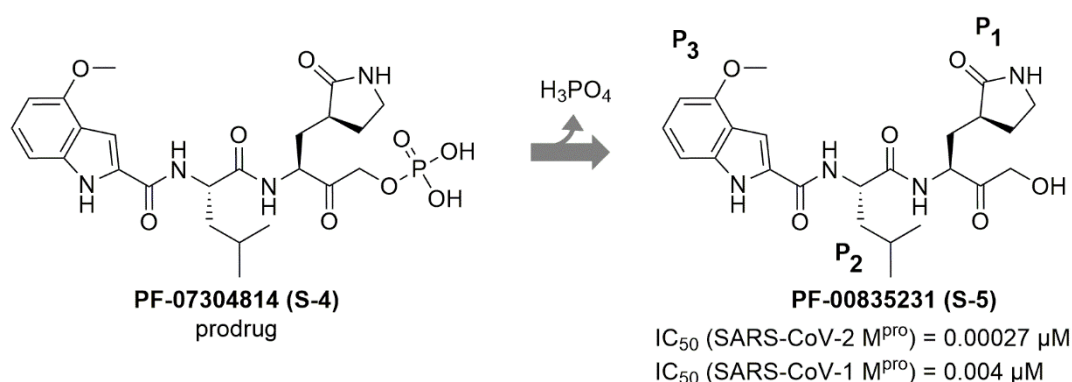
Covalent inhibitors attack and covalently bind to the M<sup>pro</sup> enzyme. Irreversible inhibitors inherently have to be very reactive due to their mode of action. But promiscuously reacting compounds are easily metabolized, which limits their bioavailability.<sup>157</sup> Therefore, it is essential for these compounds to possess a high affinity and selectivity for their target, in order to reduce side effects and toxicity.<sup>174</sup>

Peptidomimetic inhibitors emulate the substrate recognition motif from P<sub>1</sub>' to P<sub>4</sub> and replace part of the substrate by a chemical warhead that targets the catalytic Cys<sub>145</sub> residue of the enzyme. Regularly, the glutamine side chain in the P<sub>1</sub> position is replaced by a  $\gamma$ -lactam ring, which is able to occupy the S<sub>1</sub> pocket. Typical warheads include Michael acceptors, nitriles, aldehydes, epoxy ketones and halomethyl ketones.<sup>155,157,159</sup> The inhibition mechanism consists of two steps: first non-covalent interaction with the binding site and subsequent nucleophilic attack on Cys<sub>145</sub> with covalent bond formation.

In **ketone-based** warheads, the electrophilic carbonyl C forms a covalent bond with the thiol-group of the M<sup>pro</sup> active site cysteine (Cys<sub>145</sub>), creating a tetrahedral hemithioketal adduct. A hydroxymethylketone-derived inhibitor, named PF-00835231 (**S-5**), was initially designed during the SARS-CoV-1 pandemic by the pharmaceutical company Pfizer (see **Figure 14**). Although the development was discontinued after containment of the disease, it was resumed, as it potently inhibits SARS-CoV-2 M<sup>pro</sup> as well (IC<sub>50</sub> = 0.27 nM).<sup>189</sup> Its potency on the viral replication in cell-based assays strongly depends on the

cell line and addition of efflux transport inhibitors.<sup>189,196,197</sup> For example, the effective concentration for a 50 % reduction of SARS-CoV-2 replication was decreased from 39.8  $\mu\text{M}$  to 0.236  $\mu\text{M}$  in Vero-E6-enACE2 cells by addition of 2  $\mu\text{M}$  permeability glycoprotein (P-gp) inhibitor CP-100356.<sup>197</sup> However, the peptide analog PF-00835231 was effective without the addition of an efflux inhibitor in a human airway model (adenocarcinoma alveolar epithelial cell line A549 exogenously expressing ACE-2:  $\text{EC}_{50}(\text{A549}^{\text{+ACE2}}) = 0.158 - 0.422 \mu\text{M}$ ;  $\text{CC}_{50} > 10 \mu\text{M}$ ).<sup>196</sup>

The compound **S-5** is administered to patients in its prodrug form (PF-07304814, **S-4**) which has an improved solubility, mediated by a phosphate group. In human tissues the prodrug is hydrolyzed by alkaline phosphatase (see **Figure 14**). Advantages of this compound are its high metabolic stability and effectiveness against multiple viral strains, while disadvantages include high effective doses and the need for intravenous application, due to the high polarity of the peptidomimetic. Currently, PF-07304814 (**S-4**) is in phase 3 clinical trials as part of the ACTIV-3 study where several therapeutics for hospitalized patients with COVID-19 are evaluated for their safety and effectiveness (NCT04501978).

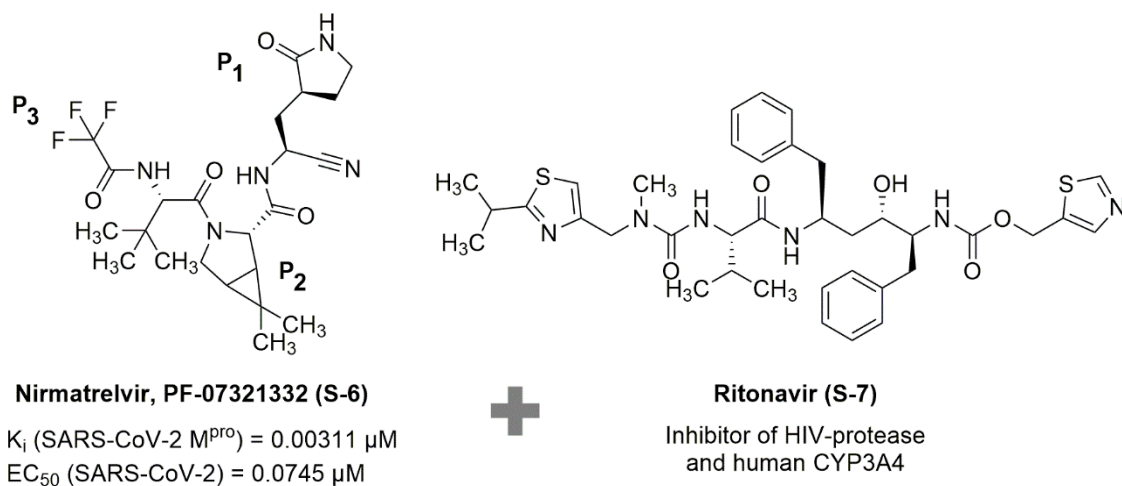


**Figure 14.** Ketone-based inhibitor of SARS-CoV  $M^{\text{pro}}$ , PF-00835231 (**S-5**) including its respective potencies towards inhibition of SARS-CoV-1 and -2, and its prodrug PF-07304814 (**S-4**).<sup>189</sup> The SARS-CoV-1 antiviral activity of PF-00835231 in Vero 76 cells was shown to be increased by addition of 0.5  $\mu\text{M}$  P-gp inhibitor CP-100356 from an  $\text{EC}_{50}$  value of 4.8  $\mu\text{M}$  to 0.11  $\mu\text{M}$ .<sup>189</sup>

From the same compound series of peptidomimetic drugs, nirmatrelvir (PF-07321332, **S-6**, Paxlovid<sup>®</sup>), a **nitrile-based** inhibitor of  $M^{\text{pro}}$ , was developed and approved as the first antiviral targeting SARS-CoV-2  $M^{\text{pro}}$  (see **Figure 15**).<sup>163</sup> The nitrile attacks Cys<sub>145</sub> and forms a reversible covalent thioimidate adduct. Similar to PF-00835231 (**S-5**), it is able to

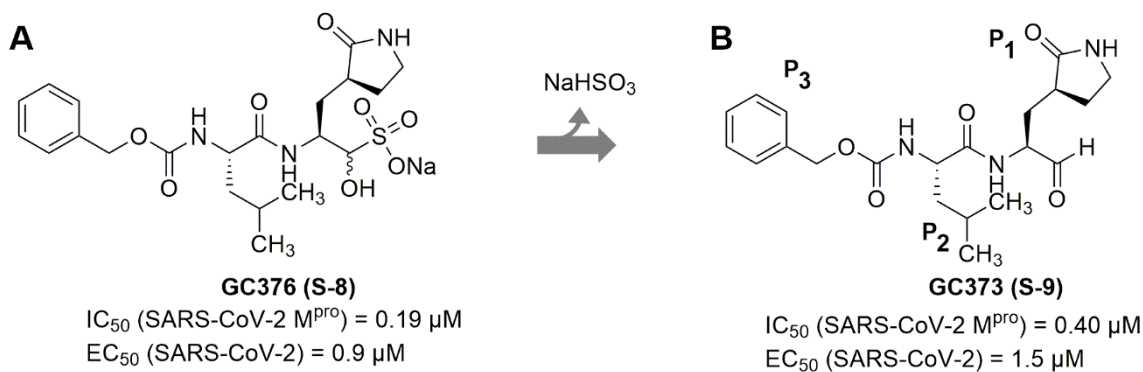


inhibit other coronaviruses, like SARS-CoV-1 and MERS *in vitro*,<sup>163</sup> and is potent *versus* virus variants.<sup>198</sup> The inhibitor is suitable for oral administration in combination with ritonavir (**S-7**, **Figure 15**), in order to reduce its metabolism by the cytochrome P<sub>450</sub> liver enzyme CYP3A4. In clinical trials, the drug was able to reduce the risk of hospitalization or death by 89%.<sup>199</sup>



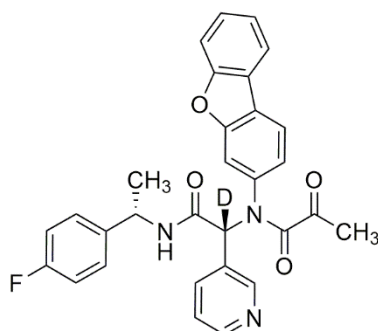
**Figure 15.** Nitrile-based inhibitor of SARS-CoV M<sup>pro</sup>, nirmatrelvir (PF-07321332, **S-6**), which is co-administered with ritonavir (**S-7**) in form of the approved drug Paxlovid®.<sup>163</sup>

The di-peptide protease inhibitor GC376 (**S-8**) was developed as an antiviral prodrug for the treatment of feline infectious peritonitis (FIP), which is a coronavirus infection of cats. GC376 (**S-8**) is an aldehyde hydrogensulfite adduct and acts as a prodrug of the **aldehyde-based** inhibitor GC373 (**S-9**) (see **Figure 16**). The prodrug has an improved water solubility, but is unstable and hydrolyzed to the respective drug GC373 (**S-9**), which in turn forms a reversible hemithioacetal with Cys<sub>145</sub> of the M<sup>pro</sup> enzyme.<sup>200</sup> The compounds show broad-spectrum coronavirus protease inhibition (FIPV, MERS-CoV and SARS-CoV-1) and low cytotoxicity towards Vero E6 and A549 cells.<sup>200,201</sup> Its safety, however, is put into question by the high reactivity of the electrophilic aldehyde warhead, which was shown to inhibit other cysteine proteases including calpain 1 cathepsin L and cathepsin K, that may lead to unintended side effects.<sup>157,202</sup>



**Figure 16.** Aldehyde-based inhibitor of SARS-CoV-2  $M^{pro}$  GC373 (**S-9**), its potencies, and its prodrug GC376 (**S-8**), which was originally developed to treat feline infectious peritonitis (FIP).<sup>200</sup>

The  **$\alpha$ -ketoamide** diamide derivative Y180 (**S-10**) was shown to be a potent covalent and selective inhibitor of SARS-CoV-2  $M^{pro}$ , including its variants (see **Figure 17**).<sup>203</sup> A crystal structure of  $M^{pro}$  with Y180 (**S-10**) illustrates the covalent bond of the carbonyl warhead to the thiol group of Cys<sub>145</sub> (PDB-ID: 7FAZ).<sup>203</sup> The more active (R)-epimer configuration was stabilized by introduction of a deuterium at the chiral carbon. The viral replication in VeroE6 and the lung epithelial cell line Calu-3 was abolished by Y180 (**S-10**) with nanomolar potencies, while the compound displayed no significant toxicity. Prophylactic and therapeutic application of Y180 (**S-10**) in mice decreased the viral replication, disease outcome and severity, indicated by a reduction in the production of pro-inflammatory cytokines.<sup>203</sup> Similar to PF-07321332 (**S-6**), Y180 (**S-10**) benefits from co-administration of ritonavir (**S-7**) in order to boost its metabolic stability. In a direct comparison of SARS-CoV-2 Omicron antiviral infection of K18-hACE-2 transgenic mice the treatment combination Y180/ritonavir was superior to PF-07321332/ritonavir.<sup>203</sup> Furthermore, Y180 (**S-10**) demonstrated good pharmacokinetic properties and oral availability, which makes it an ideal candidate for clinical trials.

**Y180 (S-10)** $IC_{50}$  (SARS-CoV-2 M<sup>pro</sup>) = 0.0081  $\mu$ M $EC_{50}$  (SARS-CoV-2) = 0.0114 - 0.0344  $\mu$ M

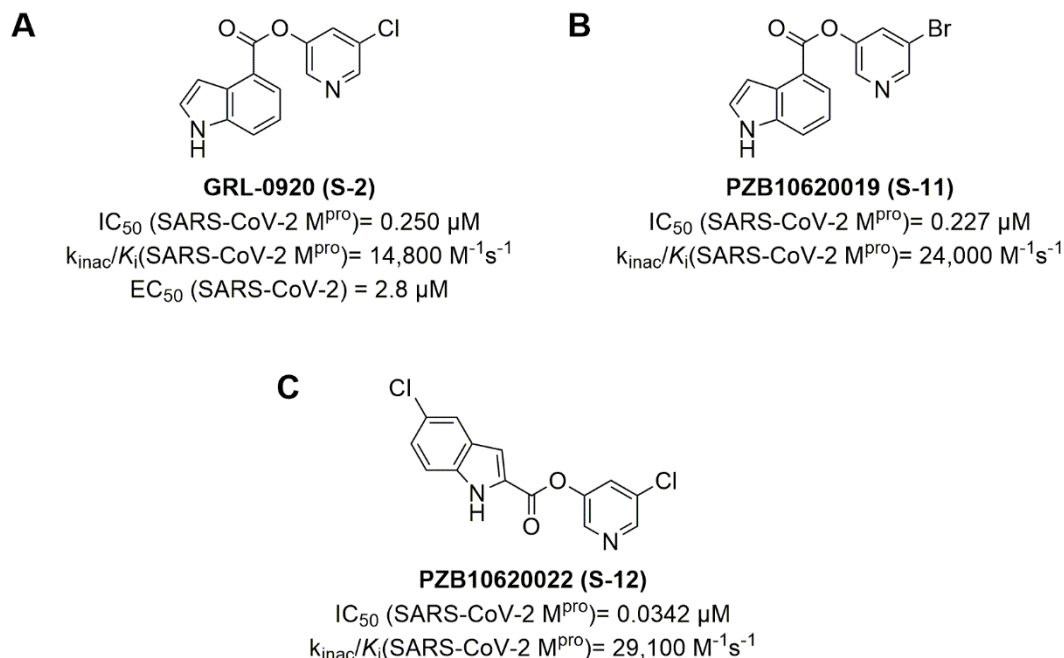
**Figure 17.**  $\alpha$ -ketoamide-based inhibitor of SARS-CoV-2 M<sup>pro</sup> Y180 (**S-10**). The enzyme kinetics of the covalent irreversible inhibitor and SARS-CoV-2 M<sup>pro</sup> were characterized with an  $K_i$  value of 0.001  $\mu$ M and  $k_{inac}$  of  $2.6 \times 10^{-4} s^{-1}$  ( $k_{inac}/K_i$ (SARS-CoV-2 M<sup>pro</sup>) = 260,000  $M^{-1}s^{-1}$ ); plaque formation reduction assays with SARS-CoV-2 variants yielded  $EC_{50}$  values of 0.0114  $\mu$ M, 0.0203  $\mu$ M, 0.0344  $\mu$ M and 0.0237  $\mu$ M against wild type SARS-CoV-2, B.1.1.7, B.1.617.1 and P.3, respectively.<sup>203</sup>

#### *Covalent small molecule inhibitors*

The affinity of small molecule modulators of SARS-CoV-2 M<sup>pro</sup>, such as **ester-based** covalent inhibitors, is not primarily based on their similarity to the endogenous peptide sequence. Subsequent to non-covalent attachment to the substrate binding site, the nucleophilic cysteine is attacked by formation of a thioester between the thiol of Cys<sub>145</sub> and the carbonyl group of the inhibitor.<sup>204</sup> The acylated M<sup>pro</sup> is inactive, but can be reactivated by hydrolysis of the thioester and release of an incapacitated inhibitor fragment. Esters can be promiscuous in their reactivity towards various nucleophiles, so their target selectivity as well as their stability towards physiologically abundant agents like glutathione need to be assessed.

Originally, 5-chloropyridyl esters were developed for SARS-CoV-1 M<sup>pro</sup>, and have proven to be potent inhibitors of SARS-CoV-2 M<sup>pro</sup> as well (see **Figure 13** and **Figure 18**).<sup>190,191,205,206</sup> By selection of suitable moieties attached to the ester, the inhibitory potency was optimized at the isolated M<sup>pro</sup> enzyme, as well as in cell culture experiments. For example, the position of the carboxyl group and the substitution on the benzene ring of the indole is vital for the inhibitory potency at M<sup>pro</sup>, as demonstrated by the ten-fold increase in inhibitory potency of PZB10620022 (**S-12**) towards GRL-0920 (**S-2**, see **Figure 18 A** and **C**).<sup>165,204</sup> Furthermore, the replacement of the chlorine atom at the

pyridine ring with a bromine atom boosts the reactivity of the ester warhead, which increases the second order rate constant of inactivation ( $k_{\text{inac}}/K_i$ ) of PZB10620019 (**S-11**) compared to GRL-0920 (**S-2**), as shown in **Figure 18 A and B**.



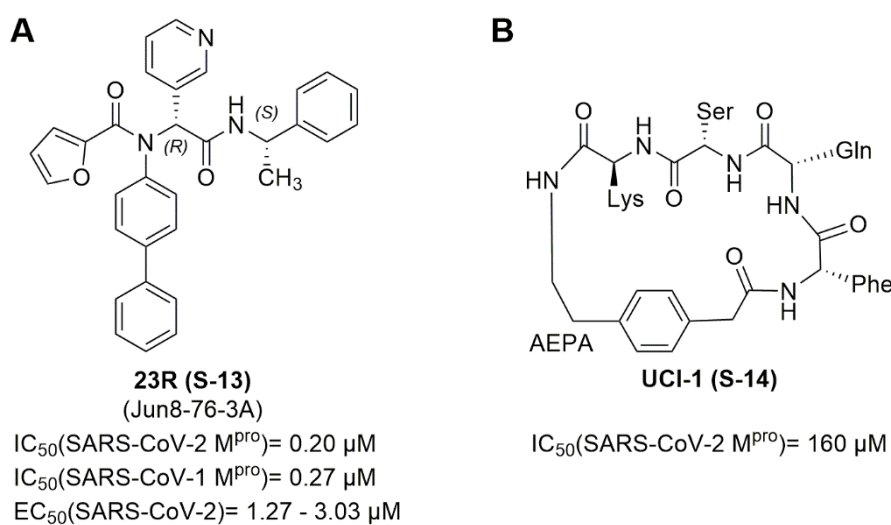
**Figure 18.** 5-Halopyridyl ester-based inhibitors of SARS-CoV-2  $M^{\text{pro}}$  and their respective potencies: **A.** GRL-0920 (**S-2**);<sup>165,191,204</sup> **B.** PZB10620019 (**S-11**);<sup>165</sup> and **C.** PZB10620022 (**S-12**).<sup>165</sup>

### Noncovalent peptide analogs

Short peptide substrate analogs without a warhead were demonstrated to competitively inhibit SARS-CoV-2  $M^{\text{pro}}$  with mere micromolar potency, thereby being significantly less potent inhibitors compared to their covalently binding analogs.<sup>207</sup> Yet the development of a non-covalent dipeptide inhibitor of  $M^{\text{pro}}$  was successful with 23R (**S-13** see **Figure 19A**).<sup>202</sup> The R-diastereomer proved to be the active conformation in enzymatic activity assays and the cocrystal structure (PDB-ID: 7KX5).<sup>202</sup> The  $S_2$  pocket is occupied by the hydrophobic biphenyl group and the pyridinyl ring is oriented towards the  $S_1$  pocket. The compound is stabilized in its conformation by intramolecular  $\pi$ -stacking between the biphenyl and benzyl moieties. Interestingly, the benzyl ring occupies both  $S_2$  and  $S_4$  pockets, constituting a new ligand-induced binding position, that can be utilized in future drug developments.<sup>202</sup> Importantly, the compound was selective towards other cysteine

proteases, which is an advantage to the frequently non-selective covalent inhibitors, like GC376 (**S-8**).<sup>202</sup>

Next to linear peptides, cyclic substrate analogs were explored as drug candidates, as they often have improved efficacy and stabilities.<sup>208</sup> These molecules do not follow traditional specifications of drug-like compounds (e.g. Lipinski's rules of five) but were found to be effective towards intracellular targets. The cyclic form stabilizes the conformation of the peptide that is similar to the native substrate recognition sequence of M<sup>pro</sup>. Furthermore, the peptide is more rigid.<sup>208</sup> The designed cyclic pentapeptide UCI-1 (**S-14**), is interconnected via a [4-(2-aminoethyl)phenyl]-acetic acid (AEPA) linker, and is stable to proteolysis (see **Figure 19B**).<sup>208</sup> In summary, cyclic substrate analogs have the potential to be more stable and potent than linear peptides, but so far the non-covalent interactions do not provide the level of affinity that is required for potent inhibition of the viral protease.<sup>207</sup>



**Figure 19.** Noncovalent peptidomimetic inhibitors of SARS-CoV-2 M<sup>pro</sup>: **A.** 23R (**S-13**) characterized in cellular assays with Vero E6 cells ( $EC_{50}(\text{SARS-CoV-2}) = 1.27 \mu\text{M}$ ) and Calu-3 cells ( $EC_{50}(\text{SARS-CoV-2}) = 3.03 \mu\text{M}$ ) without observable cytotoxicity ( $CC_{50} > 100 \mu\text{M}$ );<sup>202</sup> and **B.** UCI-1 (**S-14**, University of California, Irvine Coronavirus Inhibitor-1)<sup>208</sup>

#### *Non-covalent small molecule inhibitors*

Promiscuous reactivity of warheads can lead to unintended covalent modifications of peptides and problems with off-target toxicity. Therefore, noncovalent inhibitors are considered to have a generally decreased risk profile.<sup>157</sup> Interestingly, certain compounds that are covalent inhibitors at some other targets have been shown to inhibit M<sup>pro</sup> in a

non-covalent manner. This can be explained by the positioning of the warhead in distance of the nucleophilic Cys<sub>145</sub>, rendering a reaction unlikely.

Isatin derivatives were characterized as irreversible, covalent inhibitors to human rhinovirus 3C protease, but exhibit a non-covalent, reversible inhibition type towards SARS-CoV-1 and -2 M<sup>pro</sup> (see **Figure 20A**).<sup>209,210</sup> An *N*-substituted derivative (**S-15**) bearing a carboxamide at the C-5 position is among the most potent M<sup>pro</sup> inhibitors so far. Unfortunately, the compound is highly cytotoxic, which directs the primary research objective towards reduction of toxicity.<sup>210</sup>

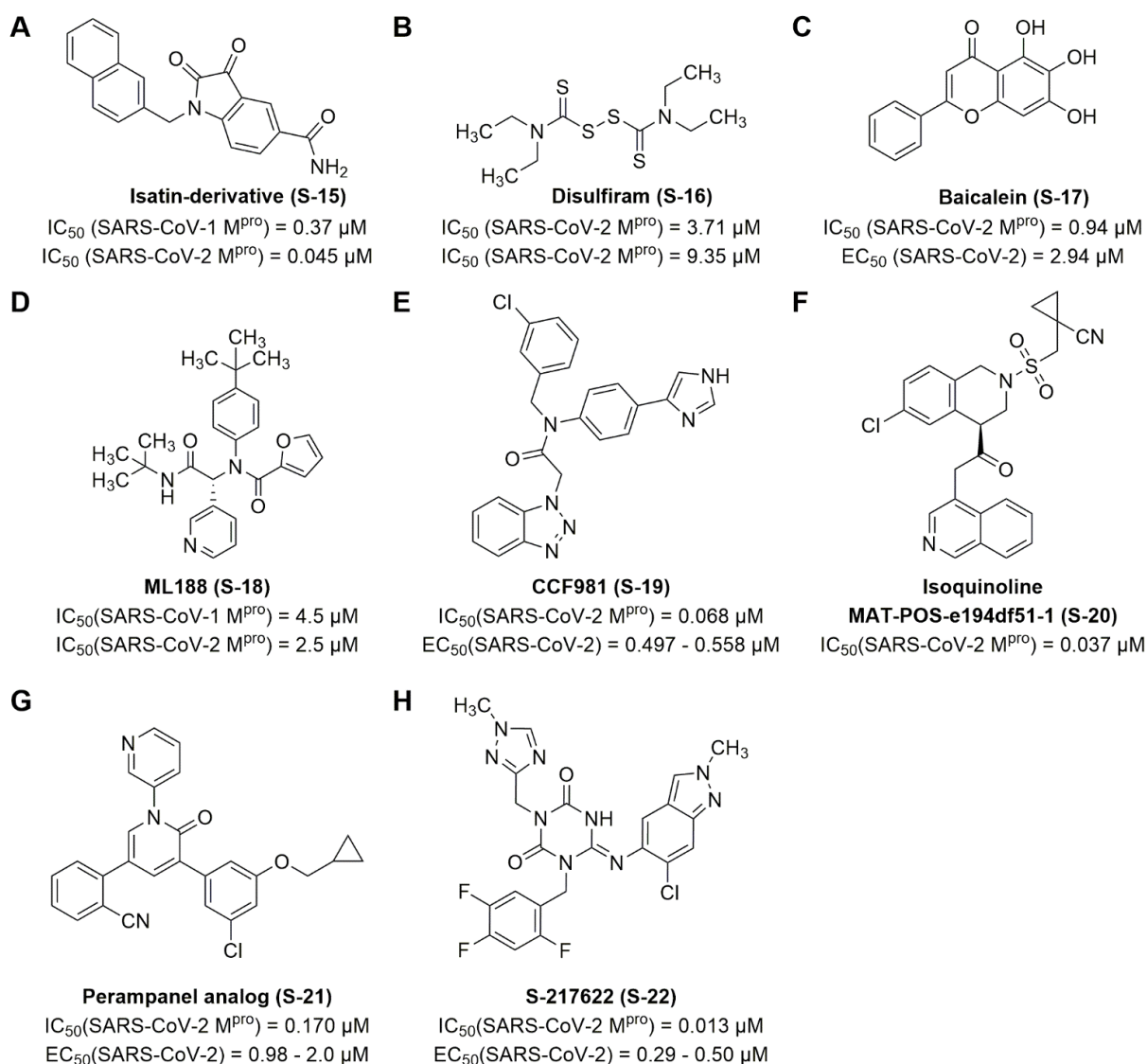
Disulfide-based inhibitors like disulfiram have the potential to react with thiol groups, leading to the formation of new disulfide bonds. However, this class of compounds was shown to inhibit M<sup>pro</sup> in a non-covalent manner. The effect of disulfiram (**S-16**) in cellular assay systems is limited (see **Figure 20B**),<sup>160</sup> and disulfides are expected to be quickly metabolized by reaction with endogenous glutathione *in vivo*.<sup>157</sup> In later studies disulfiram was shown to be a non-selective cysteine protease inhibitor, and its inhibition in enzymatic assays could be significantly be diminished by addition of DTT.<sup>175</sup>

Further substances were identified in high throughput or drug repurposing screenings, e.g. baicalein (**S-17**, see **Figure 20C**). Many of the initial hit compounds lack specificity, and have already been reported as modulators of various other targets, which labels them as pan-assay interference compounds (PAINS); or they have cytotoxic effects, which limits their direct application. Therefore, potential lead structures should be assessed thoroughly whether they can be good starting points for the development of improved inhibitors.

The SARS-CoV-1 M<sup>pro</sup> inhibitor ML188 (**S-18**) is an even more potent inhibitor of SARS-CoV-2 M<sup>pro</sup> with an IC<sub>50</sub> value of 2.5 μM, compared to an IC<sub>50</sub> value of 4.5 μM at SARS-CoV-1 M<sup>pro</sup> in the same FRET-substrate based assay (see **Figure 20D**).<sup>211</sup> The compound non-covalently interacts with the catalytic residues of the enzyme. The crystal-structure of ML-188 (**S-18**) and SARS-CoV-2 M<sup>pro</sup> (PDB-ID: 3V3M)<sup>211</sup> was used as a lead structure for the development of more potent inhibitors (e.g. S-217622 (**S-22**)).<sup>212</sup>

In a similar approach, the non-covalent SARS-CoV-1 M<sup>pro</sup> inhibitor ML300 (benzotriazole) was utilized as a starting point for an extensive SARs study yielding the imidazole and 3-chlorobenzyl containing compound CCF981 (**S-19**, see **Figure 20E**).<sup>213</sup> The metabolic

stability and pharmacokinetics of this series of compounds is not ideal, which warrants further development in regard to reduction of its clearance and inhibition of CYP enzymes.



**Figure 20.** Noncovalent inhibitors of SARS-CoV-2  $M^{pro}$  and their potencies **A.** most potent isatin derivative (**S-13**);<sup>209,210</sup> **B.** Disulfiram (**S-14**);<sup>160,165</sup> **C.** Baicalein (**S-15**);<sup>214</sup> **D.** ML188 (**S-16**);<sup>211</sup> **E.** CCF981 (**S-17**) (additional characterization at SARS-CoV-1  $M^{pro}$   $IC_{50}$  = 0.19  $\mu$ M and antiviral activity in infected Vero E6 ACE2 cells (CPE  $EC_{50}$  = 0.497  $\mu$ M and plaque reduction assay  $EC_{50}$  = 0.558  $\mu$ M);  $CC_{50}$  > 50  $\mu$ M);<sup>213</sup> **F.** Isoquinoline lead (**S-18**, MAT-POS-e194df51-1) from Moonshot COVID-19 program;<sup>215</sup> **G.** Perampanel analog (**S-19**, compound 26 in original publication) antiviral activity in infected Vero E6 cells via MTT assay ( $EC_{50}$  = 2.0  $\mu$ M) and plaque reduction assay ( $EC_{50}$  = 0.98  $\mu$ M);<sup>216</sup> and **H.** S-217622 (**S-20**) antiviral activity in infected VeroE6/TMPRSS2 cells ( $EC_{50}$ (SARS-CoV-2) = 0.29 -0.50  $\mu$ M;  $CC_{50}$  > 100 $\mu$ M).<sup>212</sup>

The COVID-19 Moonshot program set out to develop broad-spectrum and affordable treatments directed against SARS-CoV-2  $M^{pro}$ . In pursuing an open science and

crowdsourced approach, coordinated via an online platform (<http://postera.ai/covid>), they developed a patent-free antiviral, that is structurally distinct. The isoquinoline-based M<sup>pro</sup> inhibitor MAT-POS-e194df51-1 (**S-20**) was simultaneously characterized in multiple laboratories, antiviral assays and cell lines (see **Figure 20F**).<sup>215</sup> Its inhibitory potency was in the nanomolar range ( $IC_{50}(\text{SARS-CoV-2 M}^{\text{pro}}) = 37 \text{ nM}$ ) and it was able to potently inhibit viral replication in combination with P-gp inhibitors ( $EC_{50}(\text{A549-ACE2-TMPRSS2 cells}) = 0.064 \mu\text{M}$ ;  $EC_{50}(\text{HelaACE2}) = 0.126 \mu\text{M}$ ), without measurable cytotoxicity.<sup>215</sup> The compound is currently in preclinical development and is envisaged as an orally available drug with a direct-to-generics production and distribution, forgoing extra profits related to intellectual properties.<sup>215</sup>

Perampanel was identified as a weak hit in a screening campaign and designated as a worthwhile scaffold for optimization.<sup>216</sup> The branched structure of perampanel occupies the S<sub>1</sub>, S<sub>1</sub>' and S<sub>2</sub> pockets of the protease, which enabled the design of tailored inhibitors based on a docked complex.<sup>216</sup> The inhibitory potency for the most potent derivative (**S-21**, see **Figure 20G**) was increased about 10.000-fold from an approximate  $IC_{50}$  value of 100-250  $\mu\text{M}$  for perampanel. Worthy of note, perampanel is fluorescent and interacted with the enzyme kinetic assay readout at concentrations relevant for the generation of its concentration-inhibition curve. The fluorescence was not a disrupting element for the more potent derivatives.<sup>216</sup> The most potent pyridone derivative (**S-21**, compound 26 in the publication, PDB-ID: 7L14) was able to inhibit the replication of SARS-CoV-2 in Vero E6 cells, while being non-toxic towards Vero E6 and human bronchial epithelial cells (NHBE) in MTT (3-(4,5-dimethylthiazol-2-yl)-2,5-diphenyltetrazolium bromide) assays ( $CC_{50} < 100 \mu\text{M}$ ).<sup>216</sup>

Finally S-217622 (**S-22**) emerged from a focused virtual screening and structure-based drug design study (see **Figure 20H**).<sup>212</sup> The virtual screening was based on the analysis of pharmacophores of known inhibitors and docking to the crystal structure of ML188 (**S-18**) and SARS-CoV-2 M<sup>pro</sup>. The conformation in presence of a non-covalent inhibitor was expected to support the rate of true positive hits.<sup>212</sup> From the virtual screening hits a lead structure with good pharmacokinetic properties was selected. Derivatization of P<sub>1</sub>' and P<sub>1</sub> moieties lead to the generation of S-217662 (**S-22**, PDB-ID: 7VTH) and a >600-fold potency increase compared to the initial hit.<sup>212</sup> The compound exhibited potent antiviral activity *versus* SARS-CoV-1 ( $EC_{50} = 0.21$ ), all SARS-CoV-2 variants ( $EC_{50} = 0.29 - 0.50 \mu\text{M}$ ) and other coronaviruses that are known to infect humans (MERS-CoV, HCoV-229E and



HCoV-OC43).<sup>212</sup> Therefore it is a potential effective drug for newly emerging coronaviruses as well. S-217622 (**S-22**) is currently in phase3 clinical trials (NCT05305547) and represents the first oral noncovalent, nonpeptidic inhibitor of SARS-CoV-2 M<sup>pro</sup> to reach this developmental stage.<sup>195</sup>

#### *Dimerization inhibitors*

So far, all inhibitors described in this introduction are orthosteric, meaning they bind in the substrate binding pocket of the protease. A second approach to M<sup>pro</sup> inhibition is based on the fact that the protease is catalytically active solely in its homodimeric form.<sup>217,218</sup> The N-terminal parts of the two monomers interconnect with each other and shape the S<sub>1</sub> pocket by interaction with Glu<sub>166</sub>. As a result, the so-called N-finger fragment and its binding pocket are targets for the development of dimerization inhibitors. An octapeptide consisting of the first eight corresponding N-terminal residues was able to decrease the protease activity of SARS-CoV-1 M<sup>pro</sup> at the millimolar level.<sup>217</sup> In a more recent study, inhibitors of SARS-CoV-2 M<sup>pro</sup> were identified by virtual screening and molecular docking to allosteric binding sites. The hit molecules interacting with Glu<sub>166</sub> were shown to decrease the dimerization, as well as enzymatic activity with micromolar potencies.<sup>218</sup> However, no clear lead structure could be identified, and the findings were not yet confirmed in cell culture experiments and need to be replicated and validated in order to be considered for drug development.

## 3 Publications on NTPDases

### 3.1 Anthraquinone derivatives

#### **Development of Anthraquinone Derivatives as Ectonucleoside Triphosphate Diphosphohydrolase(NTPDase) Inhibitors With Selectivity for NTPDase2 and NTPDase3**

*Younis Baqi, Mahmoud Rashed, **Laura Schäkel**, Enas M. Malik, Julie Pelletier, Jean Sévigny, Amelie Fiene and Christa E. Müller*

*Front. Pharmacol.* **2020** 11:1282. doi: 10.3389/fphar.2020.01282

#### **Introduction**

Purinergic signaling is regulated by ecto-nucleotidases, which catalyze the hydrolysis of nucleotides. The most important families of ecto-nucleotidases are ecto-nucleoside triphosphate diphosphohydrolases (NTPDases), ectonucleotide pyrophosphatases/phosphodiesterases (NPPs), alkaline phosphatases (APs), and the ecto-5'-nucleotidase (ecto-5'-NT, CD73).<sup>22,37,219,220</sup> The hydrolytic dephosphorylation of extracellular nucleoside tri- and di-phosphates to mono-phosphates is mainly facilitated by membrane-bound NTPDases1, -2, -3 and -8 (the other members of the NTPDase family are expressed intracellularly). For example, the terminal phosphate groups of adenosine triphosphate (ATP) are sequentially cleaved by NTPDase 1 (CD39), yielding adenosine monophosphate (AMP), which is in turn transformed to adenosine by CD73. The effects of NTPDases are determined by their substrate specificities and expression patterns. NTPDase2 has a much higher affinity for ATP compared to ADP, leading to the accumulation of the latter.<sup>37,42</sup> As ADP is one of the ligands for P2Y<sub>1</sub>, P2Y<sub>12</sub> and P2Y<sub>13</sub> receptors, their activation is affected by the NTPDase2 activity at sites of co-expression,<sup>37</sup> e.g. in blood vessels, cancer cells and in the central nervous system.<sup>85</sup> NTPDase3 is highly expressed in the brain, where it was proposed to contribute to the processing of sensory inputs, and in the pancreas, where it is connected to insulin secretion.<sup>85,87</sup> Potent inhibitors with selectivity for a particular NTPDase isoenzyme are scarcely available, and none of the published compounds are ideal as they typically lack metabolic stability or do not possess drug-like properties.<sup>100,111,114</sup> Reactive blue 2 (RB-2) and related dyes were

discovered to be privileged ligands with regard to their ability to bind to a broad range of proteins, especially those involved in purinergic signaling.<sup>221</sup> RB-2 is able to non-covalently bind to nucleotide binding sites, in particular to those for adenosine phosphates. The interaction of RB-2 is promiscuous, but synthesis of derivatives, especially truncated ones, enables the generation of more selective compounds.<sup>221</sup>

Our laboratory has a history of studying anthraquinones and their pharmacological effects on selected targets.<sup>221-225</sup> The predecessor study related to the paper presented in this chapter focused on the optimization of anthraquinone derivatives as inhibitors of rat NTPDases1, -2 and -3; it presented PSB-071, an NTPDases inhibitor with IC<sub>50</sub> values in the micromolar range.<sup>104</sup> The binding mode of PSB-071 at rat NTPDase2 was determined by X-ray crystallography.<sup>54</sup> Interestingly, two molecules of the anthraquinone-derived inhibitor simultaneously bind to the active site of the enzyme, facilitated by self-association via  $\pi$ - $\pi$ -stacking interactions.<sup>54</sup>

The following publication pursues the development of selective human ecto-NTPDase inhibitors based on an anthraquinone scaffold.<sup>105</sup> Examination of the structure-activity relationships enabled the synthesis of compounds with distinct selectivity for NTPDase2 or NTPDase3.

### Summary and outlook

A library of 203 anthraquinone compounds was screened at a concentration of 2  $\mu$ M on human NTPDases subtype 1, 2, 3 and 8 using the malachite green assay.<sup>120</sup> 48 of those compounds are featured in the publication. This work comprises the description of the synthesis of 14 novel anthraquinone derivatives and the detailed *in vitro* assessment of the featured compounds with respect to their inhibitory potencies and selectivity at human ecto-NTPDases. No potent inhibitors of NTPDase1 (CD39) or -8 were identified, while selective NTPDase2 and -3 inhibitors emerged and were further characterized.

Regarding the structure-activity relationships, inferences were non-transferable between human and rat NTPDases. PSB-071 (**6**) was not able to inhibit human ecto-NTPDases at relevant concentrations. Similarly, rat CD39 and NTPDase3 were efficiently inhibited by naphthylamino-substituted anthraquinone derivatives **15** and **18**.<sup>104</sup> However, these compounds had no effect on the corresponding human NTPDases. The basic anthraquinone structure was essential for the ability to modulate the enzymes. But the

overall size and polarity of RB-2 was not required for inhibition. This enabled the synthesis of smaller derivatives. NTPDase3 modulators generally possessed negatively charged groups, such as hydroxyl, carboxylate or sulfonate. The most potent inhibitors of NTPDase3, PSB-1011 (**42**, IC<sub>50</sub> of 390 nM) and PSB-2046 (**33**, IC<sub>50</sub> of 723 nM) are both rather polar, which suggests a more hydrophilic binding pocket compared to NTPDase2. Inhibitors targeting the NTPDase2 enzyme were more spacious and lipophilic, such as the phenanthryl derivative PSB-16131 (**20**) and the diphenyl sulfide PSB-2020 (**48**), exhibiting IC<sub>50</sub> values of 539 and 551 nM respectively.

So far RB-2 and the anthraquinone derivatives were described as competitive inhibitors of rat NTPDases.<sup>54,104</sup> The inhibition type studies conducted on the human NTPDases for the most potent inhibitors yielded different modes of inhibition, which do not support the hypothesis of a purely competitive inhibition type. NTPDase2 was inhibited by PSB-16131 (**20**) in a non-competitive manner and NTPDase3 was inhibited by PSB-1011 (**42**) with a mixed-type inhibition, which is a special case of non-competitive inhibition. Consequently, the mechanism of action is connected to the substitution pattern and disparate for NTPDase isoenzymes and species.

All in all, several anthraquinone derivatives were established as lead structures for specific NTPDase2 and NTPDase3 inhibitors. These compounds may be employed for biological studies on the (patho)physiological effects of NTPDases. Furthermore, they are promising candidates for the pharmacological treatment of cardiovascular and neurodegenerative diseases, inflammation and cancer.

### **Author's contribution**

For this publication, the concentration-inhibition curves of 28 anthraquinones were determined for NTPDase2 or -3. Out of those, 19 were determined by the author of this thesis, while the foundation was laid by Amelie Fiene, who performed the screening at 2 μM as well as IC<sub>50</sub> value determination for nine compounds with an initial inhibition above 70 %. The selectivity of potent NTPDase2 and NTPDase 3 inhibitors *versus* the ecto-NTPDases, and the inhibition type experiments were executed by the author, as well as the inhibition type determinations of derivatives **20** (PSB-16131) at NTPDase2, and **42** (PSB-1011) at NTPDase3. The experimental work is depicted in Figures 2, 3 and 5, and inhibition constants are collected in Table 1.

## 3.2 ARL67156

### Nucleotide Analog ARL67156 as a Lead Structure for the Development of CD39 and Dual CD39/CD73 Ectonucleotidase Inhibitors

*Laura Schäkel, Constanze C. Schmies, Riham M. Idris, Xihuan Luo, Sang-Yong Lee, Vittoria Lopez, Salahuddin Mirza, The Hung Vu, Julie Pelletier, Jean Sévigny, Vigneshwaran Namasisvayam and Christa E. Müller*

*Front Pharmacol* 2020 Sep 8;11:1294. doi: 10.3389/fphar.2020.01294. eCollection 2020.

#### Introduction

The inhibition of ecto-nucleotidase activities is a novel approach in the treatment of cancers,<sup>74</sup> which overexpress nucleoside triphosphate diphosphohydrolase1 (NTPDase1, CD39) and ecto-5'-nucleotidase (CD73) in order to facilitate immune escape by hydrolysis of inflammatory ATP to immunosuppressive adenosine.<sup>226</sup> Therefore, small molecules that are able to inhibit either or both of the enzymes are in demand.<sup>74</sup> For the target CD73, several potent small molecule inhibitors as well as antibodies have been developed and are currently investigated in clinical trials.<sup>140,142,145</sup> The design and production of CD39-specific antibodies was also successful.<sup>126,127,153</sup> However, no promising small molecule lead structures for CD39 have been available and comprehensively characterized. The ideal lead structure candidate for CD39 is metabolically stable and has a high potency and selectivity for its target. Currently known inhibitors are lacking at least one of the aforementioned properties.

Therefore, the work leading to the publication presented in this chapter took the approach of extensively characterizing the current standard ecto-ATPase inhibitor *N*<sup>6</sup>-diethyl-D-β,γ-dibromo-methylene-ATP (ARL67156).<sup>94</sup> The nucleotide analog is based on ATP, with a β,γ-dibromo-methylene bridge aiming to stabilize the phosphate chain. It demonstrated moderate competitive inhibition of the human enzymes CD39, NTPDase3 and NPP1 with *K<sub>i</sub>* values in the micromolar range (*K<sub>i</sub>* (CD39) = 11 ± 3 μM, *K<sub>i</sub>* (NTPDase3) = 18 ± 4 μM and *K<sub>i</sub>* (NPP1) = 12 ± 3 μM).<sup>93,138</sup> P2 receptors are not modulated by the ATP-analog.<sup>55</sup> As ARL67156 is so far the only commercially available CD39 inhibitor, it was frequently used in *in vitro* and *in vivo* experiments.<sup>95-97</sup> Despite its modest inhibitory

potency, ARL6175 was selected as a compelling starting point for further characterization and development of potent, subtype-specific CD39 inhibitors. The competitive inhibition type at CD39 points to an orthosteric binding at the site of the ATP substrate and should therefore enable *in silico*-assisted optimization of derivatives.<sup>52</sup>

### Summary and outlook

In our hands, ARL67156 displayed a micromolar affinity for human CD39 with respective  $K_i$  values of 0.973 and 3.45  $\mu\text{M}$  in capillary electrophoresis- and colorimetric-based enzyme activity assays respectively.<sup>93</sup> By synthesis of  $N^6$ - and 8-substituted adenosine derivatives and subsequent phosphorylation,<sup>227</sup> new insights into the structure activity relationships (SARs) of this compound class at human CD39 were attained. None of the variations in the  $N^6$ - and 8-position led to derivatives with increased potency compared to the lead structure. The new compounds **31**, **33**, and  $\alpha,\beta$ -methylene-ATP were of similar CD39-inhibitory potency as ARL67156. In compound **33**, an  $N^6$ -monomethyl residue is combined with an 8-butylamino substitution of the adenine base, which resulted in  $K_i$  values of 1.51 and 3.35  $\mu\text{M}$  in the aforementioned assays. The 8-substituted compounds were inspired by 8-butylthio-adenosine nucleotides, which were shown to be potent CD39 inhibitors.<sup>91</sup> Our own studies on the optimization of (8-butylthio-)AMP-derivatives are currently being compiled and will be published in the near future. The importance of the dibromo substitution of the methylene bridge was assessed. Electron-withdrawing substituents were essential to the inhibition potency at CD39, since halogen-substituted analogs retained some potency, whereas a compound with an unsubstituted methylene bridge was not able to elicit inhibition. This indicates that full deprotonation of the terminal phosphate group is required for a high binding affinity in the ATP-binding pocket of CD39.

The selectivity of ARL67156, and the most potent derivatives **31** and **33**, was studied on a broader selection of human ectonucleotidases, including CD39, NTPDases2, -3 and 8, NPP1, -3, -4 and -5, CD73 and CD38. All three compounds were able to decrease NTPDase3, CD73, and NPP1 activities in addition to their CD39 inhibition. Compound **31** also weakly inhibited NTPDase2, while compound **33** displayed a preference for CD73 inhibition with a  $K_i$  value of 0.185  $\mu\text{M}$ . Modification of the lead structure had no significant effect on the selectivity towards CD39. Therefore, this compound class was designated as multi-target ecto-nucleotidase inhibitors.

All three compounds were metabolically unstable since the analytes could not be detected by liquid chromatography coupled to electrospray ionization mass spectrometry (LC/ESI-MS) analysis shortly after addition to mouse or human liver microsomes. The stock solutions were stable, which excluded a general chemical instability. Since ARL67156 is commonly utilized in *in vivo* studies as a CD39 inhibitor, these results were quite surprising, especially, because it had always been assumed that ARL67156 is metabolically stable due to its  $\beta,\gamma$ -dibromomethylene-group.<sup>93,138</sup>

Docking studies were performed using the previously described homology model of human CD39 and the X-ray structure of CD73.<sup>52,144</sup> ARL67156 was docked into the catalytic site of the respective enzyme, as it had been shown to competitively inhibit CD39. In comparison to ATP, ARL67156 is oriented in a very similar position with identical key residue interactions of the phosphate chain, and the 3'-hydroxy-group and the adenine ring. The necessity of a fully deprotonated  $\gamma$ -phosphate was rationalized by interactions with amino acid residues and the calcium ion in the binding pocket of CD39. In the docking studies on CD73, the phosphonate chain pointed towards the two zinc ions. The conformation around the nucleosidic bond was transformed from anti to syn by the introduction of the 8-butylthio-substituent in compound **31**.

To summarize, the work presented in this chapter contributed much needed insights into the characteristics of the multi-target ecto-nucleotidase inhibitor ARL67156. Noteworthy, we discovered that ARL6156 and its derivatives possess poor metabolic stability and can therefore be recommended only for use as pharmacological tool compounds in *in vitro*, but not in *in vivo*, experiments. This detailed characterization will be of substantial benefit for fellow researchers applying ARL67156 in their studies, and for the further development of these lead structures.

### **Author's contribution**

The modulation of human CD39 and ecto-NTPDase2, -3 and -8 activities was studied by the author utilizing the natural substrate ATP, as well as a fluorescence-labeled ATP derivative.<sup>52</sup> The nucleotide analogs were initially tested at a single concentration. Subsequently, promising derivatives were characterized by concentration-inhibition curves and calculation of  $K_i$  values. The molecular modeling studies were executed by the author in close cooperation with Vigneshwaran Namasivayam, who designed the figures

presenting the putative binding positions at CD39 and CD73. All other figures and tables were assembled by the author of this thesis. In addition, she contributed to form and content of the draft in assistance to the corresponding author Christa E. Müller.



### 3.3 2-Substituted Thienotetrahydropyridines

#### 2-Substituted Thienotetrahydropyridine Derivatives: Allosteric Ectonucleotidase Inhibitors

*Laura Schäkel, Salahuddin Mirza, Markus Pietsch, Sang-Yong Lee, Tim Keuler, Katharina Sylvester, Julie Pelletier, Jean Sévigny, Thanigaimalai Pillaiyar, Vigneshwaran Namasivayam, Michael Gütschow, Christa E. Müller*

*Arch Pharm (Weinheim)* **2021** Dec;354(12):e2100300. doi: 10.1002/ardp.202100300.

#### Introduction

ATP belongs to the damage-associated molecular patterns, exerting its effects on the innate immune response by activation of purinergic P1 and P2 receptors.<sup>20</sup> The molecule is increasingly released upon hypoxia-related conditions such as inflammation and stress via exocytosis, nucleotide channels and transporters, or passively released in consequence to cell death.<sup>28,57</sup> The nucleotide evokes a self-reinforcing inflammatory process by recruitment and activation of immune cells. This so-called purinergic signaling is regulated by the enzymatic hydrolysis of the nucleotides by ecto-nucleotidases, most prominently CD39. The ATPase operates in tandem with CD73, which transforms AMP, the product of CD39, to adenosine. This nucleoside in turn elicits the opposite effects to ATP, by downregulating the immune system via adenosine receptors.<sup>23,28</sup> Modulators of these enzymes are of interest in pharmaceutical treatment of cancer immune escape and regulation of infections.<sup>74</sup> Small molecule inhibitors are especially attractive drugs as they can be synthesized in bulk and are potentially suited for per oral application, which is not the case for antibodies. Furthermore, the pharmacokinetic properties of lead structures may be designed to enable accumulation in tumor tissues. To date, no suitable drug candidates have been identified for CD39. Yet, the thienotetrahydropyridine derivatives ticlopidine and clopidogrel may be repurposed as CD39 inhibitors, as they were shown to be moderately potent inhibitors.<sup>108,109</sup>

The structurally closely related compounds are prodrugs, that are metabolically activated via cytochrome P450 enzymes in the liver to reactive thiols that are able to covalently attach to and thereby exert irreversible inhibition of P2Y<sub>12</sub> receptors on thrombocytes.

The antithrombotic effect of these drugs is utilized in the treatment of acute coronary syndromes and for the prevention of stroke and heart infarction.

Both ticlopidine and clopidogrel were reported to decrease the hydrolysis of adenine nucleotides by CD39 in their native, unmetabolized form. In the published studies, the compounds inhibited the human enzyme with a mixed-type of inhibition with apparent  $K_{i,app}$  values of 14  $\mu\text{M}$  for ticlopidine and 10  $\mu\text{M}$  for clopidogrel.<sup>109</sup> The authors claimed that the hydrolysis of ADP as a substrate of CD39 was inhibited more effectively than ATP, and that the inhibition was selective for the CD39 isoenzyme.<sup>108,109</sup>

In the publication of this chapter, our objective was the validation of previously reported inhibition results, as well as the investigation of the effects of 2-substituted thienotetrahydropyridine derivatives as inhibitors of human CD39.

### Summary and outlook

Initially, we confirmed the concentration-dependent inhibition of both ticlopidine and clopidogrel, with lower potency than previously claimed.<sup>109</sup> As a next step we comprehensively investigated the effects of ticlopidine on different preparations of CD39, namely native enzyme from human umbilical cord membranes and recombinant human CD39 either expressed in COS-7 membranes, or the soluble purified form, which lacks the transmembrane domains. The potency of ticlopidine was consistent among the different forms of the enzyme within orthogonal assay systems. In addition, we replicated the experiments with ATP and ADP substrates and found no statistical difference of ticlopidine inhibition potency of CD39. The inhibition type was characterized as allosteric, non-competitive with a  $K_i$  value of 127  $\mu\text{M}$ , which is in the same range as the determined  $\text{IC}_{50}$  values (33.3 – 81.7  $\mu\text{M}$ ). A direct repurposing of ticlopidine as CD39 inhibitor is not practical, as the compound is lacking in potency and will be metabolized to a P2Y<sub>12</sub> receptor antagonist.

Therefore, we initiated the search for more potent and metabolically stable inhibitors by screening a library of closely related thienotetrahydropyridine derivatives, in which the 2-position was blocked by introduction of amino, carboxamido, ureido or thioureido groups. These substitutions were thought to prevent metabolism by CYP-enzymes and unintended off-target actions. Structure activity relationship analysis revealed that 2-substitution was tolerated as several of the investigated 2-substituted

thienotetrahydropyridine derivatives displayed inhibition of CD39 at 100  $\mu\text{M}$ . The most potent derivative **32** was selected for further characterization. Similar to ticlopidine, compound **32** was able to inhibit different CD39 preparations in three different assay systems. The observation that inhibition of the soluble form of CD39 was retained indicates that the allosteric binding site is independent of the transmembrane regions. The potency of derivative **32** was similar to ticlopidine with  $\text{IC}_{50}$  values ranging from 45.2 to 84.8  $\mu\text{M}$ . Likewise, the compound displayed a non-competitive inhibition type. Remarkably, the selectivity profile of **32** was improved in comparison to ticlopidine, which inhibited all ecto-NTPDases and CD73, while **32** solely inhibited CD39 and CD73 activities. Therefore, compound **32** can be classified as better lead structure for CD39 modulation, as it was assessed *in silico* to not be converted to a thiol-reactive derivative and potential P2Y<sub>12</sub> antagonist.

In conclusion, ticlopidine was shown to be a multi-target ecto-nucleotidase inhibitor, and we were able to identify several structurally related derivatives with similar CD39 inhibitory potency that cannot be oxidized to reactive thiols. In addition, our laboratory performed similar studies on the SARs and selectivity of a large series of ticlopidine derivatives and analogs which will soon be published.

#### **Author's contribution**

The experimental work on membrane-bound CD39 and NTPDases 2, -3 and 8 was conducted by the first author of this publication, including the screening and selectivity experiments, as well as the determination of  $\text{IC}_{50}$  values and inhibition types of ticlopidine and the most potent derivative **32**. All figures were created by the author, and she was responsible for writing the manuscript jointly with professors Christa E. Müller and Michael Gütschow.

### 3.4 Ceritinib

#### **Protein Kinase Inhibitor Ceritinib Blocks Ectonucleotidase CD39 – a Promising Target for Cancer Immunotherapy**

*Laura Schäkel, Salahuddin Mirza, Riekje Winzer, Vittoria Lopez, Riham Idris, Haneen Al-Hroub, Julie Pelletier, Jean Sévigny, Eva Tolosa and Christa E. Müller*

*Journal for ImmunoTherapy of Cancer* **2022** 10:e004660. doi:10.1136/jitc-2022-004660

#### **Introduction**

Cancer cells were shown to facilitate immune escape via the hypoxia- $A_{2A}$ -adenosinergic signaling pathway.<sup>30</sup> Hypoxia is characteristic for the tumor microenvironment and induces an increased production of extracellular adenosine via the transcription factors specificity protein 1 (SP-1) and hypoxia-inducible factor 1 $\alpha$  (HIF-1 $\alpha$ ).<sup>31</sup> Adenosine suppresses the immune response via  $A_{2A}$  and  $A_{2B}$  receptor signaling. Successful pharmaceutical intervention with the aim to re-activate the cellular immune response has been demonstrated with the adenosine  $A_{2A}$  receptor antagonist ciferadenant and the CD73 inhibitor AB680, small molecules that are currently evaluated in advanced clinical trials.<sup>33,145,146</sup> An alternative route to prevent immune escape and to activate the immune response may be achieved by inhibition of the ecto-nucleotidase-catalyzed degradation of ATP.<sup>71</sup> One of the most prominent ecto-nucleotidases in the cancer microenvironment is CD39, an enzyme that dephosphorylates ATP via ADP to AMP. The product AMP is subsequently hydrolyzed by CD73, to produce adenosine.<sup>37</sup> Tumor cells overexpress these enzymes in order to maintain an immunosuppressive and proliferation-enhancing microenvironment.

CD39 presents a novel target for the immunotherapy of cancer.<sup>72</sup> Its inhibition would have the advantage of increasing extracellular ATP concentrations, thereby further boosting the cellular immune response. But so far, no potent and selective small molecule inhibitors for CD39 are available or in clinical trials (see section 2.2.3). Therefore, new scaffolds for CD39 inhibitors are in demand. It is favorable to consider the pharmacokinetic properties, like metabolic stability, at early stages of drug development.

Thus, it has been postulated that it may be easier to optimize target potency than pharmacokinetic properties without losing a compound's inhibitory potency.<sup>212</sup>

In this publication, we identified a new scaffold for CD39 inhibitors and performed a detailed characterization of the hit compounds' inhibition mode, selectivity and effect on the ATPase activity in immune and cancer cells. The hit compound, ceritinib, has very high chemical and metabolic stabilities, and may be further optimized with regard to its ecto-NTPDase-inhibitory potency and selectivity.

### Summary and outlook

We assembled a library consisting of 50 approved protein kinase inhibitors on the assumption, that these compounds are optimized drugs with regard to their pharmacokinetic properties. Protein kinases contain a binding site for their co-factor ATP, which is competitively targeted by many protein kinase inhibitors. Our hypothesis was, that some protein kinase inhibitors may bind to and inhibit extracellular ATP-hydrolyzing enzymes as well.

We screened the library of protein kinase inhibitors at human CD39 and identified one hit, namely ceritinib. The drug significantly decreased the activity of membrane-bound CD39 by 56% at 10  $\mu\text{M}$ . This initial finding was confirmed by the generation of  $\text{IC}_{50}$  values of 11.3 and 13.7  $\mu\text{M}$  in two orthogonal enzymatic activity assays using different preparations of the CD39 enzyme. The inhibition type for ceritinib at CD39 was determined to be non-competitive with a  $K_i$  value of 11.0  $\mu\text{M}$ . This fact proposes the existence of a secondary, allosteric nucleotide binding site on CD39 that modulates the catalytic turnover of the substrate ATP. Furthermore, we performed selectivity studies for ceritinib at relevant ecto-nucleotidases. At a concentration of 50  $\mu\text{M}$ , ceritinib was able to inhibit the activities of NTPDases3 and -8, but showed limited or no modulation of NTPDase2, CD73, CD38 and ecto-NPPs. The inhibitory potency was further characterized by determining  $\text{IC}_{50}$  values of 22.7 and 20.3  $\mu\text{M}$  for NTPDase3 and NPTDase8, respectively.

As a next step, the effect of ceritinib on the ATP-degrading abilities of native immune cells, namely peripheral blood mononuclear cells and two membrane preparations of cancer cells was assessed. Ceritinib showed a concentration-dependent inhibition of ATP hydrolysis and consequently an accumulation of ATP. This effect could be confirmed in living cells. However, ceritinib was cytotoxic at higher concentrations and upon longer

exposure time. The cytotoxicity may be caused by protein kinase inhibition and may be reduced by the synthesis of derivatives with increased NTPDase selectivity in future studies.

Ceritinib (Zykadia®) is approved as an inhibitor of anaplastic lymphoma kinase (ALK), which it competitively inhibits with a potency in the low nanomolar range.<sup>9,228</sup> It was optimized with regard to its metabolic stability and was intensively characterized as part of the approval process.<sup>228-230</sup> The drug is distributed as capsules for oral administration, as the active ingredient, ceritinib, shows good membrane permeability and even a capacity to overcome the blood-brain barrier.<sup>231</sup> Micromolar levels were found in tumor tissues and low micromolar levels in plasma.<sup>229-231</sup> Thus, ceritinib's inhibition of CD39 could potentially be a synergistic factor in the treatment of some cancer patients, as local tumor concentrations of ceritinib can reach levels of over 100  $\mu\text{M}$ .<sup>231</sup> As previously mentioned, the poly-pharmacology of ceritinib contributes to the observed cytotoxicity. The ALK-inhibitor was shown to inhibit various additional targets, including other protein kinases, the insulin-like growth factor 1 receptor (IGF-1R), the insulin receptor, and the serine/threonine protein kinase STK22D (TSSK1).<sup>232-234</sup>

Thus, further efforts directed towards the analysis of structure-activity relationships of ceritinib analogs and derivatives as CD39 inhibitors are warranted. The initial aim will be to decrease the inhibition of protein kinases and to increase CD39 inhibitory potency. An alternative approach would be the generation of optimized dual CD39/protein kinase inhibiting drugs, which could have a synergistic effect in the anti-proliferative treatment of tumors.

### **Author's contribution**

The author of this thesis assembled and organized the acquisition of the protein kinase inhibitor library and performed the screening of this library, characterization by concentration-inhibition curves, and determination of the inhibition type at CD39, as well as the selectivity studies *versus* ecto-NTPDases. Furthermore, she conducted the experiments on membrane preparations of cancer cells. All tables and figures were created and edited by the first author and she wrote this the manuscript in cooperation with Prof. Christa E. Müller with contributions from all co-authors.

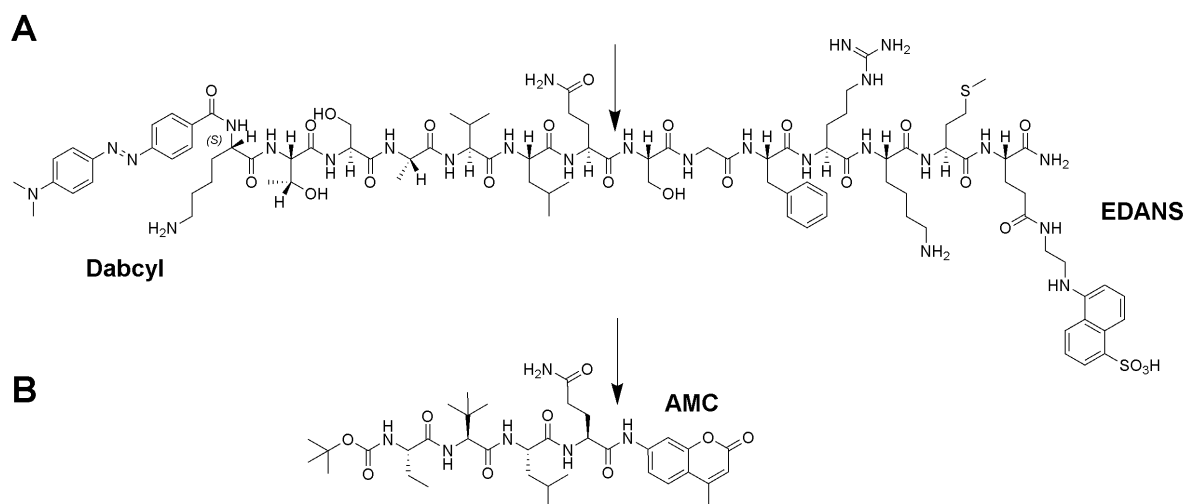
## 4 SARS-CoV-2 Main protease experiments

### 4.1 Development of an activity assay for SARS-CoV-2 M<sup>pro</sup>

In order to perform biochemical enzyme activity assays, the basic ingredients, namely an active enzyme preparation and its corresponding substrate, have to be obtained. This preliminary work was performed in the groups of Prof. Christa Müller and Prof. Michael Gütschow by an interdisciplinary team of molecular biologists and chemists and was published in Breidenbach et al. 2021.<sup>165</sup> In brief, the M<sup>pro</sup> protein was recombinantly expressed in BL21 *E. coli* bacteria. The protease was complemented with an N-terminal cleavage site for M<sup>pro</sup>, which allows for auto-cleavage of the fusion protein, and a C-terminal His<sub>10</sub> tag for purification. The native M<sup>pro</sup> enzyme was generated by digestion with HRV 3C protease, which cleaves off the His-tag.<sup>165</sup>

Two specific substrates, each containing an M<sup>pro</sup> recognition sequence and cleavage site following a glutamine in the P<sub>1</sub> position, were considered for the assay establishment (see **Figure 21**). An internally quenched fluorescent peptide substrate, Dabcyl-Lys-Thr-Ser-Ala-Val-Leu-Gln-Ser-Gly-Phe-Arg-Lys-Met-Glu(EDANS)-NH<sub>2</sub> (Dabcyl-EDANS, **Figure 21A**) was purchased, as it had been demonstrated to be an effective substrate.<sup>158,168,169</sup> On the basis of a shorter, internally quenched fluorescent peptide substrate consisting of 7-methoxy-coumarin-4-yl-acetic acid (MCA) as fluorophore and the 2,4-dinitrophenyl (Dnp) quencher,<sup>160,164,235</sup> a fluorogenic substrate was designed which releases fluorescent 7-amino-4-methylcoumarin (AMC) upon proteolysis. The artificial peptide Boc-Abu-Tle-Leu-Gln-AMC was synthesized by Lan Phuong Vu (Prof. Gütschow group) and will be referred to as AMC-substrate (**Figure 21B**).

The assay development and validation experiments described in section 4.1.1 were performed in close collaboration with Dr. Carina Wirtz (maiden name Lemke) and supported by the expertise of Prof. Christa Müller and Prof. Gütschow.



**Figure 21.** Structures of specific SARS-CoV-2 M<sup>pro</sup> substrates. **A.** Commercial fluorophore-quencher substrate Dabcyl-Lys-Thr-Ser-Ala-Val-Leu-Gln- $\downarrow$ -Ser-Gly-Phe-Arg-Lys-Met-Glu-(EDANS)-NH<sub>2</sub> (Dabcyl-EDANS, fluorophore 4-((4-(dimethylamino)phenyl)azo) benzoic acid (Dabcyl) and quencher 5-((2-aminoethyl)amino)naphthalene-1-sulfonic acid (EDANS), ( $\lambda_{\text{ex}}= 340 \text{ nm}$ ;  $\lambda_{\text{em}}= 490 \text{ nm}$ )) purchased from Biosytan (Berlin). **B.** Fluorogenic substrate Boc-Abu-Tle-Leu-Gln- $\downarrow$ -AMC ( $\lambda_{\text{ex}}= 360 \text{ nm}$ ;  $\lambda_{\text{em}}= 460 \text{ nm}$ ) synthesized by Lan Phuong Vu (Prof. Gütschow group). The arrow marks the cleavage site of M<sup>pro</sup>.

#### 4.1.1 Assay establishment and validation

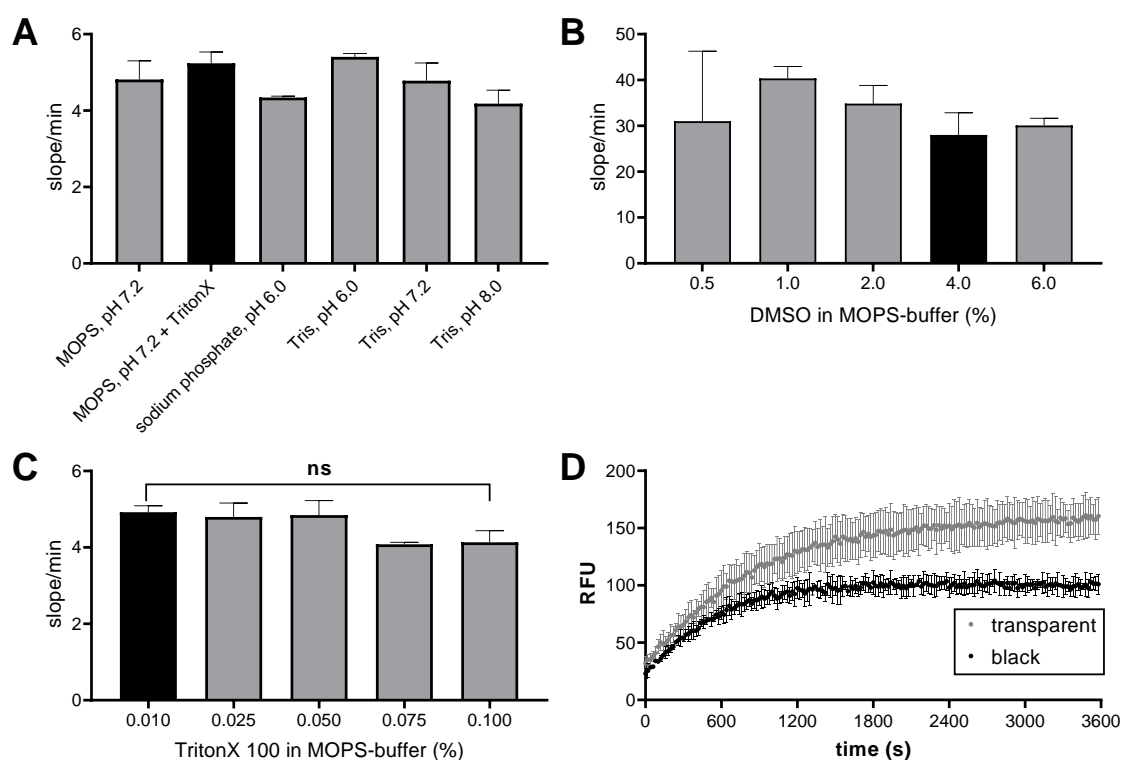
##### Parameter optimization

The initial experiments aimed to observe a time-dependent increase of fluorescence upon addition of the enzyme compared to samples without the protease. Subsequent to this proof of concept, the assay ingredients and parameters were optimized for both substrates and instruments (FLUOstar and PHERAstar by BMG Labtech) with the purpose of establishing a high throughput screening (HTS) compatible assay.

Various buffer compositions at relevant pH ranges, as well as different concentrations of dimethyl sulfoxide (DMSO), Triton X-100, and different types of 96-well plates were compared (see **Figure 22**). The activity is expressed as fluorescence increase upon product formation in the initial 10 minutes of the protease reaction (slope/min). The buffering ingredient of the chosen compositions did not have a major influence on the assay readout (**Figure 22A**). Therefore, MOPS-buffer was chosen at a pH of 7.2, which is imitating physiological intracellular conditions. MOPS is frequently used in biochemical assays and its  $pK_a$  is in the desired range with a value of 7.2. DMSO is an organic solvent



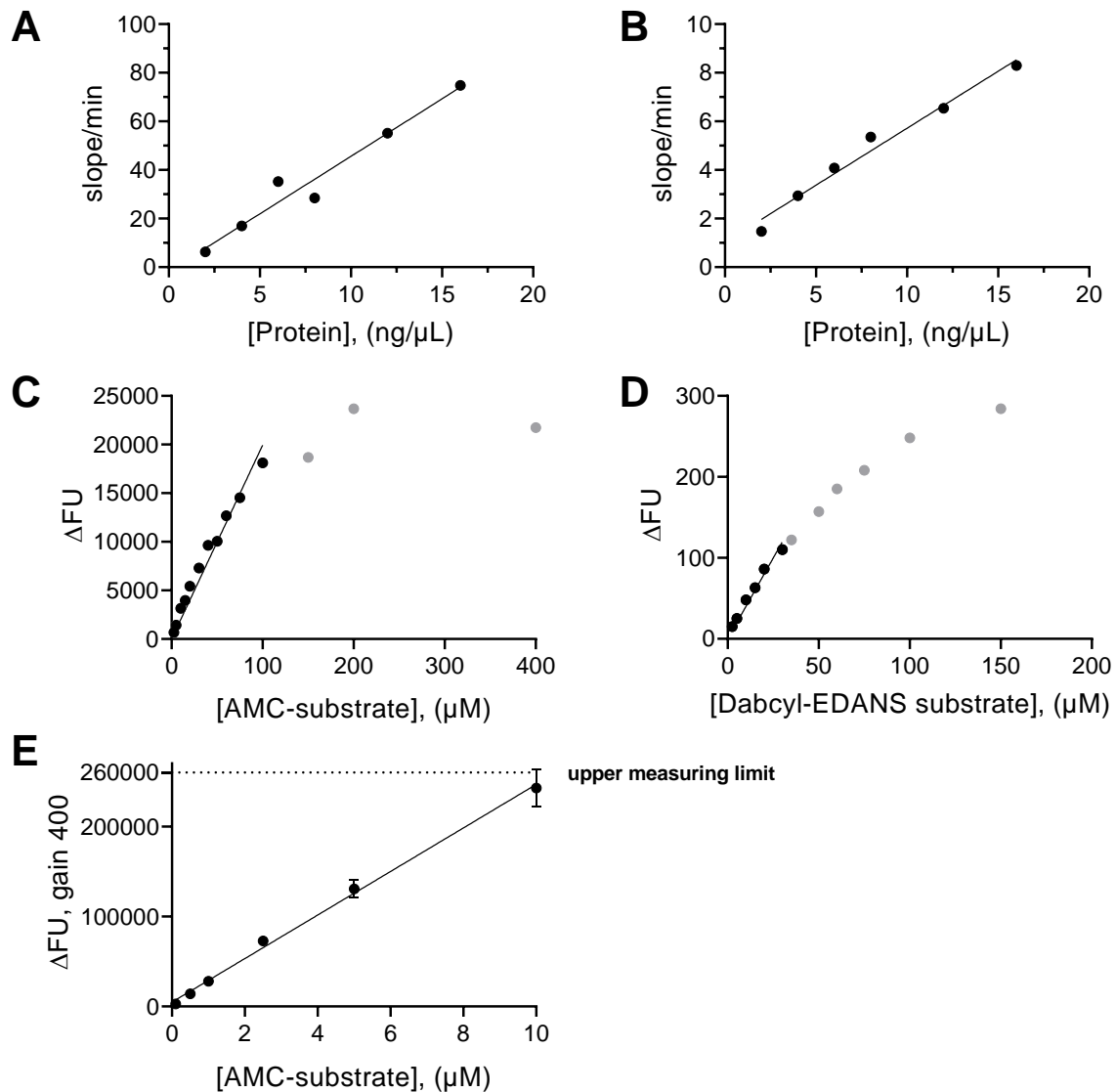
used for preparing stock solutions of substrates and inhibitors. Therefore, a suitable concentration range, which enables a reasonably high solubility under retained enzymatic activity was determined (**Figure 22B**). The enzyme activity level was not impaired by the added amounts of DMSO under these test conditions. For the screening experiments a final concentration of 4% DMSO was chosen. The detergent Triton X-100 is added to decrease non-specific protein binding of test compounds.<sup>236,237</sup> No significant difference in slope/min was detected for the tested Triton X-100 amounts (**Figure 22C**). We decided to keep 0.01% Triton X-100 in the MOPS buffer (pH 7.2). As Triton X-100 is not stable at low percentages, the assay buffer needs to be complemented from a 1% Triton X-100 stock in assay buffer before each experiment. Finally, the progression curves of samples in different types of 96-well plates were compared (**Figure 22D**). The use of black well plates resulted in a decrease of standard deviation and was therefore chosen for subsequent experiments.



**Figure 22.** Influence of different parameters on SARS-CoV-2 M<sub>pro</sub> activity performed on FLUOstar instrument; **A.** Buffer compositions: 50 mM MOPS, pH 7.2, 10 mM NaCl, 1 mM EDTA without or with 0.01% Triton X-100; 100 mM sodium phosphate buffer, pH 6.0, 100 mM NaCl, 5 mM EDTA, 0.01% Brij 35; 50 mM Tris-HCl buffer pH 8.0, pH 6.0 or pH 7.2, each containing 10 mM NaCl and 1 mM EDTA. **B.** DMSO addition to 50 mM MOPS, pH 7.2, 10 mM NaCl, 1 mM EDTA buffer; **C.** TritonX 100 detergent addition to 50 mM MOPS, pH 7.2, 10 mM NaCl, 1 mM EDTA buffer; **D.** Comparison of duplicate progression curves

of standard samples in a transparent Sarstedt or black Greiner 96-well plate. Error bars represent SEM values. Data were previously published by us.<sup>165</sup>

After determination of the assay ingredients, namely 50 mM MOPS, pH 7.2, 10 mM NaCl, 1 mM EDTA with 0.01% Triton X-100 and 4% DMSO in black 96-well plates, the optimal  $M^{\text{pro}}$  concentration and the linearity of product formation were examined (see **Figure 23**).



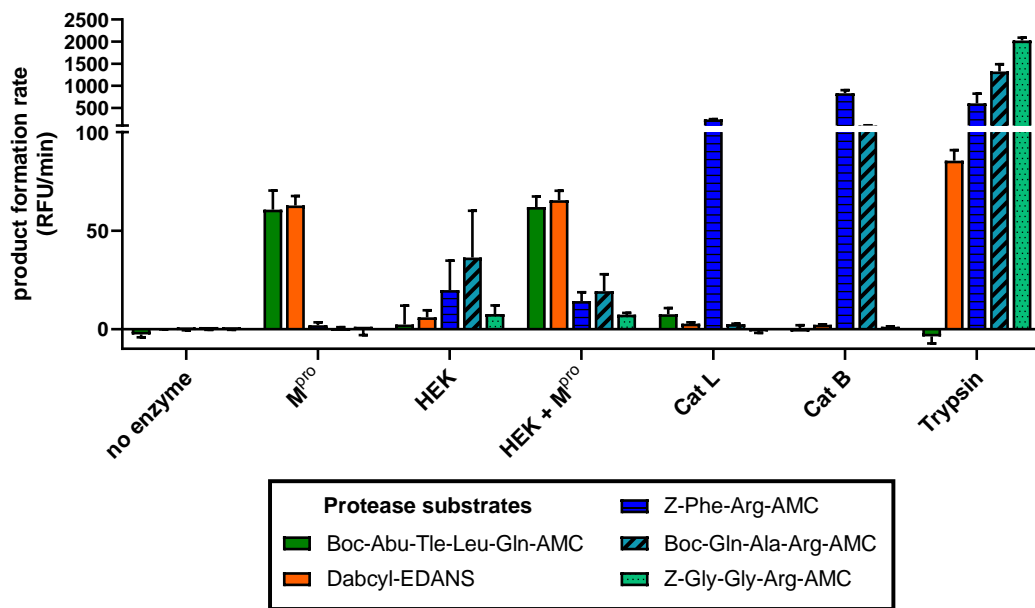
**Figure 23.** Effect of  $M^{\text{pro}}$  protein concentration on initial velocity of substrate turnover; **A.** AMC-substrate at 50  $\mu\text{M}$  and **B.** Dabcyl-EDANS substrate at 20  $\mu\text{M}$ ; linearity of fluorescence readout caused by product formation of **C.** AMC-substrate and **D.** Dabcyl-EDANS substrate on the Fluostar instrument, and **E.** AMC-substrate on the PHERAstar instrument. Data were previously published by us.<sup>165</sup>

The assay readout increased proportionally to the protein concentration of M<sup>pro</sup> samples for both substrates (**Figure 23A and B**). The influence of substrate concentration on the fluorescence intensity readout after complete transformation to product was determined by following the reaction until a plateau is reached. Due to the slower turnover, the AMC-substrate was incubated for 6.5 h (or 3.5 h for the PHERAstar instrument), while the Dabcyl-EDANS substrate was completely converted after already 30 min. The differences in fluorescence intensities at the beginning of the reaction and after complete substrate consumption ( $\Delta$ FU) were plotted *versus* initial substrate concentrations (**Figure 23C, D and E**). The AMC-substrate provides a much higher fluorescence readout. Furthermore, the solubility is superior to the Dabcyl-EDANS substrate, as linearity can be observed up to 100  $\mu$ M with the AMC-substrate, whereas the  $\Delta$ FU values were only linear up to 30  $\mu$ M with the Dabcyl-EDANS-substrate. On the PHERAstar instrument, the standard curve for AMC was linear up to 10  $\mu$ M. The signal for 50  $\mu$ M of converted AMC-substrate was above the measurement range ( $> 260\,000$  relative fluorescence units (RFU)).

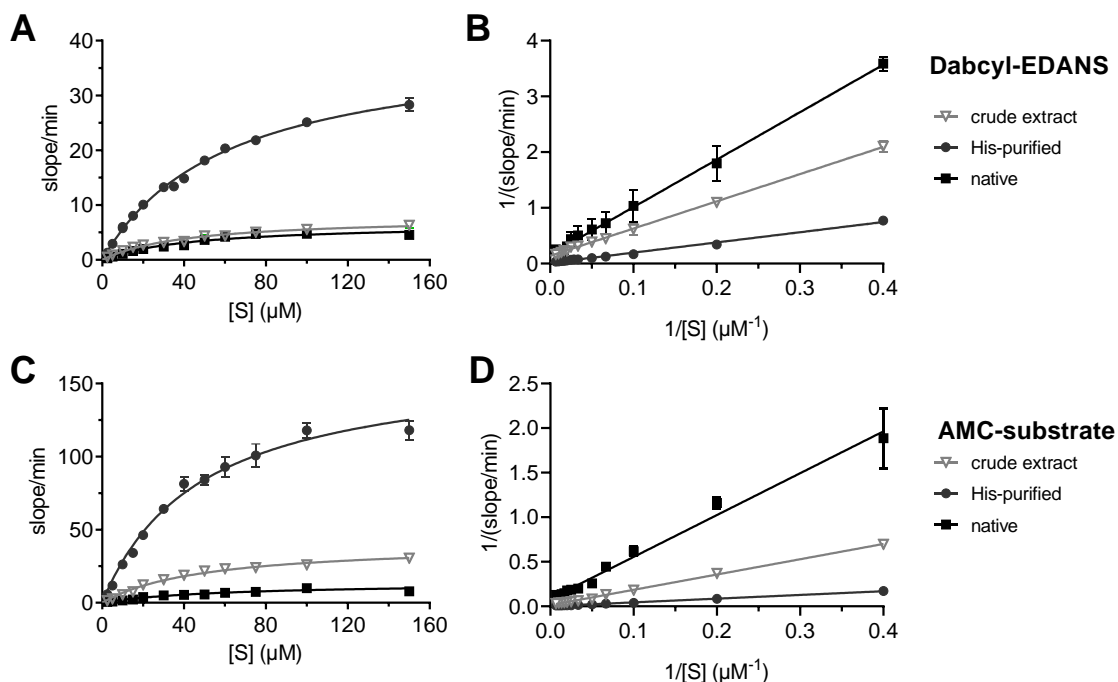
#### 4.1.2 Comparison of substrates

Substrate specificity was investigated by incubating selected protein preparations with Dabcyl-EDANS and AMC-substrate, as well as three additional AMC-based protease substrates (see **Figure 24**). The concentrations of substrates and enzymes were adjusted to ensure a significant fluorescence readout. With the exception of the Boc-Abu-Tle-Leu-Gln-AMC substrate, all artificial peptides were hydrolyzed by human trypsin, which is able to digest a wide range of proteins by cutting the peptide chain subsequent to the amino acids lysine or arginine. This qualifies the AMC-substrate as the most specific M<sup>pro</sup> substrate of this experimental series, as it was not significantly cleaved by HEK-lysates, cathepsin L, B and trypsin.

$K_m$  values for Dabcyl-EDANS and AMC-substrate were determined for SARS-CoV-2 M<sup>pro</sup> enzyme preparations at different states purification (see **Figure 25**). The crude extract of the bacterial expression containing His-tagged M<sup>pro</sup> was compared to the purified His-tagged M<sup>pro</sup> and to the native M<sup>pro</sup>, subsequent to cleavage of the His-tag. Non-transformed BL21 *E. coli* crude extract was unable to cleave the AMC-substrate (slope/min  $< 1$ ,  $n = 3$ ).<sup>165</sup> The  $K_m$  values were similar for both substrates and across all preparations of the enzyme (see **Table 9**), allowing the use of His-tagged protein in subsequent inhibitor characterization studies.



**Figure 24.** Conversion of selected fluorogenic protease substrates by SARS-CoV-2 M<sup>pro</sup>, human embryonic kidney (HEK)-cell lysates without or with M<sup>pro</sup> addition, human cathepsins L and B (Cat L and Cat B) and bovine trypsin compared to samples without the addition of protein samples (no enzyme). The initial product formation rate of 50  $\mu$ M substrate was observed over 10 min at 37°C. Data were previously published by us.<sup>165</sup>



**Figure 25.** Determination of  $K_m$  values of DabcyI-EDANS (A, B) and AMC-substrate (C, D) with M<sup>pro</sup> protein from different states of the production process. The crude extract from *E. coli* expression containing His-tagged M<sup>pro</sup> and impurities, the His-tag purified crude extract sample and the pure, native M<sup>pro</sup> sample, obtained by cleavage of the His-tag. Shown are Michaelis-Menten (A, C) and Lineweaver-Burk (B, D) plots ( $n = 3$ ).  $K_m$  values are allocated in **Table 9**. Data were previously published by us.<sup>165</sup>

In comparisons of different substrates for an enzyme, it is not unusual that the  $K_m$  values are similar, as they express the initial binding affinity of the ES-complex. Here the binding affinity of the two substrates is similar as both share the M<sup>pro</sup> specific recognition sequence and cleavage site. It is evident in **Figure 25** that the maximum velocities of product formation in the respective experiments depend on the amount and activity of the M<sup>pro</sup> enzyme added to initiate the reaction. M<sup>pro</sup> is only active in its homodimeric form, and the crude extract additionally contains other proteins, hence the concentration of catalytically active enzyme can only be approximated for the purified samples.<sup>218</sup> The efficiency of substrate turnover is expressed by the single-first order constant  $k_{cat}$  and the ratio  $k_{cat}/K_m$ . The latter, the so-called specificity constant, combines substrate affinity and conversion efficiency, which enables a more balanced comparison of a substrate's suitability as an enzymatic probe. The specificity constant of Dabcyl-EDANS (literature  $k_{cat}/K_m$  values for SARS-CoV-2 M<sup>pro</sup> 3,426 M<sup>-1</sup>s<sup>-1</sup>, 5,624 M<sup>-1</sup>s<sup>-1</sup>)<sup>158,169</sup> is higher for both purified His-tag and native M<sup>pro</sup> enzyme preparations with  $k_{cat}/K_m$  values of 5,800 and 2,590 M<sup>-1</sup>s<sup>-1</sup> compared to the AMC-substrate with 604 and 81.0 M<sup>-1</sup>s<sup>-1</sup> respectively (see **Table 9**). This indicates that the Dabcyl-EDANS substrate is cleaved faster, which can be explained by faster recognition and processing of the elongated peptide linker between the fluorophore and quencher. However, a higher turnover is not necessarily desirable, as the study of slow-binding inhibitors necessitates experimental steady-state conditions of the positive control sample over a prolonged time period. Therefore, the AMC-substrate, which is cleaved more slowly, has a higher fluorescence readout and lower production costs, and was therefore chosen for *in vitro* inhibitor characterization studies.

**Table 9.**  $K_m$  and  $k_{cat}/K_m$  values of M<sup>pro</sup> samples for Dabcyl-EDANS and AMC-substrates.<sup>165</sup> Samples include the crude extract from *E. coli* expression, which contains the His-tagged M<sup>pro</sup> along with other proteins, a His-tag purified preparation and the native M<sup>pro</sup> subsequent to cleavage of the His-tag. The product formation/min was calculated with the help of the linear regression curves, which were determined in the third iteration of the experiment (see **Figure 23**).  $k_{cat}/K_m$  was calculated with  $k_{cat} = V_{max} / \text{enzyme amount (mol/L)}$  and a molecular weight of 33,8 kDa for the M<sup>pro</sup> enzyme and 35,0 kDa for the His-tagged enzyme.  $k_{cat}/K_m$  values were not determined for the crude extract as the concentration of M<sup>pro</sup> is unknown.

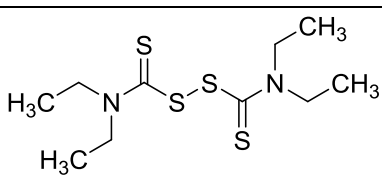
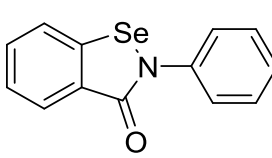
Enzyme sample	$K_m \pm \text{SEM} (\mu\text{M}, n = 3)$		$k_{cat}/K_m (\text{M}^{-1}\text{s}^{-1})$	
	Dabcyl-EDANS	AMC-substrate	Dabcyl-EDANS	AMC-substrate
M <sup>pro</sup> crude extract	42.0 ± 7.2	50.1 ± 4.8	-	-
M <sup>pro</sup> His-purified	60.6 ± 3.6	48.2 ± 5.6	5,800	604
M <sup>pro</sup> native	45.5 ± 17.0	60.2 ± 13.3	2,590	81.0

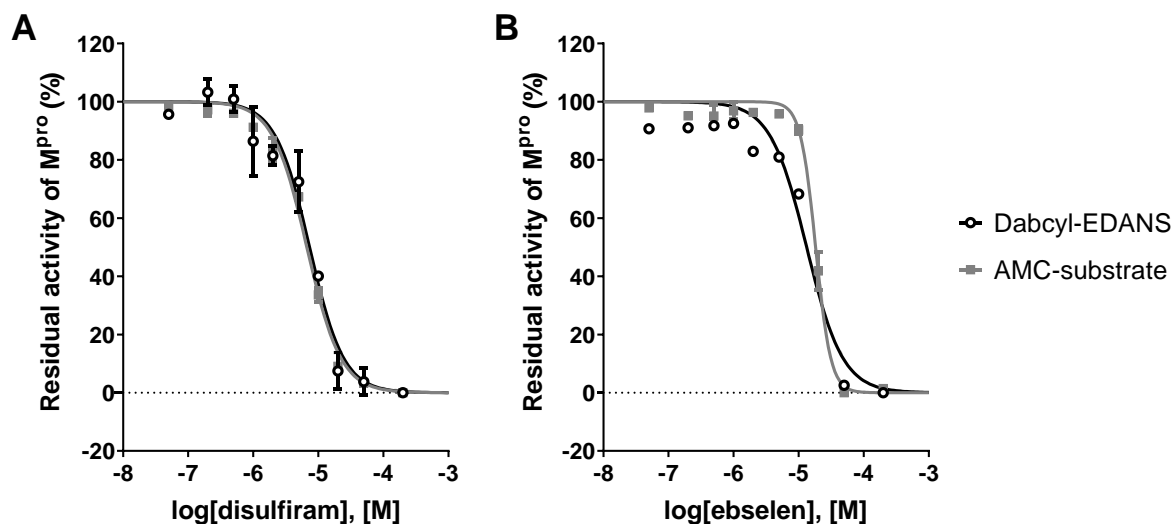
## 4.2 Characterization of first inhibitors of M<sup>pro</sup>

### 4.2.1 Reference inhibitors disulfiram and ebselen

Two compounds, disulfiram and ebselen, were reported to inhibit M<sup>pro</sup> and therefore tested with the newly established assay (see **Table 10**). The concentration-inhibition curves were prepared by observing the initial velocity of the enzymatic proteolysis for both substrates *versus* a dilution series of the respective compound. A positive control without an inhibitor defines full enzymatic activity, while a negative control, containing merely the substrate in assay buffer specifies the readout for complete inhibition. Both compounds displayed concentration-dependent inhibition of M<sup>pro</sup>. As the assay conditions, e.g. substrate concentration and assay buffer composition, differ between publications, the IC<sub>50</sub> values were corrected in analogy to the Cheng-Prusoff equation.<sup>238</sup> These corrected half maximal inhibition constants (IC<sub>50</sub> values) were comparable for both substrates and within the range of literature values (**Table 10**). Reported IC<sub>50</sub> values for M<sup>pro</sup> inhibition were 9.35 and 8.01 μM for disulfiram (**M-1**) and 0.67 μM for ebselen (**M-2**).<sup>160</sup> Since the inhibitory potency of these compounds was demonstrated to be non-specific and abrogated by addition of reducing agents DTT or glutathione (GSH),<sup>175</sup> these compounds were not further pursued as lead structures for M<sup>pro</sup>-targeted inhibitors.

**Table 10.** Comparison of inhibition constants of disulfiram and ebselen in M<sup>pro</sup> activity assay with Dabcyl-EDANS and AMC-substrates. Data were previously published by us.<sup>165</sup>

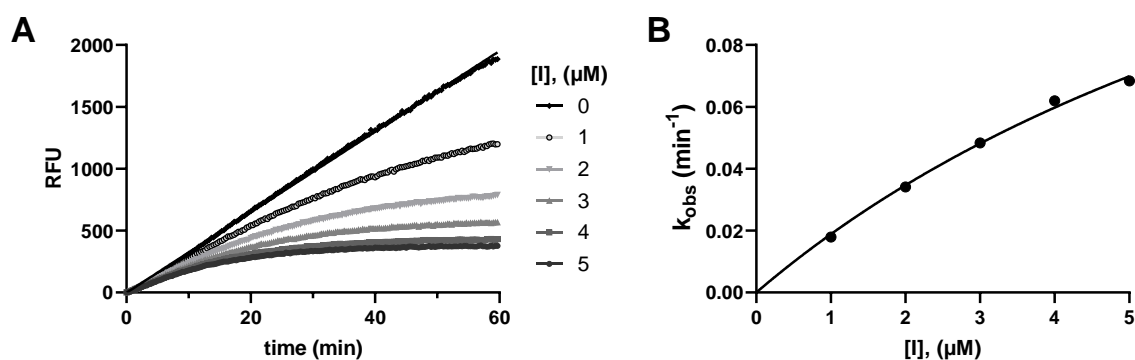
# M-	Name	Structure	AMC-substrate		Dabcyl-EDANS	
			IC <sub>50</sub> (μM)	IC <sub>50</sub> / (1+[S] /K <sub>m</sub> ) (μM)	IC <sub>50</sub> (μM)	IC <sub>50</sub> / (1+[S] /K <sub>m</sub> ) (μM)
1	Disulfiram		7.54 ± 0.24	3.71 ± 0.12	8.29 ± 0.89	6.23 ± 0.67
2	Ebselen		23.1 ± 5.3	11.4 ± 2.6	22.0 ± 1.3	16.5 ± 1.0



**Figure 26.** Concentration-dependent inhibition of SARS-CoV-2 M<sup>pro</sup> by **A.** disulfiram (**M-1**) and **B.** ebselen (**M-2**). The enzymatic activities were determined with Dabcyl-EDANS or AMC-substrate. IC<sub>50</sub> values are collected in **Table 10**.

#### 4.2.2 Chloroacetamide derivatives

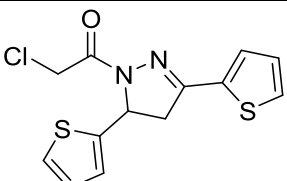
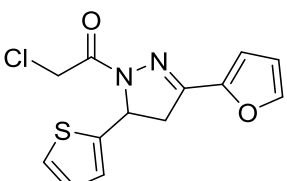
Irreversible inhibitors of SARS-CoV-1 M<sup>pro</sup> are known to target the cysteine (Cys<sub>145</sub>) in the catalytic center and form a covalent bond.<sup>159</sup> Therefore, compounds which contain a cysteine-reactive, electrophilic warhead were among the first to be tested for their potential inhibition of M<sup>pro</sup>. Chloroacetamide derivatives were able to irreversibly inhibit the M<sup>pro</sup> activity. Next to IC<sub>50</sub> values, which characterize the concentration-dependent inhibition of the initial velocity of the M<sup>pro</sup> proteolytic activity, the time-dependent onset of inhibition can be characterized by the second-order rate constant of inactivation  $k_{\text{inac}}/K_i$ . For the determination of this constant, separate experiments evaluating the first 60 minutes of the progress curves of product formation in the presence of five linearly distributed concentrations of the investigated inhibitor were performed (see **Figure 27**). The pseudo-first-order rate constant  $k_{\text{obs}}$  was subsequently plotted *versus* the inhibitor concentration, in order to determine the second-order rate constant of inhibition ( $k_{\text{inac}}/K_i$ ) from a non-linear fit of the data.



**Figure 27.** Determination of second order rate constant of inhibition of  $M^{pro}$  by **M-3** Z56347597. **A.** Progress curves of enzyme-catalyzed hydrolysis of AMC-substrate in the absence (black) or presence of increasing concentrations of inhibitor. **B.** A plot of pseudo-first-order rate constants  $k_{obs}$  versus inhibitor concentration analyzed by non-linear regression gave a  $k_{inac}/K_i$  value of  $777 \text{ M}^{-1}\text{s}^{-1}$ .

The  $IC_{50}$  values of chloroalkyl-derived inhibitors were in the micromolar range. The compound Z56347597 (**M-3**) was the most potent one with an  $IC_{50}$  value of  $4.70 \mu\text{M}$ . Formation of a covalent bond for this inhibitor class is slow as indicated by low  $k_{inac}/K_i$  values. Due to their low potency and assumed lack of specific  $M^{pro}$  inhibition, none of the compounds was considered as lead structure for further development of  $M^{pro}$  inhibitors.

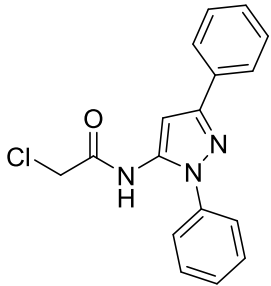
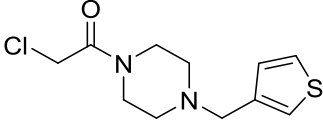
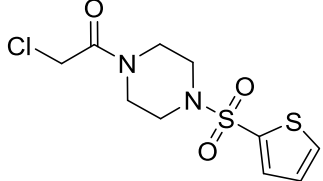
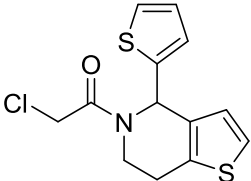
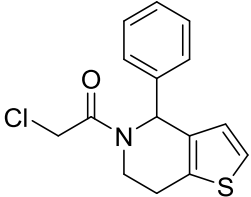
**Table 11.** Chloroalkyl derivatives: structures and characterization as inhibitors of SARS-CoV-2  $M^{pro}$ . Inhibition constants were determined with the  $M^{pro}$  activity assay and were previously published.<sup>165</sup> Compounds were purchased from ENAMINE.

# M-	Name (PZB-number)	Structure	Inhibition of $M^{pro}$ at $50 \mu\text{M}$ (%)	$IC_{50} \pm \text{SEM}$ ( $\mu\text{M}$ )	$k_{inac}/K_i$ ( $\text{M}^{-1}\text{s}^{-1}$ )
3	Z56347597 (PZB16820028A)		103	$4.70 \pm 0.82$	777
4	Z57055805 (PZB16820037A)		90	$46.4 \pm 11.1$	176



## 4.2 Characterization of first inhibitors of Mpro

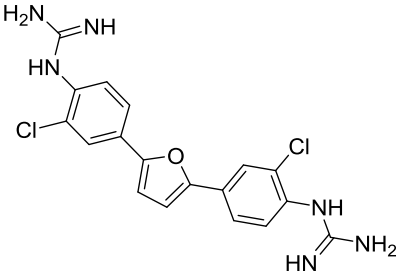
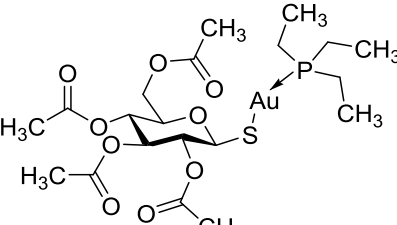
Dissertation, 2022

5	Z56914785 (PZB16820032A)		65	80.9 ± 10.2	85.5
6	Z1562120350 (PZB16820042A)		93	14.4 ± 0.2	307
7	Z212045150 (PZB16820041A)		102	5.95 ± 0.52	770
8	Z221429166 (PZB16820005A)		71	37.5 ± 3.9	147
9	Z1562121586 (PZB16820034A)		57	55.0 ± 4.1	79.8

### 4.2.3 Pathogen Box

A collection of anti-Malaria agents was obtained in form of the Pathogen Box library.<sup>239</sup> Two hit structures were identified by screening them against SARS-CoV-2 M<sup>pro</sup> (see **Table 12**). The bisbenzguanidine MMV688271 (**M-10**) was proposed to be a reversible inhibitor of M<sup>pro</sup> as the progression curves were linear in the observed time of the experiment. This class of guanidine inhibitors was further investigated by the synthesis of derivatives (see section 4.4.4). The second hit auranofin (**M-11**) is an FDA-approved drug for the treatment of rheumatoid arthritis. It is currently in phase II clinical trials for cancer therapy and is also investigated for reducing the viral load of HIV. The drug is known to inhibit redox enzymes, thereby boosting cellular oxidative stress and intrinsic apoptosis. Auranofin was identified as SARS-CoV-2-inhibiting compound by other research groups as well.<sup>240</sup>

**Table 12.** Hit compounds from the Pathogen Box library<sup>239</sup> and their characterization as inhibitors of SARS-CoV-2 M<sup>pro</sup>. Inhibition constants were determined with the M<sup>pro</sup> activity assay and were published by us.<sup>165</sup>

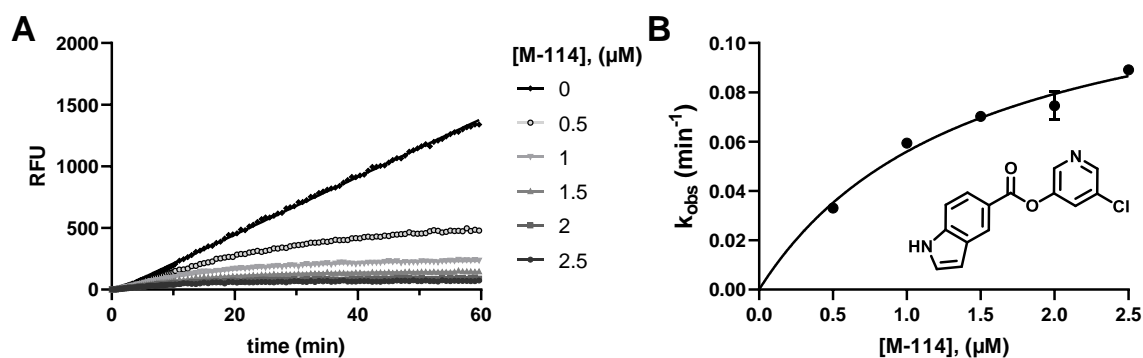
# M-	Name	Structure	Inhibition of M <sup>pro</sup> at 10 $\mu$ M (%)	IC <sub>50</sub> $\pm$ SEM ( $\mu$ M)	K <sub>i</sub> $\pm$ SEM ( $\mu$ M)	k <sub>inac</sub> /K <sub>i</sub> (M <sup>-1</sup> s <sup>-1</sup> )
10	MMV688271 (PZB16417289)		100	1.60 $\pm$ 0.16	0.709 $\pm$ 0.078	n.d.
11	Auranofin (PZB16417394)		52	19.8 $\pm$ 1.8	n.d.	133

#### 4.2.4 SARS-CoV-1 M<sup>pro</sup> inhibiting pyridyl esters

The small, orthosteric, covalently-binding inhibitor GRL-0920 (compound **M-106**) is a SARS-CoV-1 M<sup>pro</sup> inhibitor with a pyridyl ester warhead.<sup>190,191</sup> The indole ester's mode of action involves the acylation of the active-site cysteine, leading to a time-dependent inactivation of the catalytic abilities of the protease. In addition, GRL-0920 was shown to effectively reduce the replication of SARS-CoV-2 in Vero E6 cells.<sup>181,191</sup>

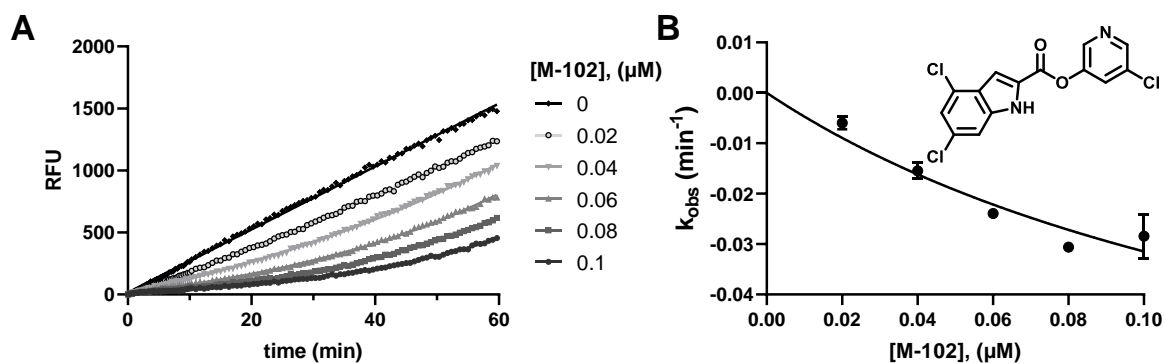
On the basis of this lead structure, consisting of an indole ester with a chloro-substituted pyridinolic group, a library was assembled with the aim to strategically investigate structure-activity relationships. The position of the ester substituent on the indole, as well as the substitutions on the pyridyl warhead were varied (see **Table 13**). All indole ester isomers were irreversible inhibitors of M<sup>pro</sup>. The esters at positions 2, 7 and 4 had the lowest IC<sub>50</sub> values, in the nanomolar range (24.7, 55.5 and 313 nM). However, for irreversible inhibitors it is more vital to regard the k<sub>inac</sub>/K<sub>i</sub> values (see **Figure 28** for an example for a time-dependent inhibition of M<sup>pro</sup> by an indole pyridyl ester). The ester at position 7 (**M-116**, PZB10620067A, k<sub>inac</sub>/K<sub>i</sub> = 20,200 M<sup>-1</sup>s<sup>-1</sup>) led to the strongest inactivation of M<sup>pro</sup> followed by the 4-position (**M-106**, PZB10620017, k<sub>inac</sub>/K<sub>i</sub> = 14,800

$M^{-1}s^{-1}$ ). The addition of a chloro substituent at position 5 of the 2-indole ester increased the  $k_{inac}/K_i$  value significantly (**M-63**, PZB10620022,  $k_{inac}/K_i = 29,100 M^{-1}s^{-1}$ ). Interestingly, di-chloro substitution at 4- and 6- position in **M-102** lead to a compound that inhibited the initial velocity to the same degree as the unsubstituted or the 5-chloro derivative **M-63**, indicated by similar  $IC_{50}$  values of 23.3 and 34.3 nM, respectively, but was not able to maintain the covalent bond leading to an observable reactivation of enzymatic activity during the experiment (60 minutes) (see **Figure 29**). As the compounds are destroyed upon hydrolytic cleavage by the enzyme, the concentration of inhibitor decreases over time. Therefore, they can only be evaluated by their initial inhibition in form of the  $IC_{50}$  value.



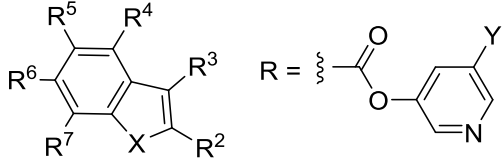
**Figure 28.** Determination of second order rate constant of inhibition of  $M^{pro}$  by **M-114** (Yazh-2K174, PZB10620024); **A.** Progression curves of enzyme-catalyzed hydrolysis of AMC-substrate in the absence or presence of increasing concentrations of inhibitor. **B.** A plot of pseudo-first-order rate constants  $k_{obs}$  versus inhibitor concentration analyzed by non-linear regression gave a  $k_{inac}/K_i$  value of  $3,200 M^{-1}s^{-1}$ .

The substitution of the pyridyl ring influences the second-order rate of inactivation as the replacement of chlorine by bromine led to an improvement for 4-indole pyridyl esters (**M-106**, PZB10620017,  $Y=Cl$  versus **M-108**, PZB10620019,  $Y=Br$ ). This is curious, as the pyridyl ring is proposed to leave the active site after formation of the thioester. An explanation could be improved initial binding, decreasing the activation energy of the electrophilic attack on the cysteine, or persistent binding of the pyridyl ring to a pocket that stabilizes the covalent bond of the inhibitor-enzyme complex. Indole bioisosters benzofuran (**M-50**, PZB10620068A) and benzothiophene (**M-52**, PZB10620066A) had high affinities to the  $M^{pro}$  enzyme resulting in  $IC_{50}$  values of 5.41 and 26.1 nM, but were rapidly cleaved and therefore did not cause a permanent inhibition.



**Figure 29.** Example of unstable covalent inhibition of  $M^{pro}$  by **M-102** (Yazh-2K171, PZB10620023) during the experimental determination of the second order rate constant of inhibition; **A.** Progression curves of enzyme-catalyzed hydrolysis of AMC-substrate in the absence or presence of increasing concentrations of inhibitor. **B.** A plot of pseudo-first-order rate constants  $k_{obs}$  versus inhibitor concentration analyzed by non-linear regression. The upward curving of the progression curves indicates an inhibitor that covalently binds to the enzyme and then dissociates again, so the enzyme activity is restored. Consequently, the inhibitor concentration decreases over time and the enzyme activity is not inhibited after the inhibitor is completely degraded. This compound can only be characterized by its  $IC_{50}$  value.

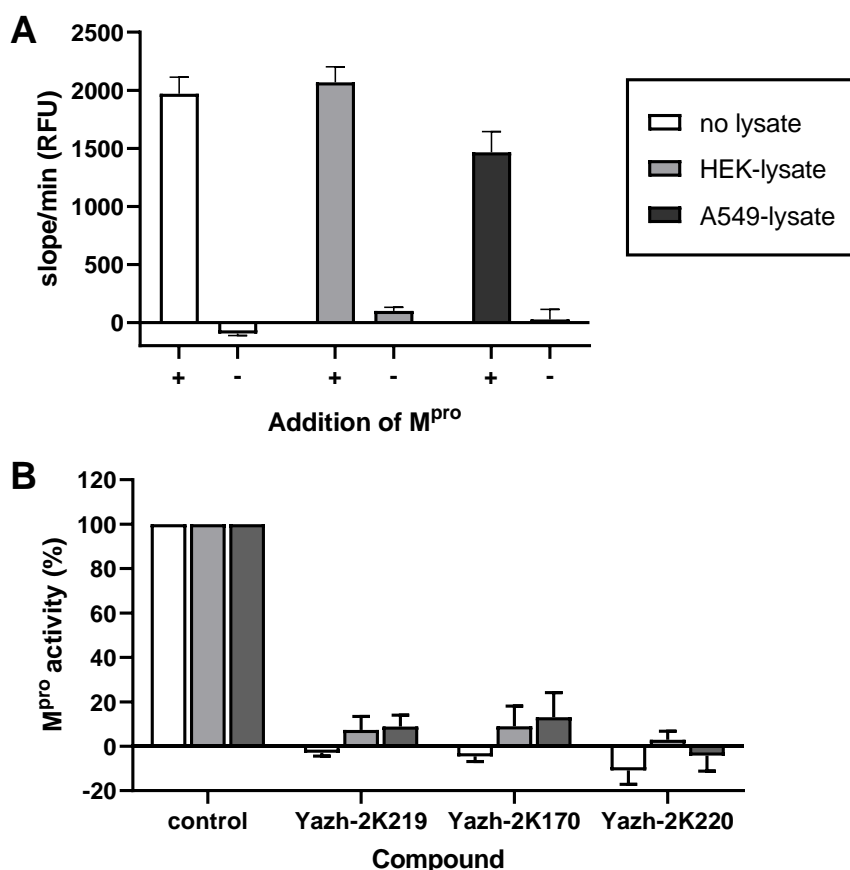
These initial findings led to the conclusion, that a balance of specific non-covalent interactions and reactivity of the ester has to be established. Irreversible inhibitors with highly reactive warheads are known for promiscuous reaction with off-targets. Therefore, a warhead with low to medium reactivity has to be combined with a structure that possesses high affinity for the intended target in order to obtain a potent and selective inhibitor. The class of pyridyl esters has several advantages. The relatively small molecular weight and simple structure allows for a straightforward synthesis of derivatives. Steep structure-activity relationships, which cover potencies of  $IC_{50}$  values in the low nanomolar range, and high inactivation constants enable rational drug design. Therefore, we considered them to be excellent lead structures for the further development as potential drugs targeting  $M^{pro}$ . The ongoing characterization of this compound class pursuing the first publication is compiled in section 4.5.

**Table 13.** Overview of pyridyl ester positional scanning for SARS-CoV-2 M<sup>pro</sup> inhibition<sup>165</sup>


# M-	Internal ID PZB-number	X	R <sup>2</sup>	R <sup>3</sup>	R <sup>4</sup>	R <sup>5</sup>	R <sup>6</sup>	R <sup>7</sup>	Y	IC <sub>50</sub> (nM)	k <sub>inac</sub> /K <sub>i</sub> (M <sup>-1</sup> s <sup>-1</sup> )
44	Yazh-2K169 PZB10620021	NH	R	H	H	H	H	H	Cl	24.7	7,600
105	Yazh-2K168 PZB10620027	NH	H	R	H	H	H	H	Cl	21,700	6,090
106	Yazh-2K164 PZB10620017	NH	H	H	R	H	H	H	Cl	313	14,800
114	Yazh-2K174 PZB10620024	NH	H	H	H	R	H	H	Cl	1,930	3,200
115	Yazh-2K207 PZB10620061	NH	H	H	H	H	R	H	Cl	586	4,400
116	Yazh-2K219 PZB10620067	NH	H	H	H	H	H	R	Cl	55.5	20,200
63	Yazh-2K170 PZB10620022	NH	R	H	H	Cl	H	H	Cl	34.2	29,100
102	Yazh-2K171 PZB10620023	NH	R	H	Cl	H	Cl	H	Cl	23.3	n.d.
108	Yazh-2K166 PZB10620019	NH	H	H	R	H	H	H	Br	227	24,000
123	Yazh-2K213 PZB10620065	NH	-(CH <sub>2</sub> ) <sub>4</sub> -		H	R	H	H	Cl	354	5,620
50	Yazh-2K220 PZB10620068	O	R	H	H	H	H	H	Cl	5.41	n.d.
52	Yazh-2K218 PZB10620066	S	R	H	H	H	H	H	Cl	26.1	n.d.

**M<sup>pro</sup> inhibition in the presence of mammalian cell lysates**

In addition to previous experiments (see **Figure 24** and section 4.1.2) the AMC-substrate was incubated with two mammalian cell lysates, namely HEK and the adenocarcinomic human alveolar basal epithelial cell line A549. The lysates were unable to cleave the AMC-substrate, but did not affect the catalytic ability of added M<sup>pro</sup> enzyme (see **Figure 30A**). The inhibitory potencies of selected pyridyl esters were maintained in the presence of the cell lysates, even though high protein concentrations of the HEK lysate were added (see **Figure 30B**). No statistically significant increase in enzyme activity was observed in a Bonferroni's multiple comparisons test. This evidence suggests that the M<sup>pro</sup> inhibitors are equally potent in a cellular context within the observed time of the experiment.



**Figure 30.** Conversion of fluorogenic AMC-substrate (50  $\mu$ M) by purified His-tagged SARS-CoV-2 M<sup>pro</sup> (0.3  $\mu$ g/well) in the presence and absence of cell lysates (HEK cell lysates, 150  $\mu$ g protein/well; A549 cells, 7  $\mu$ g/well); **A.** Positive (+) and negative controls (-) of substrate hydrolysis by samples in the presence or absence of M<sup>pro</sup>; **B.** The effect of cell lysate addition on the M<sup>pro</sup> inhibitory activity of pyridyl esters was investigated. Product formation was observed for 10 min at 37°C. Data represent means  $\pm$  SEM from four (A) or three (B) separate experiments. Data were previously published by us.<sup>165</sup>

### 4.3 High-throughput screening campaign for M<sup>pro</sup> inhibitors

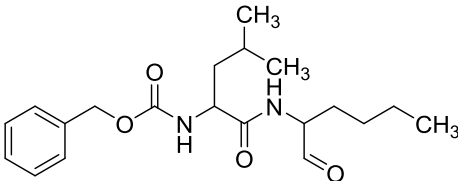
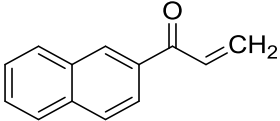
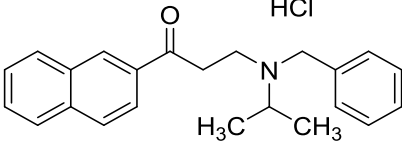
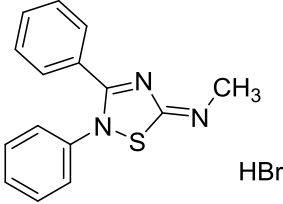
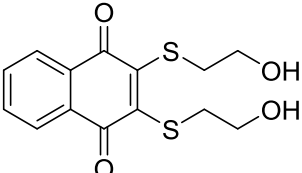
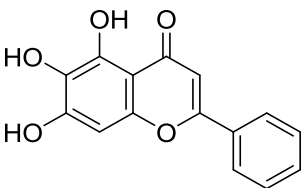
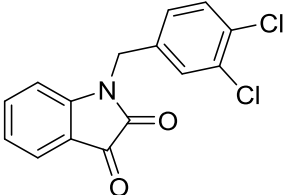
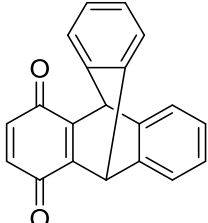
A high-throughput screening (HTS) campaign was performed with a collection of in-house libraries with the M<sup>pro</sup> enzyme inhibition assay (see **Table 14**). Most hit compounds were validated and featured in our publication.<sup>165</sup> Further hit compounds were characterized in the following section (see **Table 15** and following sections).

**Table 14.** Overview of M<sup>pro</sup> HTS campaign

Library	Plates	Screening conc.	No. of hits
ENAMINE cysteine-reactive library and related compounds	1	50 $\mu$ M	8
M <sup>pro</sup> virtual screening plates and known SARS-CoV-1 inhibitors	2	50 $\mu$ M	13
Pathogen Box	5	50 $\mu$ M	3
Indoles	1	10 $\mu$ M	1
Natural products	2	10 $\mu$ M	0
Chromenones	2	10 $\mu$ M	0
Tocris + Kinase inhibitor plates	1-2,4-10,12-14	10 $\mu$ M	11
Xanthines	13	10 $\mu$ M	0
Fragments	2	100 $\mu$ M	8

**Table 15.** M<sup>pro</sup> screening hits not included in the first manuscript<sup>165</sup>

# M-	Internal-ID (PZB-number)	Structure	Inhibition (%) of M <sup>pro</sup> at 10 $\mu$ M (n = 1)	Inhibition (%) of M <sup>pro</sup> at 50 $\mu$ M (n = 1)
<b>M<sup>pro</sup> virtual screening</b>				
12	EB 337	-	18	70
13	PZB14415175	-	20	82
14	MRP 307-2	-	19	63
15	PZB13416028	-	20	104
16	PZB15518293	-	22	57
	CLP 39 R-enantiomer	-		
	PZB15116043	-		

# M-	Internal-ID (PZB-number)	Structure	Inhibition (%) of M <sup>pro</sup> at 10 μM (n = 1)	Inhibition (%) of M <sup>pro</sup> at 50 μM (n = 1)
<b>Indole</b>				
17	VH 365 PZB05312046	-	54	-
<b>Tocris library and kinase inhibitor plate</b>			Inhibition (%) of M <sup>pro</sup> at <b>10 μM</b> (n = 3)	
18	Calpeptin		79 ± 0 [a]	
19	ZM 449829		57 ± 0	
20	ZM 39923 hydrochloride		70 ± 1	
21	SCH 202676 hydrobromide		106 ± 1	
22	NSC 95397		55 ± 10	
23	Baicalein		83 ± 1 [b]	
24	Apoptosis Activator 2		73 ± 1	
25	INCA-6		103 ± 1 [c]	



# M-	Internal-ID (PZB-number)	Structure	Inhibition (%) of M <sup>pro</sup> at 10 μM (n = 3)
26	BI 78D3		57 ± 0
27	SU 3327		105 ± 1 [d]
28	IPA 3		98 ± 2 [e]

[a] Calpeptin literature IC<sub>50</sub>(SARS-CoV-2 M<sup>pro</sup>) = 2.3 μM,<sup>241</sup> antiviral activity in Vero E6 cells EC<sub>50</sub> ≥ 1.56 μM<sup>242</sup>

[b] Baicalein literature IC<sub>50</sub>(SARS-CoV-2 M<sup>pro</sup>) = 0.94 μM,<sup>214</sup> antiviral activity in Vero E6 cells EC<sub>50</sub> = 2.94 μM and CC<sub>50</sub> > 200 μM<sup>214</sup>

[c] The inhibitory potency of this compound could not be confirmed; see section 4.4.1

[d] SU 3327 alternative name is halicin, literature IC<sub>50</sub>(SARS-CoV-2 M<sup>pro</sup>) = 0.1817 μM<sup>243</sup>

[e] IPA 3 literature IC<sub>50</sub>(SARS-CoV-2 M<sup>pro</sup>) = 0.07 μM<sup>244</sup>

## 4.4 Characterization of hit compounds

### 4.4.1 Tocris library

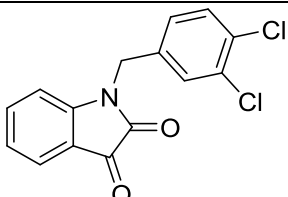
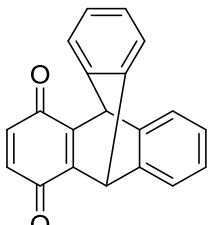
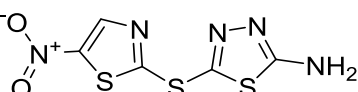
In the screening campaign, several compounds were discovered as hits with over 50 % inhibition at 10 μM. Concentration-inhibition curves were determined for these compounds using eight different concentrations depending on the inhibitory potency with three repetitions. The last measurement was performed for 1 h in order to observe the bending of the progression curves, which is characteristic for an irreversible inhibition type. Some experiments were performed under my supervision by the master student Marvin Petry. INCA-6 (**M-25**) showed no inhibitory potency at 10 μM in this experimental series. The other two hits from the Tocris library, Apoptosis Activator 2 (**M-24**) and SU3327 (**M-27**), were confirmed.

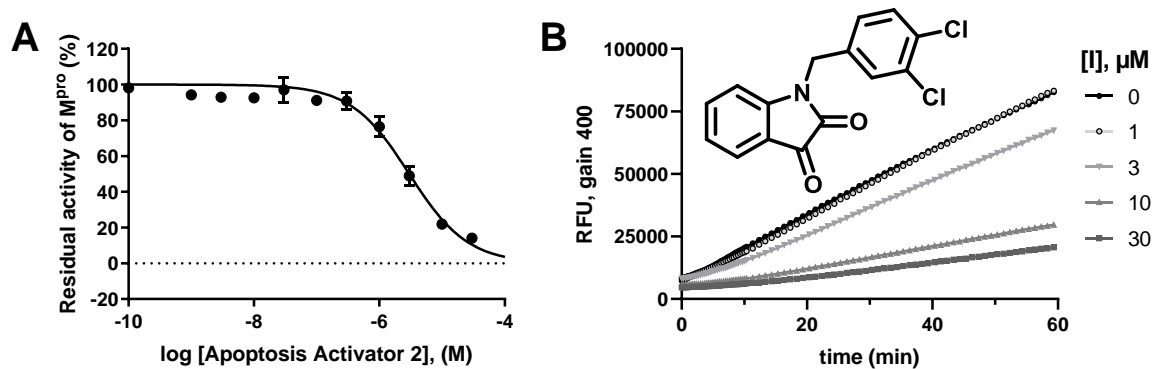
Apoptosis Activator 2 (**M-24**) was shown to induce apoptosis in tumor cells (IC<sub>50</sub> = 4 - 9 μM for leukemia cells). The isatin derivative likely has a non-covalent inhibition

mechanism at SARS-CoV-2 M<sup>pro</sup>, which should be further characterized by inhibition type studies (see **Figure 31**). On the preliminary assumption of a competitive inhibition type, a  $K_i$  value of 1.63  $\mu\text{M}$  was calculated with the Cheng-Prusoff equation. Isatin derivatives, which possess a similar structure to Apoptosis Activator 2 were first developed on SARS-CoV-1 M<sup>pro</sup>.<sup>209</sup> The SARs of isatin-related compounds *versus* SARS-CoV-2 M<sup>pro</sup> have been explored in a publication by Liu et al.<sup>210</sup> However, these compounds were shown to be cytotoxic, which impedes their *in vivo* application as M<sup>pro</sup> inhibitors.

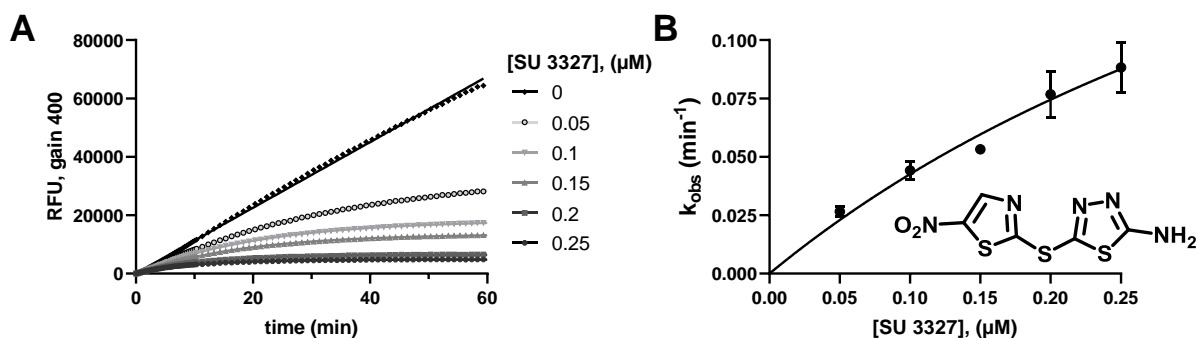
SU3327 (**M-27**) is an inhibitor of c-Jun N-terminal kinase (JNK) ( $\text{IC}_{50} = 0.7 \mu\text{M}$ ) and shows a time-dependent inhibition of M<sup>pro</sup> activity with a good initial inhibition characterized by an  $\text{IC}_{50}$  value of 0.174  $\mu\text{M}$  and permanent inhibition indicated by a high  $k_{\text{inac}}/K_i$  value of 16,900  $\text{M}^{-1}\text{s}^{-1}$  (see **Figure 32**). The compound was recently published as a potent SARS-CoV-2 M<sup>pro</sup> inhibitor under its alternative name halicin.<sup>243</sup> The study by Yang et al. confirmed the *in vitro* inhibitory potency of the nitrothiazole with an  $\text{IC}_{50}$  value of 0.1817  $\mu\text{M}$ . Furthermore, its covalent reaction with the active site Cys<sub>145</sub> was evidenced by native mass spectrometry and X-ray crystallography.<sup>243</sup> However, the compound showed no inhibition of M<sup>pro</sup> in cellular experiments, suggesting that it is lacking stability or cell permeability.<sup>243</sup>

**Table 16.** SARS-CoV-2 M<sup>pro</sup> inhibition results of hit compounds from the Tocris compound library; the  $K_i$  value for Apoptosis Activator 2 was calculated using the Cheng-Prusoff equation; and the  $K_i$  value of SU 3327 was derived from non-linear regression fit of  $k_{\text{obs}}$  *versus* [I]. Inhibition potency of INCA-6 could not be confirmed in follow-up experiments.

# M-	Name	Structure	Inhibitor at 10 $\mu\text{M}$ (%)	$\text{IC}_{50} \pm$ SEM ( $\mu\text{M}$ )	$K_i$ ( $\mu\text{M}$ )	$k_{\text{inac}}/K_i$ ( $\text{M}^{-1}\text{s}^{-1}$ )
24	Apoptosis Activator 2		69	3.31 $\pm$ 0.47	1.63	n.d.
25	INCA-6		(101)	> 10	-	n.d.
27	SU 3327		107	0.174 $\pm$ 0.067	0.294	16,900



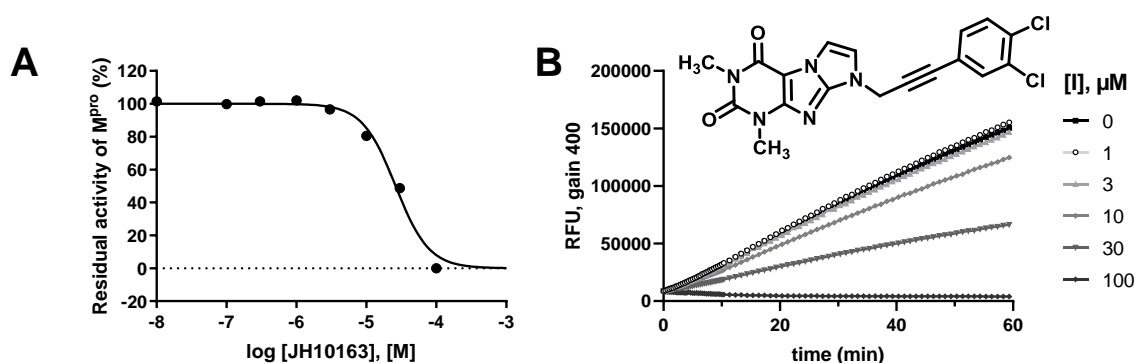
**Figure 31.** Inhibition of SARS-CoV-2 M<sup>pro</sup> by Apoptosis Activator 2 (**M-24**). **A.** Enzyme-catalyzed hydrolysis of 50 μM AMC-substrate in the absence or presence of increasing concentrations of inhibitor. **B.** Raw progression curves at selected concentrations. Straight lines indicate a non-covalent interaction of inhibitor and protease.



**Figure 32.** Time-dependent inhibition of SARS-CoV-2 M<sup>pro</sup> by SU3327 (**M-27**). **A.** Progression curves of enzyme-catalyzed hydrolysis of 50 μM AMC-substrate in the absence or presence of increasing concentrations of inhibitor. **B.** First-order rate constant  $k_{obs}$  is plotted *versus* the inhibitor concentrations and non-linear regression gave a  $k_{inac}/K_i$  value of 16,900 M<sup>-1</sup>s<sup>-1</sup>.

#### 4.4.2 Xanthine derivatives

The xanthine derivative **M-29** (JH10163, PZB00410075) was identified by virtual screening and published as an inhibitor of SARS-CoV-2 M<sup>pro</sup> by us.<sup>165</sup> Due to the straight progression curves during the observed first 60 minutes of the enzymatic substrate proteolysis, it was assumed, that this xanthine derivative binds reversibly to the M<sup>pro</sup> protein (see **Figure 33**).



**Figure 33.** Inhibition of SARS-CoV-2 M<sup>pro</sup> by **M-29** (JH10163, PZB00410075). **A.** Enzyme-catalyzed hydrolysis of 50 μM AMC-substrate in the absence or presence of increasing concentrations of inhibitor. **B.** Raw progression curves at selected concentrations. Straight lines indicate a non-covalent interaction of inhibitor and protease.

In order to assess the structure-activity relationships of M<sup>pro</sup> inhibition by this compound class, similar compounds were tested at 20 and 100 μM concentrations for their effect on the enzymatic activity. In fact, only two analogs were able to inhibit M<sup>pro</sup> in these experiments, namely **M-30** and **M-31** (see **Table 17**).

**Table 17.** SARS-CoV-2 M<sup>pro</sup> inhibition by xanthine derivatives

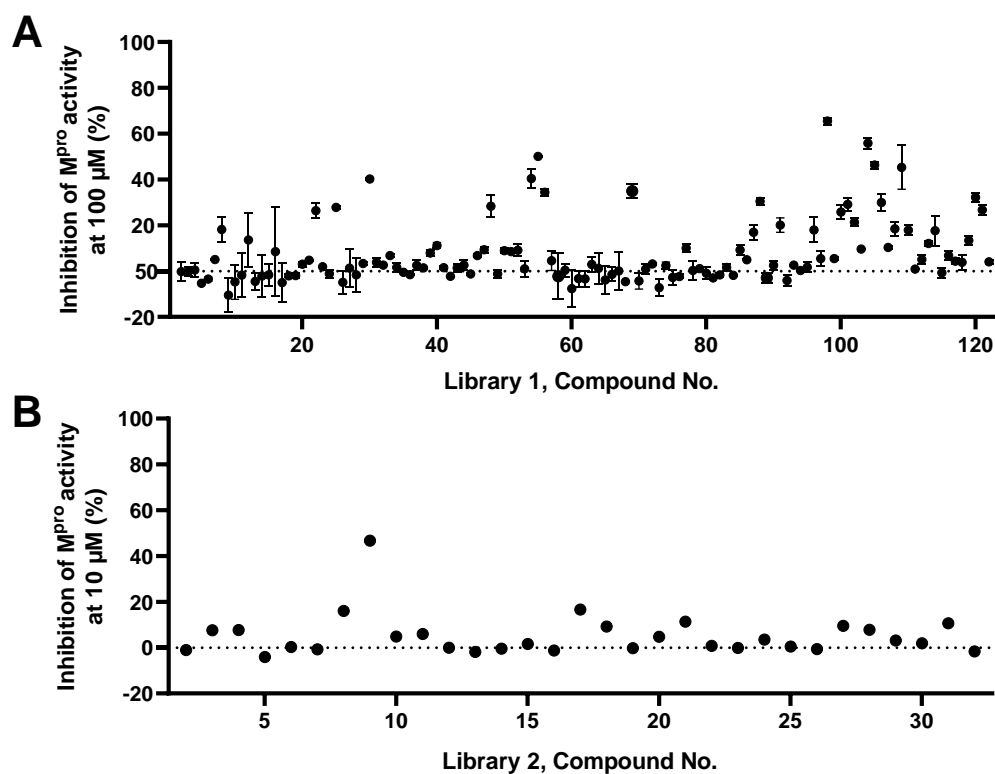
# M-	Internal ID PZB number	Structure	Inhibition (%) at 20 μM	Inhibition (%) at 100 μM	IC <sub>50</sub> ± SEM (μM)
29	JH10163 PZB00410075A		33	109	22.5 ± 0.5 165 / 35.2 ± 3.4 [a]
30	JH10153 PZB00410070A		33	96	18.1 ± 4.7 [a]
31	JH10141 PZB00410072A		-1	57	74.5 ± 4.3 [a]

[a] IC<sub>50</sub> values determined by Katharina Sylvester.

### 4.4.3 Apicidine derivatives

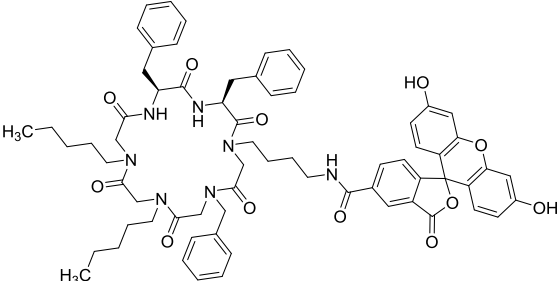
Two libraries were provided by a cooperation partner from the Karlsruhe Institute of Technology (KIT), Prof. Dr. Stefan Bräse. Three compounds inhibited the  $M^{pro}$  enzymatic activity by over 50 % in the initial screening at 100  $\mu\text{M}$  (see **Figure 34A** and **Table 18**). X15874 (**M-32**) and X10971 (**M-33**) showed inhibition values of 50 and 56 % respectively. The most potent inhibition was detected for the compound X12433 (**M-34**), which inhibited  $M^{pro}$  activity by 65 %. Interestingly, this compound was already found to be the most potent inhibitor from this series for human CD39 and further characterized to inhibit the CD39 enzyme showing a competitive inhibition type ( $K_i = 0.843 \mu\text{M}$ , data not shown). In the experiment with SARS-CoV-2  $M^{pro}$ , the overall fluorescence readout in the samples containing X12433 (**M-34**) was significantly lower (2-fold) compared to other control and compound samples. The compound could have an inner-filter effect, that may interfere with the  $M^{pro}$  activity assay. The CD39 malachite green activity assay was not impaired by X12433 (**M-34**). The absorptions at 600 nm subsequent to formation of the phosphomolybdate complex were identical for negative control samples containing the substrate ATP and denatured enzyme with or without addition of the test compound. Interestingly, compound X15874 (**M-32**), which contains a fluorescein moiety as part of its structure, did not interfere with the assay readout, likely due to distinct excitation and emission wavelengths from the AMC-substrate. The overall medium potency with expected  $IC_{50}$  values of approximately 100  $\mu\text{M}$  lead to the decision not to pursue these compounds further as inhibitors of SARS-CoV-2  $M^{pro}$ .

A second batch of compounds from the same cooperation partner was screened at a concentration of 10  $\mu\text{M}$  versus SARS-CoV-2  $M^{pro}$ . The compound **M-36** inhibited the  $M^{pro}$  enzyme activity by over 40 % in the screening, but it displayed an auto-fluorescence in the same range of the fluorogenic substrate, which can interfere with the assay results (see **Figure 34B** and **Table 18**). A similar observation was made for the structure-related compound **35**. The inhibition of these compounds could be reinvestigated with an LC/MS-based activity assay for  $M^{pro}$ , as the generation of complete concentration-inhibition curve with the fluorogenic substrate-based assay is not promising.

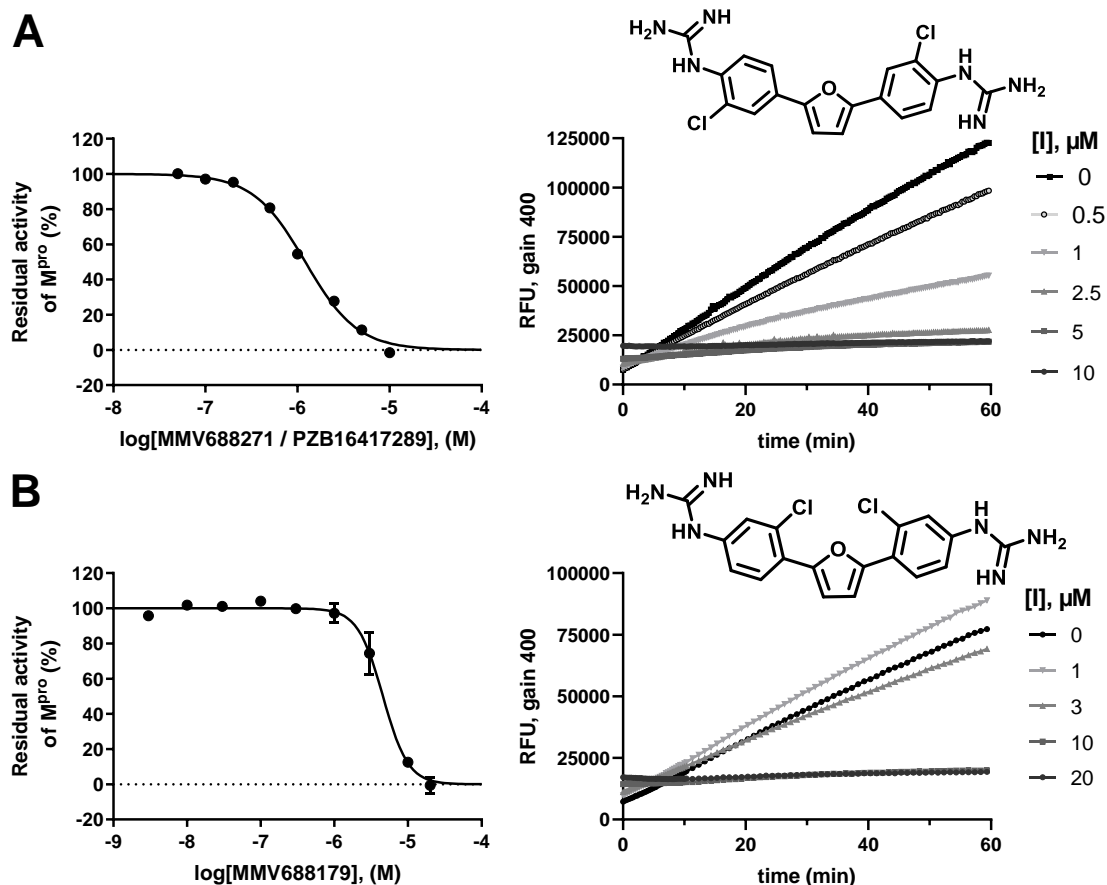


**Figure 34.** SARS-CoV-2  $M^{pro}$  inhibition of compounds from collaboration partner Prof. Bräse. **A.** Apicidine derivative library screening at 100  $\mu\text{M}$  ( $n=2$ ); **B.** Compounds from batch 2 at 10  $\mu\text{M}$  ( $n=1$ ); The enzyme activity assay was performed with the fluorogenic AMC-substrate at 50  $\mu\text{M}$  ( $K_m = 48.2 \mu\text{M}$ ) and pooled crude extract of recombinant His-tagged  $M^{pro}$ . The experiments were performed in collaboration with Marvin Petry.

**Table 18.** Structures of selected compounds from the apicidine derivative library and their inhibition potencies at SARS-CoV-2  $M^{pro}$  at 10  $\mu\text{M}$  ( $n=1$ ) or 100  $\mu\text{M}$  ( $n=2$ ).

# M-	Name	Structure	Inhibition (%) $\pm$ SEM	
			at 10 $\mu\text{M}$	at 100 $\mu\text{M}$
32	X15874		n.d.	50 $\pm$ 0 ( $IC_{50} \approx 100 \mu\text{M}$ )

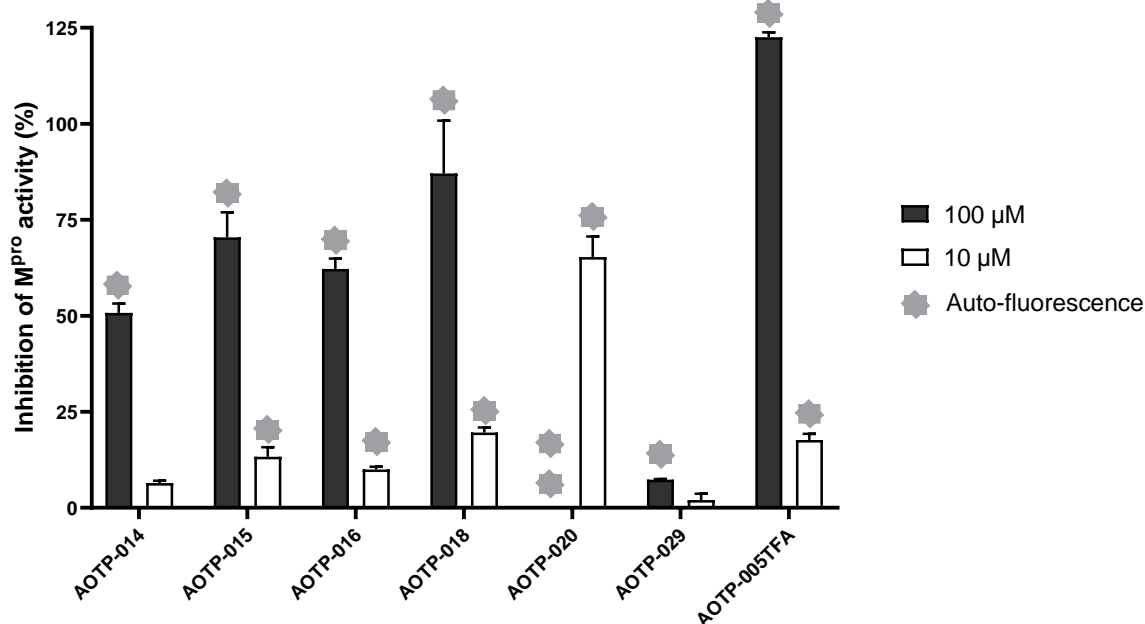




**Figure 35.** Inhibition of SARS-CoV-2  $M^{pro}$  by **A. M-10** (MMV688271) and **B. M-37** (MMV688179). Enzyme-catalyzed hydrolysis of 50  $\mu$ M AMC-substrate in the absence or presence of increasing concentrations of inhibitor. On the right-side representative progression curves are depicted. Straight lines indicate a non-covalent interaction of inhibitor and protease. The parallel increase of RFU at higher inhibitor concentration is due to auto-fluorescence.

The compounds were initially tested at 10 and 100  $\mu$ M (see **Figure 36**,  $n = 2$ ). At 10  $\mu$ M none of the compounds was able to inhibit the  $M^{pro}$  enzymatic activity by over 50 %. The compound **M-42** (AOTP-020) had an apparently greater inhibition, but as it possessed a high auto-fluorescence at the readout conditions of the assay ( $\lambda_{ex} = 360$  nm;  $\lambda_{em} = 460$  nm), this was considered an artifact. At 100  $\mu$ M of **M-42** the enzyme activity could not be determined, as the readout was out of range (relative fluorescence unit (RFU) > 260,000; control samples starting value at RFU 7,000 – 8,000).





**Figure 36.** SARS-CoV-2 M<sup>pro</sup> inhibition by guanidine derivatives. The enzyme activity assay was performed twice in duplicates ( $n = 2$ ) at 10 and 100  $\mu\text{M}$  with the fluorogenic AMC-substrate at 50  $\mu\text{M}$  ( $K_m = 48.2 \mu\text{M}$ ) and recombinant His-tagged SARS-CoV-2 M<sup>pro</sup>.

Therefore, the three compounds with the most promising inhibition values and medium auto-fluorescence were chosen for  $IC_{50}$  determination. The third repetition of the experiments was performed for over one hour in order to observe the course of the progression curves. Experiments were performed in collaboration with Katharina Sylvester. **M-10b** (batch AOTP-005TFA) had a 4-fold better potency than the previous batch (**M-10a**, AOTP-005). The auto-fluorescence was apparent at concentrations over 10  $\mu\text{M}$ . At 100 and 200  $\mu\text{M}$  the progression curves decrease over time (negative slopes) (see **Figure 37A**). The reason for this is so far unclear. Compounds **M-39** and **M-41** (AOTP-015 and -018) showed decreased potency of M<sup>pro</sup> inhibition (see **Figure 37B** and **C**). Interestingly, the core fragment **M-41** (AOTP-018) seems to be more vital for inhibition than the guanidine substituents.

In conclusion, some guanidine derivatives show moderate potency of SARS-CoV-2 M<sup>pro</sup> inhibition, but the auto-fluorescence impairs the assay readout. For future studies, the establishment of an alternative method, that does not rely on a fluorescence readout or uses distinct excitation and emission wavelengths, is recommended. For example, the degradation of an unlabeled substrate could be monitored by HPLC and mass

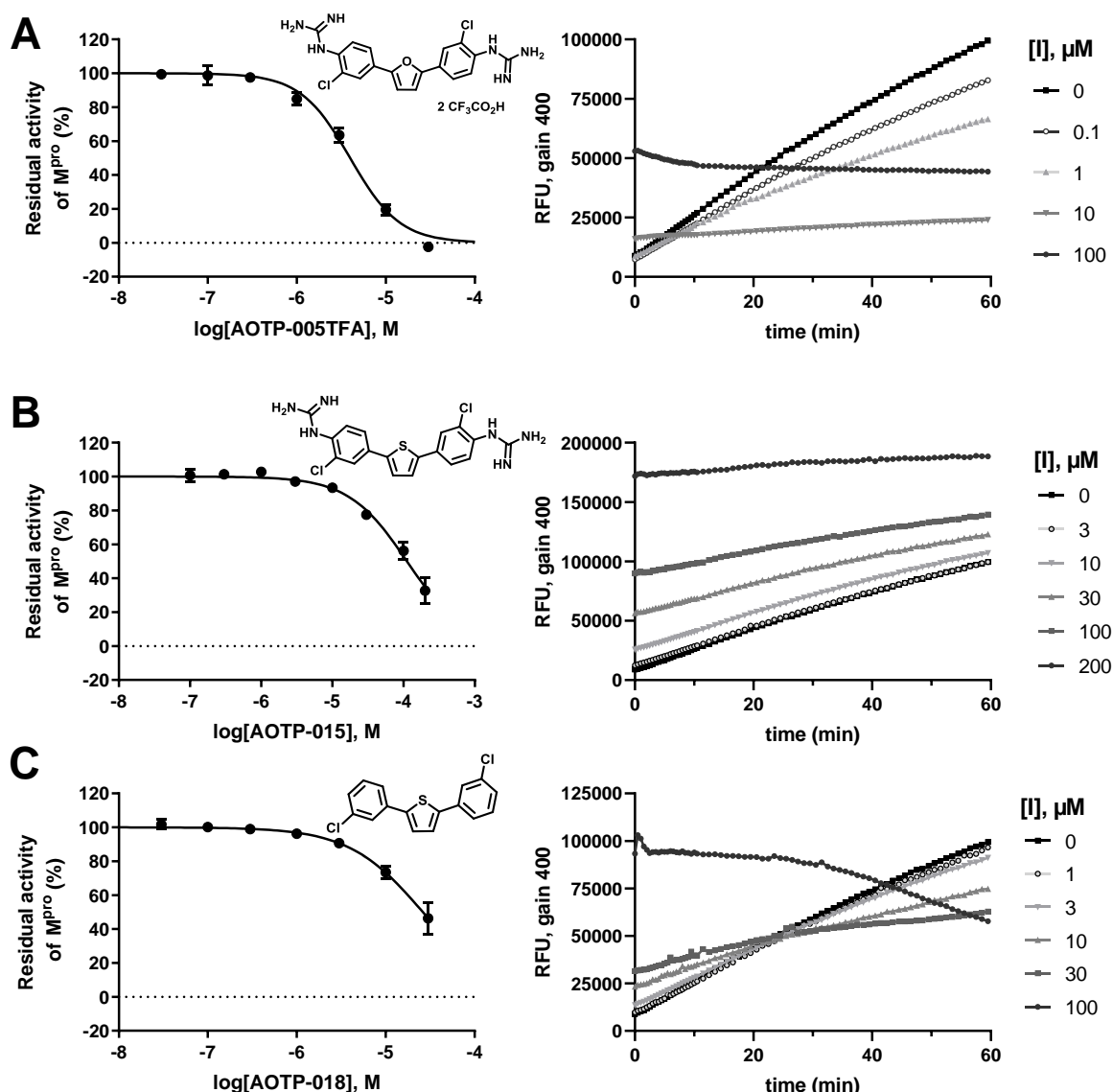
spectrometry or microscale thermophoresis (MST) could be performed (see section 2.3.4), since the inherent fluorescence of tryptophan is detected at an emission wavelength of 336 nm, which is much smaller than the emission setting for the AMC-substrate ( $\lambda_{\text{ex}} = 360 \text{ nm}$ ,  $\lambda_{\text{em}} = 460 \text{ nm}$ ).

**Table 19.** SARS-CoV-2 M<sup>pro</sup> inhibition results by guanidine derivatives

# M-	PZB-ID/ Internal-ID	Structure	Inhibitory activity (%) at 10 $\mu\text{M}$	Inhibitory activity (%) at 100 $\mu\text{M}$	IC <sub>50</sub> $\pm$ SEM ( $\mu\text{M}$ ) (n=3)
<b>Pathogen Box</b>					
37	PZB16417212 MMV688179		84	n.d.	4.15 $\pm$ 0.72
10	PZB16417289 MMV688271		100	n.d.	1.60 $\pm$ 0.16
<b>Synthesis</b>					
10a	AOTP-005		n.d.	n.d.	18.9 $\pm$ 1.3
10b	AOTP-005TFA		18 $\pm$ 2 [a]	123 $\pm$ 1 [a]	4.00 $\pm$ 0.53
		2 CF <sub>3</sub> CO <sub>2</sub> H			
38	AOTP-014		6 $\pm$ 1	51 $\pm$ 2 [a]	n.d.
39	AOTP-015 PZB18921107A		13 $\pm$ 3 [a]	70 $\pm$ 7 [a]	116 $\pm$ 16
40	AOTP-016		10 $\pm$ 1 [a]	62 $\pm$ 3 [a]	n.d.
41	AOTP-018 PZB18921108A		20 $\pm$ 1 [a]	87 $\pm$ 14 [a]	31.0 $\pm$ 8.1
42	AOTP-020 PZB18921109A		65 $\pm$ 5 [a]	out of range [a]	n.d.

# M-	PZB-ID/ Internal-ID	Structure	Inhibitory activity (%) at 10 $\mu\text{M}$	Inhibitory activity (%) at 100 $\mu\text{M}$	$\text{IC}_{50} \pm$ SEM ( $\mu\text{M}$ ) (n=3)
43	AOTP-029 PZB18921110A		$2 \pm 2$ [a]	$7 \pm 0$ [a]	n.d.

[a] Assay interference due to auto-fluorescence



**Figure 37.** Inhibition of SARS-CoV-2  $\text{M}^{\text{pro}}$  by **A. M-10b** (AOTP-005TFA); **B. M-39** (AOTP-015) and **C. M-41** (AOTP-018). Enzyme-catalyzed hydrolysis of 50  $\mu\text{M}$  AMC-substrate in the absence or presence of increasing concentrations of inhibitor. On the right-side representative progression curves are depicted. Straight lines indicate a non-covalent interaction of inhibitor and protease. The parallel increase of RFU at higher inhibitor concentration is due to auto-fluorescence.

## 4.5 M<sup>pro</sup> inhibition by pyridyl esters and related compounds

Previously reported SARS-CoV-1 inhibitors with a pyridyl ester warhead proved to be potent inhibitors of the SARS-CoV-2 M<sup>pro</sup> in the newly established *in vitro* activity assay, as well as in viral replication studies.<sup>165,190,191,205</sup>

### 4.5.1 Structure-activity relationship studies of pyridyl esters

Using the pyridyl ester structure as a starting point, the structure-activity relationships of the compounds were investigated by synthesis of pyridyl ester derivatives and additionally by variations of the leaving group. All the compounds were synthesized by Dr. Thanigaimalai Pillaiyar and Angelo Oneto. Some of the *in vitro* enzyme kinetics were determined by the master student Marvin Petry and Katharina Sylvester. The stability tests on HPLC and LC/MS instruments were performed by Mariam Tahoun with the help of the master student Chiara Molinar. The pretesting of the stability of compounds during incubation with glutathione is outlined in the next section (see 4.5.2).

As noted in section 4.2.4, the inhibition potency of pyridyl esters depends on the position of the carboxyl group. Therefore, the SARs are individually examined for each position.

Otherwise unsubstituted indole 2-carboxylic ester derivatives show differences in their respective potencies, depending on the substitution of the pyridyl ring. The initial binding affinity to the M<sup>pro</sup> active site is expressed by IC<sub>50</sub> values and increased in the following order of pyridyl ester substitution: Br  $\approx$  Cl > F  $\approx$  CH<sub>3</sub> > H (see **Table 20**, comp. **M-44** - **M-49**). The fluoropyridyl ester (**Table 20**, comp. **M-47**) has an increased reactivity towards the active M<sup>pro</sup> Cys<sub>145</sub>, as demonstrated by a high  $k_{inac}/K_i$  of 12,600 M<sup>-1</sup>s<sup>-1</sup>. However, it is ten times less potent in its initial binding to M<sup>pro</sup> compared to the chloro- or bromo-substituted analogs (IC<sub>50</sub> values **M-44** = 24.7 nM and **M-45** = 18.6 nM *versus* **M-47** = 239 nM) and seems to be promiscuous in its reactivity, since after one hour incubation with 1 mM GSH, only 0.25 % of the compound remained intact. Chloropyridyl esters displayed increased potency, represented by lower IC<sub>50</sub> values, depending on the heterocyclic ring substitution in the following ascending order NH < S < O (see **Table 20**, comp. **M-44**, **M-52**, **M-50**). However, only *N*-heterocycles lead to irreversible inhibition, while the *S*- and *O*-substituted derivatives merely form a fragile bond, resulting in reactivation of M<sup>pro</sup> activity over time.

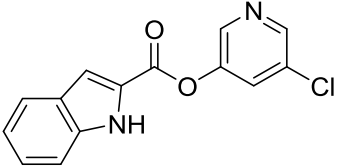
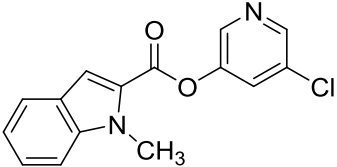
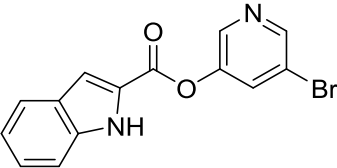
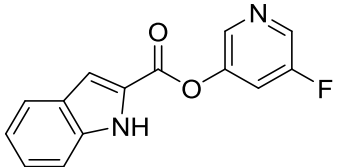
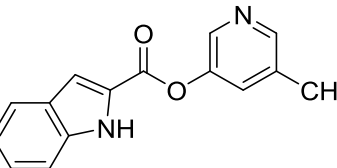
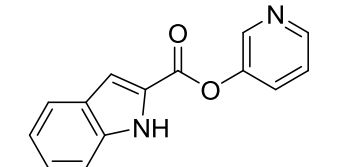
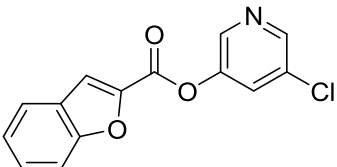
Small substituents in the 5-position did not significantly influence the inhibitory potency compared to the unsubstituted derivatives (see **Table 20**, comp. **M-54 - M-70**). Larger substituents, like methoxy or *O*-benzyl, were not tolerated (comp. **M-65** and **M-69**).

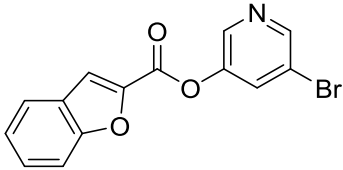
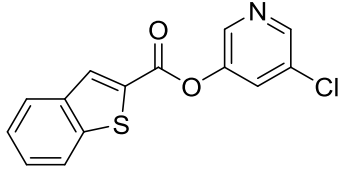
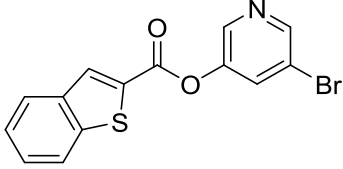
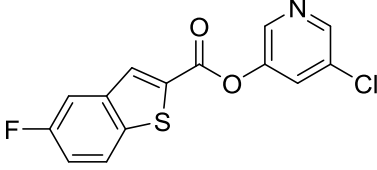
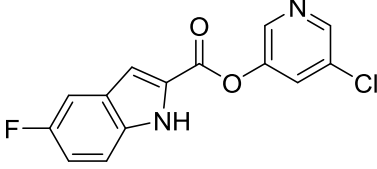
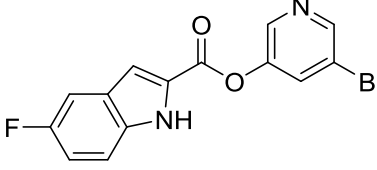
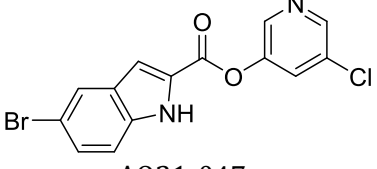
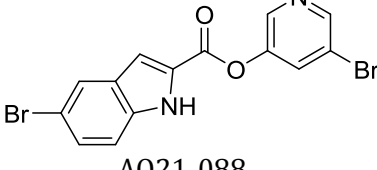
In contrast, substitution at the 6-position led to inhibitors with improved characteristics (see **Table 20**, comp. **M-71 - M-92**). The two compounds with the highest  $k_{\text{inac}}/K_i$  values combined with  $\text{IC}_{50}$  values in the nanomolar range share a substitution in the 6-position by a fluoro- or methyl group (comp. **M-72**  $\text{IC}_{50} = 10.4$  nM,  $k_{\text{inac}}/K_i = 99,900$   $\text{M}^{-1}\text{s}^{-1}$ ; comp. **M-87**  $\text{IC}_{50} = 10.5$  nM,  $k_{\text{inac}}/K_i = 104,000$   $\text{M}^{-1}\text{s}^{-1}$ ). Interestingly, *N*-methylation of 6-chloro and 6-bromo derivatives transformed them into irreversible inhibitors of  $\text{M}^{\text{pro}}$  (comp. **M-77/ M-78** vs **M-79/M-80**; comp. **M-81/M-82** vs **M-83/M-84**). The  $\text{IC}_{50}$  values of *N*-methylated derivatives were ten times higher compared to the NH indoles, but improved compared to the unsubstituted *N*-methylated derivative (comp. **M-45**). The stabilizing effect of 6-bromo-substitution also applied to 2-carboxylic ester thiophenes, which were characterized as potent irreversible inhibitors (comp. **M-86** and **M-87** vs **M-49**). Unlike in the 5-position, *O*-methyl and *O*-ethyl groups are tolerated in position 6 of the indole (comp. **M-89 - M-92**). This makes them suitable starting points for the development of labeled ligands, as a linker could potentially be attached at the same position.

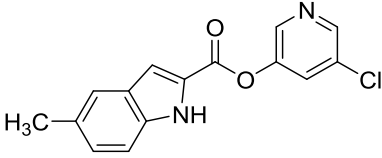
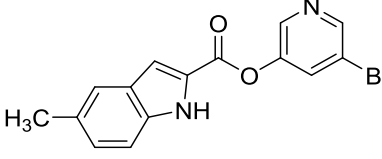
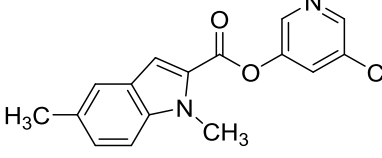
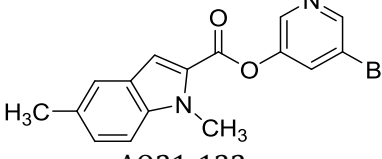
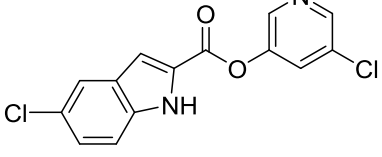
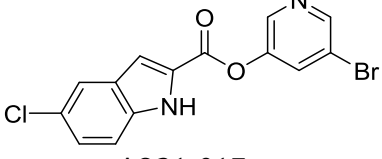
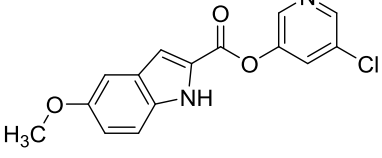
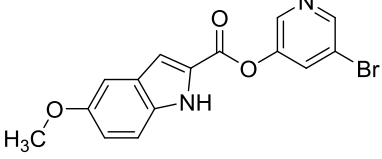
Substitutions at the 7-, 4- or 3-position lead to fragile inhibitors, that were not able to permanently inhibit  $\text{M}^{\text{pro}}$  activity (see **Table 20**, comp. **M-93 - M-95**; **M-97 - M-101**). The irreversibility was obtained for the 7-bromo derivative in combination with the *N*-methylation, but the inhibitory potency was not improved compared to the unsubstituted indoles (comp. **M-96** vs. **M-45**). The data for 4- and 7- substitution is similar due to a rotation of the 2-carboxylic bond resulting in comparable interactions with the binding pocket of  $\text{M}^{\text{pro}}$  (comp. **M-93** vs **M-100**).

The disubstitution did not improve inhibition characteristics (see **Table 20**, comp. **M-102 - M-104**). The 5,6-difluoro derivative was equivalent to the 5- or 6- monofluoro-substituted inhibitors (comp. **M-104** vs **M-54** or **M-71**).

**Table 20.** Investigated **2-carboxylic acid ester derivatives** and their SARS-CoV-2 M<sup>pro</sup> inhibitory potencies

# M-	Structure Internal identifier	IC <sub>50</sub> ± SEM (nM)	K <sub>i</sub> (nM) <sup>[a]</sup>	K <sub>inac.</sub> /K <sub>i</sub> (M <sup>-1</sup> s <sup>-1</sup> ) <sup>[b]</sup>	Progression curves / inhibition type <sup>[c]</sup>	Stable vs GSH <sup>[d]</sup>	Stability test rec. rate <sup>[e]</sup>
44	 Yazh-2K169	24.7 ± 4.4	169	7,600	bend down / covalent irreversible	no	-
45	 Yazh-2K212	327 ± 28	567	6800	bend down / covalent irreversible	no	-
46	 Yazh-2K208	18.6 ± 2.8	9.17	n.d.	Straight / ambiguous	yes	77 %
47	 Yazh-2K240	239 ± 49	106	12,600	bend down / covalent irreversible	no	0.25 %
48	 Yazh-2K235	284 ± 21	132	6,200	bend down / covalent irreversible	no	7.3 %
49	 Yazh-2K238	2,120	977	1,750	bend down / covalent irreversible	no	-
50	 Yazh-2K220	5.41 ± 0.3	-	-	curve up / covalent reversible (fragile)	no	-

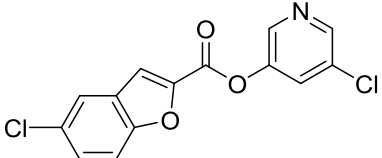
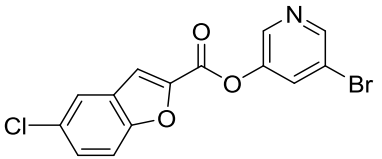
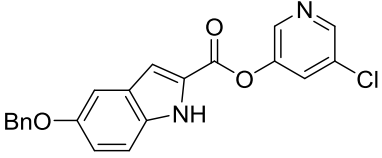
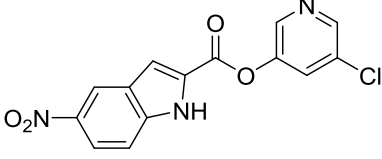
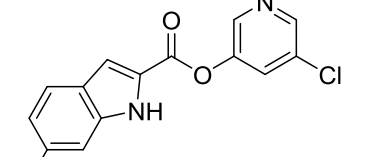
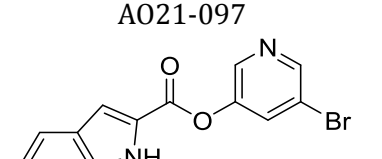
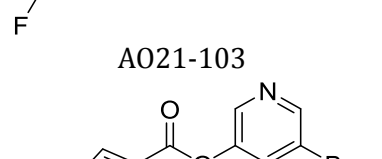
# M-	Structure Internal identifier	IC <sub>50</sub> ± SEM (nM)	K <sub>i</sub> (nM) [a]	k <sub>inac.</sub> /K <sub>i</sub> (M <sup>-1</sup> s <sup>-1</sup> ) [b]	Progression curves / inhibition type [c]	Stable vs GSH [d]	Stability test rec. rate [e]
51	 A021-086	11.5 ± 3.6	-	-	curve up / covalent reversible (fragile)	no	-
52	 Yazh-2K218	26.1 ± 5.1	-	-	curve up / covalent reversible (fragile)	yes	5 %
53	 A021-104	11.1 ± 1.9	-	-	Straight / ambiguous	yes	n.d.
54	 A021-150	23.4 ± 3.5	-	-	Straight / ambiguous	n.d.	-
55	 A021-029	17.4 ± 6.7	9.00	71,600	bend down / covalent irreversible	yes	5 %
56	 A021-107	9.10 ± 1.60	11.2	92,500	bend down / covalent irreversible	yes	-
57	 A021-047	22.3 ± 7.4	18.0	65,800	bend down / covalent irreversible	yes	24.8 %
58	 A021-088	23.8 ± 5.2	125	34,400	bend down / covalent irreversible	no	-

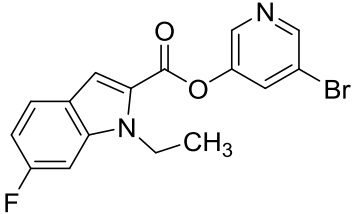
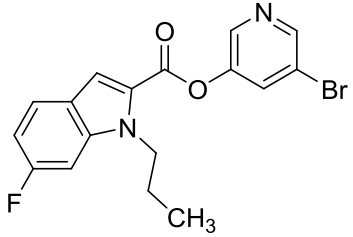
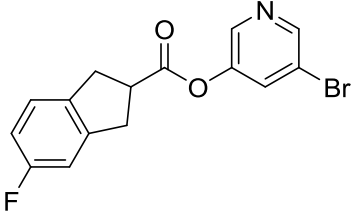
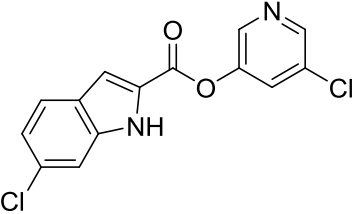
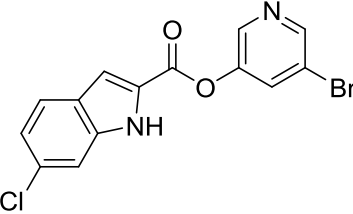
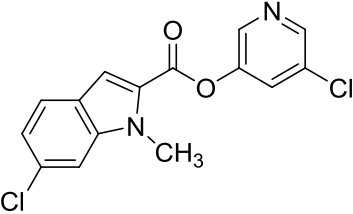
# M-	Structure Internal identifier	IC <sub>50</sub> ± SEM (nM)	K <sub>i</sub> (nM) [a]	k <sub>inac.</sub> /K <sub>i</sub> (M <sup>-1</sup> s <sup>-1</sup> ) [b]	Progression curves / inhibition type [c]	Stable vs GSH [d]	Stability test rec. rate [e]
59	 A021-028	44.0 ± 4.3	14.0	60,800	bend down / covalent irreversible	no	-
60	 A021-079	18.6 ± 4.4	-	-	Straight / ambiguous	yes	34 %
61	 A021-131	305 ± 47	223	13,000	bend down / covalent irreversible	no	-
62	 A021-132	290 ± 74	180	15,600	bend down / covalent irreversible	no	-
63	 Yazh-2K170	34.2 ± 2.1	70.2	29,000	bend down / covalent irreversible	yes	67 %
64	 A021-017	34.4 ± 3.2	19.0	57,500	bend down / covalent irreversible	no	-
65	 A021-025	208 ± 30.0	24.0	30,800	bend down / covalent irreversible	yes	6 %
66	 A021-078	93.5 ± 17	88.0	15,700	bend down / covalent irreversible	no	-



## 4.5 Mpro inhibition by pyridyl esters and related compounds

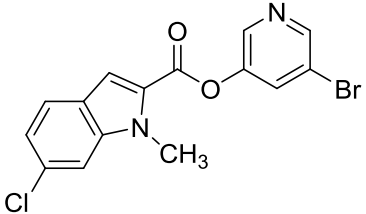
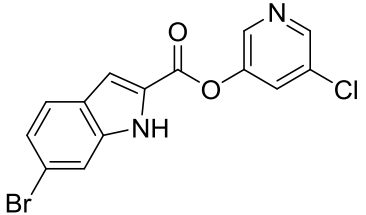
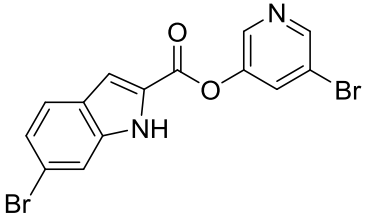
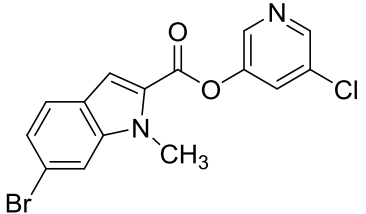
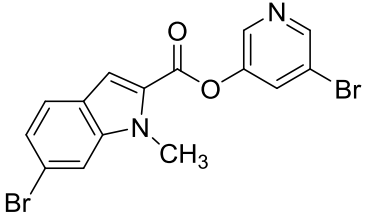
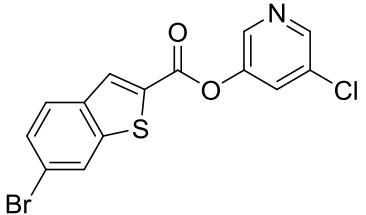
Dissertation, 2022

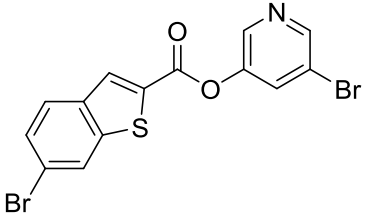
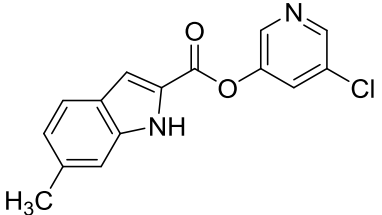
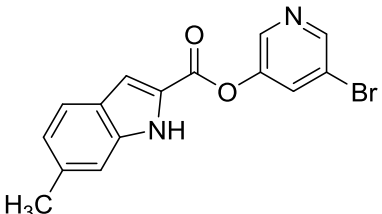
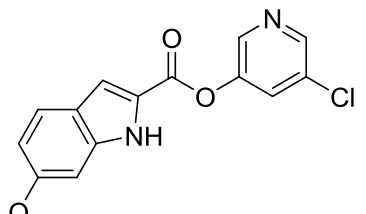
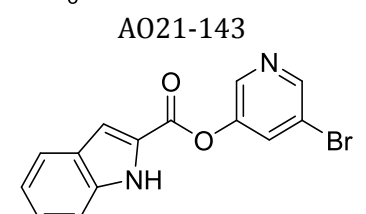
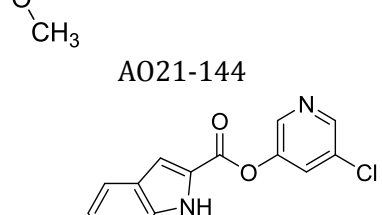
# M-	Structure Internal identifier	IC <sub>50</sub> ± SEM (nM)	K <sub>i</sub> (nM) [a]	k <sub>inac.</sub> /K <sub>i</sub> (M <sup>-1</sup> s <sup>-1</sup> ) [b]	Progression curves / inhibition type [c]	Stable vs GSH [d]	Stability test rec. rate [e]
67	 A021-077	9.35 ± 1	-	-	curve up / covalent reversible (fragile)	no	-
68	 A021-089	11.9 ± 2.2	-	-	curve up / covalent reversible (fragile)	no	-
69	 A021-048	>> 10 μM	-	-	Low potency (14 % inhibition at 10 μM)	n.d.	-
70	 A021-076	20.1 ± 3.8	-	-	curve up / covalent reversible (fragile)	n.d.	n.d.
71	 A021-097	21.1 ± 1.4	33.7	29,200	bend down / covalent irreversibl e	yes	43 %
72	 A021-103	10.4 ± 2.2	11.9	99,900	bend down / covalent irreversibl e	yes	-
73	 A021-156	255 ± 34	1292	13,400	bend down / covalent irreversibl e	n.d.	-

# M-	Structure Internal identifier	IC <sub>50</sub> ± SEM (nM)	K <sub>i</sub> (nM) [a]	k <sub>inac.</sub> /K <sub>i</sub> (M <sup>-1</sup> s <sup>-1</sup> ) [b]	Progression curves / inhibition type [c]	Stable vs GSH [d]	Stability test rec. rate [e]
74	 A021-157	2650 ± 640	602	3,190	bend down / covalent irreversible	n.d.	-
75	 A021-158	5170 ± 1350	2610	435	bend down / covalent irreversible	n.d.	-
76	 A021-160	259 ± 81	-	-	curve up / covalent reversible (fragile)	n.d.	-
77	 A021-035	16.1 ± 2.4	-	-	curve up / covalent reversible (fragile)	no	-
78	 A021-080	14.9 ± 3.7	-	-	curve up / covalent reversible (fragile)	yes	40 %
79	 A021-044	284 ± 41	195	16,400	bend down / covalent irreversible	yes	72 %

## 4.5 Mpro inhibition by pyridyl esters and related compounds

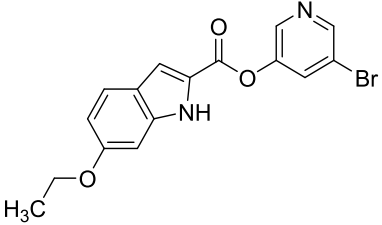
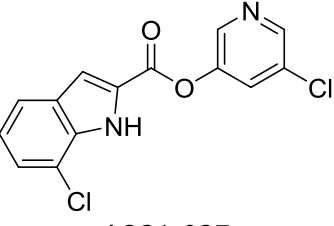
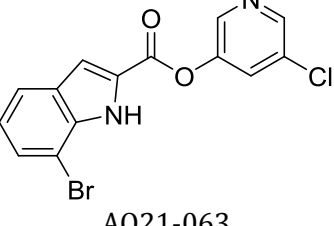
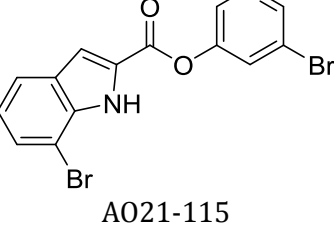
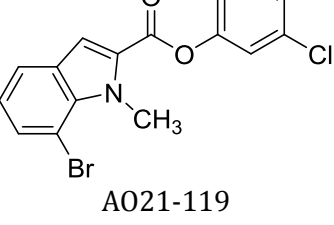
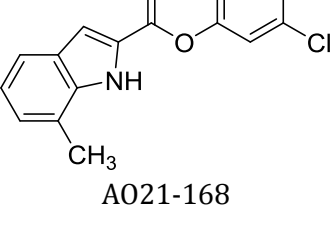
Dissertation, 2022

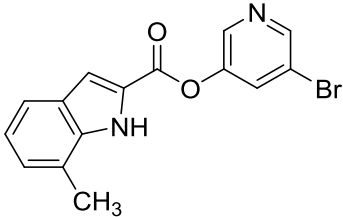
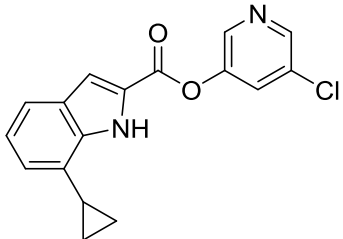
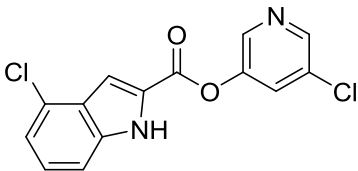
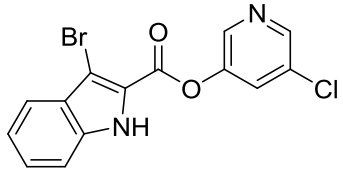
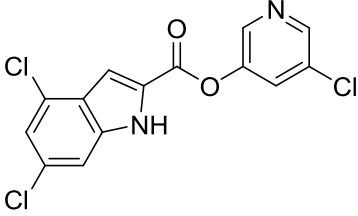
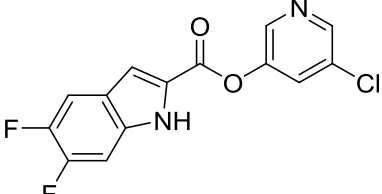
# M-	Structure Internal identifier	IC <sub>50</sub> ± SEM (nM)	K <sub>i</sub> (nM) [a]	k <sub>inac.</sub> /K <sub>i</sub> (M <sup>-1</sup> s <sup>-1</sup> ) [b]	Progression curves / inhibition type [c]	Stable vs GSH [d]	Stability test rec. rate [e]
80	 A021-120	125 ± 28	935	21,700	bend down / covalent irreversible	no	-
81	 A021-046	9.09 ± 1.7	-	-	curve up / covalent reversible (fragile)	yes	32 %
82	 A021-087	23.0 ± 7.8	-	-	Straight / ambiguous	n.d.	-
83	 A021-126	183 ± 9	344	18,000	bend down / covalent irreversible	no	-
84	 A021-127	140 ± 19	1621	16,300	bend down / covalent irreversible	no	-
85	 A021-149	24.8 ± 4.2	28.3	31,800	bend down / covalent irreversible	n.d.	-

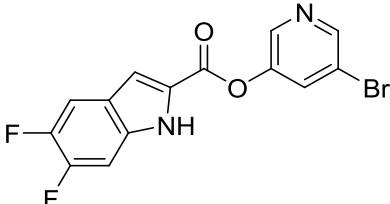
# M-	Structure Internal identifier	IC <sub>50</sub> ± SEM (nM)	K <sub>i</sub> (nM) [a]	k <sub>inac.</sub> /K <sub>i</sub> (M <sup>-1</sup> s <sup>-1</sup> ) [b]	Progression curves / inhibition type [c]	Stable vs GSH [d]	Stability test rec. rate [e]
86	 A021-171	31.9 ± 6.1	n.d.	25,300 ± 4,000 [f]	bend down / covalent irreversible	n.d.	-
87	 A021-102	10.5 ± 1.8	13.3	104,000	bend down / covalent irreversible	yes	-
88	 A021-102	11.6 ± 3.3	-	-	curve up / covalent reversible (fragile)	n.d.	-
89	 A021-138	76.3 ± 9.2	238	21,000	bend down / covalent irreversible	n.d.	-
90	 A021-143	104 ± 23	312	29,200	bend down / covalent irreversible	n.d.	-
91	 Yazh-2K274	196 ± 21	125	16,800	bend down / covalent irreversible	yes	85 %

## 4.5 Mpro inhibition by pyridyl esters and related compounds

Dissertation, 2022

# M-	Structure Internal identifier	IC <sub>50</sub> ± SEM (nM)	K <sub>i</sub> (nM) [a]	k <sub>inac.</sub> /K <sub>i</sub> (M <sup>-1</sup> s <sup>-1</sup> ) [b]	Progression curves / inhibition type [c]	Stable vs GSH [d]	Stability test rec. rate [e]
92	 A021-167	239 ± 63	234	17,200	bend down / covalent irreversible	n.d.	-
93	 A021-027	64.1 ± 21	-	-	curve up / covalent reversible (fragile)	yes	7.1 %
94	 A021-027	30.4 ± 1.7	-	-	curve up / covalent reversible (fragile)	yes	219 %
95	 A021-063	8.9 ± 2.24	-	-	Straight / ambiguous	yes	n.d.
96	 A021-115	391 ± 21	330	98,60	bend down / covalent irreversible	no	-
97	 A021-119 A021-168	88.0 ± 23.8	-	-	Straight / ambiguous	n.d.	-

# M-	Structure Internal identifier	IC <sub>50</sub> ± SEM (nM)	K <sub>i</sub> (nM) [a]	k <sub>inac.</sub> /K <sub>i</sub> (M <sup>-1</sup> s <sup>-1</sup> ) [b]	Progression curves / inhibition type [c]	Stable vs GSH [d]	Stability test rec. rate [e]
98	 A021-172	27.5 ± 5.7	-	-	Straight / ambiguous	n.d.	-
99	 A021-070	36.8 ± 14	-	-	curve up / covalent reversible (fragile)	yes	66 %
100	 A021-026	62.3 ± 14	-	-	curve up / covalent reversible (fragile)	yes	47 %
101	 A021-075	92.7 ± 21.1	-	-	curve up / covalent reversible (fragile)	n.d.	-
102	 Yazh-2K171	23.3 ± 6.3	-	-	curve up / covalent reversible (fragile)	n.d.	-
103	 A021-121	12.4 ± 3.5	75.6	85,300	bend down / covalent irreversible	no	-

# M-	Structure Internal identifier	IC <sub>50</sub> ± SEM (nM)	K <sub>i</sub> (nM) [a]	k <sub>inac</sub> /K <sub>i</sub> (M <sup>-1</sup> s <sup>-1</sup> ) [b]	Progression curves / inhibition type [c]	Stable vs GSH [d]	Stability test rec. rate [e]
104	 <p>A021-139</p>	18.0 ± 3.4	-	-	Straight / ambiguous	n.d.	-

Abbreviations: cPr = cyclopropyl; Bn = benzyl; Et = ethyl; n.d. = not determined; (-) not applicable

[a]  $K_i$  was determined by plotting  $k_{obs}$  versus  $[I]$  and non-linear regression using the equation  $k_{obs} = (k_{inac} \times [I]) / ([I] + K_i \times (1 + [S]/K_m))$ .

[b] The second-order rate constant,  $k_{inac}/K_i$ , was determined by plotting  $k_{obs}$  versus  $[I]$  and non-linear regression using the equation  $k_{obs} = (k_{inac} \times [I]) / ([I] + K_i \times (1 + [S]/K_m))$ . Deviation of each data point from the calculated non-linear regression was less than 10%.

[c] Compounds display time-dependent inhibition, but if progression curves bend upwards, this indicates that the inhibitor covalently binds to the enzyme and then dissociates again, so the enzyme activity is restored. Consequently, the inhibitor concentration decreases over time as it is degraded and the enzyme is no longer inhibited. This compound can only be characterized by its IC<sub>50</sub> value.

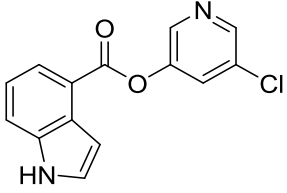
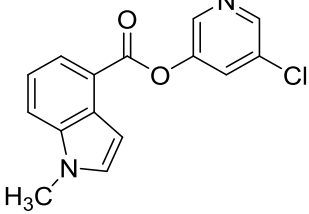
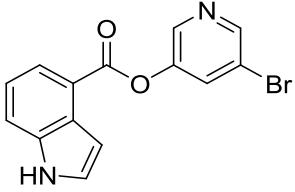
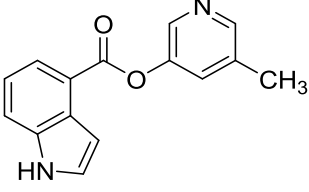
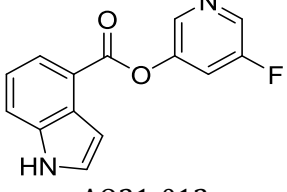
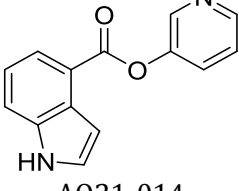
[d] Residual inhibition potency versus SARS-CoV-2 M<sup>pro</sup> after 1h incubation in assay buffer with 1 mM glutathione (GSH). Compounds labeled with yes keep at least 75 % inhibition potency compared to the non-incubated compounds at 1 μM.

[e] Stability measured by LC/MS or HPLC by Mariam Tahoun and Chiara Molnar. The compounds were incubated in PBS-buffer with 1 mM GSH for 1 h at 37 °C. The given percentage corresponds to the remaining amount of compound comparing the measurements at time 0 and after 1h.

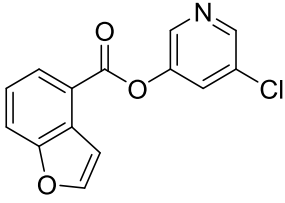
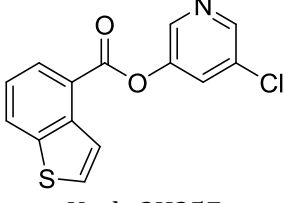
[f] The second-order rate constant of irreversible enzyme inhibition,  $k_{inac}/K_i$ , was determined by plotting  $k_{obs}$  versus  $[I]$  and correcting the slope with the equation  $k_{inac}/K_i = (1 + [S]/K_m) \times k_{obs}/[I]$ . The standard error (SE) refers to the linear regression.

Variations to the 4-carboxylindole pyridyl ester are collected in **Table 21**. *N*-methylation and bromo-substitution on the pyridyl ring had little influence on the moderate inhibitory potency of the chloropyridyl lead structure (comp. **M-106** - **M-108**). In analogy to the 2-carboxylic ester derivatives, methyl-, or fluoro-substituted or unsubstituted pyridyl rings lead to less potent inhibitors with higher IC<sub>50</sub> values (comp. **M-109** - **M-111**). Remarkably, the benzofurane of this series was an irreversible inhibitor of M<sup>pro</sup> with medium potency (comp. **M-112**), while the inhibition mode of the benzothiopene derivative could not be clearly deduced from the shape of its product formation progression curves (comp. **M-113**).

**Table 21.** Investigated 4-carboxylic acid ester derivatives and their SARS-CoV-2 M<sup>pro</sup> inhibitory potencies

# M-	Structure Internal identifier	IC <sub>50</sub> ± SEM (nM)	K <sub>i</sub> (nM) [a]	k <sub>inac.</sub> /K <sub>i</sub> (M <sup>-1</sup> s <sup>-1</sup> ) [b]	Progression curves / inhibition type [c]	Stable vs GSH [d]	Stability test rec. rate [e]
106	 Yazh-2K164	312 ± 15	98.3	14,800	bend down / covalent irreversible	yes	65 %
107	 A021-064	137 ± 47	359	13,400	bend down / covalent irreversible	no	-
108	 Yazh-2K166	227 ± 7	64.9	24,000	bend down / covalent irreversible	yes	63 %
109	 A021-011	3090 ± 80	927	1,450	bend down / covalent irreversible	no	-
110	 A021-012	1027 ± 110	161	6,067	bend down / covalent irreversible	no	-
111	 A021-014	≈ 10 μM	-	-	Low potency (51 % inhibition at 10 μM)	no	-

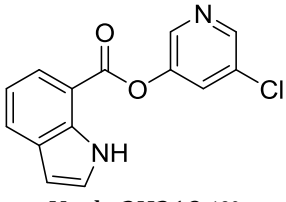


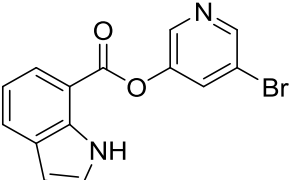
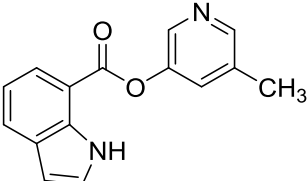
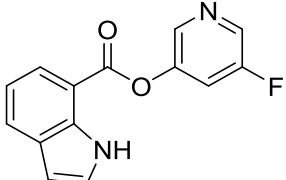
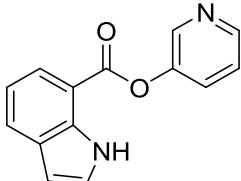
# M-	Structure Internal identifier	IC <sub>50</sub> ± SEM (nM)	K <sub>i</sub> (nM) [a]	k <sub>inac</sub> /K <sub>i</sub> (M <sup>-1</sup> s <sup>-1</sup> ) [b]	Progress- ion curves / inhibition type [c]	Stable vs GSH [d]	Stabi- lity test rec. rate [e]
112	 Yazh-2K250	127 ± 15	129	9,030	bend down / covalent irreversible	no	-
113	 Yazh-2K257	61.0 ± 8	-	-	Straight / ambiguous	no	-

For descriptions see **Table 20**.

For 7-carboxylic acid esters, the substitution of the pyridine esters was investigated (see **Table 22**). This led to the same observations as with other isomeric carboxylic acid esters ( $IC_{50}$ : Cl  $\approx$  Br < F < CH<sub>3</sub> < H;  $k_{inac}/K_i$ : Br > Cl > F > CH<sub>3</sub> > H). The bromopyridyl derivative possesses a secondary inhibition constant, which is 2-fold higher than that of the chloropyridyl derivatives (comp. **M-116** vs **M-117**), while initial affinities are similar with IC<sub>50</sub> values of 55.5 and 60.5 nM respectively.

**Table 22.** Investigated 7-carboxylic acid ester derivatives and their SARS-CoV-2 M<sup>pro</sup> inhibitory potencies

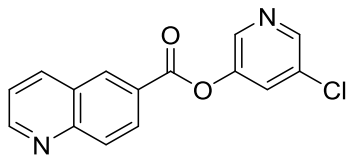
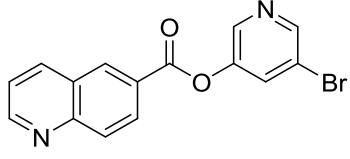
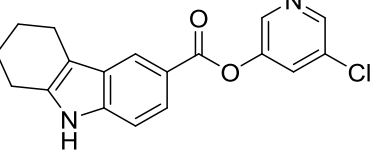
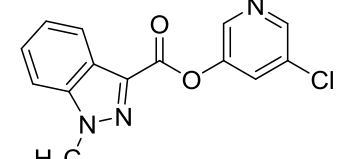
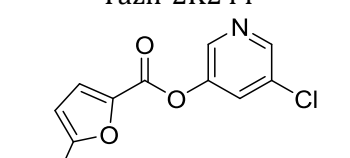
# M-	Structure Internal identifier	IC <sub>50</sub> ± SEM (nM)	K <sub>i</sub> (nM) [a]	k <sub>inac</sub> /K <sub>i</sub> (M <sup>-1</sup> s <sup>-1</sup> ) [b]	Progress- ion curves / inhibition type [c]	Stable vs GSH [d]	Stabi- lity test rec. rate [e]
116	 Yazh-2K219 <sup>190</sup>	55.5 ± 0.7	-	22,000 ± 800 [f]	bend down / covalent irreversible	yes	0.5 %

# M-	Structure Internal identifier	IC <sub>50</sub> ± SEM (nM)	K <sub>i</sub> (nM) [a]	k <sub>inac.</sub> /K <sub>i</sub> (M <sup>-1</sup> s <sup>-1</sup> ) [b]	Progression curves / inhibition type [c]	Stable vs GSH [d]	Stability test rec. rate [e]
117	 AO21-004	60.5 ± 7.7	28.0	44,000	bend down / covalent irreversible	yes	42.6 %
118	 AO21-006	1,250 ± 60	678	3,100	bend down / covalent irreversible	no	-
119	 AO21-007	401 ± 9	134	9,800	bend down / covalent irreversible	no	-
120	 AO21-009	5,550 ± 640	510	1,800	bend down / covalent irreversible	no	-

For descriptions see **Table 20**.

The combination of halogenated pyridylesters with other heteroaromatic esters was considered and realized by the synthesis of the compounds collected in **Table 23**. No potent irreversible inhibitors were identified with exception of the tetrahydrocarbazol derivative, that exhibits improved inhibition of M<sup>pro</sup> compared to the 5-carboxylic indole ester (comp. **M-123** (PZB10620065A) vs **M-114** (PZB10620024)).<sup>165</sup>

**Table 23.** Investigated **heteroaromatic ester derivatives** and their SARS-CoV-2 M<sup>pro</sup> inhibitory potencies

# M-	Structure Internal identifier	IC <sub>50</sub> ± SEM (nM)	K <sub>i</sub> (nM) [a]	k <sub>inac</sub> /K <sub>i</sub> (M <sup>-1</sup> s <sup>-1</sup> ) [b]	Progression curves / inhibition type [c]	Stable vs GSH [d]	Stability test rec. rate [e]
121	 Yazh-2K247	144 ± 7	-	-	Straight / ambiguous	no	-
122	 A021-109	46.9 ± 9.4	-	-	Straight / ambiguous	yes	n.d.
123	 Yazh-2K213	354 ± 9	401	5,260	bend down / covalent irreversible	no	-
124	 Yazh-2K244	274 ± 5	-	-	curve up / covalent reversible (fragile)	no	-
125	 Yazh-2K249	43.5 ± 10.2	-	-	curve up / covalent reversible (fragile)	no	-

For descriptions see **Table 20**.

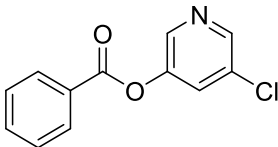
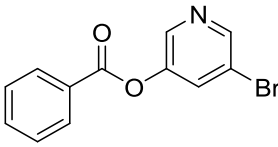
Finally, benzoic acid ester derivatives proved to be an interesting alternative to the indole carboxylates (see **Table 24**). The unsubstituted benzoic acid esters had a good binding affinity to M<sup>pro</sup> with IC<sub>50</sub> values of 40.4 and 40.5 nM, respectively (Comp. **M-126** and **M-127**). But only combination with the bromopyridyl resulted in an irreversible inhibition with a k<sub>inac</sub>/K<sub>i</sub> value of 3450 M<sup>-1</sup>s<sup>-1</sup> (comp. **M-127**). Addition of a chlorine atom in the 2-position doubles this value, while the IC<sub>50</sub> value remains constant (comp. **M-130**). Among the 2-substituted benzoic acid esters, the 2-methoxy substituted compound is a

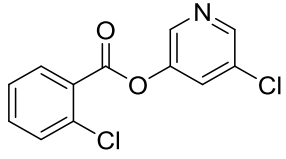
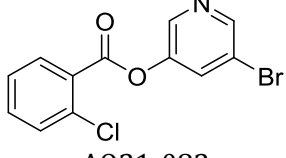
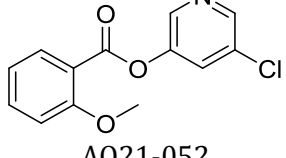
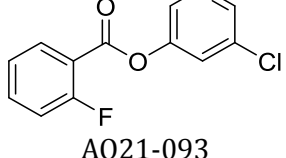
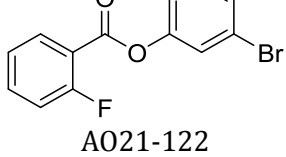
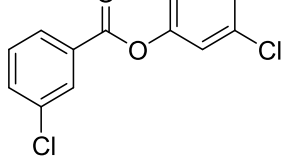
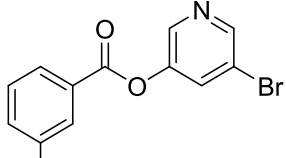
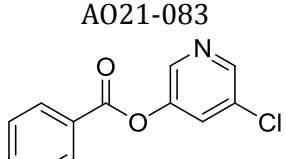
promising inhibitor, as it exhibits medium inhibition constants and remains partly stable upon incubation with glutathione (comp. **M-130**, recovery rate = 47.5 %).

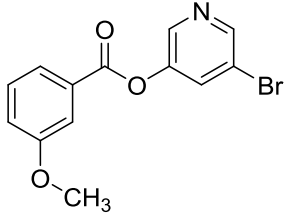
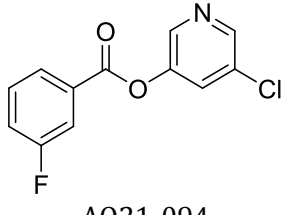
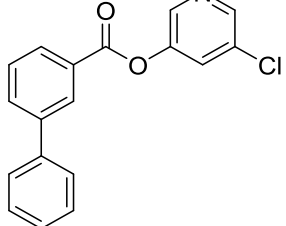
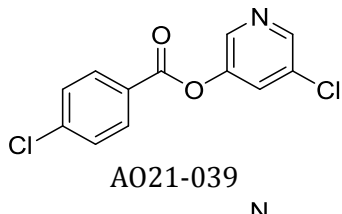
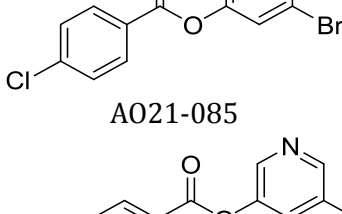
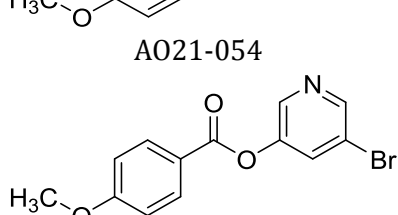

All of the 3-substituted benzoic acid esters were not able to irreversibly inhibit M<sup>pro</sup> regardless of pyridyl substitution (comp. **M-133** - **M-138**). In contrast, substitution in the 4-position yielded irreversible inhibitors (comp. **M-139** - **M-144**). Interestingly, the bromopyridyl derivatives of 4-chloro and 4-methoxy benzoic acid esters had two-fold higher affinity and  $k_{\text{inac}}/K_i$  values compared to the respective chloropyridyl analogs (comp. **M-139** vs **M-140** and **M-141** vs **M-142**).

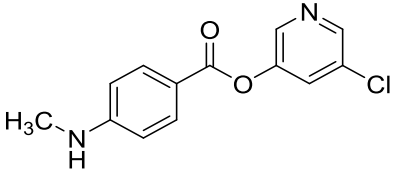
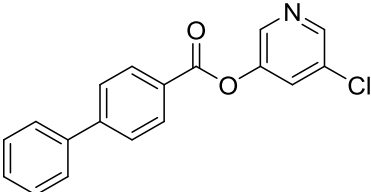
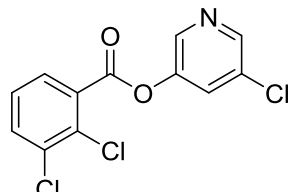
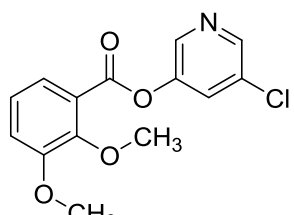
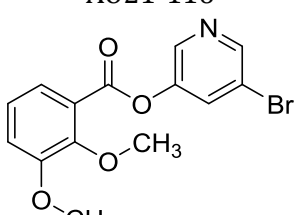
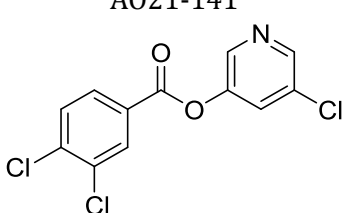
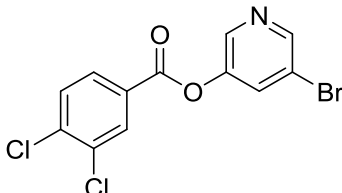
Disubstitution of the phenyl ring mostly resulted in stable covalent inhibition of M<sup>pro</sup> (comp. **M-145** - **M-165**). Notable exceptions to this observation are 3,5-di-chloro and 3,5-di-fluoro derivatives (comp. **M-163**, **M-164**). Benzoic acid ester substitution of 2-fluoro in combination with 4-chloro generated the most potent disubstituted derivative, with comparable potencies to the potent 2-carboxylic acid indole esters (comp. **M-154**  $\text{IC}_{50}$  = 35.6 nM;  $k_{\text{inac}}/K_i$  = 131,000  $\text{M}^{-1}\text{s}^{-1}$  compare to **Table 20** comp. **M-72** and **M-87**). Larger substituents at position 4, like a benzyl ether, led to decreased potency (comp. **M-156**, **M-157**).

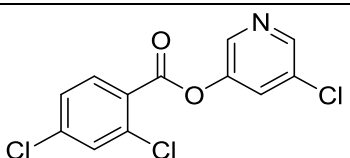
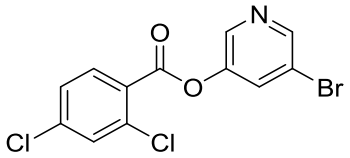
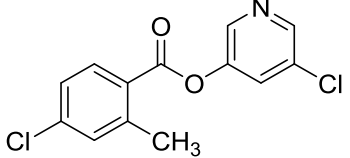
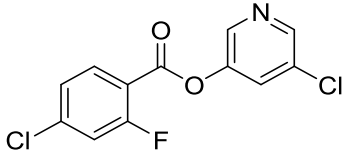
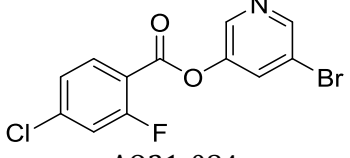
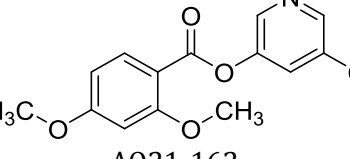
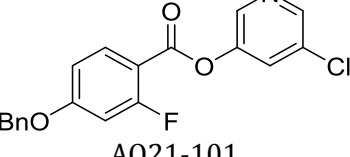
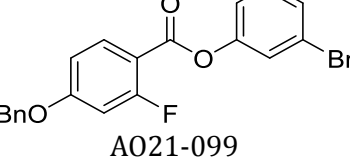
**Table 24.** Investigated **benzoic acid ester derivatives** and their SARS-CoV-2 M<sup>pro</sup> inhibitory potencies

# M-	Structure Internal identifier	$\text{IC}_{50}$ ± SEM (nM)	$K_i$ (nM) [a]	$k_{\text{inac}}/K_i$ ( $\text{M}^{-1}\text{s}^{-1}$ ) [b]	Progress- ion curves / inhibition type [c]	Stable vs GSH [d]	Stabi- lity test rec. rate [e]
126	 A021-019	40.4 ± 13.3	-	-	curve up / covalent reversible (fragile)	no	-
127	 A021-081	40.5 ± 5.2	123	3,450	bend down / covalent irreversible	yes	2.4 %

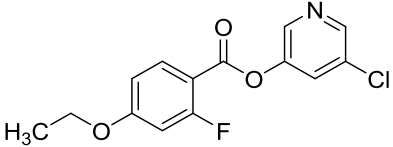
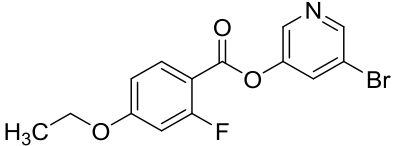
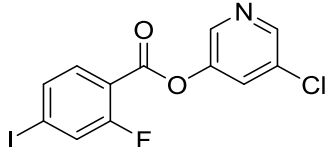
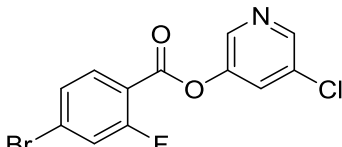
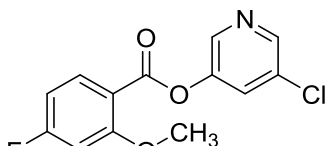
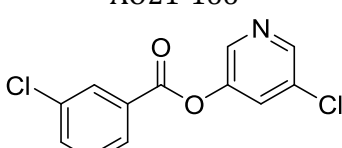
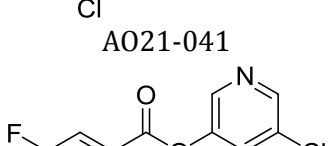
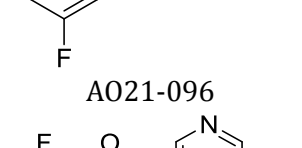
# M-	Structure Internal identifier	IC <sub>50</sub> ± SEM (nM)	K <sub>i</sub> (nM) [a]	k <sub>inac</sub> /K <sub>i</sub> (M <sup>-1</sup> s <sup>-1</sup> ) [b]	Progression curves / inhibition type [c]	Stable vs GSH [d]	Stability test rec. rate [e]
128	 A021-020	60.4 ± 15.6	-	-	curve up / covalent reversible (fragile)	no	-
129	 A021-082	39.2 ± 9.3	80	6,700	bend down / covalent irreversible	no	-
130	 A021-052	264 ± 47	141	16,100	bend down / covalent irreversible	yes	47.5 %
131	 A021-093	25.9 ± 5.2	-	-	curve up / covalent reversible (fragile)	no	-
132	 A021-122	10.7 ± 2.0	-	-	Straight / ambiguous	no	-
133	 A021-022	55.1 ± 16.3	-	-	curve up / covalent reversible (fragile)	no	-
134	 A021-083	50.5 ± 11	-	-	curve up / covalent reversible (fragile)	no	-
135	 A021-053	5.1 ± 0.6	-	-	curve up / covalent reversible (fragile)	yes	27.2 %

# M-	Structure Internal identifier	IC <sub>50</sub> ± SEM (nM)	K <sub>i</sub> (nM) [a]	k <sub>inac.</sub> /K <sub>i</sub> (M <sup>-1</sup> s <sup>-1</sup> ) [b]	Progression curves / inhibition type [c]	Stable vs GSH [d]	Stability test rec. rate [e]
136	 A021-108	19.9 ± 4.6	-	-	Straight / ambiguous	yes	-
137	 A021-094	46.4 ± 7.6	-	-	Straight / ambiguous	no	-
138	 Yazh-2K254	117 ± 21	-	-	curve up / covalent reversible (fragile)	no	-
139	 A021-039	218 ± 30	76	18,700	bend down / covalent irreversible	no	-
140	 A021-085	95.7 ± 5.7	184	26,500	bend down / covalent irreversible	yes	
141	 A021-054	164 ± 59	274	13,900	bend down / covalent irreversible	yes	68 %
142	 A021-140	96.3 ± 19.4	169	26,700	bend down / covalent irreversible	n.d.	-

# M-	Structure Internal identifier	IC <sub>50</sub> ± SEM (nM)	K <sub>i</sub> (nM) [a]	k <sub>inac</sub> /K <sub>i</sub> (M <sup>-1</sup> s <sup>-1</sup> ) [b]	Progression curves / inhibition type [c]	Stable vs GSH [d]	Stability test rec. rate [e]
143	 A021-161	3,940 ± 1,100	3580	11,70	bend down / covalent irreversible	n.d.	-
144	 A021-129	150 ± 26	1579	19,300	bend down / covalent irreversible	no	-
145	 A021-040	126 ± 11	5.96	46,000	bend down / covalent irreversible	yes	1.3 %
146	 A021-116	84.5 ± 27.1	60.8	37,300	bend down / covalent irreversible	yes	n.d.
147	 A021-141	78.2 ± 24.3	363	35,300	bend down / covalent irreversible	n.d.	-
148	 A021-021	96.4 ± 28.3	5.83	56,500	bend down / covalent irreversible	yes	0.3 %
149	 A021-114	37.5 ± 9.9	-	-	Straight / ambiguous	yes	n.d.

# M-	Structure Internal identifier	IC <sub>50</sub> ± SEM (nM)	K <sub>i</sub> (nM) [a]	k <sub>inac</sub> /K <sub>i</sub> (M <sup>-1</sup> s <sup>-1</sup> ) [b]	Progression curves / inhibition type [c]	Stable vs GSH [d]	Stability test rec. rate [e]
150	 Yazh-2K273	108 ± 15	104	17,500	bend down / covalent irreversible	no	-
151	 A021-018	84.5 ± 31	13.0	47,300	bend down / covalent irreversible	no	-
152	 A021-037	3,400 ± 560	974	1,700	bend down / covalent irreversible	no	-
153	 A021-038	45.7 ± 8.2	17.0	56,700	bend down / covalent irreversible	no	-
154	 A021-084	35.6 ± 2.7	11.0	131,000	bend down / covalent irreversible	no	-
155	 A021-162	1,670 ± 180	1750	2,320	bend down / covalent irreversible	n.d.	-
156	 A021-101	322 ± 28	490	11,400	bend down / covalent irreversible	no	-
157	 A021-099	232 ± 24	290	14,800	bend down / covalent irreversible	no	-

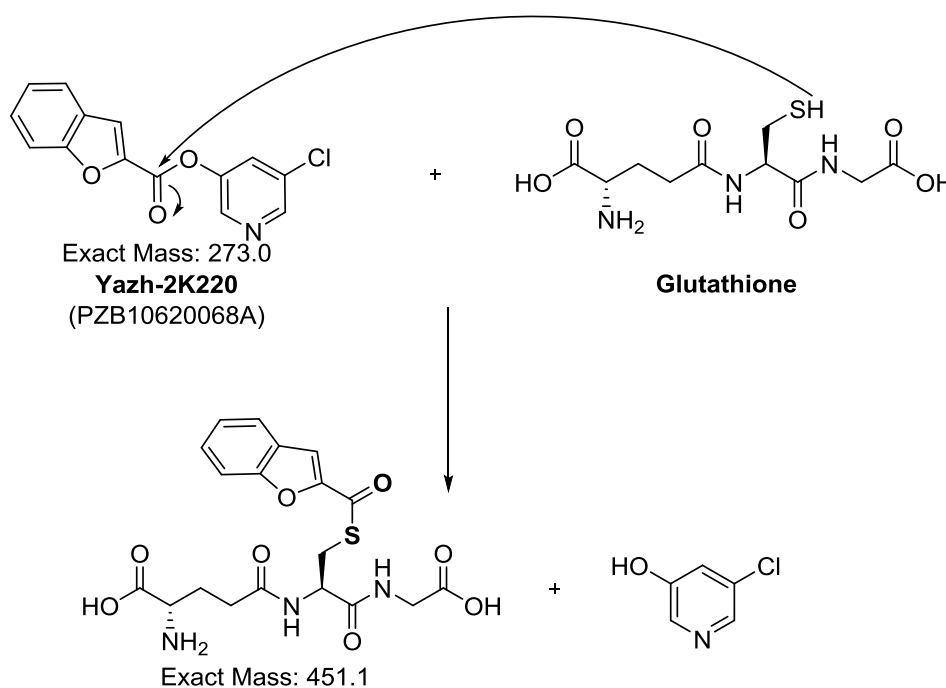


# M-	Structure Internal identifier	IC <sub>50</sub> ± SEM (nM)	K <sub>i</sub> (nM) [a]	k <sub>inac</sub> /K <sub>i</sub> (M <sup>-1</sup> s <sup>-1</sup> ) [b]	Progression curves / inhibition type [c]	Stable vs GSH [d]	Stability test rec. rate [e]
158	 A021-110	47.4 ± 8.4	64.4	51,600	bend down / covalent irreversible	yes	n.d.
159	 A021-145	107 ± 34	277	28,100	bend down / covalent irreversible	yes	n.d.
160	 A021-111	15.3 ± 3.5	74.1	84,400	bend down / covalent irreversible	yes	n.d.
161	 A021-112	34.9 ± 8.8	24.8	71,800	bend down / covalent irreversible	no	-
162	 A021-166	249 ± 45	403	10,200	bend down / covalent irreversible	n.d.	-
163	 A021-041	133 ± 8	-	-	curve up / covalent reversible (fragile)	no	-
164	 A021-096	38.3 ± 7.9	-	-	curve up / covalent reversible (fragile)	no	-
165	 A021-095	29.2 ± 4.8	45.7	7,160	bend down / covalent irreversible	no	-

For descriptions see **Table 20**.

#### 4.5.2 Stability of pyridyl esters towards glutathione

The applied stability test is an assay, which aims to evaluate the stability of compounds with electrophilic warheads to promiscuous reaction with intracellular reduced glutathione (GSH). GSH is an endogenous antioxidant, a tripeptide that consists of the amino acids glutamine, cysteine and glycine. It is present in almost all cells of the human body; hence potential intracellularly active drugs must be unreactive towards this compound. The compound of interest is incubated for 1 hour in the presence of 5 or 1 mM of GSH at a concentration of 100  $\mu$ M in nucleophile free phosphate-buffered saline (PBS) at a pH of 7.4 and 37°C. The pH must be adjusted at this concentration and temperature as the nucleophilic properties are pH-dependent. The potential reaction mechanism of pyridyl esters with GSH is depicted in **Figure 38**. The compound concentration is analyzed by HPLC or LC/MS before and after the incubation period, and a recovery rate is determined. The stability tests were performed by PhD-Student Mariam Tahoun and the master student Chiara Molinar, and results are included in **Table 20** to **Table 24**. On account of the time intensiveness of this assay, a quicker, HTS-suitable alternative to the LC/MS-based stability test was developed in order to pre-test the stability of the M<sup>pro</sup> inhibitors.

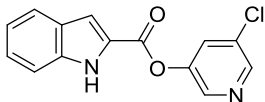
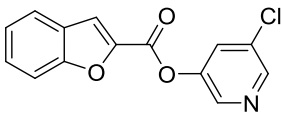
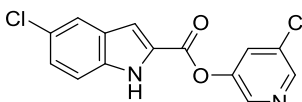


**Figure 38.** Reaction mechanism of pyridyl esters with GSH for the example of **M-50** (Yazh-2K220 / PZB10620068A)

**Exploratory studies of M<sup>pro</sup> activity in the presence of GSH**

Initially, the activity of His-tagged M<sup>pro</sup> in the presence of GSH and inhibitors with known stabilities was tested. The enzymatic activity was tested in the absence or presence of GSH at 0.05, 0.1, 0.5, 1.0, and 5.0 mM concentration. The inhibitors **M-63** (Yazh-2K170 / PZB10620022) and **M-50** (Yazh-2K220 / PZB10620068A) were chosen for the first test series due to their different recovery rates in the LCMS stability test performed by Mariam Tahoun (see **Table 25**).

**Table 25.** Overview of selected pyridyl esters

# M-	Compound	Structure	IC <sub>50</sub> (nM)	K <sub>i</sub> (nM)	k <sub>inac</sub> /K <sub>i</sub> (M <sup>-1</sup> s <sup>-1</sup> )	Recovery rate [a]
44	Yazh 2K169 PZB10620021		24.7	16.9	7600	n.d.
50	Yazh-2K220 PZB10620068A		5.41	-	n.d. [b]	0 % [c]
63	Yazh 2K170 PZB10620022		34.2	70.2	29100	67 %

[a] Compounds were incubated at 100  $\mu$ M with 1 mM L-glutathione (GSH) in nucleophile-free phosphate-buffered saline (PBS; 137 mM NaCl, 2.7 mM KCl, 12 mM PO<sub>4</sub><sup>2-</sup>, adjusted to pH 7.4 at 37°C) for 1h at 37°C. Zero-time and 1h measurements were carried out on an Agilent 1260 Infinity II HPLC system coupled to InfinityLab LC/MSD mass spectrometer with an ESI source. The mobile phase consisted of acetonitrile (A) and water + 2 mM ammonium acetate (B). The method started with 10% A and 90% B. The linear gradient reached 100% (A) after 10 min. This was maintained for 5 min, then the column was reconditioned. The flow rate was 0.5 mL/min and the column temperature was 40°C. 4  $\mu$ L were injected on the column EC 50/3 NUCLEODUR C18 Gravity, 3  $\mu$ m (Macherey-Nagel, Düren, Germany). Positive and negative scan modes were observed in the mass spectrometer from 150 to 1200 m/z. The compounds were identified by their respective m/z values ( $\pm$  0.70). Peak areas from zero time and after 1 h were calculated from extracted ion chromatograms by the software OpenLab CDS version 2.5 and compared.

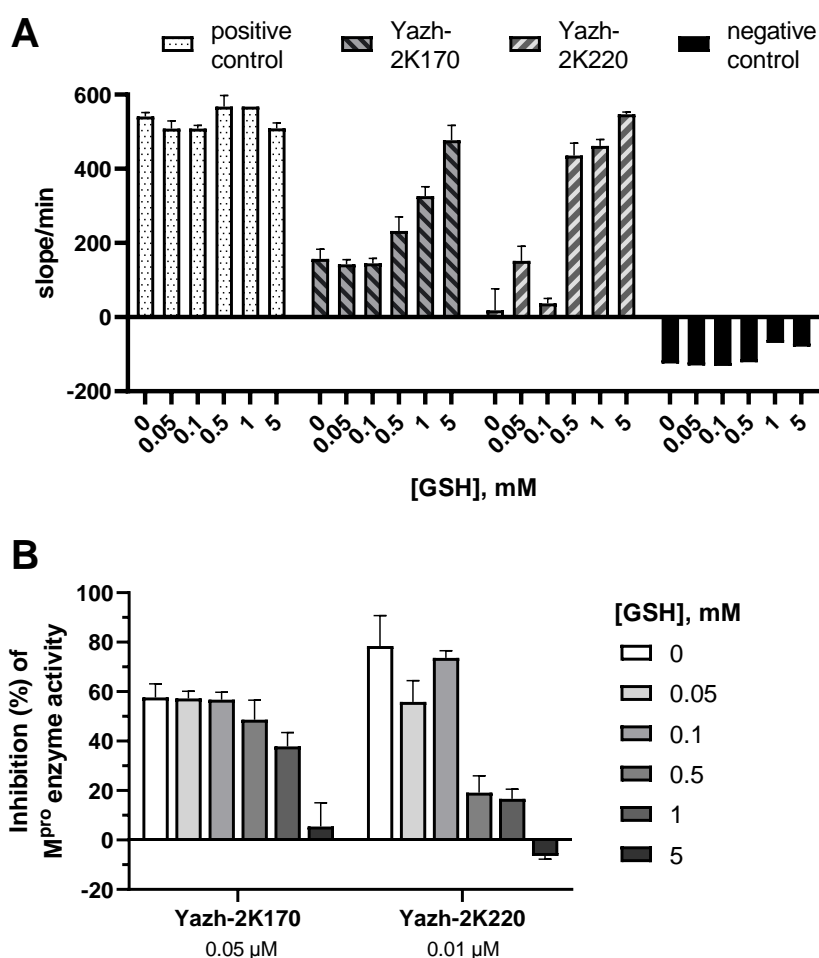
[b] Compound displayed time-dependent inhibition, but progression curves bend upwards, which indicates that the inhibitor covalently binds to the enzyme and then dissociates again, so the enzyme activity is restored. Consequently, the inhibitor concentration decreases over time as it is degraded and the enzyme is no longer inhibited. This compound can only be characterized by its IC<sub>50</sub> value.

[c] The respective m/z value could not be found in the zero-time and 1 h measurement.

The experiment was performed with concentrations of the inhibitors set at an expected inhibition of 50-90% SARS-CoV-2 M<sup>pro</sup> enzyme activity in order to easily observe concentration changes of the inhibitor that would result in a reduced potency.

The enzymatic activity of the positive control sample without inhibitors was not affected by the presence of GSH at the chosen concentration range of 0.05 – 5 mM (see **Figure 39A**), while the ability of both compounds to inhibit  $M^{\text{pro}}$  was affected by the addition of GSH (see **Figure 39A** and **B**). However, the potency of inhibition by **M-63** (Yazh-2K170) was less reduced at > 0.5 mM GSH compared to that by **M-50** (Yazh-2K220).

This preliminary experiment demonstrated that the enzyme activity-assay could be adapted to a stability screening assay, that enables the preselection of compounds to be further evaluated by the stability test using LCMS.

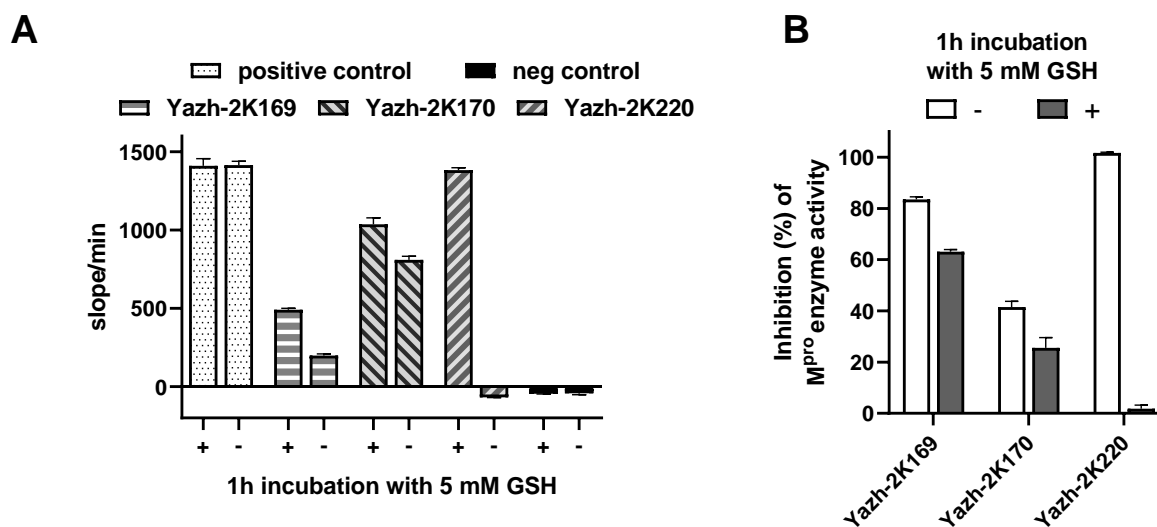


**Figure 39. A.** SARS-CoV-2  $M^{\text{pro}}$  activity determination with glutathione (GSH) and pyridyl ester type inhibitors. The enzymatic activity assay was performed in duplicates ( $n = 1$ ) with the fluorogenic AMC-substrate at 50  $\mu\text{M}$  ( $K_m = 48.2 \mu\text{M}$ ) and with purified extract of recombinant His-tagged SARS-CoV-2  $M^{\text{pro}}$ . **B.** Relative inhibition of  $M^{\text{pro}}$  enzymatic activity by 0.05  $\mu\text{M}$  **M-63** (Yazh-2K170) and 0.01  $\mu\text{M}$  **M-50** (Yazh-2K220) in the presence of GSH. The product formation rate of the uninhibited control was set at 100%, and samples without enzyme addition were set at 0%, and the inhibition activity of test compounds was determined in relation.

### Development of an HTS compatible dilution assay

On the basis of the preliminary experiment, an HTS compatible pipetting scheme was tested for three known M<sup>pro</sup> inhibitors (see **Table 25**). The inhibitors were incubated for 60 min at a concentration of 100  $\mu$ M with or without 5 mM GSH and then diluted to an assay concentration of 1  $\mu$ M. This ensures a significant inhibition of M<sup>pro</sup> for potent inhibitors, and a standardized pipetting scheme.

The effect of incubation with GSH is most prominent on **50** (Yazh-2K220), which already was shown to be very reactive towards GSH in the previous LC/MS-based test (see **Table 25**). In contrast, **M-44** and **M-63** (Yazh-2K169 and -170) partially retained their ability to inhibit M<sup>pro</sup> activity (see **Figure 40**). In conclusion, this experiment presents proof of concept for the application on a wide selection of M<sup>pro</sup> inhibiting compounds, in order to make a preselection for subsequent sophisticated stability-testing of the recovery rate by LC/MS.



**Figure 40.** **A.** SARS-CoV-2 M<sup>pro</sup> activity determination with GSH and pyridyl ester inhibitors. The enzyme activity assay was performed in duplicates ( $n = 1$ ) with the fluorogenic AMC-substrate at 50  $\mu$ M ( $K_m = 48.2$   $\mu$ M), and with purified extract of recombinant His-tagged SARS-CoV-2 M<sup>pro</sup>. The pyridyl esters were incubated at 100  $\mu$ M with or without 5 mM GSH for 1h at 37°C, then diluted to a final concentration of 1  $\mu$ M compound and 50  $\mu$ M GSH in the enzyme activity assay. **B.** Relative inhibition of M<sup>pro</sup> enzymatic activity by **M-44**, **M-63** and **M-50** (Yazh-2K169, -170 and Yazh2K220) at 1  $\mu$ M with or without 1h of incubation with 5 mM GSH. The product formation rate of the uninhibited control was set to 100% and samples without enzyme addition were set at 0%, the inhibition activity of test compounds was determined in relation.

### HTS stability testing of SARS-CoV-2 M<sup>pro</sup> inhibitors versus GSH

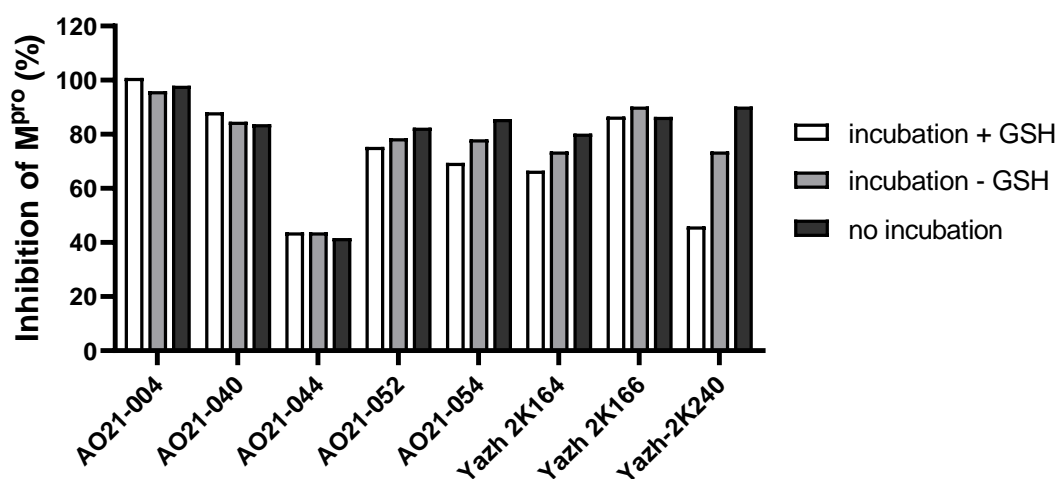
In this HTS stability pretesting the activity of His-tagged M<sup>pro</sup> after incubation with 1 mM GSH was assessed for inhibitors of interest. For this purpose, the inhibitory potency of each inhibitor was tested under three conditions: (i) 100  $\mu$ M compound incubated with 1 mM GSH for 1 h at 37°C in assay buffer; (ii) 100  $\mu$ M compound incubated for 1 h at 37°C in assay buffer (without GSH) and (iii) 100  $\mu$ M compound prepared immediately before dilution and enzymatic activity assay.

The samples were subsequently diluted with assay buffer to a final compound concentration of 1  $\mu$ M and the respective inhibitory potencies were tested with the established assay.<sup>165</sup> The concentrations of the inhibitors were set at an equal concentration of 1  $\mu$ M in order to enable a simple test realization. The chosen concentration should ensure both high inhibition of the non-incubated control, as well as the identification of concentration decreases by means of a reduced inhibitory potency.

The ability of some compounds to inhibit M<sup>pro</sup> was affected by the addition of 1 mM GSH, suggesting a reaction with the thiol group that abrogates the compound's ability to inhibit the enzyme. The inhibition for few compounds was also reduced by mere incubation in assay buffer without GSH, which indicates an instability due to hydrolysis. Compounds, which lost 25% of inhibitory potency in relation to the inhibition of the non-incubated samples were considered as unstable (labeled 'no' in **Table 20** to **Table 24**). With the help of this HTS stability prescreening, compounds were recommended for further stability evaluation by the stability test conducted with LC/MS or HPLC-UV methods. Examples of recommended compounds with their respective recovery rates are presented in **Table 26** and **Figure 41**.

**Table 26.** Example of results from HTS stability prescreening with 1 mM GSH of pyridyl esters and the respective recovery rates determined in the stability test using LC/MS.

# M-	Internal ID	$IC_{50}$ [nM]	Inhibition (%) at 1 $\mu$ M w/o incubation	Relative loss of inhibition after incubation in assay buffer (%)	Relative loss of inhibition after incubation in assay buffer with 1 mM GSH (%)	Results of LCMS stability test: Recovery rate (%)
117	A021-004	60.5	98	2	-3	42.5
145	A021-040	126	84	-1	-5	1.3
79	A021-044	284	42	-5	-5	72
130	A021-052	264	82	5	9	47.5
141	A021-054	164	86	9	19	68
106	Yazh 2K164	312	80	8	17	65
108	Yazh 2K166	227	86	-4	0	63
47	Yazh-2K240	239	90	18	49	0.25

**Figure 41.** Examples of SARS-CoV-2 M<sup>pro</sup> activity determination after incubation of 100  $\mu$ M pyridyl ester inhibitors with or without 1 mM glutathione (GSH) at 37°C for 1h in assay buffer. The incubated samples were diluted 1:20 and the enzymatic activity was determined in singlicates (n = 1) with the fluorogenic AMC-substrate at 50  $\mu$ M ( $K_m$  = 48.2  $\mu$ M) and the purified extract of recombinant His-tagged SARS-CoV-2 M<sup>pro</sup>, respectively. The enzymatic activity of the uninhibited control was set at 100% and samples without enzyme addition were set at 0%. The inhibition activity of non-incubated test compounds at 1  $\mu$ M was determined in relation. The experiments for the first batch of compounds, tested with this method, were performed by Laura Schäkel with assistance by Chiara Molinar. A second batch of compounds was tested by Marvin Petry.

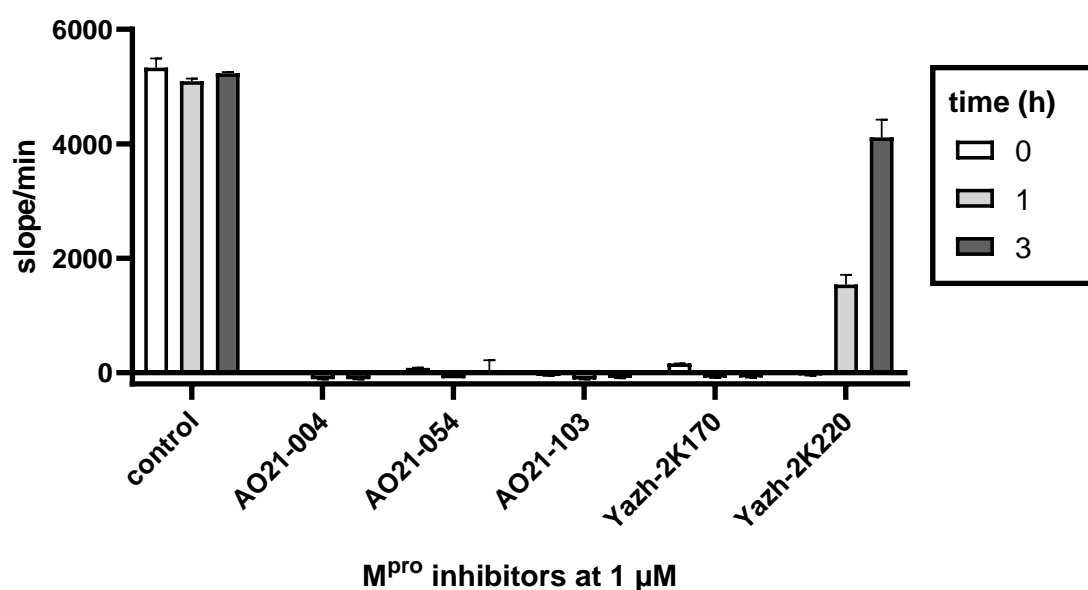
### 4.5.3 Stability of enzymatic activity and enzyme-pyridyl thioester bond

Regarding the class of pyridyl esters as inhibitors of the M<sup>pro</sup> enzyme, some representatives are not able to inhibit the enzymatic activity for a prolonged period of time. Initially, a covalent bond is formed between the compound and the reactive thiol group located in the active center of the enzyme. In the course of the reaction, the indole carboxylic acid or benzoic acid remains in the binding pocket, while the pyridol is the leaving group. In previous experiments it was noticed, that for some inhibitors, the initially formed covalent thioester bond to the enzyme is not permanent. The inhibitor fragment is expelled from the active site, leading to a restoration of the enzymatic activity.

In the standard activity assay for M<sup>pro</sup>, the inhibition potency and IC<sub>50</sub> values are determined by observation of the initial M<sup>pro</sup> reaction velocity for 10 min. For the characterization of time-dependent inhibition the initial 60 min of enzymatic reaction are monitored. In order to further assess the persistence of the covalent bond and prolonged inhibition of M<sup>pro</sup>, the enzyme was incubated with the respective inhibitors, and subsequently the ability to cleave the substrate was tested.

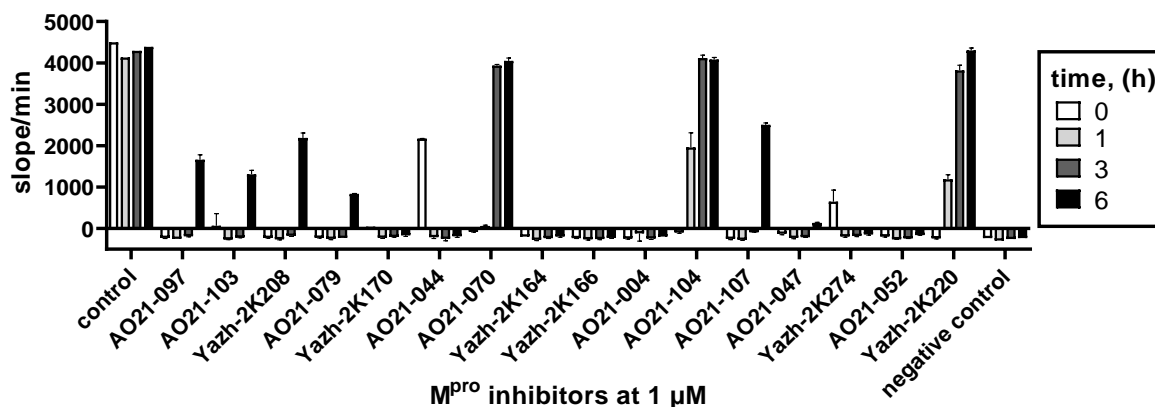
The crude *E. coli* extract of SARS-CoV-2 M<sup>pro</sup> was chosen for the experiments, as it was assumed that the enzymatic activity could decrease over time due to its protease activity. The crude extract contains additional proteins which could potentially stabilize the enzyme. Surprisingly, the enzymatic activity did not decrease after up to 3 h of incubation at 37°C in assay buffer (see **Figure 42**). The inhibitors that were chosen for the initial stability experiment retained their ability to block the enzymatic activity of M<sup>pro</sup> at 1 µM concentration (see **Figure 42**). Compound **M-50** (Yazh-2K220) was chosen as control, since the compound is known to be a covalent reversible inhibitor of M<sup>pro</sup>, that is not able to permanently inhibit the enzymatic activity, despite its high initial inhibition potency.





**Figure 42.** SARS-CoV-2 M<sup>pro</sup> activity determination after incubation of pyridyl ester inhibitors with crude extract of recombinant His-tagged SARS-CoV-2 M<sup>pro</sup> at 37°C for 0, 1 or 3 h in assay buffer. The incubated samples were diluted 1:2 with AMC-substrate ( $K_m = 48.2 \mu\text{M}$ ) in assay buffer, and the enzyme activity assay was performed once in duplicates ( $n = 1$ ) with final concentrations of the fluorogenic substrate at 50  $\mu\text{M}$  and compound concentrations at 1  $\mu\text{M}$ . Fluorescence increase as slope/min over the initial 10 min of the enzymatic cleavage of the AMC-substrate.

As the first experiment was successful, the stability of M<sup>pro</sup> inhibition of a wider selection of pyridyl esters was tested up to an incubation time of 6 h. The enzymatic activity of the control samples without inhibitors did not decrease in the observed time window (see **Figure 43**). The inhibitors were chosen based on a selection that was sent to a cooperation partner for SARS-CoV-2 viral replication assays. Seven compounds retained their ability to block the enzymatic activity of M<sup>pro</sup> at 1  $\mu\text{M}$  concentration (see **Figure 43**). Some compounds lost their ability to block the enzymatic activity of M<sup>pro</sup> only after an incubation time of 6 h. Interestingly, **M-79** (AO21-044), an *N*-methyl indole derivative, was initially unable to completely block the M<sup>pro</sup> activity, but showed complete inhibition at later time points. This could be explained by the time-dependent slow onset of the irreversible inhibition. Compounds **M-53** and **M-99** (AO21-104 and AO21-070) were both reversible-covalent inhibitors and lost their ability to inhibit M<sup>pro</sup> after 1-3 h of incubation.



**Figure 43.** SARS-CoV-2  $M^{pro}$  activity determination after incubation of 16 pyridyl ester inhibitors with crude extract of recombinant His-tagged SARS-CoV-2  $M^{pro}$  at 37°C for 0, 1, 3 or 6 h in assay buffer. The incubated samples were diluted 1:2 with AMC-substrate ( $K_m = 48.2 \mu M$ ) stock in assay buffer and the enzyme activity assay was performed once in duplicates ( $n = 1$ ) with final concentrations of the fluorogenic substrate at 50  $\mu M$  and a compound concentration of 1  $\mu M$ . Fluorescence increase as slope/min over the initial 10 min of the enzymatic cleavage of the fluorogenic substrate.

In conclusion, the selection of pyridyl esters mostly showed a permanent (over 6 h) inhibition of the enzymatic activity of SARS-CoV-2  $M^{pro}$  in *in vitro* activity assays.

## 4.6 Experimental

The expression of SARS-CoV-2 M<sup>pro</sup> and experiments described in sections 4.1 to 4.3 were performed as previously detailed in the supporting information of our publication, Breidenbach et al. 2021.<sup>165</sup> The research described in sections 4.4 and 4.5 was conducted according to the following protocols.

### 4.6.1 SARS-CoV-2 M<sup>pro</sup> activity assay

#### General procedure

Recombinant His-tagged or native SARS-CoV-2 M<sup>pro</sup> was defrosted and immediately used for the enzyme assays which were performed on a Pherastar FSX plate reader (BMG Labtech, Offenburg, Germany) at 37 °C with an excitation wavelength of 360 nm and an emission wavelength of 460 nm. Black half area 96-well plates with a flat bottom were obtained from Greiner Bio-One (Kremsmünster, Austria). The assay buffer was 50 mM 3-(*N*-morpholino)propanesulfonic acid (MOPS) at pH 7.2 containing 10 mM NaCl, 1 mM EDTA and 0.01% Triton X-100. A 2.5 mM stock solution of the substrate (Boc-Abu-Tle-Leu-Gln-AMC) was prepared in DMSO. Test compounds were dissolved in DMSO to obtain x50 concentrated stock solutions. The substrate was diluted with assay buffer (1 µL [2.5 mM AMC-substrate] + 33 µL assay buffer) and pipetted into a well containing 1 µL of inhibitor stock. This mixture was incubated at 37 °C for 5 - 10 min. Upon addition of 15 µL of enzyme solution (e.g. 1 µL 0.4 µg/µL His-tagged M<sup>pro</sup> diluted in 14 µL assay buffer) the measurement was started and followed for 10 min or 1 h. The protein concentration of His-tagged or native M<sup>pro</sup> was adjusted to a relative fluorescence slope increase of approximately 2000 per minute. The final AMC-substrate concentration was 50 µM which approximately corresponds to its  $K_m$  value of 48.2 µM and the DMSO concentration in all samples was 4%. For inhibition % calculations the product formation rate of the positive control without inhibitor was set at 100% M<sup>pro</sup> activity and the negative control, containing assay buffer instead of enzyme was set to 0%. All data was analyzed and plotted with the help of GraphPad Prism 8 (GraphPad software, San Diego, CA, USA).

### Concentration inhibition curves

Determination of  $IC_{50}$  values were performed by generation of concentration-inhibition curves of at least eight different inhibitor concentrations. The product formation rate during the initial 10 min of the enzymatic reaction was evaluated and plotted *versus* the corresponding inhibitor concentration.<sup>165</sup>  $IC_{50}$  values were calculated by non-linear regression  $v = v_0 / (1 + [I] / IC_{50})$ , where  $v$  is the product formation rate at different inhibitor concentrations,  $v_0$  is the uninhibited product formation rate,  $[I]$  is the inhibitor concentration, and  $IC_{50}$  is the half-maximal inhibitory concentration. The standard error of the mean (SEM) refers to the individual  $IC_{50}$  values resulting from three independent experiments in singlicates ( $n=3$ ). The corresponding  $K_i$  values for reversible inhibitors, which are assumed to possess a competitive inhibition type, were calculated by correcting the  $IC_{50}$  value using the Cheng-Prusoff equation  $IC_{50} = K_i \times (1 + [S] / K_m)$ , where  $[S]$  is the substrate concentration at 50  $\mu\text{M}$  and  $K_m$  is the determined Michaelis constant for the substrate at 48.4  $\mu\text{M}$ .<sup>238</sup>

### Time-dependent inhibition

Slow onset, irreversible inhibitors showed time-dependent inhibition. For the determination of the first-order rate constant of inactivation,  $k_{obs}$ , the progress curves of product formation in the presence of five different inhibitor concentrations were followed over 60 min and analyzed by non-linear regression using the equation  $[P] = v_i \times (1 - \exp(-k_{obs} \times t)) / k_{obs} + d$ , where  $[P]$  is the product concentration,  $v_i$  the initial rate,  $k_{obs}$  the observed first-order rate constant and  $d$  is the offset. The second-order rate constant,  $k_{inac} / K_i$ , was determined by plotting  $k_{obs}$  *versus*  $[I]$  and non-linear regression using the equation  $k_{obs} = (k_{inac} \times [I]) / ([I] + K_i \times (1 + [S] / K_m))$ . Deviation of each data point from the calculated non-linear regression was less than 10%.<sup>165</sup>

### Stability to incubation with glutathione (GSH)

In the stability pretesting to the LCMS-based Laufer test detailed in section 0 the activity of M<sup>Pro</sup>His after incubation with 1 mM GSH was assessed for inhibitors of interest. For this purpose, the inhibition potency of each inhibitor was tested in three conditions: (i) 100  $\mu\text{M}$  compound incubated with 1 mM GSH for 1 h at 37°C in assay buffer (1  $\mu\text{L}$  [10 mM inhibitor stock in DMSO] + 2  $\mu\text{L}$  [50 mM GSH stock in water] + 97  $\mu\text{L}$  assay buffer); (ii) 100  $\mu\text{M}$  compound incubated for 1 h at 37°C in assay buffer (1  $\mu\text{L}$  [10 mM inhibitor stock in

DMSO] + 99  $\mu\text{L}$  assay buffer ) and (iii) 100  $\mu\text{M}$  compound prepared immediately before dilution and enzyme activity assay (preparation analog to (ii)). The samples were subsequently diluted 1:20 (10  $\mu\text{L}$  [100  $\mu\text{M}$ ] + 190  $\mu\text{L}$  assay buffer) and the  $\text{M}^{\text{pro}}$  activity at presence of 1  $\mu\text{M}$  compounds was tested with the established assay with an adjusted pipetting scheme (10  $\mu\text{L}$  [5  $\mu\text{M}$  inhibitor dilution] + 25  $\mu\text{L}$  AMC-substrate stock [1  $\mu\text{L}$  2.5 mM AMC-substrate in DMSO + 24  $\mu\text{L}$  assay buffer] + 15  $\mu\text{L}$   $\text{M}^{\text{pro}}$  sample [1  $\mu\text{L}$  His-tagged  $\text{M}^{\text{pro}}$  aliquot + 14  $\mu\text{L}$  assay buffer]).<sup>165</sup>

### **Stability to incubation with $\text{M}^{\text{pro}}$ enzyme**

The investigation of pyridyl esters towards prolonged incubation with  $\text{M}^{\text{pro}}$  samples is presented in section 4.5.3. The first experiment was performed in closed reaction tubes, containing each 0.003 mg/mL crude extract of his-tagged SARS-CoV-2  $\text{M}^{\text{pro}}$  (KS3C 0.03 mg/mL) and 2  $\mu\text{M}$  of compound in a final volume of 100  $\mu\text{L}$ . The samples were incubated in a ThermoShaker (Eppendorf Thermomixer comfort) at 37°C with gentle shaking. At time points 0, 1 and 3h aliquots of each 25.0  $\mu\text{L}$  were taken in order to test the enzymatic activity after addition of 25  $\mu\text{L}$  AMC-substrate stock (100  $\mu\text{M}$ ).<sup>165</sup> In the second experiment the irreversibility of  $\text{M}^{\text{pro}}$  inhibition of a wider selection of pyridyl esters was tested up to an incubation time of 6 h. The incubation was performed in a 96 well plate with assay buffer in adjacent wells. Each well contained 0.003 mg/mL crude extract of his-tagged SARS-CoV-2  $\text{M}^{\text{pro}}$  (KS3C 0.03 mg/mL) and 2  $\mu\text{M}$  of compound in a final volume of 150  $\mu\text{L}$ . At time points 0, 1, 3 and 6 h aliquots of each 25.0  $\mu\text{L}$  were removed in order to test the enzymatic activity upon AMC-substrate addition.<sup>165</sup>

## 5 Publications on M<sup>pro</sup>

### 5.1 Electrophilic Arylketones

#### 3CL Protease Inhibitors with an Electrophilic Arylketone Moiety as Anti-SARS-CoV-2 Agents

*Sho Konno, Kiyotaka Kobayashi, Miki Senda, Yuta Funai, Yuta Seki, Ikumi Tamai, **Laura Schäkel**, Kyouzuke Sakata, Thanigaimalai Pillaiyar, Akihiro Taguchi, Atsuhiko Taniguchi, Michael Gütschow, Christa E. Müller, Koh Takeuchi, Mikako Hirohama, Atsushi Kawaguchi, Masaki Kojima, Toshiya Senda, Yoshiyuki Shirasaka, Wataru Kamitani, and Yoshio Hayashi*

*J Med Chem* **2022** Feb 24;65(4):2926-2939. doi: 10.1021/acs.jmedchem.1c00665.

#### Introduction

The global spread of severe acute respiratory syndrome coronavirus 2 (SARS-CoV-2), causing COVID-19 upon infection, enticed the need for an effective antiviral treatment. The pathogen SARS-CoV-2 is a single-stranded, positive-sense RNA virus of the coronavirus family. The viral proteases 3C-like protease (3CL<sup>pro</sup> or main protease, M<sup>pro</sup>) and papain-like protease (PL<sup>pro</sup>) are essential to viral replication by catalyzing the hydrolysis of polyproteins into individual proteins. M<sup>pro</sup> cleaves the peptide amide bond following the amino acid glutamine. The M<sup>pro</sup> recognition sequence is not found in humans, which enables the design of specific substrate-based analogs.<sup>158,194</sup>

The work featured in this chapter details the development of lead structures for SARS-CoV-2 M<sup>pro</sup>-inhibiting drugs, that decrease the severity and fatality of a COVID-19 infection. In order to study the effects of potential modulators, we produced recombinant SARS-CoV-2 M<sup>pro</sup> and established a protease activity assay beforehand.<sup>165</sup> This enabled the screening and characterization of previously published SARS-CoV-1 M<sup>pro</sup> inhibitors, namely SH-5, YH-53 and YH-71.<sup>245,246</sup> These compounds had been described to possess suitable drug properties and high potency against SARS-CoV-1 M<sup>pro</sup> with  $K_i$  values of 4.1, 6.3 and 22.0 nM for SH-5, YH-53 and YH-71 respectively.<sup>245,246</sup> The opportunity to develop these and other drugs targeting coronaviruses for therapeutic use after the outbreaks of SARS-CoV-1 in 2003 and MERS in 2012 was not pursued because the infections were under control. However, research efforts yielded lead structures, which were recently

reconsidered for evaluation against SARS-CoV-2 and potential development as therapeutics. At the time of the experiments, in 2020, no antiviral drugs specifically targeting the SARS-CoV-2 M<sup>pro</sup> were available or approved. Two years later, various vaccines and treatment options are ready for use in the fight against the COVID-19 pandemic. This circumstance is in part owed to scientists shifting their research interests and joining forces in interdisciplinary teams in order to accelerate research and development.

### Summary and outlook

As SARS-CoV-1 M<sup>pro</sup> shares a high sequence similarity to SARS-CoV-2 M<sup>pro</sup> the most promising compounds from prior publications were selected for evaluation at the newly emerged pathogen's main protease. As expected, the compounds were similarly potent at both viral proteases.<sup>245–247</sup> SH-5, YH-53 and YH-71 were shown to be potent inhibitors of SARS-CoV-2 M<sup>pro</sup> with respective *in vitro*  $K_i$  values of 14.5, 34.7 and 32.1 nM.<sup>247</sup> The potency of YH-53 was consistent with that determined by other research groups, reporting a  $K_i$  value of 17.6 nM.<sup>181</sup> The three substrate-derived inhibitors contain a unique benzothiazolyl ketone as an electrophilic warhead, which was shown to form a reversible hemithioketal by covalently binding to the active site cysteine (Cys<sub>145</sub>). The mode of inhibition of the protease by the most potent inhibitor SH-5 was determined to be competitive in *in vitro* activity assays, supporting the hypothesis of an orthosteric binding site and transient nature of the covalent bond, as no time-dependent effects were observed in the progress curves of product formation. A transient nature of the enzyme-inhibitor-complex decreases the risk profile of the compounds, considering a lower chance of reactivity towards off-target thiol groups. The binding site and mode were then confirmed by determining X-ray structures for YH-53 and SH-5.

The viral replication of SARS-CoV-2 in Vero cells was successfully blocked, although at concentrations greater than 25  $\mu$ M. YH-53 was the most potent derivative in the viral replication tests; it abrogated the viral replication at lower concentrations of 10  $\mu$ M, while displaying no cytotoxicity at a tenfold higher concentration of 100  $\mu$ M. Therefore, this study focused on the characterization of the compound YH-53 by compiling an exceptionally detailed assessment of the dipeptide with respect to its *in vitro* activities, X-ray structural analysis, pharmacodynamics and metabolic analysis.

The bioavailability was investigated in rats and proved to be low, likely caused by metabolism in the liver. Putative metabolites were identified by LC/UV/MS subsequent to incubation with rat or human hepatocytes. The substantial difference of *in vitro* protease inhibition and cell-based studies indicates that the peptidomimetics experience difficulties to reach the intracellular target. As the cell permeability was high in Caco-2 cells, the evidence pointed to metabolism or efflux transporters as the reason for the efficacy gap. Indeed, the antiviral potency of YH-53 in cell assays was increased by addition of the multidrug-resistance-protein 1 (MDR-1, also known as P-gp) efflux transport inhibitor CP-100356. Additional experiments confirmed the M<sup>pro</sup> inhibitor to be a substrate of the permeability-glycoprotein (P-gp) efflux pump.

To summarize, YH-53 can be considered as a potential candidate for clinical studies, as its drug potential was comprehensively analyzed. The compound was shown to have a good safety profile, and show effective inhibition of SARS-CoV-2 *in vitro* in combination with P-gp blockers. The next step for drug development entails experiments on the *in vivo* antiviral activity in animal models.

The approval of the first antiviral, Paxlovid®, that specifically targets the M<sup>pro</sup> of coronaviruses proved that the approach to develop peptidomimetic inhibitors is successful.<sup>163,189</sup> This publication contributed to the rapidly evolving search for effective antiviral drugs for the treatment of COVID-19 and is still of great interest to this rapidly developing field.

### **Author's contribution**

The author of this thesis performed the *in vitro* pharmacological characterization of the three featured compounds on recombinant SARS-CoV-2 M<sup>pro</sup> with the previously established protease activity assay.<sup>165</sup> The evaluation of inhibitory potencies, type of inhibition and progress curves led to Figure 2 and Figure S1 in the Supporting Information, which were all prepared by the author. Reports discussing the obtained results contributed to the written content of the manuscript.

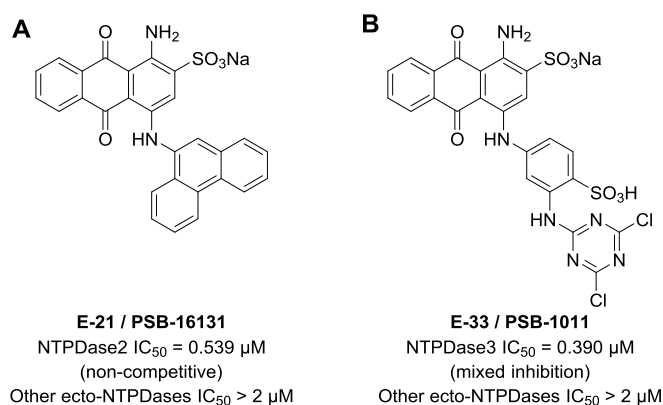


## 6 Summary

### 6.1 Ecto-Nucleoside triphosphate diphosphohydrolases (NTPDases)

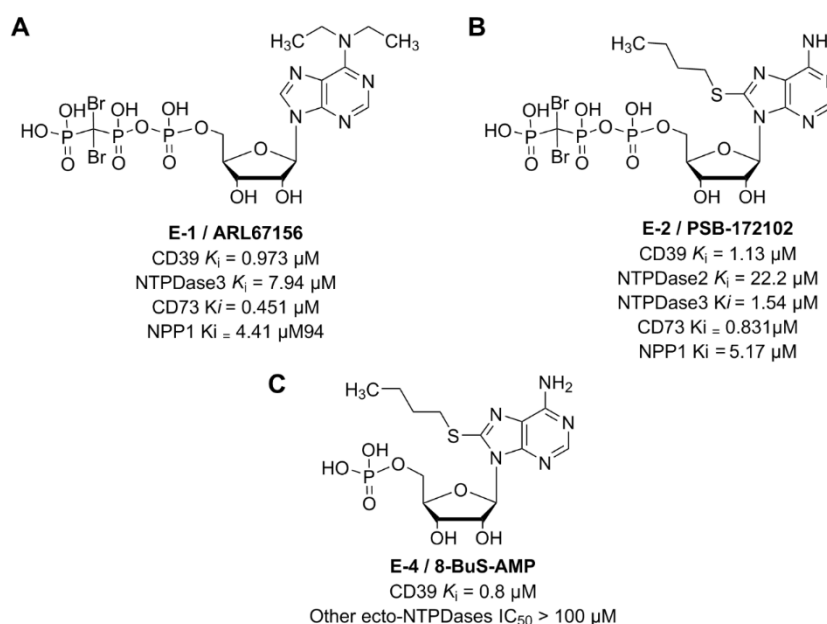
NTPDase1 (CD39) is the key enzyme hydrolyzing extracellular ATP.<sup>37,43</sup> Its inhibitors have potential as drugs for the immunotherapy of cancers and infections, while activators could be useful for the treatment of auto-immune diseases. At the start of the work for this thesis few CD39 modulators were available, all of which lacked potency, selectivity and drug-like properties. Therefore, we aimed to identify, characterize and optimize small molecules as inhibitors of NTPDases, in particular CD39. This work was supported by the SFB1328 'Adenine Nucleotides in Immunity and Inflammation' (project A11). The first funding period focused on the development of competitive as well as allosteric modulators of CD39. Recombinant human CD39 was expressed in COS-7 cells, and cell membrane preparations were used for studying inhibitors in complementary enzyme activity assays (see chapter 2.2). Various compound classes were characterized regarding their potency, selectivity, inhibition type and metabolic stability. Positive modulators of CD39's catalytic activity could not be identified, while the development of orthosteric as well as allosteric inhibitors was successful. The main findings are described below.

**Anthraquinone derivatives**, were studied as inhibitors of ecto-NTPDases1, -2, -3 and -8 (see chapter 3.1) and proved to be potent and selective inhibitors of human NTPDase2 and 3.<sup>105</sup> PSB-16131 (**E-21**) was found to be a non-competitive NTPDase2 inhibitor, while PSB-1011 (**E-33**) inhibited NTPDase3 with a mixed inhibition type (see **Figure 44**). These compounds will be important tools for researching the functions of NTPDase2 and -3 in physiology and pathology.



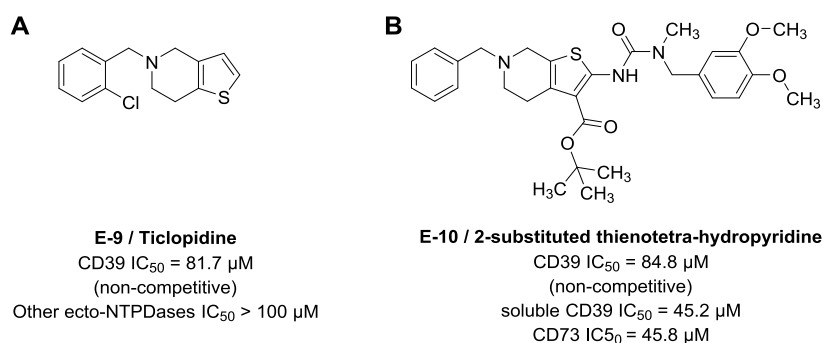
**Figure 44.** Structure and characterization of anthraquinone derivatives as inhibitors of ecto-nucleotidases: **A.** PSB-16131 (**E-21**);<sup>105</sup> and **B.** PSB-1011 (**E-33**).<sup>105</sup>

The substrate analog **ARL67156 (E-1)** was selected as a lead structure for competitive CD39 inhibitors. ARL6716 is a commercially available ATPase inhibitor of moderate potency at NTPDases. Due to the replacement of the O-bridge between the  $\beta$ - and  $\gamma$ -phosphate by a dibromomethylene bridge, it has been assumed to be metabolically stable. We studied ARL67156 along with a series of derivatives and analogs synthesized by our group (see chapter 3.2).<sup>94</sup> ARL67156 and the two most potent compounds of the series were characterized as dual CD39/CD73 inhibitors, that additionally inhibited NTPDase3 and NPP1, although with lower potencies. We confirmed the competitive inhibition type on CD39 and performed docking studies of ARL67156 utilizing a CD39 homology model in order to rationalize its putative binding mode and insights from the SAR study. We demonstrated that full deprotonation of the terminal phosph(on)ate group was required for high inhibition of CD39. Surprisingly, ARL67156 and its derivatives proved to be completely unstable upon incubation with mouse and human liver microsomes, and can therefore not be recommended for use in *in vivo* studies.<sup>94</sup> Another nucleotide-derived lead structure for CD39 inhibitors is **8-butylthio-AMP**. Synthesis of derivatives and analogs allowed the analysis of SARs regarding various substituents at the adenine ring. The most potent derivatives were characterized with respect to their inhibitory potency in two orthogonal assays. Additionally, the metabolic stability was investigated and selectivity studies and docking studies were performed. The results will be published in three separate manuscripts.



**Figure 45.** Structure and characterization of nucleotide derivatives as inhibitors of ecto-nucleotidases: **A.** ARL67156 (**E-1**);<sup>94</sup> **B.** PSB-172102(**E-2**);<sup>94</sup> and **C.** 8-BuS-AMP(**E-4**).<sup>91</sup>

The anti-thrombotic prodrugs of the P2Y<sub>12</sub> receptor antagonists clopidogrel and **ticlopidine** were confirmed as inhibitors of CD39.<sup>109,110</sup> The investigation of **2-substituted thienotetrahydropyridine derivatives** revealed that similar compounds which cannot be metabolized to P2Y<sub>12</sub> receptor antagonists have equivalent potencies and show a non-competitive inhibition type at CD39 (see chapter 3.3).<sup>110</sup> Furthermore, we worked on the synthesis and characterization of ticlopidine derivatives and analogs with the aim to study the SARs and to improve potency. The results of this extensive study are not featured in this thesis but will be published elsewhere.

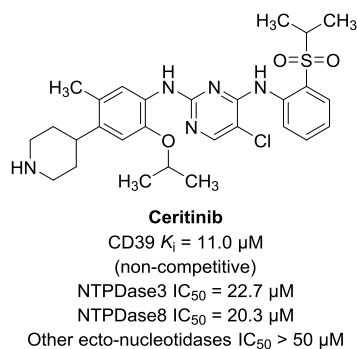


**Figure 46.** The antithrombotic prodrug **A. ticlopidine (E-9)** and its metabolically stable 2-substituted analog **B. E-10** and their inhibitory potencies at ecto-nucleotidases.<sup>110</sup>

We discovered several **sulfated polysaccharides**, derived from macroalgae, to be strong dual inhibitors of the two major ATP-hydrolyzing enzymes CD39 and NPP1.<sup>121</sup> The most potent preparation was obtained from the algal species *Fucus vesiculosus* and it was broadly characterized. It inhibited NPP1 and CD39 with an allosteric non-competitive/mixed inhibition type, and  $K_i$  values of 1.19 nM for human NPP1, and 12.3 nM for human CD39 were determined. Their inhibition of ATP hydrolysis could contribute to the reported anticancer properties of sulfated algae polysaccharides from sea weeds.

Finally, we screened several in-house sub-libraries of the PharmaZentrum Bonn (PZB) compound library in the search for novel CD39 inhibitors. In total, more than 5500 compounds were tested for their modulation of the enzyme's activity, and several hits with distinct chemical structures were identified. In this context, a library consisting of 50 approved protein kinase inhibiting drugs was tested at human CD39, based on the assumption, that these compounds interact with the ATP co-substrate binding site of protein kinases, and therefore might bind to and modulate ecto-nucleotidases as well.

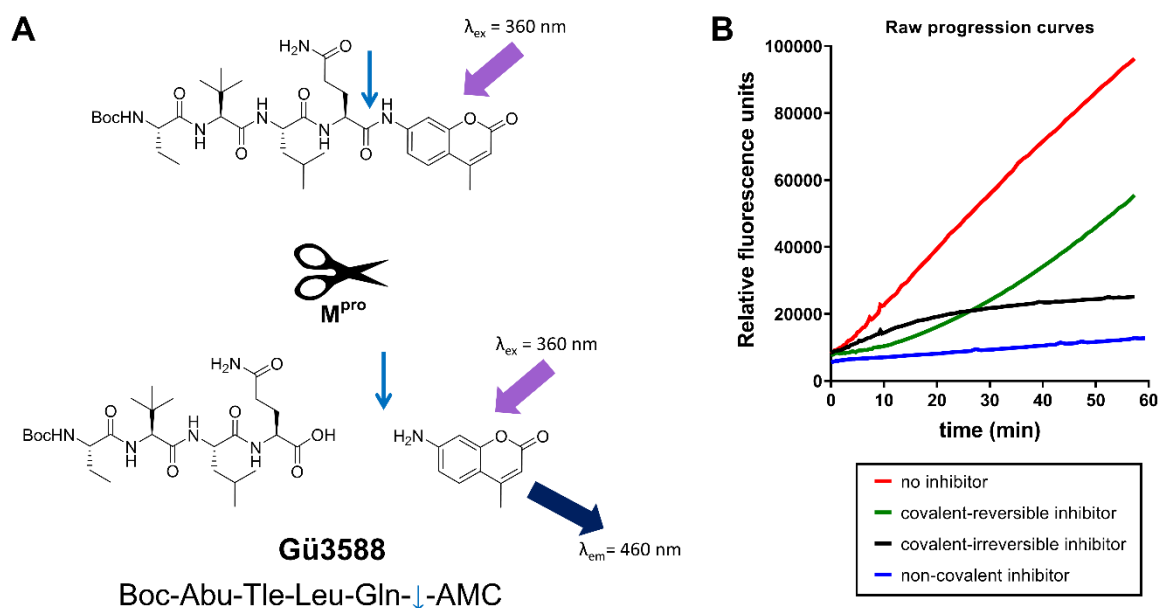
This led to the discovery of **ceritinib** (see **Figure 47**), an inhibitor of anaplastic lymphoma kinase (ALK), as an allosteric inhibitor of human CD39 (see chapter 3.4). This drug has an excellent metabolic stability and may be used as a new starting point for optimization eventually resulting in the development of specific NTPDase inhibitors.



**Figure 47.** Structure of ceritinib and its characterization as inhibitor of ecto-nucleotidases.

## 6.2 SARS-CoV-2 main protease

When the coronavirus pandemic started in early 2020, Prof. Christa E. Müller's and Prof. Gütschow's groups immediately decided to join efforts to help in fighting this life-threatening infectious disease. Thus, a drug development project aimed at the main protease ( $\text{M}^{\text{pro}}$ ) of SARS-CoV-2 as a suitable target for anti-COVID-19 therapeutics was started in collaboration with an interdisciplinary team. SARS-CoV-2  $\text{M}^{\text{pro}}$  was successfully expressed in *E. coli*, and an enzyme assay, based on a fluorogenic substrate, was developed for the focused screening of selected compound libraries and the characterization of hit compounds (see **Figure 48**). The first manuscript describing the assay establishment and the optimization of peptides (Prof. Gütschow), as well as halopyridyl indole esters (Prof. Müller), was published in 2021.<sup>165</sup> The characterization of three known SARS-CoV-1  $\text{M}^{\text{pro}}$  inhibitors from a collaboration partner in Japan was issued shortly after.<sup>247</sup> The experiments performed for the second publication on SARS-CoV-2  $\text{M}^{\text{pro}}$  are described in section 5.1 (see **Figure 49A** for most representative  $\text{M}^{\text{pro}}$  inhibitor YH-53). Chapter 4 describes the pharmacological studies for the implementation of the  $\text{M}^{\text{pro}}$  activity assay and the ongoing project on the characterization of inhibitors.

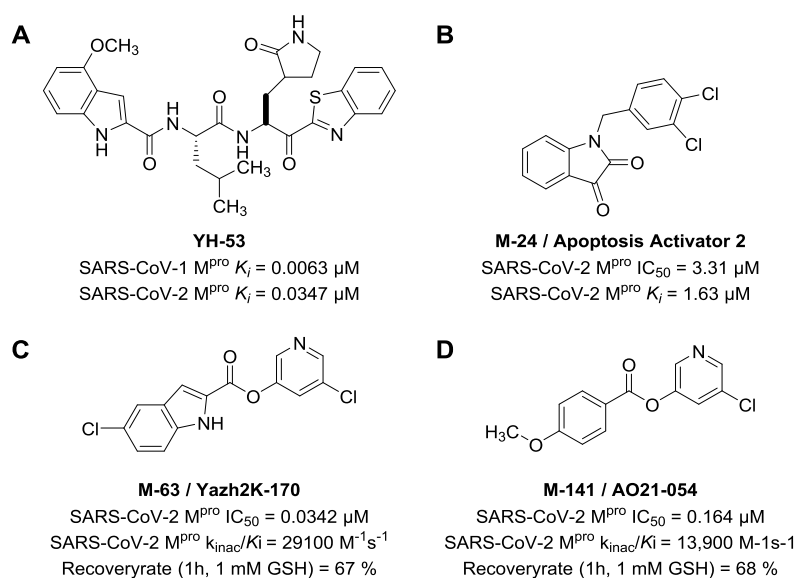


**Figure 48.** A. Aminomethylcoumarine-based fluorescent substrate (AMC-substrate) and its  $M^{pro}$  catalyzed proteolysis resulting in fluorescence emission ( $\lambda_{excitation} = 360 \text{ nm}$ ,  $\lambda_{emission} = 460 \text{ nm}$ ) and B. relative fluorescence increase in proportion to the enzymatic activity over time. Straight increase (red) control without inhibitor compared to the decreased enzymatic activity in the presence of slowly reversible (green), slowly irreversible (black) covalently binding inhibitors, as well as non-covalent inhibitors forming a rapid equilibrium (blue) with the protease.

Additional hits from virtual as well as experimental compound library screening campaigns were characterized at SARS-CoV-2  $M^{pro}$ . The isatin derivative Apoptosis activator 2 (**M-24**, **Figure 49B**) was found to be a non-covalent inhibitor with a  $K_i$  value of  $1.63 \mu\text{M}$ , based on the published orthosteric binding mode of related compounds.<sup>210</sup> Several xanthine derivatives and two further heterocyclic compounds demonstrated the ability to non-covalently inhibit  $M^{pro}$  with potencies in the low micromolar range.

A series of novel pyridyl ester derivatives was studied to explore the structure-activity relationships (SARs) of this class of compounds. In addition to the compounds' inhibitory activity, enzyme inhibition kinetics and inhibition mechanism, as well as further properties were evaluated, in order to optimize the compounds' potency and drug-like properties. The stability of pyridyl esters *versus* incubation with 1 mM glutathione (GSH) was estimated using a high-throughput screening approach. Based on the established pretest, compounds were selected for further analysis by HPLC or LCMS. Moreover, time-dependent stability of pyridyl esters towards incubation with SARS-CoV-2  $M^{pro}$  was

assessed to determine their suitability for crystallization studies and potential therapeutic application.



**Figure 49.** Structure and characteristics of selected inhibitors of SARS-CoV-2 M<sup>pro</sup>; **A.** most potent peptidomimetic M<sup>pro</sup> inhibitor, YH-53, with a benzothiazolyl ketone as a warhead group;<sup>247</sup> **B.** M-24 Apoptosis Activator 2; **C.** M-63 Yazh2K-170;<sup>165</sup> and **D.** M-141 AO21-054.

Variations to the indole ester scaffolds were examined by analysis of SARs, and rational drug design was performed in the search for potential SARS-CoV-2 M<sup>pro</sup> inhibiting drugs. Bioisosters of the core structure indole, namely thiophene and benzofuran, produce inhibitors with good initial inhibition, but showed degradation of the covalent bond to the M<sup>pro</sup> Cys<sub>145</sub>. The ester position on the indole was investigated, identifying 2-, 4- and 7-carboxylic acid esters to be the most promising lead structures for further development. 2-Carboxylic acid ester-derived inhibitors paved the way to the most potent inhibitors and at the same time high stability during incubation with glutathione. Small changes of substituents and their position resulted in steep SARs with regard to potency and stability of the irreversible, covalent inhibitor-enzyme complex. The best compound with regard to both *in vitro* inhibitory potency and glutathione stability is Yazh-2K170 (Compound **M-63**, 5-chloropyridin-3-yl 5-chloro-1*H*-indole-2-carboxylate **Figure 49C**).

A novel scaffold was evaluated with the halopyridyl benzoic acid ester derivatives. Monosubstituted compounds were among the most potent derivatives. The 4-methoxy

derivative **M-141** (A021-054, **Figure 49D**) showed the highest stability upon incubation with GSH. This compound could be further optimized (e.g. by introduction of a second substituent or by the conversion to its bromopyridyl ester) in order to increase its potency and second order rate constant of inactivation ( $k_{\text{inac}}/K_i$  value).

New syntheses and experiments on cell penetration and potency in cell culture are in progress and will add important information for the fine-tuning to obtain a suitable drug candidate.

In conclusion, highly potent SARS-CoV-2 small molecule  $M^{\text{pro}}$  inhibitors were designed and characterized, which may be superior to peptidomimetic drugs, at least in some aspects, and provide excellent starting points for further drug development.

## 7 Abbreviations

<b>Abbreviation</b>	<b>Name</b>
3CL <sup>pro</sup>	3chymotrypsin-like protease
8-BuS-AMP	8-Butylthio-adenosine-5'-monophosphate
A549 cells	Adenocarcinomic human alveolar basal epithelial cells
ACE	Angiotensin converting enzyme
ACRs	Apyrase-conserved regions
ADP	Adenosine 5'-diphosphate
ADPR	ADP-ribose
AK	Adenylate kinase
ALK	Anaplastic lymphoma kinase
AMC	7-amino-4-methylcoumarin
AMP	Adenosine-5'-monophosphate
AMPCP	$\alpha,\beta$ -methylene adenosine 5'-diphosphate
AP	Alkaline phosphatase
ARL67156	<i>N</i> <sup>6</sup> -diethyl-D- $\beta,\gamma$ -dibromo-methylene-ATP
ATP	Adenosine-5'-triphosphate
<i>CC</i> <sub>50</sub>	Compound concentration at 50% of cytotoxicity
CD38	Cluster of differentiation 38, cyclic ADP ribose hydrolase
CD39	Ecto-nucleoside triphosphate diphosphohydrolase1, NTPDase1
CD73	Ecto-5'-nucleotidase, cluster of differentiation 73
CE	Capillary electrophoresis
COVID-19	Coronavirus disease 2019
Dabcyl	4-((4-(dimethylamino)phenyl)azo)benzoic acid
DMSO	Dimethyl sulfoxide
DTT	1,4- dithiothreitol
<i>E. coli</i>	Escherichia coli bacteria
<i>EC</i> <sub>50</sub>	Compound concentration at 50% of maximum effect
EDANS	5-((2-aminoethyl)amino)naphthalene-1-sulfonic acid
EDTA	Ethylenediaminetetraacetic acid
EI-complex	Enzyme-inhibitor complex
E-NPP	Ecto-nucleotide pyrophosphatase/ phosphodiesterase
E-NTPDase	Ecto-nucleoside triphosphate diphosphohydrolase
ES-complex	Enzyme-substrate complex
FDA	Food and Drug Administration
FIP	Feline infectious peritonitis
FPIA	Fluorescence polarization-based immunoassay
FRET	Fluorescence resonance energy transfer
GFP	Green fluorescent protein
GSH	Glutathione
HEK	Human Embryonic Kidney
HIF-1 $\alpha$	Hypoxia-inducible-factor-1 $\alpha$
HIV	Human immunodeficiency virus
HPLC	High performance liquid chromatography



HTS	High throughput screening
IC <sub>50</sub>	Inhibitor concentration at 50% residual enzyme activity
ITC	Isothermal titration calorimetry
$k_{cat}$	Turnover number
$k_{cat}/K_m$	Kinetic efficiency constant
$K_i$	Enzyme-inhibitor dissociation constant
$k_{inac}$	First-order rate of inhibition
$k_{inac}/K_i$	Second-order rate constant of inhibition, $k_{2nd}$
$K_m$	Michaelis constant
$k_{obs}$	Pseudo-first-order rate constant
$k_{off}$	Dissociation rate constant or off-rate
$K_s$	Dissociation constant
LC/MS	Liquid chromatography coupled to mass spectrometry
MERS	Middle East respiratory syndrome
MOPS	3-( <i>N</i> -morpholino)propanesulfonic acid
M <sup>pro</sup>	Main protease of coronaviruses
MS	Mass spectrometry
MST	Microscale thermophoresis
NAD <sup>+</sup>	Nicotinamide dinucleotide
NCT number	National clinical trial number assigned by <a href="https://clinicaltrials.gov">clinicaltrials.gov</a>
NDP	Nucleoside diphosphate
nsp	Nonstructural protein
NTP	Nucleoside triphosphate
P1 receptor	Adenosine receptor
P2 receptor	Nucleotide receptor
PBS	Phosphate-buffered saline
PD-1	Programmed cell death protein 1
PDB	Protein data base
PL <sup>pro</sup>	Papain-like protease
POM	Polyoxometalate
PP <sub>i</sub>	Pyrophosphate
PSB	Pharmaceutical sciences Bonn
qRT-PCR	Quantitative real-time polymerase chain reaction
RB-2	Reactive blue 2
RFU	Relative fluorescence units
SARs	Structure-activity relationships
SARS-CoV	Severe acute respiratory syndrome coronavirus
SEM	Standard error of the mean
TLC	Thin layer chromatography
TMPRSS2	transmembrane protease serine subtype 2
Tris	2-Amino-2-(hydroxymethyl)propane-1,3-diol
UDP	Uridine-5'-diphosphate
UTP	Uridine-5'-triphosphate
UV	ultraviolet
$v_i$	Initial velocity

$V_{\max}$	Maximal velocity
$v_s$	Steady-state velocity
$\tau$	Residence time

---

## 8 References

- (1) Copeland, R. A. *Enzymes: A Practical Introduction to Structure, Mechanism, and Data Analysis*, 2nd ed.; Wiley-VCH, Inc., 2000.
- (2) Rufer, A. C. Drug Discovery for Enzymes. *Drug Discovery Today* **2021**, *26* (4), 875–886.
- (3) Patrick, G. L. *An Introduction to Medicinal Chemistry*, 5th ed.; Oxford university press, 2013.
- (4) Yari, M.; Ghoshoon, M. B.; Vakili, B.; Ghasemi, Y. Therapeutic Enzymes: Applications and Approaches to Pharmacological Improvement. *Curr. Pharm. Biotechnol.* **2017**, *18* (7), 531–540.
- (5) Alexander, S. Ph.; Fabbro, D.; Kelly, E.; Mathie, A.; Peters, J. A.; Veale, E. L.; Armstrong, J. F.; Faccenda, E.; Harding, S. D.; Pawson, A. J.; et al. The Concise Guide to Pharmacology 2021/22: Enzymes. *Br. J. Pharmacol.* **2021**, *178* (Suppl 1), S313–S411.
- (6) *The IUPHAR/BPS Guide to PHARMACOLOGY*.  
<https://www.guidetopharmacology.org/about.jsp> (accessed 14 December 2021).
- (7) Wang, X.; Wang, R.; Zhang, Y.; Zhang, H. Evolutionary Survey of Druggable Protein Targets with Respect to Their Subcellular Localizations. *Genome Biol. Evol.* **2013**, *5* (7), 1291–1297.
- (8) Lüllmann, H.; Mohr, K.; Hein L. *Pharmakologie und Toxikologie*, 17th ed.; Thieme, 2010.
- (9) Bossi, R. T.; Saccardo, M. B.; Ardini, E.; Menichincheri, M.; Rusconi, L.; Magnaghi, P.; Orsini, P.; Avanzi, N.; Borgia, A. L.; Nesi, M.; et al. Crystal Structures of Anaplastic Lymphoma Kinase in Complex with ATP Competitive Inhibitors. *Biochemistry* **2010**, *49* (32), 6813–6825.
- (10) Copeland, R. A. *Evaluation of Enzyme Inhibitors in Drug Discovery*, 2nd ed.; Wiley, 2013.
- (11) Bisswanger, H. *Enzyme: Struktur, Kinetik und Anwendungen*, 1st ed.; Wiley, 2015.
- (12) Copeland, R. A.; Pompliano, D. L.; Meek, T. D. Drug–Target Residence Time and Its Implications for Lead Optimization. *Nat. Rev. Drug Discovery* **2006**, *5* (9), 730–739.
- (13) Ludewig, S.; Kossner, M.; Schiller, M.; Baumann, K.; Schirmeister, T. Enzyme Kinetics and Hit Validation in Fluorimetric Protease Assays. *Curr. Top. Med. Chem.* **2010**, *10* (3), 368–382.
- (14) Burnstock, G. Historical Review: ATP as a Neurotransmitter. *Trends Pharmacol. Sci.* **2006**, *27* (3), 166–176.
- (15) Burnstock, G. Purinergic Signalling. *Br. J. Pharmacol.* **2006**, *147*, 172–181.
- (16) Helenius, M.; Jalkanen, S.; Yegutkin, G. G. Enzyme-Coupled Assays for Simultaneous

- Detection of Nanomolar ATP, ADP, AMP, Adenosine, Inosine and Pyrophosphate Concentrations in Extracellular Fluids. *Biochim. Biophys. Acta, Mol. Cell Res.* **2012**, *1823* (10), 1967–1975.
- (17) Trautmann, A. Extracellular ATP in the Immune System: More than Just a “Danger Signal”. *Sci. Signaling* **2009**, *2* (56), pe6.
- (18) Burnstock, G. Physiology and Pathophysiology of Purinergic Neurotransmission. *Am. J. Physiol.* **2007**, *87* (2), 659–797.
- (19) Burnstock, G.; Verkhratsky, A. Evolutionary Origins of the Purinergic Signalling System. *Acta Physiol.* **2009**, *195* (4), 415–447.
- (20) Burnstock, G.; Verkhratsky, A. Receptors for Purines and Pyrimidines. In *Purinergic Signalling in the Nervous System*, 1st ed.; Springer, 2012, pp 119–244.
- (21) Lazarowski, E. R. Vesicular and Conductive Mechanisms of Nucleotide Release. *Purinergic Signalling* **2012**, *8* (3), 359–373.
- (22) Yegutkin, G. G. Nucleotide- and Nucleoside-Converting Ectoenzymes: Important Modulators of Purinergic Signalling Cascade. *Biochim. Biophys. Acta, Mol. Cell Res.* **2008**, *1783* (5), 673–694.
- (23) Idzko, M.; Ferrari, D.; Eltzschig, H. K. Nucleotide Signalling during Inflammation. *Nature* **2014**, *509* (7500), 310–317.
- (24) Brunschweiler, A.; Müller, C. E. P2 Receptors Activated by Uracil Nucleotides--an Update. *Curr. Med. Chem.* **2006**, *13* (3), 289–312.
- (25) Thimm, D.; Knospe, M.; Abdelrahman, A.; Moutinho, M.; Alsdorf, B. B. A.; von Kügelgen, I.; Schiedel, A. C.; Müller, C. E. Characterization of New G Protein-Coupled Adenine Receptors in Mouse and Hamster. *Purinergic Signalling* **2013**, *9* (3), 415–426.
- (26) Borrmann, T.; Abdelrahman, A.; Volpini, R.; Lambertucci, C.; Alksnis, E.; Gorzalka, S.; Knospe, M.; Schiedel, A. C.; Cristalli, G.; Müller, C. E. Structure-Activity Relationships of Adenine and Deazaadenine Derivatives as Ligands for Adenine Receptors, a New Purinergic Receptor Family. *J. Med. Chem.* **2009**, *52* (19), 5974–5989.
- (27) Fredholm, B. B.; IJzerman, A. P.; Jacobson, K. A.; Linden, J.; Müller, C. E. International Union of Basic and Clinical Pharmacology. LXXXI. Nomenclature and Classification of Adenosine Receptors-an Update. *Pharmacol. Rev.* **2011**, *63* (1), 1–34.
- (28) Di Virgilio, F.; Vuerich, M. Purinergic Signaling in the Immune System. *Auton. Neurosci.* **2015**, *191*, 117–123.
- (29) Burnstock, G. Pathophysiology and Therapeutic Potential of Purinergic Signaling. *Pharmacol Rev* **2006**, *58* (1), 58–86.
- (30) Allard, B.; Beavis, P. A.; Darcy, P. K.; Stagg, J. Immunosuppressive Activities of Adenosine in Cancer. *Curr. Opin. Pharmacol.* **2016**, *29*, 7–16.
- (31) Poth, J. M.; Brodsky, K.; Ehrentraut, H.; Grenz, A.; Eltzschig, H. K. Transcriptional

- Control of Adenosine Signaling by Hypoxia-Inducible Transcription Factors during Ischemic or Inflammatory Disease. *J. Mol. Med.* **2013**, *91* (2), 183–193.
- (32) Boison, D.; Yegutkin, G. G. Adenosine Metabolism: Emerging Concepts for Cancer Therapy. *Cancer Cell* **2019**, *36* (6), 582–596.
- (33) Sitkovsky, M. V. Lessons from the A<sub>2A</sub> Adenosine Receptor Antagonist-Enabled Tumor Regression and Survival in Patients with Treatment-Refractory Renal Cell Cancer. *Cancer Discovery* **2020**, *10* (1), 16–19.
- (34) Burnstock, G. Purinergic Signalling: From Discovery to Current Developments. *Exp. Physiol.* **2014**, *99* (1), 16–34.
- (35) Sitkovsky, M. V.; Hatfield, S.; Abbott, R.; Belikoff, B.; Lukashev, D.; Ohta, A. Hostile, Hypoxia-A<sub>2</sub>-Adenosinergic Tumor Biology as the next Barrier to Overcome for Tumor Immunologists. *Cancer Immunol. Res.* **2014**, *2* (7), 598–605.
- (36) Fong, L.; Hotson, A.; Powderly, J. D.; Sznol, M.; Heist, R. S.; Choueiri, T. K.; George, S.; Hughes, B. G. M.; Hellmann, M. D.; Shepard, D. R.; et al. Adenosine 2A Receptor Blockade as an Immunotherapy for Treatment-Refractory Renal Cell Cancer. *Cancer Discovery* **2020**, *10* (1), 40–53.
- (37) Zimmermann, H.; Zebisch, M.; Sträter, N. Cellular Function and Molecular Structure of Ecto-Nucleotidases. *Purinergic Signalling* **2012**, *8* (3), 437–502.
- (38) Zimmermann, H. Extracellular Metabolism of ATP and Other Nucleotides. *Naunyn-Schmiedeberg's Arch. Pharmacol.* **2000**, *362* (4–5), 299–309.
- (39) Schneider, E.; Rissiek, A.; Winzer, R.; Puig, B.; Rissiek, B.; Haag, F.; Mittrücker, H. W.; Magnus, T.; Tolosa, E. Generation and Function of Non-Cell-Bound CD73 in Inflammation. *Front. Immunol.* **2019**, *10* (July), 1729.
- (40) Zimmermann, H. History of Ectonucleotidases and Their Role in Purinergic Signaling. *Biochem. Pharmacol.* **2021**, *187*, 114322.
- (41) Kukulski, F.; Lévesque, S. A.; Sévigny, J. Impact of Ectoenzymes on P<sub>2</sub> and P<sub>1</sub> Receptor Signaling. *Adv. Pharmacol.* **2011**, *61*, 263–299.
- (42) Kukulski, F.; Lévesque, S. A.; Lavoie, É. G.; Lecka, J.; Bigonnesse, F.; Knowles, A. F.; Robson, S. C.; Kirley, T. L.; Sévigny, J. Comparative Hydrolysis of P<sub>2</sub> Receptor Agonists by NTPDases 1, 2, 3 and 8. *Purinergic Signalling* **2005**, *1* (2), 193–204.
- (43) Yegutkin, G. G. Enzymes Involved in Metabolism of Extracellular Nucleotides and Nucleosides: Functional Implications and Measurement of Activities. *Crit. Rev. Biochem. Mol. Biol.* **2014**, *49* (6), 473–497.
- (44) Handa, M.; Guidotti, G. Purification and Cloning of a Soluble ATP-Diphosphohydrolase (Apyrase) from Potato Tubers (*Solanum Tuberosum*). *Biochem. Biophys. Res. Commun.* **1996**, *218* (3), 916–923.
- (45) Schulte Am Esch, J.; Sévigny, J.; Kaczmarek, E.; Siegel, J. B.; Imai, M.; Koziak, K.; Beaudoin, A. R.; Robson, S. C. Structural Elements and Limited Proteolysis of CD39 Influence ATP Diphosphohydrolase Activity. *Biochemistry* **1999**, *38* (8), 2248–

- 2258.
- (46) Grinthal, A.; Guidotti, G. Transmembrane Domains Confer Different Substrate Specificities and Adenosine Diphosphate Hydrolysis Mechanisms on CD39, CD39L1, and Chimeras. *Biochemistry* **2002**, *41* (6), 1947–1956.
- (47) Failer, B. U.; Aschrafi, A.; Schmalzing, G.; Zimmermann, H. Determination of Native Oligomeric State and Substrate Specificity of Rat NTPDase1 and NTPDase2 after Heterologous Expression in *Xenopus* Oocytes. *Eur. J. Biochem.* **2003**, *270* (8), 1802–1809.
- (48) Grinthal, A.; Guidotti, G. CD39, NTPDase 1, Is Attached to the Plasma Membrane by Two Transmembrane Domains. Why? *Purinergic Signalling* **2006**, *2* (2), 391–398.
- (49) Zebisch, M.; Krauss, M.; Schäfer, P.; Lauble, P.; Sträter, N. Crystallographic Snapshots along the Reaction Pathway of Nucleoside Triphosphate Diphosphohydrolases. *Structure* **2013**, *21* (8), 1460–1475.
- (50) Fausther, M.; Lecka, J.; Kukulski, F.; Lévesque, S. A.; Pelletier, J.; Zimmermann, H.; Dranoff, J. A.; Sévigny, J. Cloning, Purification, and Identification of the Liver Canalicular Ecto-ATPase as NTPDase8. *Am J Physiol Gastrointest Liver Physiol* **2007**, *292* (3), 785–795.
- (51) Zebisch, M.; Krauss, M.; Schäfer, P.; Sträter, N. Crystallographic Evidence for a Domain Motion in Rat Nucleoside Triphosphate Diphosphohydrolase (NTPDase) 1. *J. Mol. Biol.* **2012**, *415* (2), 288–306.
- (52) Lee, S.-Y.; Luo, X.; Namasivayam, V.; Geiss, J.; Mirza, S.; Pelletier, J.; Stephan, H.; Sévigny, J.; Müller, C. E. Development of a Selective and Highly Sensitive Fluorescence Assay for Nucleoside Triphosphate Diphosphohydrolase1 (NTPDase1, CD39). *Analyst* **2018**, *143* (22), 5417–5430.
- (53) Zebisch, M.; Sträter, N. Structural Insight into Signal Conversion and Inactivation by NTPDase2 in Purinergic Signaling. *Proc. Natl. Acad. Sci. U. S. A.* **2008**, *105* (19), 6882–6887.
- (54) Zebisch, M.; Baqi, Y.; Schäfer, P.; Müller, C. E.; Sträter, N. Crystal Structure of NTPDase2 in Complex with the Sulfoanthraquinone Inhibitor PSB-071. *J. Struct. Biol.* **2014**, *185* (3), 336–341.
- (55) Robson, S. C.; Sévigny, J.; Zimmermann, H. The E-NTPDase Family of Ectonucleotidases: Structure Function Relationships and Pathophysiological Significance. *Purinergic Signalling* **2006**, *2* (2), 409–430.
- (56) Dwyer, K. M.; Deaglio, S.; Gao, W.; Friedman, D.; Strom, T. B.; Robson, S. C. CD39 and Control of Cellular Immune Responses. *Purinergic Signalling* **2007**, *3* (1–2), 171–180.
- (57) Deaglio, S.; Robson, S. C. Ectonucleotidases as Regulators of Purinergic Signaling in Thrombosis, Inflammation, and Immunity. *Adv. Pharmacol.* **2011**, *61*, 301–332.
- (58) Mizumoto, N.; Kumamoto, T.; Robson, S. C.; Sévigny, J.; Matsue, H.; Enjyoji, K;

- Takashima, A. CD39 Is the Dominant Langerhans Cell – Associated Ecto- NTPDase : Modulatory Roles in Inflammation and Immune Responsiveness. *Nature* **2002**, *8* (4), 358–365.
- (59) Marcus, A. J.; Broekman, M. J.; Drosopoulos, J. H. F.; Olson, K. E.; Islam, N.; Pinsky, D. J.; Levi, R. Role of CD39 (NTPDase-1) in Thromboregulation, Cerebroprotection, and Cardioprotection. *Semin. Thromb. Hemostasis* **2005**, *31* (2), 234–246.
- (60) Kauffenstein, G.; Fürstenau, C. R.; D’Orléans-Juste, P.; Sévigny, J. The Ecto-Nucleotidase NTPDase1 Differentially Regulates P2Y<sub>1</sub> and P2Y<sub>2</sub> Receptor-Dependent Vasorelaxation. *Br. J. Pharmacol.* **2010**, *159* (3), 576–585.
- (61) Banz, Y.; Beldi, G.; Wu, Y.; Atkinson, B.; Usheva, A.; Robson, S. C. CD39 Is Incorporated into Plasma Microparticles Where It Maintains Functional Properties and Impacts Endothelial Activation. *Br. J. Haematol.* **2008**, *142* (4), 627–637.
- (62) Zhong, E. H.; Ledderose, C.; De Andrade Mello, P.; Enjyoji, K.; Lunderberg, J. M.; Junger, W.; Robson, S. C. Structural and Functional Characterization of Engineered Bifunctional Fusion Proteins of CD39 and CD73 Ectonucleotidases. *Am. J. Physiol.* **2021**, *320* (1), C15-C29.
- (63) Abraham, M.-K.; Jost, E.; Hohmann, J. D.; Searle, A. K.; Bongcaron, V.; Song, Y.; Wendel, H. P.; Peter, K.; Krajewski, S.; Wang, X. A Recombinant Fusion Construct between Human Serum Albumin and NTPDase CD39 Allows Anti-Inflammatory and Anti-Thrombotic Coating of Medical Devices. *Pharmaceutics* **2021**, *13* (9), 1504.
- (64) Clayton, A.; Al-Taei, S.; Webber, J.; Mason, M. D.; Tabi, Z. Cancer Exosomes Express CD39 and CD73, Which Suppress T Cells through Adenosine Production. *J. Immunol.* **2011**, *187* (2), 676–683.
- (65) Tan, D. B. A.; Ong, N. E.; Zimmermann, M.; Price, P.; Moodley, Y. P. An Evaluation of CD39 as a Novel Immunoregulatory Mechanism Invoked by COPD. *Hum. Immunol.* **2016**, *77* (10), 916–920.
- (66) Lazar, Z.; Müllner, N.; Lucattelli, M.; Ayata, C. K.; Cicko, S.; Yegutkin, G. G.; De Cunto, G.; Müller, T.; Meyer, A.; Hossfeld, M.; et al. NTPDase1/CD39 and Aberrant Purinergic Signalling in the Pathogenesis of COPD. *Eur. Respir. J.* **2016**, *47* (1), 254–263.
- (67) Zhao, H.; Bo, C.; Kang, Y.; Li, H. What Else Can CD39 Tell Us? *Front. Immunol.* **2017**, *8*, 727.
- (68) Pelus, L. M.; Broxmeyer, H. E. Peripheral Blood Stem Cell Mobilization; A Look Ahead. *Curr. Stem Cell Rep.* **2018**, *4* (4), 273–281.
- (69) Adamiak, M.; Bujko, K.; Brzezniakiewicz-Janus, K.; Kucia, M.; Ratajczak, J.; Ratajczak, M. Z. The Inhibition of CD39 and CD73 Cell Surface Ectonucleotidases by Small Molecular Inhibitors Enhances the Mobilization of Bone Marrow Residing Stem Cells by Decreasing the Extracellular Level of Adenosine. *Stem Cell Rev. Rep.* **2019**, *15* (6), 892–899.

- (70) Zeng, J.; Ning, Z.; Wang, Y.; Xiong, H. Implications of CD39 in Immune-Related Diseases. *Int. Immunopharmacol.* **2020**, *89* (Pt A), 107055.
- (71) Allard, D.; Allard, B.; Stagg, J. On the Mechanism of Anti-CD39 Immune Checkpoint Therapy. *Journal for Immunotherapy of Cancer* **2020**, *8* (1), e000186.
- (72) Moesta, A. K.; Li, X.-Y.; Smyth, M. J. Targeting CD39 in Cancer. *Nat. Rev. Immunol.* **2020**, *20* (12), 739–755.
- (73) Feng, L.; Xiaofeng, S.; Csizmadia, E.; Han, L.; Bian, S.; Murakami, T.; Wang, X.; Robson, S. C.; Wu, Y. Vascular CD39/ENTPD1 Directly Promotes Tumor Cell Growth by Scavenging Extracellular Adenosine Triphosphate. *Neoplasia* **2011**, *13* (3), 206–216.
- (74) Allard, B.; Longhi, M. S.; Robson, S. C.; Stagg, J. The Ectonucleotidases CD39 and CD73: Novel Checkpoint Inhibitor Targets. *Immunol. Rev.* **2017**, *276* (1), 121–144.
- (75) Bastid, J.; Regairaz, A.; Bonnefoy, N.; Déjou, C.; Giustiniani, J.; Laheurte, C.; Cochaud, S.; Laprevotte, E.; Funck-Brentano, E.; Hemon, P.; et al. Inhibition of CD39 Enzymatic Function at the Surface of Tumor Cells Alleviates Their Immunosuppressive Activity. *Cancer Immunol. Res.* **2015**, *3* (3), 254–265.
- (76) Duhén, T.; Duhén, R.; Montler, R.; Moses, J.; Moudgil, T.; Miranda, N. F. De; Goodall, C. P.; Blair, T. C.; Fox, B. A.; McDermott, J. E.; et al. Co-Expression of CD39 and CD103 Identifies Tumor-Reactive CD8 T Cells in Human Solid Tumors. *Nat. Commun.* **2018**, *9* (1), 2724.
- (77) Ghiringhelli, F.; Bruchard, M.; Chalmin, F.; Rébé, C. Production of Adenosine by Ectonucleotidases: A Key Factor in Tumor Immunoescape. *J. Biomed. Biotechnol.* **2012**, *2012*, 473712.
- (78) Bastid, J.; Cottalorda-Regairaz, A.; Alberici, G.; Bonnefoy, N.; Eliaou, J.-F.; Bensussan, A. ENTPD1/CD39 Is a Promising Therapeutic Target in Oncology. *Oncogene* **2013**, *32* (14), 1743–1751.
- (79) Cai, X.-Y.; Wang, X.-F.; Li, J.; Dong, J.-N.; Liu, J.-Q.; Li, N.-P.; Yun, B.; Xia, R.-L.; Qin, J.; Sun, Y.-H. High Expression of CD39 in Gastric Cancer Reduces Patient Outcome Following Radical Resection. *Oncol. Lett.* **2016**, *12* (5), 4080–4086.
- (80) Deli, T.; Csernoch, L. Extracellular ATP and Cancer: An Overview with Special Reference to P2 Purinergic Receptors. *Pathology Oncology Research* **2008**, *14* (3), 219–231.
- (81) Antonioli, L.; Pacher, P.; Vizi, E. S.; Haskó, G. CD39 and CD73 in Immunity and Inflammation. *Trends Mol. Med.* **2013**, *19* (6), 355–367.
- (82) Nikolova, M.; Carriere, M.; Jenabian, M.-A.; Limou, S.; Younas, M.; Kök, A.; Huë, S.; Seddiki, N.; Hulin, A.; Delaneau, O.; et al. CD39/Adenosine Pathway Is Involved in AIDS Progression. *PLoS Pathog.* **2011**, *7* (7), e1002110.
- (83) Bönner, F.; Borg, N.; Burghoff, S.; Schrader, J. Resident Cardiac Immune Cells and Expression of the Ectonucleotidase Enzymes CD39 and CD73 after Ischemic Injury.



- PLoS One* **2012**, 7 (4), e34730.
- (84) Zhang, B. CD73 Promotes Tumor Growth and Metastasis. *Oncoimmunology* **2012**, 1 (1), 67–70.
- (85) Knowles, A. F. The GDA1\_CD39 Superfamily: NTPDases with Diverse Functions. *Purinergic Signalling* **2011**, 7 (1), 21–45.
- (86) Massé, K.; Bhamra, S.; Eason, R.; Dale, N.; Jones, E. A. Purine-Mediated Signalling Triggers Eye Development. *Nature* **2007**, 449 (7165), 1058–1062.
- (87) Lavoie, E. G.; Fausther, M.; Kauffenstein, G.; Kukulski, F.; Künzli, B. M.; Friess, H.; Sévigny, J. Identification of the Ectonucleotidases Expressed in Mouse, Rat, and Human Langerhans Islets: Potential Role of NTPDase3 in Insulin Secretion. *Am. J. Physiol.: Endocrinol. Metab.* **2010**, 299 (4), E647–656.
- (88) Zimmermann, H. Ectonucleoside Triphosphate Diphosphohydrolases and Ecto-5'-Nucleotidase in Purinergic Signaling: How the Field Developed and Where We Are Now. *Purinergic Signalling* **2021**, 17 (1), 117–125.
- (89) Gendron, F. P.; Benrezzak, O.; Krugh, B. W.; Kong, Q.; Weisman, G. A.; Beaudoin, A. R. Purine Signaling and Potential New Therapeutic Approach: Possible Outcomes of NTPDase Inhibition. *Curr. Drug Targets* **2002**, 3 (3), 229–245.
- (90) Munkonda, M. N.; Kauffenstein, G.; Kukulski, F.; Lévesque, S. A.; Legendre, C.; Pelletier, J.; Lavoie, E. G.; Lecka, J.; Sévigny, J. Inhibition of Human and Mouse Plasma Membrane Bound NTPDases by P2 Receptor Antagonists. *Biochem. Pharmacol.* **2007**, 74 (10), 1524–1534.
- (91) Lecka, J.; Gillerman, I.; Fausther, M.; Salem, M.; Munkonda, M. N.; Brosseau, J.-P.; Cadot, C.; Martín-Satué, M.; d'Orléans-Juste, P.; Rousseau, E.; et al. 8-BuS-ATP Derivatives as Specific NTPDase1 Inhibitors. *Br. J. Pharmacol.* **2013**, 169 (1), 179–196.
- (92) Gendron, F. P.; Halbfinger, E.; Fischer, B.; Duval, M.; d'Orléans-Juste, P.; Beaudoin, A. R. Novel Inhibitors of Nucleoside Triphosphate Diphosphohydrolases: Chemical Synthesis and Biochemical and Pharmacological Characterizations. *J. Med. Chem.* **2000**, 43 (11), 2239–2247.
- (93) Lévesque, S. A.; Lavoie, E. G.; Lecka, J.; Bigonnesse, F.; Sévigny, J. Specificity of the Ecto-ATPase Inhibitor ARL 67156 on Human and Mouse Ectonucleotidases. *Br. J. Pharmacol.* **2007**, 152 (1), 141–150.
- (94) Schäkel, L.; Schmies, C. C.; Idris, R. M.; Luo, X.; Lee, S.-Y.; Lopez, V.; Mirza, S.; Vu, T. H.; Pelletier, J.; Sévigny, J.; et al. Nucleotide Analog ARL67156 as a Lead Structure for the Development of CD39 and Dual CD39/CD73 Ectonucleotidase Inhibitors. *Front. Pharmacol.* **2020**, 11, 1294.
- (95) Mandapathil, M.; Hilldorfer, B.; Szczepanski, M. J.; Czystowska, M.; Szajnik, M.; Ren, J.; Lang, S.; Jackson, E. K.; Gorelik, E.; Whiteside, T. L. Generation and Accumulation of Immunosuppressive Adenosine by Human CD4<sup>+</sup>CD25<sup>high</sup>FOXP3<sup>+</sup> Regulatory T

- Cells. *J. Biol. Chem.* **2010**, *285* (10), 7176–7186.
- (96) Zhou, J. Z.; Riquelme, M. A.; Gao, X.; Ellies, L. G.; Sun, L. Z.; Jiang, J. X. Differential Impact of Adenosine Nucleotides Released by Osteocytes on Breast Cancer Growth and Bone Metastasis. *Oncogene* **2015**, *34* (14), 1831–1842.
- (97) Li, P.; Gao, Y.; Cao, J.; Wang, W.; Chen, Y.; Zhang, G.; Robson, S. C.; Wu, Y.; Yang, J. CD39<sup>+</sup> Regulatory T Cells Attenuate Allergic Airway Inflammation. *Clin. Exp. Allergy* **2015**, *45* (6), 1126–1137.
- (98) Gillerman, I.; Lecka, J.; Simhaev, L.; Munkonda, M. N.; Fausther, M.; Martín-Satué, M.; Senderowitz, H.; Sévigny, J.; Fischer, B. 2-Hexylthio- $\beta,\gamma$ -CH<sub>2</sub>-ATP Is an Effective and Selective NTPDase2 Inhibitor. *J. Med. Chem.* **2014**, *57* (14), 5919–5934.
- (99) Brunschweiler, A.; Iqbal, J.; Umbach, F.; Scheiff, A. B.; Munkonda, M. N.; Sévigny, J.; Knowles, A. F.; Müller, C. E. Selective Nucleoside Triphosphate Diphosphohydrolase-2 (NTPDase2) Inhibitors: Nucleotide Mimetics Derived from Uridine-5'-Carboxamide. *J. Med. Chem.* **2008**, *51* (15), 4518–4528.
- (100) Lee, S.-Y.; Fiene, A.; Li, W.; Hanck, T.; Brylev, K. A.; Fedorov, V. E.; Lecka, J.; Haider, A.; Pietzsch, H.-J.; Zimmermann, H.; et al. Polyoxometalates--Potent and Selective Ecto-Nucleotidase Inhibitors. *Biochem. Pharmacol.* **2015**, *93* (2), 171–181.
- (101) Müller, C. E.; Iqbal, J.; Baqi, Y.; Zimmermann, H.; Röllich, A.; Stephan, H. Polyoxometalates--a New Class of Potent Ecto-Nucleoside Triphosphate Diphosphohydrolase (NTPDase) Inhibitors. *Bioorg Med. Chem. Lett.* **2006**, *16* (23), 5943–5947.
- (102) Zhang, H.; Vijayan, D.; Li, X.-Y.; Robson, S. C.; Geetha, N.; Teng, M. W. L.; Smyth, M. J. The Role of NK Cells and CD39 in the Immunological Control of Tumor Metastases. *Oncoimmunology* **2019**, *8* (6), e1593809.
- (103) Battastini, A. M. O.; Figueiró, F.; Leal, D. B. R.; Doleski, P. H.; Schetinger, M. R. C. CD39 and CD73 as Promising Therapeutic Targets: What Could Be the Limitations? *Front. Pharmacol.* **2021**, *12*, 633603.
- (104) Baqi, Y.; Weyler, S.; Iqbal, J.; Zimmermann, H.; Müller, C. E. Structure-Activity Relationships of Anthraquinone Derivatives Derived from Bromaminic Acid as Inhibitors of Ectonucleoside Triphosphate Diphosphohydrolases (E-NTPDases). *Purinergic Signalling* **2009**, *5* (1), 91–106.
- (105) Baqi, Y.; Rashed, M.; Schäkel, L.; Malik, E. M.; Pelletier, J.; Sévigny, J.; Fiene, A.; Müller, C. E. Development of Anthraquinone Derivatives as Ectonucleoside Triphosphate Diphosphohydrolase (NTPDase) Inhibitors With Selectivity for NTPDase2 and NTPDase3. *Front. Pharmacol.* **2020**, *11*, 1282.
- (106) Baqi, Y.; Müller, C. E. Antithrombotic P2Y<sub>12</sub> Receptor Antagonists: Recent Developments in Drug Discovery. *Drug Discovery Today* **2019**, *24* (1), 325–333.
- (107) Bernlochner, I.; Sibbing, D. Thienopyridines and Other ADP-Receptor Antagonists. In *Handbook of Experimental Pharmacology*; Vol. 210; Springer, 2012; pp 165–198.

- (108) Lecka, J.; Rana, M. S.; Sévigny, J. Inhibition of Vascular Ectonucleotidase Activities by the Pro-Drugs Ticlopidine and Clopidogrel Favours Platelet Aggregation. *Br. J. Pharmacol.* **2010**, *161* (5), 1150–1160.
- (109) Lecka, J.; Fausther, M.; Künzli, B.; Sévigny, J. Ticlopidine in Its Prodrug Form Is a Selective Inhibitor of Human NTPDase1. *Mediators Inflammation* **2014**, *2014*, 547480.
- (110) Schäkel, L.; Mirza, S.; Pietsch, M.; Lee, S.-Y.; Keuler, T.; Sylvester, K.; Pelletier, J.; Sévigny, J.; Pillaiyar, T.; Namasivayam, V.; et al. 2-Substituted Thienotetrahydropyridine Derivatives: Allosteric Ectonucleotidase Inhibitors. *Arch. Pharm. (Weinheim, Ger.)* **2021**, *354* (12), e2100300.
- (111) Kanwal, K. M. K.; Salar, U.; Afzal, S.; Wadood, A.; Taha, M.; Perveen, S.; Khan, H.; Lecka, J.; Sévigny, J.; Iqbal, J. Schiff Bases of Tryptamine as Potent Inhibitors of Nucleoside Triphosphate Diphosphohydrolases (NTPDases): Structure-Activity Relationship. *Bioorg. Chem.* **2019**, *82*, 253–266.
- (112) Abbas, S.; Afzal, S.; Nadeem, H.; Hussain, D.; Langer, P.; Sévigny, J.; Ashraf, Z.; Iqbal, J. Synthesis, Characterization and Biological Evaluation of Thiadiazole Amide Derivatives as Nucleoside Triphosphate Diphosphohydrolases (NTPDases) Inhibitors. *Bioorg. Chem.* **2022**, *118*, 105456.
- (113) Afzal, S.; Al-Rashida, M.; Hameed, A.; Pelletier, J.; Sévigny, J.; Iqbal, J. Synthesis, In-Vitro Evaluation and Molecular Docking Studies of Oxindolin Phenylhydrazine Carboxamides as Potent and Selective Inhibitors of Ectonucleoside Triphosphate Diphosphohydrolase (NTPDase). *Bioorg. Chem.* **2021**, *112*, 104957.
- (114) Afzal, S.; Al-Rashida, M.; Hameed, A.; Pelletier, J.; Sévigny, J.; Iqbal, J. Functionalized Oxindolin Hydrazine Carbothioamide Derivatives as Highly Potent Inhibitors of Nucleoside Triphosphate Diphosphohydrolases. *Front. Pharmacol.* **2020**, *11*, 585876.
- (115) Afzal, S.; Zaib, S.; Jafari, B.; Langer, P.; Lecka, J.; Sévigny, J.; Iqbal, J. Highly Potent and Selective Ectonucleoside Triphosphate Diphosphohydrolase (ENTPDase1, 2, 3 and 8) Inhibitors Having 2-Substituted-7-Trifluoromethyl-Thiadiazolo-pyrimidones Scaffold. *Med. Chem. (Sharjah, United Arab Emirates)* **2020**, *16* (5), 689–702.
- (116) Hayat, K.; Afzal, S.; Saeed, A.; Murtaza, A.; Ur Rahman, S.; Khan, K. M.; Saeed, A.; Zaib, S.; Lecka, J.; Sévigny, J.; et al. Investigation of New Quinoline Derivatives as Promising Inhibitors of NTPDases: Synthesis, SAR Analysis and Molecular Docking Studies. *Bioorg. Chem.* **2019**, *87*, 218–226.
- (117) Murtaza, A.; Afzal, S.; Zaman, G.; Saeed, A.; Pelletier, J.; Sévigny, J.; Iqbal, J.; Hassan, A. Divergent Synthesis and Elaboration of Structure Activity Relationship for Quinoline Derivatives as Highly Selective NTPDase Inhibitor. *Bioorg. Chem.* **2021**, *115*, 105240.
- (118) Jafari, B.; Ospanov, M.; Ejaz, S. A.; Yelibayeva, N.; Khan, S. U.; Amjad, S. T.; Safarov, S.; Abilov, Z. A.; Turmukhanova, M. Z.; Kalugin, S. N.; et al. 2-Substituted 7-

- Trifluoromethyl-Thiadiazolopyrimidones as Alkaline Phosphatase Inhibitors. Synthesis, Structure Activity Relationship and Molecular Docking Study. *Eur. J. Med. Chem.* **2018**, *144*, 116–127.
- (119) Zhao, Y.; Chen, X.; Ding, Z.; He, C.; Gao, G.; Lyu, S.; Gao, Y.; Du, J. Identification of Novel CD39 Inhibitors Based on Virtual Screening and Enzymatic Assays. *J. Chem. Inf. Model.* **2021**, [Online early access].  
DOI: <https://doi.org/10.1021/acs.jcim.1c00590>. Published Online: Oct 14, 2021
- (120) Fiene, A. Entwicklung und Bewertung verschiedener Methoden zur Aktivitätsbestimmung von Ectonucleotidasen und zur Identifizierung von Inhibitoren. Dissertation, University of Bonn, Germany, 2015.
- (121) Lopez, V.; Schäkel, L.; Schuh, M. H. J.; Schmidt, M. S.; Mirza, S.; Renn, C.; Pelletier, J.; Lee, S.-Y.; Sévigny, J.; Alban, S.; et al. Sulfated Polysaccharides from Macroalgae Are Potent Dual Inhibitors of Human ATP-Hydrolyzing Ectonucleotidasen NPP1 and CD39. *Mar. Drugs* **2021**, *19* (2), 51.
- (122) Pelletier, J.; Agonsanou, H.; Delvalle, N.; Fausther, M.; Salem, M.; Gulbransen, B.; Sévigny, J. Generation and Characterization of Polyclonal and Monoclonal Antibodies to Human NTPDase2 Including a Blocking Antibody. *Purinergic Signalling* **2017**, *13* (3), 293–304.
- (123) Munkonda, M. N.; Pelletier, J.; Ivanenkov, V. V.; Fausther, M.; Tremblay, A.; Künzli, B.; Kirley, T. L.; Sévigny, J. Characterization of a Monoclonal Antibody as the First Specific Inhibitor of Human NTP Diphosphohydrolase-3: Partial Characterization of the Inhibitory Epitope and Potential Applications. *FEBS J.* **2009**, *276* (2), 479–496.
- (124) Pelletier, J.; Salem, M.; Lecka, J.; Fausther, M.; Bigonnesse, F.; Sévigny, J. Generation and Characterization of Specific Antibodies to the Murine and Human Ectonucleotidase NTPDase8. *Front. Pharmacol.* **2017**, *8*, 115.
- (125) Perrot, I.; Michaud, H. A.; Giraudon-Paoli, M.; Augier, S.; Docquier, A.; Gros, L.; Courtois, R.; Déjou, C.; Jecko, D.; Becquart, O.; et al. Blocking Antibodies Targeting the CD39/CD73 Immunosuppressive Pathway Unleash Immune Responses in Combination Cancer Therapies. *Cell Rep.* **2019**, *27* (8), 2411-2425.e9.
- (126) Matissek, S.; Sicheva, M. P.; Koseoglu, S.; Masia, R.; Waaren, M.; Rausch, M.; Lee, B.; Pommey, S.; Cousineau, I.; Stagg, J.; et al. The Fully Human Antibody SRF617 Is a Potent Inhibitor of Ecto-Enzyme CD39 in Vivo. *Journal for Immunotherapy of Cancer* **2021**, *9* (Suppl 2), A1-A1054.
- (127) Spatola, B. N.; Lerner, A. G.; Wong, C.; Dela Cruz, T.; Welch, M.; Fung, W.; Kovalenko, M.; Losenkova, K.; Yegutkin, G. G.; Beers, C.; et al. Fully Human Anti-CD39 Antibody Potently Inhibits ATPase Activity in Cancer Cells via Uncompetitive Allosteric Mechanism. *MAbs* **2020**, *12* (1), 1838036.
- (128) Guo, J.; Yang, P.; Li, Y. F.; Tang, J. F.; He, Z. X.; Yu, S. G.; Yin, H. Y. MicroRNA: Crucial Modulator in Purinergic Signalling Involved Diseases. *Purinergic Signaling*, [Online early access]. DOI: [10.1007/s11302-022-09840-y](https://doi.org/10.1007/s11302-022-09840-y). Published Online: Feb 2, 2022.

- (129) Ferrari, D.; Bianchi, N.; Eltzschig, H. K.; Gambari, R. MicroRNAs Modulate the Purinergic Signaling Network. *Trends Mol. Med.* **2016**, *22* (10), 905–918.
- (130) Baykov, A. A.; Evtushenko, A.; Avaeva, S. M. A Malachite Green Procedure for Orthophosphate Determination and Its Use in Alkaline Phosphatase-Based Enzyme Immunoassay. *Anal. Biochem.* **1988**, *171* (2), 266–270.
- (131) Iqbal, J.; Vollmayer, P.; Braun, N.; Zimmermann, H.; Müller, C. E. A Capillary Electrophoresis Method for the Characterization of Ecto-Nucleoside Triphosphate Diphosphohydrolases (NTPDases) and the Analysis of Inhibitors by in-Capillary Enzymatic Microreaction. *Purinergic Signalling* **2005**, *1* (4), 349–358.
- (132) Fiene, A.; Baqi, Y.; Lecka, J.; Sévigny, J.; Müller, C. E. Fluorescence Polarization Immunoassays for Monitoring Nucleoside Triphosphate Diphosphohydrolase (NTPDase) Activity. *Analyst* **2015**, *140* (1), 140–148.
- (133) Staeben, M.; Kleman-Leyer, K. M.; Kopp, A. L.; Westermeyer, T. A.; Lowery, R. G. Development and Validation of a Transcreeper Assay for Detection of AMP- and GMP-Producing Enzymes. *Assay Drug Dev. Technol.* **2010**, *8* (3), 344–355.
- (134) Kleman-Leyer, K. M.; Klink, T. A.; Kopp, A. L.; Westermeyer, T. A.; Koeff, M. D. Larson, B. R.; Worzella, T. J.; Pinchard, C. A.; van de Kar, S. A. T.; Zaman, G. J. R.; et al. Characterization and Optimization of a Red-Shifted Fluorescence Polarization ADP Detection Assay. *Assay Drug Dev. Technol.* **2009**, *7* (1), 56–67.
- (135) Ledderose, C.; Valsami, E.-A.; Junger, W. G. Optimized HPLC Method to Elucidate the Complex Purinergic Signaling Dynamics That Regulate ATP, ADP, AMP, and Adenosine Levels in Human Blood. *Purinergic Signalling* **2022**, *18* (2), 223–239.
- (136) Akhova, A. V.; Tkachenko, A. G. HPLC–UV Method for Simultaneous Determination of Adenosine Triphosphate and Its Metabolites in Mycobacterium Smegmatis. *Acta Chromatogr.* **2019**, *31* (1), 45–48.
- (137) Goueli, S. A.; Hsiao, K. Monitoring and Characterizing Soluble and Membrane-Bound Ectonucleotidases CD73 and CD39. *PLoS One* **2019**, *14* (10), e0220094.
- (138) Crack, B. E.; Pollard, C. E.; Beukers, M. W.; Roberts, S. M.; Hunt, S. F.; Ingall, A. H.; McKechnie, K. C.; IJzerman, A. P.; Leff, P. Pharmacological and Biochemical Analysis of FPL 67156, a Novel, Selective Inhibitor of Ecto-ATPase. *Br. J. Pharmacol.* **1995**, *114* (2), 475–481.
- (139) Yegutkin, G. G.; Wieringa, B.; Robson, S. C.; Jalkanen, S. Metabolism of Circulating ADP in the Bloodstream Is Mediated via Integrated Actions of Soluble Adenylate Kinase-1 and NTPDase1/CD39 Activities. *FASEB J.* **2012**, *26* (9), 3875–3883.
- (140) Overman, M. J.; LoRusso, P.; Strickler, J. H.; Patel, S. P.; Clarke, S. J.; Noonan, A. M.; Prasanna, T.; Amin, M. A.; Nemunaitis, J. J.; Desai, J.; et al. Safety, Efficacy and Pharmacodynamics (PD) of MEDI9447 (Oleclumab) Alone or in Combination with Durvalumab in Advanced Colorectal Cancer (CRC) or Pancreatic Cancer (Panc). *J. Clin. Oncol.* **2018**, *36* (15), 4123–4123.

- (141) Hay, C. M.; Sult, E.; Huang, Q.; Mulgrew, K.; Fuhrmann, S. R.; McGlinchey, K. A.; Hammond, S. A.; Rothstein, R.; Rios-Doria, J.; Poon, E.; et al. Targeting CD73 in the Tumor Microenvironment with MEDI9447. *Oncoimmunology* **2016**, *5* (8), e1208875.
- (142) Nocentini, A.; Capasso, C.; Supuran, C. T. Small-Molecule CD73 Inhibitors for the Immunotherapy of Cancer: A Patent and Literature Review (2017–Present). *Expert Opin. Ther. Pat.* **2021**, *31* (10), 867–876.
- (143) Knapp, K.; Zebisch, M.; Pippel, J.; El-Tayeb, A.; Müller, C. E.; Sträter, N. Crystal Structure of the Human Ecto-5'-Nucleotidase (CD73): Insights into the Regulation of Purinergic Signaling. *Structure* **2012**, *20* (12), 2161–2173.
- (144) Bhattarai, S.; Pippel, J.; Meyer, A.; Freundlieb, M.; Schmies, C. C.; Abdelrahman, A.; Fiene, A.; Lee, S.-Y.; Zimmermann, H.; El-Tayeb, A.; et al. X-Ray Co-crystal Structure Guides the Way to Subnanomolar Competitive Ecto-5'-nucleotidase (CD73) Inhibitors for Cancer Immunotherapy. *Adv. Ther. (Weinheim, Ger.)* **2019**, *2* (10), 1900075.
- (145) Bowman, C. E.; da Silva, R. G.; Pham, A.; Young, S. W. An Exceptionally Potent Inhibitor of Human CD73. *Biochemistry* **2019**, *58* (31), 3331–3334.
- (146) Lawson, K. V.; Kalisiak, J.; Lindsey, E. A.; Newcomb, E. T.; Leleti, M. R.; Debien, L.; Rosen, B. R.; Miles, D. H.; Sharif, E. U.; Jeffrey, J. L.; et al. Discovery of AB680: A Potent and Selective Inhibitor of CD73. *J. Med. Chem.* **2020**, *63* (20), 11448–11468.
- (147) Du, X.; Moore, J.; Blank, B. R.; Eksterowicz, J.; Sutimantanapi, D.; Yuen, N.; Metzger, T.; Chan, B.; Huang, T.; Chen, X.; et al. Orally Bioavailable Small-Molecule CD73 Inhibitor (OP-5244) Reverses Immunosuppression through Blockade of Adenosine Production. *J. Med. Chem.* **2020**, *63* (18), 10433–10459.
- (148) Ripphausen, P.; Freundlieb, M.; Brunschweiger, A.; Zimmermann, H.; Müller, C. E.; Bajorath, J. Virtual Screening Identifies Novel Sulfonamide Inhibitors of Ecto -5'-Nucleotidase. *J. Med. Chem.* **2012**, *55* (14), 6576–6581.
- (149) Beatty, J. W.; Lindsey, E. A.; Thomas-Tran, R.; Debien, L.; Mandal, D.; Jeffrey, J. L.; Tran, A. T.; Fournier, J.; Jacob, S. D.; Yan, X.; et al. Discovery of Potent and Selective Non-Nucleotide Small Molecule Inhibitors of CD73. *J. Med. Chem.* **2020**, *63* (8), 3935–3955.
- (150) Dally, R. D.; Garcia Paredes, M. C.; Heinz, L.; Howell, J. M.; Njoroge, F. G.; Wang, Y.; Zhao, G. CD73 Inhibitors. International Publication Number WO 2019/168744 A1, September 6, 2019.
- (151) Bhattarai, S.; Freundlieb, M.; Pippel, J.; Meyer, A.; Abdelrahman, A.; Fiene, A.; Lee, S.-Y.; Zimmermann, H.; Yegutkin, G. G.; Sträter, N.; et al.  $\alpha,\beta$ -Methylene-ADP (AOPCP) Derivatives and Analogues: Development of Potent and Selective Ecto-5'-Nucleotidase (CD73) Inhibitors. *J. Med. Chem.* **2015**, *58* (15), 6248–6263.
- (152) Antonioli, L.; Blandizzi, C.; Pacher, P.; Haskó, G. Immunity, Inflammation and Cancer: A Leading Role for Adenosine. *Nat. Rev. Cancer* **2013**, *13* (12), 842–857.

- (153) Perrot, I.; Giraudon-Paoli, M.; Augier, S.; Jecko, D.; Gourdin, N.; Giribone-Thomann, C.; Royannez-Blemont, M.; Docquier, A.; Lalanne, A.; Perrier, C.; et al. Preclinical Development of Humanized CD39 (IPH52) and CD73 (IPH53) Blocking Antibodies Targeting the ATP/Adenosine Immune Checkpoint Pathway for Cancer Immunotherapy. Presented at AACR American Association for Cancer Research 2018; September 27-30, 2018; Poster ID 2718.
- (154) Su, S.; Wong, G.; Shi, W.; Liu, J.; Lai, A. C. K.; Zhou, J.; Liu, W.; Bi, Y.; Gao, G. F. Epidemiology, Genetic Recombination, and Pathogenesis of Coronaviruses. *Trends Microbiol.* **2016**, *24* (6), 490–502.
- (155) Ullrich, S.; Nitsche, C. The SARS-CoV-2 Main Protease as Drug Target. *Bioorg. Med. Chem. Lett.* **2020**, *30* (17), 127377.
- (156) De Wit, E.; van Doremalen, N.; Falzarano, D.; Munster, V. J. SARS and MERS: Recent Insights into Emerging Coronaviruses. *Nat. Rev. Microbiol.* **2016**, *14* (8), 523–534.
- (157) Gao, K.; Wang, R.; Chen, J.; Tepe, J. J.; Huang, F.; Wei, G.-W. Perspectives on SARS-CoV-2 Main Protease Inhibitors. *J. Med. Chem.* **2021**, *64* (23), 16922–16955.
- (158) Zhang, L.; Lin, D.; Sun, X.; Curth, U.; Drosten, C.; Sauerhering, L.; Becker, S.; Rox, K.; Hilgenfeld, R. Crystal Structure of SARS-CoV-2 Main Protease Provides a Basis for Design of Improved  $\alpha$ -Ketoamide Inhibitors. *Science* **2020**, *368* (6489), 409–412.
- (159) Pillaiyar, T.; Manickam, M.; Namasivayam, V.; Hayashi, Y.; Jung, S.-H. An Overview of Severe Acute Respiratory Syndrome-Coronavirus (SARS-CoV) 3CL Protease Inhibitors: Peptidomimetics and Small Molecule Chemotherapy. *J. Med. Chem.* **2016**, *59* (14), 6595–6628.
- (160) Jin, Z.; Du, X.; Xu, Y.; Deng, Y.; Liu, M.; Zhao, Y.; Zhang, B.; Li, X.; Zhang, L.; Peng, C.; et al. Structure of M<sup>pro</sup> from SARS-CoV-2 and Discovery of Its Inhibitors. *Nature* **2020**, *582* (7811), 289–293.
- (161) Rut, W.; Groborz, K.; Zhang, L.; Sun, X.; Zmudzinski, M.; Hilgenfeld, R.; Drag, M. Substrate Specificity Profiling of SARS-CoV-2 M<sup>pro</sup> Protease Provides Basis for Anti-COVID-19 Drug Design. *bioRxiv* **2020**, 2020.03.07.981928.
- (162) Venkatakrishnan, A.; Anand, P.; Lenehan, P.; Suratekar, R.; Raghunathan, B.; Niesen, M. J.; Soundararajan, V. Omicron Variant of SARS-CoV-2 Harbors a Unique Insertion Mutation of Putative Viral or Human Genomic Origin. *OSF Preprint* [Online preprint]. DOI: 10.31219/osf.io/f7txy. Published Online: December 3, 2021.
- (163) Owen, D. R.; Allerton, C. M. N.; Anderson, A. S.; Aschenbrenner, L.; Avery, M.; Berritt, S.; Boras, B.; Cardin, R. D.; Carlo, A.; Coffman, K. J.; et al. An Oral SARS-CoV-2 M<sup>pro</sup> Inhibitor Clinical Candidate for the Treatment of COVID-19. *Science*. **2021**, *347* (6575), 1586–1593.
- (164) Dai, W.; Zhang, B.; Jiang, X.-M.; Su, H.; Li, J.; Zhao, Y.; Xie, X.; Jin, Z.; Peng, J.; Liu, F.; et al. Structure-Based Design of Antiviral Drug Candidates Targeting the SARS-CoV-2 Main Protease. *Science*. **2020**, *368* (6497), 1331–1335.

- (165) Breidenbach, J.; Lemke, C.; Pillaiyar, T.; Schäkel, L.; Al Hamwi, G.; Dieltz, M.; Gedschold, R.; Geiger, N.; Lopez, V.; Mirza, S.; et al. Targeting the Main Protease of SARS-CoV-2: From the Establishment of High Throughput Screening to the Design of Tailored Inhibitors. *Angew. Chem., Int. Ed.* **2021**, *60* (18), 10423–10429.
- (166) Rut, W.; Groborz, K.; Zhang, L.; Sun, X.; Zmudzinski, M.; Pawlik, B.; Wang, X.; Jochmans, D.; Neyts, J.; Młynarski, W.; et al. SARS-CoV-2 M<sup>pro</sup> Inhibitors and Activity-Based Probes for Patient-Sample Imaging. *Nat. Chem. Biol.* **2021**, *17* (2), 222–228.
- (167) Van de Plassche, M. A. T.; Barniol-Xicotá, M.; Verhelst, S. H. L. Peptidyl Acyloxymethyl Ketones as Activity-Based Probes for the Main Protease of SARS-CoV-2. *ChemBioChem* **2020**, *21* (23), 3383–3388.
- (168) Zhu, W.; Xu, M.; Chen, C. Z.; Guo, H.; Shen, M.; Hu, X.; Shinn, P.; Klumpp-Thomas, C.; Michael, S. G.; Zheng, W. Identification of SARS-CoV-2 3CL Protease Inhibitors by a Quantitative High-Throughput Screening. *ACS Pharmacol. Transl. Sci.* **2020**, *3* (5), 1008–1016.
- (169) Ma, C.; Sacco, M. D.; Hurst, B.; Townsend, J. A.; Hu, Y.; Szeto, T.; Zhang, X.; Tarbet, B.; Marty, M. T.; Chen, Y.; et al. Boceprevir, GC-376, and Calpain Inhibitors II, XII Inhibit SARS-CoV-2 Viral Replication by Targeting the Viral Main Protease. *Cell Res.* **2020**, *30* (8), 678–692.
- (170) Shie, J.-J.; Fang, J.-M.; Kuo, T.-H.; Kuo, C.-J.; Liang, P.-H.; Huang, H.-J.; Wu, Y.-T.; Jan, J.-T.; Cheng, Y.-S. E.; Wong, C.-H. Inhibition of the Severe Acute Respiratory Syndrome 3CL Protease by Peptidomimetic  $\alpha,\beta$ -Unsaturated Esters. *Bioorganic Med. Chem.* **2005**, *13* (17), 5240–5252.
- (171) Wang, Y.-C.; Yang, W.-H.; Yang, C.-S.; Hou, M.-H.; Tsai, C.-L.; Chou, Y.-Z.; Hung, M.-C.; Chen, Y. Structural Basis of SARS-CoV-2 Main Protease Inhibition by a Broad-Spectrum Anti-Coronaviral Drug. *Am. J. Cancer Res.* **2020**, *10* (8), 2535–2545.
- (172) Xue, X.; Yang, H.; Shen, W.; Zhao, Q.; Li, J.; Yang, K.; Chen, C.; Jin, Y.; Bartlam, M.; Rao, Z. Production of Authentic SARS-CoV M<sup>pro</sup> with Enhanced Activity: Application as a Novel Tag-Cleavage Endopeptidase for Protein Overproduction. *J. Mol. Biol.* **2007**, *366* (3), 965–975.
- (173) Yang, H.; Xie, W.; Xue, X.; Yang, K.; Ma, J.; Liang, W.; Zhao, Q.; Zhou, Z.; Pei, D.; Ziebuhr, J.; et al. Design of Wide-Spectrum Inhibitors Targeting Coronavirus Main Proteases. *PLoS Biol.* **2005**, *3* (10), e324.
- (174) Ludewig, S. Entwicklung von Cysteinprotease-Assays zur Validierung von Cysteinprotease-Inhibitoren am Beispiel der SARS-CoV Hauptprotease, Dissertation, Technische Universität Braunschweig, Germany, 2011.
- (175) Ma, C.; Hu, Y.; Townsend, J. A.; Lagarias, P. I.; Marty, M. T.; Kolocouris, A.; Wang, J. Ebselen, Disulfiram, Carmofur, PX-12, Tideglusib, and Shikonin Are Nonspecific Promiscuous SARS-CoV-2 Main Protease Inhibitors. *ACS Pharmacol. Transl. Sci.* **2020**, *3* (6), 1265–1277.
- (176) Grum-Tokars, V.; Ratia, K.; Begaye, A.; Baker, S. C.; Mesecar, A. D. Evaluating the 3C-



- like Protease Activity of SARS-Coronavirus: Recommendations for Standardized Assays for Drug Discovery. *Virus Res.* **2008**, *133* (1), 63–73.
- (177) Behnam, M. A. M.; Klein, C. D. Inhibitor Potency and Assay Conditions: A Case Study on SARS-CoV-2main Protease. *Proc. Natl. Acad. Sci. U. S. A.* **2021**, *118* (36), e2106095118.
- (178) O'Brien, A.; Chen, D.-Y.; Hackbart, M.; Close, B. J.; O'Brien, T. E.; Saeed, M.; Baker, S. C. Detecting SARS-CoV-2 3CL<sup>pro</sup> Expression and Activity Using a Polyclonal Antiserum and a Luciferase-Based Biosensor. *Virology* **2021**, *556*, 73–78.
- (179) Kilianski, A.; Mielech, A. M.; Deng, X.; Baker, S. C. Assessing Activity and Inhibition of Middle East Respiratory Syndrome Coronavirus Papain-Like and 3C-Like Proteases Using Luciferase-Based Biosensors. *J. Virol.* **2013**, *87* (21), 11955–11962.
- (180) Froggatt, H. M.; Heaton, B. E.; Heaton, N. S. Development of a Fluorescence-Based, High-Throughput SARS-CoV-2 3CL<sup>pro</sup> Reporter Assay. *J. Virol.* **2020**, *94* (22), e01265-20.
- (181) Hattori, S. I.; Higashi-Kuwata, N.; Hayashi, H.; Allu, S. R.; Raghavaiah, J.; Bulut, H.; Das, D.; Anson, B. J.; Lendy, E. K.; Takamatsu, Y.; et al. A Small Molecule Compound with an Indole Moiety Inhibits the Main Protease of SARS-CoV-2 and Blocks Virus Replication. *Nat. Commun.* **2021**, *12* (1), 668.
- (182) Tripathi, P. K.; Upadhyay, S.; Singh, M.; Raghavendhar, S.; Bhardwaj, M.; Sharma, P.; Patel, A. K. Screening and Evaluation of Approved Drugs as Inhibitors of Main Protease of SARS-CoV-2. *Int. J. Biol. Macromol.* **2020**, *164*, 2622–2631.
- (183) Huynh, K.; Partch, C. L. Analysis of Protein Stability and Ligand Interactions by Thermal Shift Assay. *Curr. Protoc. Protein Sci.* **2015**, *79*, 28.9.1-28.9.14.
- (184) Jerabek-Willemsen, M.; André, T.; Wanner, R.; Roth, H. M.; Duhr, S.; Baaske, P.; Breitsprecher, D. MicroScale Thermophoresis: Interaction Analysis and Beyond. *J. Mol. Struct.* **2014**, *1077*, 101–113.
- (185) Papaj, K.; Spsychalska, P.; Kapica, P.; Fischer, A.; Nowak, J.; Bzówka, M.; Sellner, M.; Lill, M. A.; Smieško, M.; Góra, A. Evaluation of Xa Inhibitors as Potential Inhibitors of the SARS-CoV-2 M<sup>pro</sup> Protease. *PLoS One* **2022**, *17* (1), e0262482.
- (186) Mahdi, M.; Mótyán, J. A.; Szojka, Z. I.; Golda, M.; Miczi, M.; Tózsér, J. Analysis of the Efficacy of HIV Protease Inhibitors against SARS-CoV-2's Main Protease. *Virol. J.* **2020**, *17* (1), 190.
- (187) Malla, T. R.; Tumber, A.; John, T.; Brewitz, L.; Strain-Damerell, C.; Owen, C. D.; Lukacik, P.; Chan, H. T. H.; Maheswaran, P.; Salah, E.; et al. Mass Spectrometry Reveals Potential of  $\beta$ -Lactams as SARS-CoV-2 M<sup>pro</sup> Inhibitors. *Chem. Commun. (Cambridge, U. K.)* **2021**, *57* (12), 1430–1433.
- (188) Hoffmann, M.; Kleine-Weber, H.; Schroeder, S.; Krüger, N.; Herrler, T.; Erichsen, S.; Schiergens, T. S.; Herrler, G.; Wu, N.-H.; Nitsche, A.; et al. SARS-CoV-2 Cell Entry Depends on ACE2 and TMPRSS2 and Is Blocked by a Clinically Proven Protease

- Inhibitor. *Cell* **2020**, *181* (2), 271–280.
- (189) Hoffman, R. L.; Kania, R. S.; Brothers, M. A.; Davies, J. F.; Ferre, R. A.; Gajiwala, K. S.; He, M.; Hogan, R. J.; Kozminski, K.; Li, L. Y.; et al. Discovery of Ketone-Based Covalent Inhibitors of Coronavirus 3CL Proteases for the Potential Therapeutic Treatment of COVID-19. *J. Med. Chem.* **2020**, *63* (21), 12725–12747.
- (190) Ghosh, A. K.; Gong, G.; Grum-Tokars, V.; Mulhearn, D. C.; Baker, S. C.; Coughlin, M.; Prabhakar, B. S.; Sleeman, K.; Johnson, M. E.; Mesecar, A. D. Design, Synthesis and Antiviral Efficacy of a Series of Potent Chloropyridyl Ester-Derived SARS-CoV 3CL<sup>pro</sup> Inhibitors. *Bioorganic Med. Chem. Lett.* **2008**, *18* (20), 5684–5688.
- (191) Hattori, S.-I.; Higshi-Kuwata, N.; Raghavaiah, J.; Das, D.; Bulut, H.; Davis, D. A.; Takamatsu, Y.; Matsuda, K.; Takamune, N.; Kishimoto, N.; et al. GRL-0920, an Indole Chloropyridinyl Ester, Completely Blocks SARS-CoV-2 Infection. *mBio* **2020**, *11* (4), e01833-20.
- (192) Jacobs, J.; Grum-Tokars, V.; Zhou, Y.; Turlington, M.; Saldanha, S. A.; Chase, P.; Egger, A.; Dawson, E. S.; Baez-Santos, Y. M.; Tomar, S.; et al. Discovery, Synthesis, and Structure-Based Optimization of a Series of *N*-(*tert*-Butyl)-2-(*N*-Arylamido)-2-(Pyridin-3-yl) Acetamides (ML188) as Potent Noncovalent Small Molecule Inhibitors of the Severe Acute Respiratory Syndrome Coronavirus (SARS-CoV) 3CL Protease. *J. Med. Chem.* **2013**, *56* (2), 534–546.
- (193) Ghosh, A. K.; Brindisi, M.; Shahabi, D.; Chapman, M. E.; Mesecar, A. D. Drug Development and Medicinal Chemistry Efforts Toward SARS-Coronavirus and Covid-19 Therapeutics. *ChemMedChem* **2020**, *15* (11), 907–932.
- (194) Pillaiyar, T.; Meenakshisundaram, S.; Manickam, M. Recent Discovery and Development of Inhibitors Targeting Coronaviruses. *Drug Discovery Today* **2020**, *25* (4), 668–688.
- (195) Ng, T. I.; Correia, I.; Seagal, J.; DeGoey, D. A.; Schrimpf, M. R.; Hardee, D. J.; Noey, E. L.; Kati, W. M. Antiviral Drug Discovery for the Treatment of COVID-19 Infections. *Viruses* **2022**, *14* (5), 961.
- (196) De Vries, M.; Mohamed, A. S.; Prescott, R. A.; Valero-Jimenez, A. M.; Desvignes, L.; O'Connor, R.; Steppan, C.; Devlin, J. C.; Ivanova, E.; Herrera, A.; et al. A Comparative Analysis of SARS-CoV-2 Antivirals Characterizes 3CL pro Inhibitor PF-00835231 as a Potential New Treatment for COVID-19. *J. Virol.* **2021**, *95* (10), e01819-20.
- (197) Boras, B.; Jones, R. M.; Anson, B. J.; Arenson, D.; Aschenbrenner, L.; Bakowski, M. A.; Beutler, N.; Binder, J.; Chen, E.; Eng, H.; et al. Preclinical Characterization of an Intravenous Coronavirus 3CL Protease Inhibitor for the Potential Treatment of COVID19. *Nat. Commun.* **2021**, *12* (1), 6055.
- (198) Ullrich, S.; Ekanayake, K. B.; Otting, G.; Nitsche, C. Main Protease Mutants of SARS-CoV-2 Variants Remain Susceptible to Nirmatrelvir. *Bioorg. Med. Chem. Lett.* **2022**, *62*, 128629.
- (199) Pfizer. Pfizer's Novel COVID-19 Oral Antiviral Treatment Candidate Reduced Risk

- of Hospitalization or Death by 89% in Interim Analysis of Phase 2/3 EPIC-HR Study. <https://www.pfizer.com/news/press-release/press-release-detail/pfizers-novel-covid-19-oral-antiviral-treatment-candidate>. (accessed June 21, 2022)
- (200) Vuong, W.; Khan, M. B.; Fischer, C.; Arutyunova, E.; Lamer, T.; Shields, J.; Saffran, H. A.; McKay, R. T.; van Belkum, M. J.; Joyce, M. A.; et al. Feline Coronavirus Drug Inhibits the Main Protease of SARS-CoV-2 and Blocks Virus Replication. *Nat. Commun.* **2020**, *11* (1), 5409.
- (201) Kim, Y.; Liu, H.; Galasiti Kankanamalage, A. C.; Weerasekara, S.; Hua, D. H.; Groutas, W. C.; Chang, K. O.; Pedersen, N. C. Reversal of the Progression of Fatal Coronavirus Infection in Cats by a Broad-Spectrum Coronavirus Protease Inhibitor. *PLoS Pathog.* **2016**, *12* (3), e1005531.
- (202) Kitamura, N.; Sacco, M. D.; Ma, C.; Hu, Y.; Townsend, J. A.; Meng, X.; Zhang, F.; Zhang, X.; Ba, M.; Szeto, T.; et al. Expedited Approach toward the Rational Design of Noncovalent SARS-CoV-2 Main Protease Inhibitors. *J. Med. Chem.* **2022**, *65* (4), 2848–2865.
- (203) Quan, B.-X.; Shuai, H.; Xia, A.-J.; Hou, Y.; Zeng, R.; Liu, X.-L.; Lin, G.-F.; Qiao, J.-X.; Li, W.-P.; Wang, F.-L.; et al. An Orally Available Mpro Inhibitor Is Effective against Wild-Type SARS-CoV-2 and Variants Including Omicron. *Nat. Microbiol.* **2022**, *7* (5), 716–725.
- (204) Ghosh, A. K.; Raghavaiah, J.; Shahabi, D.; Yadav, M.; Anson, B. J.; Lendy, E. K.; Hattori, S.-I.; Higashi-Kuwata, N.; Mitsuya, H.; Mesecar, A. D. Indole Chloropyridinyl Ester-Derived SARS-CoV-2 3CL<sup>pro</sup> Inhibitors: Enzyme Inhibition, Antiviral Efficacy, Structure–Activity Relationship, and X-Ray Structural Studies. *J. Med. Chem.* **2021**, *64* (19), 14702–14714.
- (205) Zhang, J.; Pettersson, H. I.; Huitema, C.; Niu, C.; Yin, J.; James, M. N. G.; Eltis, L. D.; Vederas, J. C. Design, Synthesis, and Evaluation of Inhibitors for Severe Acute Respiratory Syndrome 3C-like Protease Based on Phthalhydrazide Ketones or Heteroaromatic Esters. *J. Med. Chem.* **2007**, *50* (8), 1850–1864.
- (206) Wu, C.-Y.; King, K.-Y.; Kuo, C.-J.; Fang, J.-M.; Wu, Y.-T.; Ho, M.-Y.; Liao, C.-L.; Shie, J.-J.; Liang, P.-H.; Wong, C.-H. Stable Benzotriazole Esters as Mechanism-Based Inactivators of the Severe Acute Respiratory Syndrome 3CL Protease. *Chem. Biol.* **2006**, *13* (3), 261–268.
- (207) Ullrich, S.; Sasi, V. M.; Mahawaththa, M. C.; Ekanayake, K. B.; Morewood, R.; George, J.; Shuttleworth, L.; Zhang, X.; Whitefield, C.; Otting, G.; et al. Challenges of Short Substrate Analogues as SARS-CoV-2 Main Protease Inhibitors. *Bioorg. Med. Chem. Lett.* **2021**, *50*, 128333.
- (208) Kreutzer, A. G.; Krumberger, M.; Diessner, E. M.; Parrocha, C. M. T.; Morris, M. A.; Guaglianone, G.; Butts, C. T.; Nowick, J. S. A Cyclic Peptide Inhibitor of the SARS-CoV-2 Main Protease. *Eur. J. Med. Chem.* **2021**, *221*, 113530.
- (209) Zhou, L.; Liu, Y.; Zhang, W.; Wei, P.; Huang, C.; Pei, J.; Yuan, Y.; Lai, L. Isatin

- Compounds as Noncovalent SARS Coronavirus 3C-like Protease Inhibitors. *J. Med. Chem.* **2006**, *49* (12), 3440–3443.
- (210) Liu, P.; Liu, H.; Sun, Q.; Liang, H.; Li, C.; Deng, X.; Liu, Y.; Lai, L. Potent Inhibitors of SARS-CoV-2 3C-like Protease Derived from *N*-Substituted Isatin Compounds. *Eur. J. Med. Chem.* **2020**, *206*, 112702.
- (211) Lockbaum, G. J.; Reyes, A. C.; Lee, J. M.; Tilwawala, R.; Nalivaika, E. A.; Ali, A.; Yilmaz, N. K.; Thompson, P. R.; Schiffer, C. A. Crystal Structure of SARS-CoV-2 Main Protease in Complex with the Non-Covalent Inhibitor ML188. *Viruses* **2021**, *13* (2), 174.
- (212) Unoh, Y.; Uehara, S.; Nakahara, K.; Nobori, H.; Yamatsu, Y.; Yamamoto, S.; Maruyama, Y.; Taoda, Y.; Kasamatsu, K.; Suto, T.; et al. Discovery of S-217622, a Noncovalent Oral SARS-CoV-2 3CL Protease Inhibitor Clinical Candidate for Treating COVID-19. *J. Med. Chem.* **2022**, *65* (9), 6499–6512.
- (213) Han, S. H.; Goins, C. M.; Arya, T.; Shin, W.-J.; Maw, J.; Hooper, A.; Sonawane, D. P.; Porter, M. R.; Bannister, B. E.; Crouch, R. D.; et al. Structure-Based Optimization of ML300-Derived, Noncovalent Inhibitors Targeting the Severe Acute Respiratory Syndrome Coronavirus 3CL Protease (SARS-CoV-2 3CL<sup>pro</sup>). *J. Med. Chem.* **2022**, *65* (4), 2880–2904.
- (214) Su, H.-X.; Yao, S.; Zhao, W.-F.; Li, M.-J.; Liu, J.; Shang, W.-J.; Xie, H.; Ke, C.-Q.; Hu, H.-C.; Gao, M.-N.; et al. Anti-SARS-CoV-2 Activities in Vitro of Shuanghuanglian Preparations and Bioactive Ingredients. *Acta Pharmacol. Sin.* **2020**, *41* (9), 1167–1177.
- (215) The COVID Moonshot Consortium, Achdout, H.; Aimon, A.; Bar-David, E.; Barr, H.; Ben-Shmuel, A.; Bennett, J.; Boby, M. L.; Borden, B.; Bowman, G. R.; et al. Open Science Discovery of Oral Non-Covalent SARS-CoV-2 Main Protease Inhibitor Therapeutics. *BioRxiv*, [Online preprint]. DOI: 10.1101/2020.10.29.339317. Published Online: January 30, 2022.
- (216) Zhang, C.-H.; Stone, E. A.; Deshmukh, M.; Ippolito, J. A.; Ghahremanpour, M. M.; Tirado-Rives, J.; Spasov, K. A.; Zhang, S.; Takeo, Y.; Kudalkar, S. N.; et al. Potent Noncovalent Inhibitors of the Main Protease of SARS-CoV-2 from Molecular Sculpting of the Drug Perampanel Guided by Free Energy Perturbation Calculations. *ACS Cent. Sci.* **2021**, *7* (3), 467–475.
- (217) Wei, P.; Fan, K.; Chen, H.; Ma, L.; Huang, C.; Tan, L.; Xi, D.; Li, C.; Liu, Y.; Cao, A.; et al. The N-Terminal Octapeptide Acts as a Dimerization Inhibitor of SARS Coronavirus 3C-like Proteinase. *Biochem. Biophys. Res. Commun.* **2006**, *339* (3), 865–872.
- (218) Silvestrini, L.; Belhaj, N.; Comez, L.; Gerelli, Y.; Lauria, A.; Libera, V.; Mariani, P.; Marzullo, P.; Ortore, M. G.; Palumbo Piccionello, A.; et al. The Dimer-Monomer Equilibrium of SARS-CoV-2 Main Protease Is Affected by Small Molecule Inhibitors. *Sci. Rep.* **2021**, *11* (1), 9283.
- (219) Baqi, Y. Ecto-Nucleotidase Inhibitors: Recent Developments in Drug Discovery. *Mini-Rev. Med. Chem.* **2015**, *15* (1), 21–33.

- (220) Namasivayam, V.; Lee, S.-Y.; Müller, C. E. The Promiscuous Ectonucleotidase NPP1: Molecular Insights into Substrate Binding and Hydrolysis. *Biochim. Biophys. Acta* **2017**, *1861* (3), 603–614.
- (221) Malik, E. M.; Müller, C. E. Anthraquinones As Pharmacological Tools and Drugs. *Med. Res. Rev.* **2016**, *36* (4), 704–748.
- (222) Weyler, S.; Baqi, Y.; Hillmann, P.; Kaulich, M.; Hunder, A. M.; Müller, I. A.; Müller, C. E. Combinatorial Synthesis of Anilinoanthraquinone Derivatives and Evaluation as Non-Nucleotide-Derived P2Y<sub>2</sub> Receptor Antagonists. *Bioorg. Med. Chem. Lett.* **2008**, *18* (1), 223–227.
- (223) Baqi, Y.; Müller, C. E. Convergent Synthesis of the Potent P2Y Receptor Antagonist MG 50-3-1 Based on a Regioselective Ullmann Coupling Reaction. *Molecules* **2012**, *17* (3), 2599–2615.
- (224) Baqi, Y.; Hausmann, R.; Rosefort, C.; Rettinger, J.; Schmalzing, G.; Müller, C. E. Discovery of Potent Competitive Antagonists and Positive Modulators of the P2X<sub>2</sub> Receptor. *J. Med. Chem.* **2011**, *54* (3), 817–830.
- (225) Baqi, Y.; Lee, S.-Y.; Iqbal, J.; Ripphausen, P.; Lehr, A.; Scheiff, A. B.; Zimmennann, H.; Bajorath, J.; Müller, C. E. Development of Potent and Selective Inhibitors of Ecto-5'-Nucleotidase Based on an Anthraquinone Scaffold. *J. Med. Chem.* **2010**, *53* (5), 2076–2086.
- (226) Vitiello, L.; Gorini, S.; Rosano, G.; La Sala, A. Immunoregulation through Extracellular Nucleotides. *Blood* **2012**, *120* (3), 511–518.
- (227) Ludwig, J. A New Route to Nucleoside 5'-Triphosphates. *Acta Biochim Biophys Acad Sci Hung.* **1981**, *16* (3-4), 131–133.
- (228) Marsilje, T. H.; Pei, W.; Chen, B.; Lu, W.; Uno, T.; Jin, Y.; Jiang, T.; Kim, S.; Li, N.; Warmuth, M.; et al. Synthesis, Structure-Activity Relationships, and in Vivo Efficacy of the Novel Potent and Selective Anaplastic Lymphoma Kinase (ALK) Inhibitor 5-Chloro-N2-(2-isopropoxy-5-methyl-4-(piperidin-4-yl)phenyl)-N4-(2-(isopropylsulfonyl)phenyl)pyrimidine-2,4-diamine (LDK378) Currently in Phase 1 and 2 Clinical Trials. *J. Med. Chem.* **2013**, *56* (14), 5675–5690.
- (229) Shaw, A. T.; Kim, D.-W.; Mehra, R.; Tan, D. S. W.; Felip, E.; Chow, L. Q. M.; Camidge, D. R.; Vansteenkiste, J.; Sharma, S.; De Pas, T.; et al. Ceritinib in ALK-Rearranged Non-Small-Cell Lung Cancer. *N. Engl. J. Med.* **2014**, *370* (13), 1189–1197.
- (230) Drug approval package: Zykadia (ceritinib) Capsules, Novartis Pharmaceuticals Corporation, Application No.: 205755, Approval Date: 4/29/2014. [https://www.accessdata.fda.gov/drugsatfda\\_docs/nda/2014/205755Orig1s000T0C.cfm](https://www.accessdata.fda.gov/drugsatfda_docs/nda/2014/205755Orig1s000T0C.cfm).
- (231) Mehta, S.; Fiorelli, R.; Bao, X.; Pennington-Krygier, C.; Derogatis, A.; Kim, S.; Yoo, W.; Li, J.; Sanai, N. A Phase 0 Trial of Ceritinib in Patients with Brain Metastases and Recurrent Glioblastoma. *Clin. Cancer Res.* **2022**, *28* (2), 289–297.

- (232) Kawauchi, D.; Takahashi, M.; Satomi, K.; Yamamuro, S.; Kobayashi, T.; Uchida, E.; Honda-Kitahara, M.; Narita, Y.; Iwadate, Y.; Ichimura, K.; et al. The ALK Inhibitors, Alectinib and Ceritinib, Induce ALK-Independent and STAT3-Dependent Glioblastoma Cell Death. *Cancer Sci.* **2021**, *112* (6), 2442–2453.
- (233) Kuenzi, B. M.; Rix, L. L. R.; Stewart, P. A.; Fang, B.; Kinose, F.; Bryant, A. T.; Boyle, T. A.; Koomen, J. M.; Haura, E. B.; Rix, U.; et al. Polypharmacology-Based Ceritinib Repurposing Using Integrated Functional Proteomics. *Nat. Chem. Biol.* **2017**, *13* (12), 1222–1231.
- (234) Petrazzuolo, A.; Perez-Lanzon, M.; Martins, I.; Liu, P.; Kepp, O.; Minard-Colin, V.; Maiuri, M. C.; Kroemer, G. Pharmacological Inhibitors of Anaplastic Lymphoma Kinase (ALK) Induce Immunogenic Cell Death through on-Target Effects. *Cell Death Dis.* **2021**, *12* (8), 713.
- (235) Coelho, C.; Gallo, G.; Campos, C. B.; Hardy, L.; Würtele, M. Biochemical Screening for SARS-CoV-2 Main Protease Inhibitors. *PLoS One* **2020**, *15* (10), e0240079.
- (236) McGovern, S. L.; Helfand, B. T.; Feng, B.; Shoichet, B. K. A Specific Mechanism of Nonspecific Inhibition. *J. Med. Chem.* **2003**, *46* (20), 4265–4272.
- (237) O'Donnell, H. R.; Tummino, T. A.; Bardine, C.; Craik, C. S.; Shoichet, B. K. Colloidal Aggregators in Biochemical SARS-CoV-2 Repurposing Screens. *J. Med. Chem.* **2021**, *64* (23), 17530–17539.
- (238) Cheng, Y. C.; Prusoff, W. H. Relation between the Inhibition Constant  $K_i$  and the Concentration of Inhibitor Which Causes Fifty Percent Inhibition ( $IC_{50}$ ) of an Enzymatic Reaction. *Biochem. Pharmacol.* **1973**, *22*, 3099–3108.
- (239) Duffy, S.; Sykes, M. L.; Jones, A. J.; Shelper, T. B.; Simpson, M.; Lang, R.; Poulsen, S.-A.; Sleeb, B. E.; Avery, V. M. Screening the Medicines for Malaria Venture Pathogen Box across Multiple Pathogens Reclassifies Starting Points for Open-Source Drug Discovery. *Antimicrob. Agents Chemother.* **2017**, *61* (9), e00379-17.
- (240) Rothan, H. A.; Stone, S.; Natekar, J.; Kumari, P.; Arora, K.; Kumar, M. The FDA-Approved Gold Drug Auranofin Inhibits Novel Coronavirus (SARS-CoV-2) Replication and Attenuates Inflammation in Human Cells. *Virology* **2020**, *547*, 7–11.
- (241) Kuzikov, M.; Costanzi, E.; Reinshagen, J.; Esposito, F.; Vangeel, L.; Wolf, M.; Ellinger, B.; Claussen, C.; Geisslinger, G.; Corona, A.; et al. Identification of Inhibitors of SARS-CoV-2 3CL-Pro Enzymatic Activity Using a Small Molecule in Vitro Repurposing Screen. *ACS Pharmacol. Transl. Sci.* **2021**, *4* (3), 1096–1110.
- (242) Günther, S.; Reinke, P. Y. A.; Fernández-García, Y.; Lieske, J.; Lane, T. J.; Ginn, H. M.; Koua, F. H. M.; Ehrt, C.; Ewert, W.; Oberthuer, D.; et al. X-ray Screening Identifies Active Site and Allosteric Inhibitors of SARS-CoV-2 Main Protease. *Science* **2021**, *372* (6542), 642–646.
- (243) Yang, K. S.; Alex Kuo, S.-T.; Blankenship, L. R.; Geng, Z. Z.; Li, S. G.; Russell, D. H.; Yan, X.; Xu, S.; Liu, W. R. Repurposing Halicin as a Potent Covalent Inhibitor for the SARS-CoV-2 Main Protease. *Curr. Res. Chem. Biol.* **2022**, *2*, 100025.

- (244) Malla, T. R.; Tumber, A.; John, T.; Brewitz, L.; Strain-Damerell, C.; Owen, C. D.; Lukacik, P.; Chan, H. T. H.; Maheswaran, P.; Salah, E.; et al. Supporting Information: Mass Spectrometry Reveals Potential of  $\beta$ -Lactams as SARS-CoV-2 M<sup>pro</sup> Inhibitors. *Chem. Commun. (Cambridge, U. K.)* **2021**, 57 (12), 1430-1433.
- (245) Thanigaimalai, P.; Konno, S.; Yamamoto, T.; Koiwai, Y.; Taguchi, A.; Takayama, K.; Yakushiji, F.; Akaji, K.; Chen, S.-E.; Naser-Tavakolian, A.; et al. Development of Potent Dipeptide-Type SARS-CoV 3CL Protease Inhibitors with Novel P3 Scaffolds: Design, Synthesis, Biological Evaluation, and Docking Studies. *Eur. J. Med. Chem.* **2013**, 68, 372–384.
- (246) Konno, S.; Thanigaimalai, P.; Yamamoto, T.; Nakada, K.; Kakiuchi, R.; Takayama, K.; Yamazaki, Y.; Yakushiji, F.; Akaji, K.; Kiso, Y.; et al. Design and Synthesis of New Tripeptide-Type SARS-CoV 3CL Protease Inhibitors Containing an Electrophilic Arylketone Moiety. *Bioorganic Med. Chem.* **2013**, 21 (2), 412–424.
- (247) Konno, S.; Kobayashi, K.; Senda, M.; Funai, Y.; Seki, Y.; Tamai, I.; Schäkel, L.; Sakata, K.; Pillaiyar, T.; Taguchi, A.; et al. 3CL Protease Inhibitors with an Electrophilic Arylketone Moiety as Anti-SARS-CoV-2 Agents. *J. Med. Chem.* **2022**, 65 (4), 2926–2939.

## 9 Acknowledgements

In this section I want to express my gratitude towards all, that helped me in the generation of this thesis and provided support along the way.

Zuerst möchte ich meiner Doktormutter und wissenschaftlichen Betreuerin dieser Arbeit Prof. Dr. Christa E. Müller danken. Liebe Christa, ich danke Dir für die Möglichkeit mit Dir zusammen diese interessanten Projekte zu erforschen und meine Doktorarbeit in Deinem Arbeitskreis anzufertigen. Ich habe unsere Zusammenarbeit sehr genossen und kann nur feststellen, dass ich unter deiner Forder- und Förderung gewachsen bin. Ich danke Dir für Dein Vertrauen in mich und meine wissenschaftliche Arbeit, die das eigenverantwortliche Arbeiten unterstützt und eine erfolgreiche Zusammenarbeit ermöglicht hat. Du hast mir den Übergang vom Staatsexamen zur wissenschaftlichen Arbeit erleichtert und gehst stets als Vorbild voran.

Bei Prof. Dr. Bendas möchte ich mich für die Anfertigung des Zweitgutachtens und der Teilnahme an meiner Prüfungskommission bedanken. Es freut mich festzustellen, dass ich meine Laufbahn im pharmazeutischen Institut mit einer Prüfung bei Ihnen begonnen habe und beenden werde.

Ich bedanke mich bei Prof. Dr. Ulrich Jaehde und PD Dr. Marianne Engeser für die Mitwirkung in meiner Prüfungskommission.

I want to thank all my present and former colleagues in the research group of Prof. Christa E. Müller for the collaborative work and discussions over coffee and beer that not only contributed to the work of this thesis, but created a pleasant and collegial working environment.

In particular, I want to thank Dr. Constanze C. Schmies, Chunyang Bi, Dr. Vigneshwaran Namasivayam, Salahuddin Mirza, Riham Idris, Vittoria Lopez, Dr. Sang-Yong Lee, Dr. Georg Rolshoven and my master student Areso Ahmadsay for the mutual support working on the field of ecto-nucleotidases. In that context, I express my gratitude towards the DFG for funding the project A11 in the SFB1328 on CD39 modulators, which allowed me to study and present our work on this interesting topic, as well as financing a research stay in Prof. Wätzing's group in Braunschweig.



To all co-workers from the groups of Prof. Christa E. Müller and Prof. Michael Gütschow, including the professors: I genuinely enjoyed our joined efforts and interdisciplinary teamwork, that enabled the rapid development of the SARS-CoV-2 M<sup>pro</sup> project. Especially, the close collaboration with Carina on the assay development and discussions with Angelo were highlights of my time at this institute.

An Dr. Mathias Weigt, Vladlena, Sahel, Tim und Jim: es hat enormen Spaß gemacht das Praktikum des 2. Semesters mit Euch zu betreuen!

Ich danke der Graduiertenschule BIGSDrugS für die Finanzierung meiner Teilnahme an der "Frontiers in Medicinal Chemistry online conference of 2021" und insbesondere der Koordinatorin Dorothee Müssemeier für die Organisation der spannenden Vorträge, sowie der sozialen Zusammenkünfte.

Meine Bürokollegen Jan, Riham und (Ehrenbürokollege) Robin haben in zahlreichen Kaffee- und Mittagspausen dazu beigetragen, die Motivation hochzuhalten. Lieber Jan und lieber Robin wir hatten die vielfältigsten Diskussionen, einen horizonterweiternden Lesezirkel, und auch außerhalb der Arbeit immer eine gute Zeit miteinander! Auf die Freundschaft, Prost!

Ich danke meiner Familie, die mich auf meinem Weg bis hier begleitet hat: Meiner Oma Gertrud, die mich mit ihren Werten geprägt hat und mir durch Kochen und Backen die Grundlagen der strukturierten Laborarbeit beigebracht hat; und meinen Eltern für ihre Erziehung, die Neugier für Naturwissenschaften und die Ermöglichung des Pharmazie-Studiums.

Meinen guten Freundinnen: Anne, Jasmin, Johanna, Eva, Caro, Nici, Anne, Sarah, Vladlena, Carina und Pia, die die Letzen Jahre Zeit für mich hatten und mich immer wieder an die Welt außerhalb der Promotion erinnert haben danke ich von Herzen.

Zu guter Letzt danke ich meinem Partner Tobi. Ich bin sehr glücklich, dass ich vor annähernd 10 Jahren noch ein Bierchen mit Dir geext habe. Du hast mich durch alle schönen Stunden und auch die stressigen Prüfungsphasen begleitet und mich durch Deine Art beruhigt und bestärkt. Es ist schön, dass Du bei mir bist und wir unsere Zukunft gemeinsam gestalten werden!



## 10 Appendices

### 10.1 Featured publications

The present work is a compilation of three peer-reviewed journal articles, together covering the results obtained within this dissertation:

1) Younis Baqi, Mahmoud Rashed, Laura Schäkel, Enas M. Malik, Julie Pelletier, Jean Sévigny, Amelie Fiene and Christa E. Müller. Development of Anthraquinone Derivatives as Ectonucleoside Triphosphate Diphosphohydrolase(NTPDase) Inhibitors With Selectivity for NTPDase2 and NTPDase3. *Front. Pharmacol.* **2020** 11:1282. DOI: <https://doi.org/10.3389/fphar.2020.01282>

The published article is reproduced in Chapter 3.1 of the dissertation.

2) Laura Schäkel, Constanze C. Schmies, Riham M. Idris, Xihuan Luo, Sang-Yong Lee, Vittoria Lopez, Salahuddin Mirza, The Hung Vu, Julie Pelletier, Jean Sévigny, Vigneshwaran Namasivayam and Christa E. Müller. Nucleotide Analog ARL67156 as a Lead Structure for the Development of CD39 and Dual CD39/CD73 Ectonucleotidase Inhibitors. *Front Pharmacol* **2020** Sep 8;11:1294. DOI: <https://doi.org/10.3389/fphar.2020.01294>

The published article is reproduced in Chapter 3.2 of the dissertation.

3) Laura Schäkel, Salahuddin Mirza, Markus Pietsch, Sang-Yong Lee, Tim Keuler, Katharina Sylvester, Julie Pelletier, Jean Sévigny, Thanigaimalai Pillaiyar, Vigneshwaran Namasivayam, Michael Gütschow, Christa E. Müller. 2-Substituted Thienotetrahydropyridine Derivatives: Allosteric Ectonucleotidase Inhibitors. *Arch Pharm (Weinheim)* **2021** Dec;354(12):e2100300. DOI: <https://doi.org/10.1002/ardp.202100300>.

The published article is reproduced in Chapter 3.3 of the dissertation.

4) Laura Schäkel, Salahuddin Mirza, Riekje Winzer, Vittoria Lopez, Riham Idris, Haneen Al-Hroub, Julie Pelletier, Jean Sévigny, Eva Tolosa and Christa E. Müller. Protein Kinase Inhibitor Ceritinib Blocks Ectonucleotidase CD39 – a Promising Target for Cancer Immunotherapy. *Journal for ImmunoTherapy of Cancer* **2022** 10:e004660. DOI: <https://doi.org/10.1136/jitc-2022-004660>

The published article is reproduced in Chapter 3.4 of the dissertation.

5) Sho Konno, Kiyotaka Kobayashi, Miki Senda, Yuta Funai, Yuta Seki, Ikumi Tamai, Laura Schäkel, Kyoussuke Sakata, Thanigaimalai Pillaiyar, Akihiro Taguchi, Atsuhiko Taniguchi, Michael Gütschow, Christa E. Müller, Koh Takeuchi, Mikako Hirohama, Atsushi Kawaguchi, Masaki Kojima, Toshiya Senda, Yoshiyuki Shirasaka, Wataru Kamitani, and Yoshio Hayashi. 3CL Protease Inhibitors with an Electrophilic Arylketone Moiety as Anti-SARS-CoV-2 Agents. *J Med Chem* **2022** Feb 24;65(4):2926-2939. DOI: <https://doi.org/10.1021/acs.jmedchem.1c00665>

The published article is reproduced in Chapter 5.1 of the dissertation.